

**Gypsum Scaling During  
Reverse Osmosis Desalination**  
—  
**Characterization and  
Effects of Natural Organic Matter**

Vom Promotionsausschuss der  
Technischen Universität Hamburg  
zur Erlangung des akademischen Grades  
Doktor-Ingenieur (Dr.-Ing.)

genehmigte Dissertation

von  
Jan Benecke

aus  
Berlin

2018

**Gutachter**

1. Gutachter: Prof. Dr.-Ing. Mathias Ernst
2. Gutachter: Prof. Dr. rer. nat. Harald Horn

**Vorsitzender des Prüfungsausschusses**

Prof. Dr.-Ing. habil. Dr. h.c. Stefan Heinrich

**Tag der mündlichen Prüfung**

16. August 2018

doi:10.15480/882.1835

---

## Acknowledgments

The results presented in this dissertation were obtained during my occupation as research and teaching assistant at the Institute for Water Resources and Water Supply of the Hamburg University of Technology (TUHH). During this time, I had the opportunity to collaborate with many different people and many of them have contributed to the successful completion of this dissertation. I am profoundly grateful to all of them for their contribution and support.

I would like to thank Prof. Dr.-Ing. Mathias Ernst for his supervision throughout the processes of obtaining the results and writing this dissertation and for giving me the freedom to pursue my research ideas. Many thanks to Prof. Dr. rer. nat. Harald Horn for co-reviewing this dissertation and for welcoming me to the recurring ‘Membrane Meetings’ at his Chair of Water Chemistry and Water Technology at the Karlsruhe Institute of Technology. I would also like to thank Prof. Dr.-Ing. habil. Dr. h.c. Stefan Heinrich for acting as chairman of the examination board.

For their inspiration, encouragement and advice, I would like to thank Dr.-Ing. Florencia Saravia, Dr.-Ing. Jochen Henkel and Prof. Tzahi Cath. Additional thanks to Florencia for organizing the recurring ‘Membrane Meetings’ in Karlsruhe and for providing me with ‘Hohlohsee’ water. Special thanks to Jochen and Dow Chemical for supplying me with membrane material. I would like to thank the Institute of Environmental Technology and Energy Economics of the TUHH and Dr. Joachim Gerth for giving me the opportunity to perform XRD analyses and for sharing their laboratory equipment.

The construction and automation of the experimental setups would not have been possible without the efficient support of the employees of the TUHH’s central research service, particularly Hans-Wilhelm Mehrkens and Heino Hagenah from the electrical workshop and Dirk Manning and his team from the mechanical workshop. Many thanks to the team of the TUHH’s electron microscopy unit for their support in SEM and EDX analyses.

I would like to thank all the bright M.Sc. and B.Sc. students, who spent countless hours in the lab and workshop to perform experiments and to assist in the construction and optimization of the experimental setups. Special thanks to Jelena (Rozova) Soltani, Alexander Soltani, Moritz Haas, Tjorven Struve, Lorena Gormsen, Fabian Baur, Christoph Bauernschmidt, Parisa Shaheen, Karen Mädler, Jakob Kämmler, Sarah Freericks, Maximilian Meyer and Jannes Westerman. It was a great pleasure to work with all of you.

I will forever be grateful to all my former colleagues at the Institute for Water Resources and Water Supply (TUHH) and the DVGW Research Centre TUHH. All of you contributed to the successful completion of this dissertation and I will take something away from the experiences that I have had with each of you. Special thanks to Dorota Bruniecka-Sulewski and Thorsten Dorsch for their exceptional support in all practical and laboratory manners and to Dr.-Ing. habil. Klaus Johannsen for his support in understanding water chemical aspects. I would like to thank Martin Schulz for having been the greatest office and team mate – I could not have done it without you!

Last and most important, I would like to thank my whole family and particularly my wife Friederike Benecke and my son Luke Benecke. Without all of you, none of this would have been possible. You have supported me throughout this challenging journey and have never lost your faith that I could finish what I started.



## Abstract

Reverse osmosis (RO) desalination of brackish water and seawater has been increasingly applied to augment water supplies in regions where freshwater is scarce or polluted. However, a serious limitation during RO desalination at high water recovery is membrane scaling due to the concentration and subsequent crystallization of sparingly soluble salts in the feed water stream (bulk crystallization) or directly on the membrane surface (surface crystallization). To date, interactions between RO membrane scaling and natural organic matter (NOM) at concentrations commonly found in natural waters (few  $\text{mg C}\cdot\text{l}^{-1}$ ) have been rarely investigated. The objective of this thesis is the systematic characterization of scaling by gypsum ( $\text{CaSO}_4\cdot 2\text{H}_2\text{O}$ ), representing one of the most problematic scale-forming salts in natural waters, and its interactions with different NOM sources using laboratory cross-flow RO desalination and stirred beaker crystallization experiments.

During RO desalination, the attained degree of supersaturation, the severity of concentration polarization and the hydraulic residence time determined the dominating scaling mechanism (bulk vs. surface crystallization). Complementary stirred beaker crystallization experiments demonstrated that induction and crystallization times of bulk crystallization are shorter at higher supersaturation. Investigations into the development and reproducibility of surface crystallization on RO membrane samples by real-time membrane surface imaging during desalination show that the availability and distribution of heteronucleation sites on the membrane surface are important parameters that affect the surface scaling behavior.

Selected NOM sources (alginate, bovine serum albumin, two humic acid sources of terrestrial origin and two aquatic NOM sources) prolonged induction and crystallization times of bulk crystallization in stirred beaker crystallization experiments. Retardation was consistently pronounced at higher NOM concentration. It is assumed that NOM adsorption onto nuclei and crystal faces was the relevant mechanism of retardation given that crystals were smaller and exhibited modified habits in the presence of NOM. Based on NOM characterization and previous studies, a combination rather than individual NOM properties are suggested to determine the NOM-specific retardation capability. Bulk crystallization during RO desalination was effectively retarded by NOM, however, strong fouling stimulated surface crystallization assumingly due to cake-enhanced concentration polarization and calcium ion attraction by the fouling layer.

Effects of NOM on surface crystallization were assessed by RO desalination experiments which enabled real-time membrane surface imaging and which were designed to discriminate between the effects of NOM fouling and those of dissolved NOM. The results show that surface crystal growth is significantly inhibited and distorted due to the adsorption of dissolved NOM onto crystal faces. Retardation was enhanced at increased NOM concentration and particularly strong for large humic substances with molecular weights between 5 kDa – 150 kDa. While moderate degrees of NOM fouling can affect heteronucleation and crystal growth, those effects are irrelevant in the presence of dissolved NOM. Only in cases of strong fouling layer formation by specific NOM fractions (e.g. soil-extracted humic acids with molecular sizes greater than 150 kDa), loss of RO performance is aggravated due to accelerated crystal growth assumingly due to enhanced supersaturation by cake-enhanced concentration polarization.

Although inhibition of gypsum scaling by a commercial phosphonic and polyacrylic acid-based antiscalant was considerably stronger, the results demonstrate that NOM is an effective natural antiscalant. The thesis contributes to the better understanding of membrane scaling by gypsum due to bulk and surface crystallization and its complex interactions with NOM. It suggests that NOM-supported scale inhibition can be considered as an alternative measure for scale control during membrane-based desalination of natural waters.



## **Table of Contents**

<b>Acknowledgments .....</b>	<b>I</b>
<b>Abstract.....</b>	<b>III</b>
<b>Table of Contents .....</b>	<b>V</b>
<b>1 Introduction.....</b>	<b>1</b>
1.1 Background .....	1
1.2 Objective and Structure of the Thesis .....	2
<b>2 Theoretical Background.....</b>	<b>3</b>
2.1 Reverse Osmosis for Desalination .....	3
2.2 Membrane Scaling During Reverse Osmosis Desalination .....	9
2.3 Gypsum Crystallization and Scaling.....	20
2.4 Properties and Effects of Natural Organic Matter .....	26
<b>3 Material and Methods .....</b>	<b>35</b>
3.1 Chemicals, Solutions and Materials.....	35
3.2 Experimental Setups and Procedures .....	38
3.3 Analyses.....	43
3.4 Calculations and Statistical Analyses .....	47
<b>4 Characterization of Gypsum Scaling .....</b>	<b>49</b>
4.1 Gypsum Scaling Mechanisms During RO Desalination.....	49
4.2 Gypsum Bulk Crystallization From Supersaturated Solution.....	53
4.3 Gypsum Surface Crystallization on RO Membranes.....	58
<b>5 Characterization of the Selected NOM Sources.....</b>	<b>69</b>
5.1 Molecular Size Distribution.....	69
5.2 Spectral Absorbance and Fluorescence Emission.....	73
5.3 Concentration of Acidic Functional Groups .....	74
<b>6 Effects of NOM on Gypsum Bulk Crystallization .....</b>	<b>77</b>
6.1 Effects of NOM Character and NOM Concentration .....	77
6.2 Effects of <i>pH</i> on Gypsum Bulk Crystallization in the Presence of NOM .....	85
6.3 Comparison of NOM Effects to Antiscalant Dosage.....	87
6.4 Effects of NOM on Gypsum Scaling by Bulk Crystallization During RO Desalination .....	88

<b>7</b>	<b>Effects of NOM on Gypsum Surface Crystallization on RO Membranes .....</b>	<b>93</b>
7.1	Effects of Membrane Pre-Fouling by NOM .....	93
7.2	Effects of Dissolved NOM.....	103
7.3	Comparison of NOM Effects to Antiscalant Dosage.....	114
<b>8</b>	<b>Conclusion .....</b>	<b>117</b>
8.1	Conclusions and Future Directions .....	117
8.2	Final Remarks and Implications for Practice .....	123
<b>A.</b>	<b>Appendix I – References and Lists .....</b>	<b>125</b>
	References .....	125
	List of Figures .....	140
	List of Tables .....	148
	Abbreviations and Quantities.....	151
<b>B.</b>	<b>Appendix II – Supplemental Material and Methods.....</b>	<b>154</b>
<b>C.</b>	<b>Appendix III – Lists of Conducted Experiments .....</b>	<b>157</b>
<b>D.</b>	<b>Appendix IV – Supplemental Data.....</b>	<b>160</b>
<b>E.</b>	<b>Appendix V – List of Publications.....</b>	<b>181</b>
<b>F.</b>	<b>Appendix VI – List of Supervised Student Theses .....</b>	<b>183</b>

# 1 Introduction

## 1.1 Background

Water, the Earth's most precious resource for life, is becoming increasingly scarce and contaminated [1–3]. Addressing the lack of sufficient and safe drinking water is among the most serious challenges of the twenty-first century [2]. Population growth, urbanization, industrialization and climate change further exacerbate the situation [1,4]. To alleviate the stresses on water supply, available measures, including water conservation and improved water resources management, need to be implemented [1]. However, these measures can only improve the use of existing freshwater resources, not increase them [1]. The only option to augment existing freshwater supplies beyond what is available from the hydrological water cycle, is the desalination of unconventional water sources, such as seawater, brackish water or wastewater [3].

At the end of 2015, approximately 18,000 desalination plants purified more than 86 million m<sup>3</sup> of water per day worldwide [5]. Compared to thermal desalination, state-of-the-art membrane-based desalination technologies are inherently more energy efficient [1] and produce water of superior quality [6]. Therefore, reverse osmosis (RO) has emerged as the prevalent desalination process [7] and represents the current benchmark for brackish and seawater desalination [1]. However, the crystallization of sparingly soluble salts in the feed water stream (bulk crystallization) or directly on the membrane surface (surface crystallization), referred to as membrane scaling, has always been a serious limitation in designing and operating RO systems especially at high product water recovery [8–10]. Membrane scaling can lead to severe flux decline, deterioration of solute rejection and membrane damage [10–13]. Among the various scale-forming salts, gypsum (CaSO<sub>4</sub>·2H<sub>2</sub>O) is one of the most common scaling sources of natural waters [9,10,14,15]. In addition, it cannot be controlled by *pH* adjustment and therefore requires the dosage of antiscalants, such as organic polymers [16–19]. Driven by the steadily growing number of operational RO desalination plants, the dosage of antiscalants and the subsequent discharge of concentrates into receiving water bodies has raised increased environmental concerns [16,20].

In addition to scale-forming ions, all natural waters contain natural organic matter (NOM), such as proteins, polysaccharides and most importantly humic substances [21–23]. During RO desalination, NOM will inevitably cause membrane fouling by adsorption and deposition on the membrane surface and thereby modify physicochemical membrane surface properties [12,24–30]. It is well documented that dissolved NOM can retard crystal nucleation and growth from supersaturated solution [31–35]. Similarly, dissolved NOM was reported to retard scaling during membrane-based desalination processes [14,36–40]. However, both, inhibition [39] and aggravation [41–43] of membrane scaling was observed due to membrane fouling by NOM.

## 1.2 Objective and Structure of the Thesis

Despite the widespread application of RO desalination, interactions between membrane scaling by bulk and surface crystallization and NOM at concentrations commonly found in natural waters (few  $\text{mg C}\cdot\text{l}^{-1}$ ) have been rarely investigated. Moreover, the majority of available studies did not discriminate between effects induced by dissolved NOM and those induced by NOM fouling. A better understanding of potential interactions is a fundamental prerequisite to optimize membrane-based desalination processes, to optimize scale control strategies, most importantly antiscalant dosage, and to development alternative measures for scale control. Therefore, the objective of this thesis is the systematic characterization of scaling during RO desalination and its interactions with NOM at concentrations of natural waters. In laboratory experiments, gypsum was used as model scale-forming salt together with selected NOM sources. The experimental approach was divided into four parts:

- **Characterization of gypsum scaling (Chapter 4).** Gypsum scaling during RO desalination occurs from bulk or surface crystallization. However, the occurrence and dominance of the two scaling mechanisms is uncertain in full scale RO systems. Using a laboratory scale RO system, the chapter first assesses the effects of operating conditions and antiscalant dosage on gypsum scaling mechanisms (Chapter 4.1). Subsequently, kinetic effects of supersaturation and  $pH$  on gypsum bulk crystallization from supersaturated solution is investigated using stirred beaker crystallization experiments (Chapter 4.2). Finally, the development and reproducibility of early-stage gypsum surface crystallization on RO membranes is assessed by implementing real-time membrane surface imaging during RO desalination (Chapter 4.3).
- **Characterization of the selected natural organic matter (NOM) sources (Chapter 5).** The selected NOM sources, namely bovine serum albumin (protein), alginate (polysaccharide), two humic acids of terrestrial origin and two aquatic humic substances are analyzed regarding their molecular size distribution (Chapter 5.1), spectral absorbance and fluorescence emission (Chapter 5.2) and concentration of acidic functional groups (Chapter 5.3).
- **Effects of NOM on gypsum bulk crystallization (Chapter 6).** Effects of NOM type, NOM concentration ( $3 - 12 \text{ mg C}\cdot\text{l}^{-1}$ ) and solution  $pH$  ( $4 - 10$ ) on induction time and crystal growth are assessed in stirred beaker crystallization experiments (Chapters 6.1 and 6.2), followed by a comparison to the effects exhibited by a commercial antiscalant (Chapter 6.3). Concluding, effects of NOM on gypsum scaling by bulk crystallization during RO desalination and the transferability to stirred beaker crystallization experiments is evaluated (Chapter 6.4).
- **Effects of NOM on gypsum surface crystallization on RO membranes (Chapter 7).** The chapter first assesses the effects of membrane pre-fouling by NOM on gypsum scaling by surface crystallization (Chapter 7.1). Subsequently, the effects of dissolved NOM at concentrations  $\leq 5 \text{ mg C}\cdot\text{l}^{-1}$  are assessed (Chapter 7.2), followed by a comparison to the effects exhibited by a commercial antiscalant (Chapter 7.3).

## 2 Theoretical Background

This chapter first presents the basic principles of water desalination using reverse osmosis (RO) membranes, including transport phenomena, membrane material properties and membrane fouling (Chapter 2.1). Chapter 2.2 focuses on membrane scaling by sparingly soluble salts. It presents fundamentals of the crystallization process and impacts of impurities, the mechanisms of scale formation during RO desalination and its control by antiscalant dosage. Chapter 2.3 exclusively focuses on the characteristics of gypsum ( $\text{CaSO}_4 \cdot 2\text{H}_2\text{O}$ ) crystallization and scaling. Concluding, Chapter 2.4 presents fundamentals of natural organic matter (NOM), membrane fouling by NOM and interactions between NOM and gypsum crystallization and scaling.

### 2.1 Reverse Osmosis for Desalination

Increasing local scarcity and contamination of available freshwater resources are among the most serious challenges of our time [1,2]. The supply of adequate and safe drinking water is further stressed by continuous population growth, industrialization and climate change [1]. Several measures including water conservation and optimization of water catchment, distribution and infrastructure can only alleviate the stresses on water supply and improve the efficient use of existing water resources, but cannot increase them [1]. To augment freshwater supplies beyond what is available from the hydrological cycle, efficient and sustainable treatment technologies are required to tap unconventional water resources such as seawater, brackish ground- and surface waters or wastewater [3]. Desalination of brackish and seawater can offer a seemingly unlimited and steady supply of high-quality water [1].

Early-stage desalination plants were based on thermal processes, where seawater is heated and evaporated water subsequently condensed [44]. Contrarily, the majority of desalination plants constructed during the last two decades are based on reverse osmosis technology, where semi-permeable membranes are used that let pressurized water pass through but retain salts [45]. The improvement of RO technology including improved membrane properties, installation of energy recovery devices and the use of more efficient pumps has dramatically reduced treatment costs [45]. At present, RO is the most energy-efficient technology to desalinate seawater and represents the benchmark for existing and new desalination technologies [1], such as forward osmosis (FO), where an osmotic pressure difference is generated to drive the permeation of water across a semi-permeable membrane, or membrane distillation (MD), where a temperature induced vapor pressure difference drives gaseous water molecules through a microporous hydrophobic membrane. The energy requirement of current state-of-the-art seawater RO desalination plants is within a factor of two from the limit of a reversible thermodynamic process (thermal processes: up to a factor of five) [46]. Recently, a total energy consumption rate of  $1.58 \text{ kW} \cdot \text{h} \cdot \text{m}^{-3}$  has been demonstrated in pilot scale at 42 % water recovery [47] where the calculated theoretical minimum is  $1.06 \text{ kW} \cdot \text{h} \cdot \text{m}^{-3}$  for a seawater with a total dissolved solids (TDS) concentration of  $35 \text{ g} \cdot \text{l}^{-1}$  [1].

Brackish waters are commonly defined as waters with concentrations of total dissolved solids between that of freshwater ( $c_{TDS} \leq 1,000 \text{ mg}\cdot\text{l}^{-1}$ ) and salty water ( $c_{TDS} \geq 10,000 \text{ mg}\cdot\text{l}^{-1}$ ) [48]. The choice of the most suitable technology for brackish water desalination is a site-specific combination of many factors [17]. Predominantly, RO and nanofiltration (NF) are used, while electrochemically driven membrane processes of electrodialysis, electrodialysis reversal and electrodeionization are important niche applications [17]. Especially at inland locations, management of residual concentrate (brine) is typically cost intensive and a high water recovery, which is the percent of brackish water converted to fresh water, of 85 – 95 % is often required [17].

### 2.1.1 Basic Principles of Reverse Osmosis

Membrane filtration for water separation is a physico-chemical process which separates water from suspended and/or dissolved water constituents by the use of semi-permeable membranes. The rejection of solutes by the membrane divides the feed water stream into a product and concentrate stream (Figure 2-1). Depending on the treatment goal, porous microfiltration (MF) and ultrafiltration (UF) membranes are used to separate water from suspended matter while non-porous NF and RO membranes are used to reject hydrated ions (Figure 2-2).

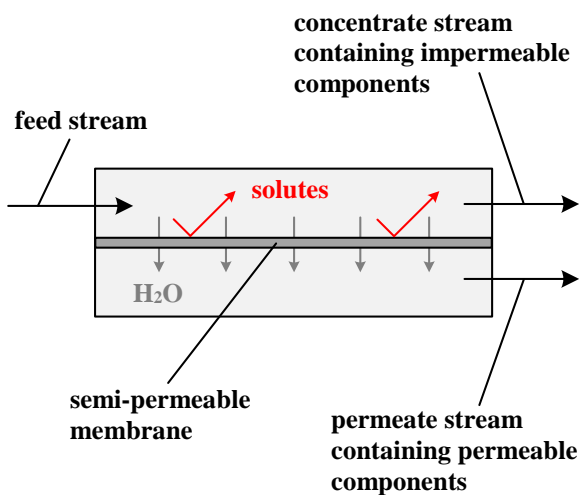


Figure 2-1: Schematic illustration of a membrane separation process.

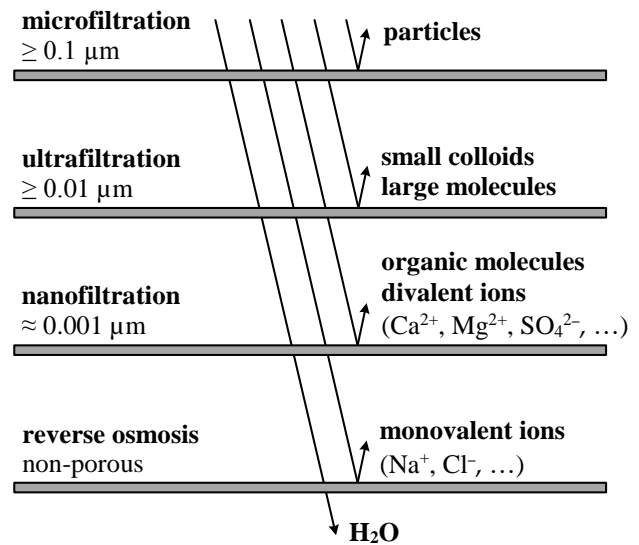


Figure 2-2: Selectivity of pressure-driven membrane processes according to [49].

For porous membranes (that is, MF and UF), flow through the membrane active layer is modelled as laminar flow through an array of cylindrical pores while transport through non-porous membranes (that is, NF and RO) is governed by solution and diffusion [6]. Rejection of solutes creates a concentration gradient across the membrane and results in a difference of osmotic pressure across the active layer of the membrane ( $\Delta\pi_m$ ) as described by Equation 2-1:

$$\Delta\pi_m = (\pi_m - \pi_p) \quad \text{Equation 2-1}$$

where  $\pi_m$  is the osmotic pressure at the membrane surface and  $\pi_p$  is the osmotic pressure in the permeate. The osmotic pressure of a thermodynamically ideal solution ( $\pi$ ) is calculated from Equation 2-2:

$$\pi = i \cdot R \cdot T \cdot c_s = (1 + \alpha \cdot (\nu - 1)) \cdot R \cdot T \cdot c_s \quad \text{Equation 2-2}$$

where  $i$  is the van't Hoff factor,  $R$  is the ideal gas constant,  $T$  is the temperature,  $c_s$  is the molar salt concentration,  $\alpha$  is the degree of dissociation and  $\nu$  is the number of dissociated ions of a respective molecule or salt. For typical MF and UF applications in water treatment,  $\Delta\pi_m$  is usually negligible [6] due to the unrestricted passage of dissolved solids. In contrast,  $\Delta\pi_m$  is a crucial parameter for NF and RO applications given that dissolved constituents are efficiently rejected [6]. At 25 °C, the osmotic pressures of typical seawater ( $c_{TDS} = 35 \text{ g}\cdot\text{l}^{-1}$ ) and brackish water ( $c_{TDS} = 2 - 5 \text{ g}\cdot\text{l}^{-1}$ ) are 23.4 bar and 1.0 – 2.8 bar, respectively [50]. To overcome the natural process of osmosis and to actively force water through the membrane, a transmembrane pressure difference greater than the osmotic pressure difference has to be applied.

### Transport mechanisms

Water flux through an RO membrane is described by Equation 2-3 [50]:

$$J_w = k_w \cdot (\Delta p - \Delta\pi_m) \quad \text{Equation 2-3}$$

where  $J_w$  is the volumetric water flux,  $k_w$  is the clean water permeability coefficient,  $\Delta p$  is the applied hydraulic transmembrane pressure and  $\Delta\pi_m$  is the osmotic pressure difference across the active layer of the membrane. Solute flux is modelled as Fickian diffusion by Equation 2-4:

$$J_s = k_s \cdot \Delta c_m \quad \text{Equation 2-4}$$

where  $k_s$  is the solute permeability coefficient and  $\Delta c_m$  is the solute concentration difference across the active layer. Flow through the active layer is governed by the solution-diffusion model considering that water and solute molecules absorb into the active layer, diffuse through the polymer matrix down their chemical potential gradients and eventually desorb into the permeate solution [6]. Diffusive water and solute permeability are defined by solubility and diffusivity and represent intrinsic membrane material properties. Water and solute permeability coefficients  $k_w$  and  $k_s$  are further dependent on active layer thickness and temperature. Together, they largely define the selectivity of the active layer of non-porous membranes. The permeability-selectivity trade-off of water separation membranes implies that an increase in the permeability of water comes along with an even greater increase in the solute permeability. Thus, an ideal membrane with high water permeability and high selectivity is difficult to attain [6].

The selectivity of semi-permeable membranes is characterized by the intrinsic salt rejection coefficient ( $R_{int}$ ) (Equation 2-5):

$$R_{int} = \frac{c_m - c_p}{c_m} = 1 - \frac{c_p}{c_m} \quad \text{Equation 2-5}$$

where  $c_m$  is the salt concentration at the membrane surface and  $c_p$  the salt concentration in the permeate solution. As  $c_m$  is often unknown, the observed salt rejection coefficient ( $R_{obs}$ ) is commonly reported (Equation 2-6):

$$R_{obs} = \frac{c_b - c_p}{c_b} = 1 - \frac{c_p}{c_b} \quad \text{Equation 2-6}$$

where  $c_b$  is the salt concentration of the bulk solution. Current state-of-the-art seawater RO membranes commonly exhibit salt rejections greater than 99.5 % [6].

### Concentration polarization

Rejected solutes accumulate and cause their concentration at the membrane surface ( $c_m$ ) to be higher than the concentration of the bulk solution ( $c_b$ ), a phenomenon referred to as concentration polarization (CP). The concentration gradient adjacent to the membrane surface drives the diffusion of rejected solutes back into the bulk solution. A steady-state concentration profile is established when the convective transport of rejected solutes towards the membrane surface is balanced by their back diffusion into the bulk solution (Figure 2-3).

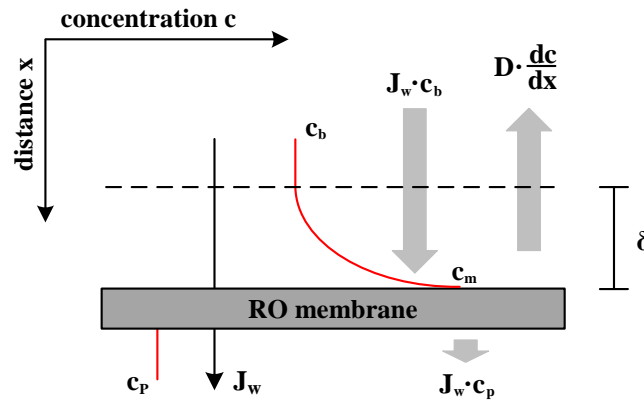


Figure 2-3: Concentration polarization over a membrane surface according to [21] and [51].  $D$ : Solute diffusion coefficient,  $\delta$ : boundary layer thickness.

For high rejections ( $R_{int} \rightarrow 100\%$ ) and for ions and small molecules with diameters smaller than 100 nm where Brownian diffusion dominates over other depolarization mechanisms [52,53], the ratio of  $c_m$  to  $c_b$ , referred to as the concentration polarization modulus ( $f_{cp}$ ), can be estimated by Equation 2-7:

$$f_{CP} = \frac{c_m}{c_b} = \exp(J_w/k) \quad \text{Equation 2-7}$$

where  $k$  is the mass transfer coefficient ( $k = D/\delta$ ) with  $D$  as the solute diffusion coefficient and  $\delta$

as the boundary layer thickness. The mass transfer coefficient  $k$  can be determined from established correlations considering membrane module geometry and flow regime as summarized by Fane et al. (2011) [51]. Equation 2-7 shows that the degree of concentration polarization increases at higher water flux  $J_w$  and reduced mass transfer coefficient  $k$ . The latter increases with molecule size, as bigger molecules generally have lower diffusion coefficients, and decreases with larger turbulence and flow velocity in cross-flow membrane modules, which reduce the boundary layer thickness. For particles and colloids with a diameter larger than 100 nm, additional depolarization mechanisms, namely lateral migration, shear-induced diffusion and surface interactions, have to be considered in addition to the Brownian diffusion [52,53]. Further, it is important to recognize that concentration polarization is different from membrane fouling (Chapter 2.1.3), where an immobile solid phase forms at the liquid-membrane interface. However, severe concentration polarization can accelerate fouling by supplying the membrane with a higher effective foulant concentration. Concentration polarization adversely affects membrane performance by resulting in increased osmotic pressure at the membrane surface, which results in lower water flux, and reduced apparent solute rejection due to an increased transmembrane solute concentration gradient. To minimize the degree of concentration polarization, technical NF and RO systems are always operated in cross-flow configuration. In addition, net-like feed spacers are used to promote turbulence in spiral wound RO membrane elements, which is the predominant design for RO elements applied to the water industry [51]. Details on the design of spiral wound RO membrane modules, where several membrane envelopes, which are connected to a permeate collection pipe, are separated by feed spacers and then rolled around a the permeate collection pipe, can be found in Fane et al. (2011) [51]. Typical cross-flow velocities in spiral wound RO elements are around  $v_{cf}=0.1 \text{ m}\cdot\text{s}^{-1}$  [54] and mass transfer coefficients ( $k$ ) range between  $10^{-5} \text{ m}\cdot\text{s}^{-1}$  and  $10^{-6} \text{ m}\cdot\text{s}^{-1}$  [55].

### **2.1.2 Reverse Osmosis Membrane Materials and Properties**

For RO desalination, the use of thin-film polyamide (PA) composite (TFC) membranes has become standard [1]. These membranes are fabricated by interfacial polymerization of diamine and triacyl chloride to form a thin cross-linked polyamide selective layer with an approximate thickness between 50 nm and 230 nm [56] over a significantly thicker porous and mechanically resistant support layer, commonly made of polysulfone [6]. Subsequent hydrolysis of non-reacted acyl chloride groups forms carboxyl groups, which yields a negative charge of the membrane surface [6]. The overall negative charge of polyamide RO and NF membranes at neutral  $pH$  has been confirmed by streaming potential measurements [25,27,57,58] and the presence of carboxyl groups has been proved by attenuated total reflectance infrared spectroscopy [59–61] and nuclear magnetic resonance measurements [62]. Many polyamide membranes synthesized from *m*-phenylenediamine have a characteristic ‘*ridge-and-valley*’ structure due to polyamide nodules [6] as depicted in Figure 2-4 and a relatively heterogeneous and rough surface with a typical root-mean-square roughness greater than 50 nm [6], which can make them prone to membrane fouling and scaling [1]. To mask the relatively rough and hydrophobic PA rejection layer, hydrophilic

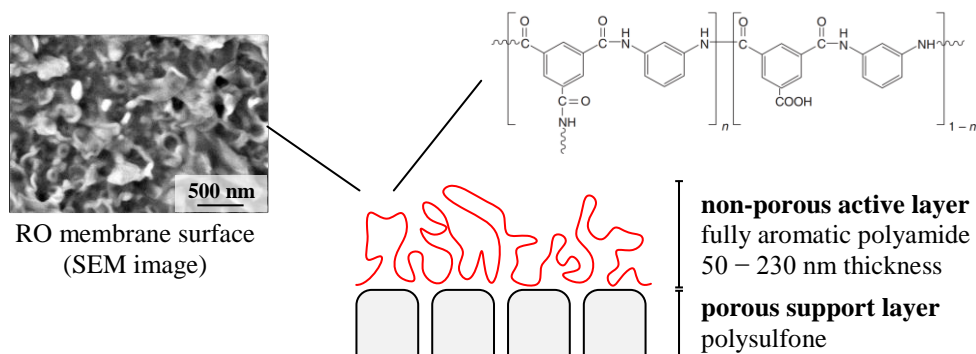


**Figure 2-4: Schematic representation of a fully aromatic polyamide (PA) thin-film composite (TFC) reverse osmosis membrane showing the porous polysulfone support layer and the dense polyamide film with ridge-and-valley morphology according to [6,51]. Scanning electron microscopy (SEM) image was taken from a virgin FILMTEC™ BW30 (Dow Chemical, MI, USA) membrane at 50,000x magnification.**

polyvinyl alcohol (PVA) coatings can be applied. In addition, PVA coatings can make surficial functional groups less accessible reducing the membrane surface charge.

Solution chemistry may affect the surface charge of PA membranes significantly [25,27]. Membrane surface carboxyl groups are protonated with decreasing  $pH$  [21,25] and PA membranes are positively charged at a  $pH$  below the isoelectric point between  $pH = 3 - 5$  [27]. Membrane negative surface charge can also be effectively screened by adsorption of divalent cations, especially calcium ions, which specifically interact with the carboxyl groups [25].

### 2.1.3 Membrane Fouling During Reverse Osmosis

Membrane fouling and scaling remain serious limitations in designing and operating membrane systems [10]. Membrane fouling (Figure 2-5a) is the undesirable deposition of rejected water constituents (referred to as foulants) inside membrane pores and on a membrane surface, which results in the formation of a new solid phase, such as a cake layer comprised of colloids\* and particles or a gel layer of organic macromolecules [15,21,51]. For RO membranes, where distinguishable pores are absent, surface fouling is the only relevant fouling mechanism. According to the nature of the foulants, membrane fouling can be classified into ‘*organic fouling*’ by natural organic matter (NOM), which is discussed in detail in Chapter 2.4.4, ‘*inorganic fouling*’ by inorganic colloids and particles and ‘*biofouling*’ by colonization of microorganisms and according biofilms. ‘*Scaling*’ (Figure 2-5b), sometimes also classified as part of inorganic fouling, is the formation of hard mineral deposits on the membrane surface due to crystallization processes as the feed water becomes supersaturated by inorganic salts following pure water separation [10,64]. A detailed discussion of membrane ‘*scaling*’ is provided in Chapter 2.2.

\* According to IUPAC, the term ‘*colloidal*’ refers to molecules or polymolecular particles dispersed in a medium which have at least in one direction a dimension roughly between 1 nm and 1 $\mu$ m [63].

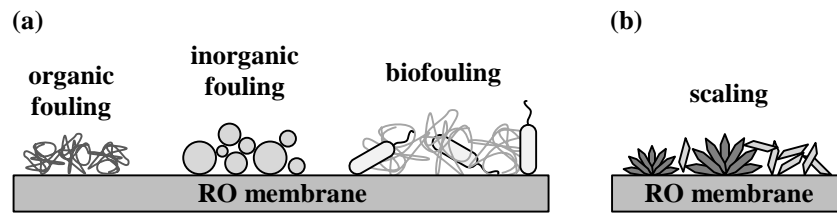


Figure 2-5: Illustration of (a) different types of membrane fouling and (b) membrane scaling during reverse osmosis desalination.

Membrane fouling and scaling can lead to an additional hydraulic resistance to water permeation and to a loss of active membrane area, which will reduce the effective membrane permeability [21,51]. In addition, a fouling layer comprised of colloids and particles can enhance concentration polarization and thereby reduce membrane permeability and apparent solute rejection, as further discussed in Chapter 2.4.5. Membrane fouling and scaling increase costs for operation and cleaning and significantly shorten membrane lifetime [10–13]. Proper feed water pretreatment and different scale control measures can alleviate the severity of membrane fouling and scaling.

## 2.2 Membrane Scaling During Reverse Osmosis Desalination

Scale formation during membrane-based desalination is considered a crystallization process [55]. Crystalline solids are characterized by the highly ordered arrangement of the constituent molecules, atoms or ions into some fixed rigid pattern known as a lattice which extends into all directions [65]. As a crystal grows, smooth crystal faces develop whose planes are parallel to atomic planes in the lattice [65]. In contrast, amorphous, non-crystalline solids are lacking this ordered molecular structure. Some of the most common scale-forming salts in natural waters are calcium sulfate dihydrate (gypsum,  $\text{CaSO}_4 \cdot 2\text{H}_2\text{O}$ ), calcium carbonate (calcite,  $\text{CaCO}_3$ ), silicon dioxide (silica,  $\text{SiO}_2$ ) and barium sulfate (barite,  $\text{BaSO}_4$ ) [15].

Although generally described as a crystallization process, the term precipitation is often used synonymously to describe the process of membrane scaling. According to IUPAC, crystallization is defined as the formation of a crystalline solid from a solution while precipitation describes the formation of a precipitate [66], which may be crystalline or amorphous. This inconsistency derives from the possibility that, at fast reaction kinetics, solid phase formation may not be limited to the formation of crystalline solids but may include the occurrence of amorphous phases [67].

The following chapters present the general mechanisms of crystal formation and the effects of impurities as well as the specifics of scaling in RO systems, its mechanisms and mitigation by antiscalant dosage.

### 2.2.1 Mechanisms of Crystallization

Crystallization involves the consecutive stages of attainment of supersaturation, nucleation and crystal growth [55,65,67].

### Attainment of supersaturation

The state of supersaturation is an essential requirement for crystallization to occur from solution. A supersaturated solution is characterized by containing more dissolved solids than that represented by equilibrium saturation. The terms '*labile*' and '*metastable*' supersaturation classify supersaturated solutions in which nucleation does or does not occur spontaneously, respectively [65]. Solubility-supersolubility diagrams (Figure 2-6) represent the metastable zone as a function of concentration and temperature. Spontaneous crystallization is impossible in the unsaturated '*stable*' zone, improbable in the supersaturated '*metastable*' zone and probable in the supersaturated '*labile*' zone [65]. During desalination processes, supersaturation can be achieved by pure water separation from an initially unsaturated solution (line A-B-C in Figure 2-6). The degree of supersaturation of sparingly soluble salts in aqueous solution is frequently expressed by the supersaturation ratio ( $S$ ) and the saturation index ( $SI$ ) given by Equation 2-8:

$$SI = \log_{10}(S) = \log_{10}\left(\frac{IAP}{K_{sp}}\right) \quad \text{Equation 2-8}$$

where  $IAP$  is the ion activity product of the salt ions in solution and  $K_{sp}$  is the activity solubility product of the salt, i.e. the value of  $IAP$  at equilibrium. Accordingly, a solution is unsaturated at  $SI < 0$ , saturated at  $SI = 0$  and supersaturated at  $SI > 0$ .

### Crystal nucleation

Any supersaturated solution will, if not spontaneously, relieve its supersaturation eventually. At constant '*metastable*' supersaturation, a certain period of time, referred to as induction time ( $\tau$ ), will elapse between the achievement of supersaturation and the detection of a new crystalline phase [65,67]. The induction time is determined by the nucleation time ( $\tau_n$ ) required for the formation of '*stable nuclei*' and the time required for the nuclei to grow to a detectable size ( $\tau_g$ ). The exact mechanism of nucleation, i.e. the formation of stable nuclei whose existence is essential to crystal development, is not known with any degree of certainty [65]. Classical nucleation theory considers that critical nuclei form directly by the assembly of ions from solution in local regions of very high supersaturation [68]. In contrast, recent studies have shown that the nucleation process proceeds through intermediate stages before reaching a thermodynamically stable phase, such as the formation of prenucleation clusters that aggregate into amorphous nanoparticles and polycrystals and eventually form crystalline domains [68–70]. During nucleation, many '*subcritical nuclei*' fail to reach a critical size before they redissolve [65]. However, after reaching a critical size, the change of free enthalpy upon adding another building block (ion or atom) becomes negative and growth becomes more favorable than dissolution of the resulting '*stable*' or '*critical nucleus*' [67].

Figure 2-7 shows the classification of nucleation processes [67]. '*Primary*' nucleation, as discussed above, occurs in the absence of any crystalline matter in solution. It can occur '*homogeneously*' in the absence of any foreign surfaces or '*heterogeneously*' on foreign surfaces

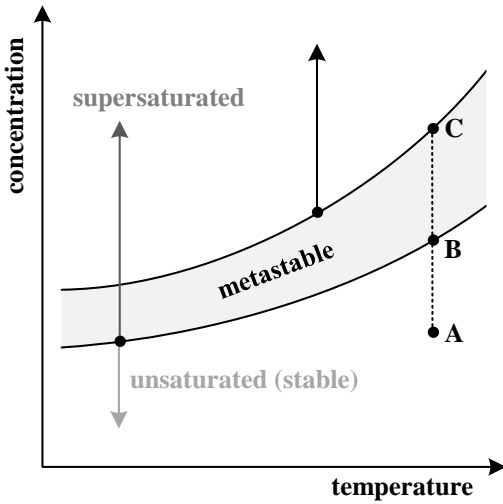


Figure 2-6: Schematic solubility-supersolubility diagram according to [65]. During desalination, supersaturation can be achieved by pure water separation from an initially unsaturated solution (line A-B-C).

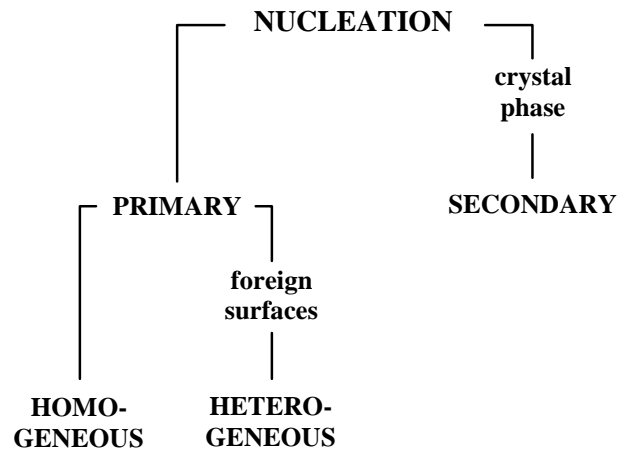


Figure 2-7: Nucleation processes and nomenclature according to [65,67].

such as particles or membrane surfaces. ‘Secondary’ nucleation is the generation of nuclei in the vicinity of existing crystals.

For a given crystalline phase and temperature, the rate of nucleation ( $J_N$ ) is strongly governed by the supersaturation ratio ( $S$ ), the temperature ( $T$ ) and the solution-mineral interfacial energy ( $\sigma / \text{J}\cdot\text{m}^{-2}$ ) [67,68] as indicated by Equation 2-9:

$$J_N \propto \exp\left[-\frac{\Delta G^*}{R \cdot T}\right] \quad \text{with} \quad \Delta G^* \propto \frac{\sigma^3}{T^2 \cdot \ln^2 S} \quad \text{Equation 2-9}$$

where  $\Delta G^*$  is the Gibbs free energy of homogeneous nucleation in  $\text{J}\cdot\text{mol}^{-1}$  and  $R$  the ideal gas constant in  $\text{J}\cdot\text{mol}^{-1}\cdot\text{K}^{-1}$ . Below a certain critical supersaturation ratio  $J_N$  is practically zero, however, at higher supersaturation ratios,  $J_N$  increases exponentially. Heterogeneous nucleation on foreign surfaces is energetically favorable and reduces the required supersaturation for spontaneous nucleation [67]. However, for high nucleation rates, the surface available for heteronucleation can become limiting. It is important to consider that the inherent presence of particles and atmospheric dust make true homogenous nucleation unlikely, even in laboratory environments [65].

The induction time ( $\tau$ ) is inversely proportional to the nucleation rate ( $J_N$ ) (Equation 2-10) and to the supersaturation ratio ( $S$ ) (Equation 2-11) [67].

$$\tau \propto \frac{1}{J_N} \quad \text{Equation 2-10}$$

$$\ln(\tau) \propto \frac{1}{(\ln S)^2} \quad \text{Equation 2-11}$$

The induction time and the metastable zone widths are, amongst other factors, considerably affected by the intensity of agitation (e.g. stirring speed), the presence of impurities and foreign surfaces, temperature and the rate at which supersaturation is generated [65]. Therefore, an experimentally determined induction time or metastable zone width is not, by itself, a fundamental characteristic of a crystallization system but strongly depends on the experimental setup and the sensitivity of crystal detection.

### Crystal growth

Crystal growth is defined as the displacement of a crystal face [67]. Critical nuclei and crystals will continue to grow as long as supersaturation prevails. Different theories have been proposed and are comprehensively summarized in reference works [65,67]. The most adapted theory, namely the adsorption-layer theory suggested by Volmer (1939) [71], considers crystal growth as a discontinuous process, taking place by adsorption, layer by layer, on the crystal surface. Accordingly, units of the crystallizing substance that arrive at the crystal face are not immediately integrated into the crystal lattice, but can diffusively migrate over the crystal face. Eventually, the migrating units will link into the lattice in positions where the attractive forces are greatest. Those 'active centers' are predominately kinks, where, for a cubic crystal unit, the integrated building unit is bound by the maximum number of three nearest neighbors (Figure 2-8) [65,67]. Real crystals will contain a variety of lattice defects, such as screw dislocations, which are a permanent source of steps promoting perpetual spiral growth over the crystal face [65,67].

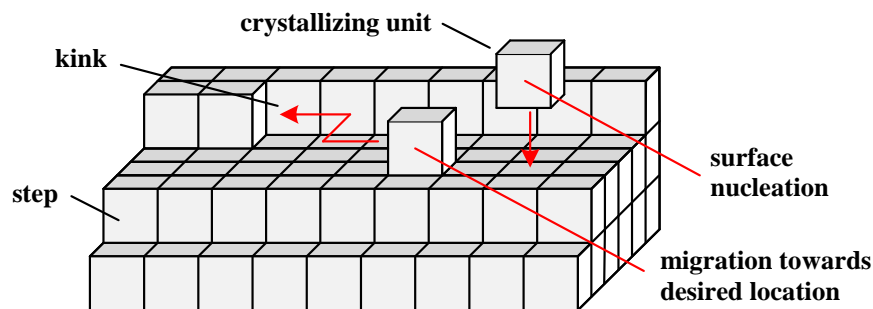


**Figure 2-8: Ideal crystal growth without dislocations according to [65]. Crystallizing units will migrate and link into positions where attractive forces are greatest and will, by step-wise build-up, complete a crystal plane. Before a crystal face can continue to grow, a new surface nucleus must be created.**

In addition to incorporation processes, crystal growth rates are determined by mass transfer phenomena in the bulk solution. At high crystal growth rates, diffusional transport of the crystal-forming ions from the bulk solution to the crystal interface can become limiting [55]. Accordingly, the crystal growth rate will increase rapidly with supersaturation until it is limited by diffusional

transport phenomena [65,67]. For low supersaturation ratios, the growth rate ( $R_G$ ) is proportional to the square of the supersaturation ratio ( $R_G \propto S^2$ ), whereas at high supersaturation ratios, the growth rate increases linearly with the supersaturation ratio ( $R_G \propto S$ ) [65,67].

### **2.2.2 Effects of Impurities on Crystallization Kinetics and Crystal Morphology**

Any substance or additive other than the crystallizing material can be considered an impurity. Impurities can be suspended particulate matter (particles and colloids) and dissolved compounds of organic or inorganic origin. In general, impurities can (i) modify the thermodynamics, (ii) directly affect crystallization kinetics and (iii) change the resulting crystal morphology and habit [65]. These general effects are described in the present chapter whereas effects caused specifically by polymeric antiscalants and natural organic matter (NOM) are reviewed in Chapter 2.2.4 and Chapter 2.4.3, respectively.

#### **Effects of impurities on thermodynamics**

The solubility of a crystallizing substance will in most cases increase with the presence of additional chemical species, unless they are common ions [67]. The presence of electrolytes other than the crystal-forming ions, increases the ionic strength of the solution. In most cases, this will reduce the individual components activity and thereby increase the solubility of crystal-forming salts. Additional increases of solubility may be experienced by formation of complexes between crystal-forming ions with impurities in solution. Any change of the equilibrium solubility will affect supersaturation in the system leading to changes of crystallization kinetics [65,67,72].

#### **Effects of impurities on crystallization kinetics**

Any solubility change caused by an impurity will change crystal nucleation and growth rates [65,67,73]. In addition, crystallization kinetics may be affected by direct interaction between impurities and developing nuclei and crystals [65,67]. Foreign surfaces, such as inorganic and organic particles and colloids, may act as heteronucleation sites, catalyze nucleation and significantly reduce induction times [67]. Contrarily, pre-existing ‘heteronuclei’, which are inherently present in solution, may be inactivated by adsorption of high molecular weight organic substances [65]. Similarly, adsorption of inorganic and organic impurities onto crystal nuclei and crystals may block their surfaces, inhibit their growth and thereby retard or suppress the detectable onset of crystal formation and crystal growth [67,74]. Further, adsorption of impurities onto nuclei may affect the solution-mineral interfacial energy ( $\sigma$ ) and thereby affect crystal nucleation [67,75,76]. Cationic impurities, such as  $\text{Cr}^{3+}$ ,  $\text{Fe}^{3+}$ ,  $\text{Cd}^{2+}$ ,  $\text{Cu}^{2+}$  and  $\text{Zn}^{2+}$  are known to increase the induction periods of inorganic salts in aqueous solution by incorporation or adsorption [55,65,77]. Inhibition by cations is frequently reported to be most powerful for cations of highest charge [65]. However, due to the large number of possible effects and the limited experimental evidence yet available, effects of impurities on crystallization kinetics often remain unpredictable [65].

### Effects of impurities on crystal morphology and habit

Crystals develop a set of symmetry equivalent faces, termed crystal ‘*form*’ [78]. For example, a crystal form can be a cube or an octahedron (Figure 2-9). The set of crystal forms that occur on a crystal determine its morphology (in German denoted as “*Tracht*”) [67,78]. The term crystal ‘*habit*’ describes the characteristic external shape and geometric appearance of an individual or an assembly of crystals, which is characterized by the dominant size of a crystal form, i.e. the relative width and length of the developed crystal faces [67,78]. Common crystal habits can be, for example, acicular (needle-like), rosette-like, or platy. Two crystals of identical morphology (identical “*Tracht*”) can have different habits and vice versa (Figure 2-9). Often, the terms crystal ‘*morphology*’ (“*Tracht*”) and crystal ‘*habit*’ are used interchangeably and no clear distinction is made between the two terms [79].

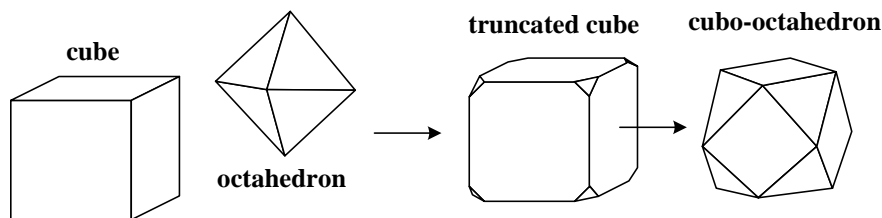


**Figure 2-9: Combination of two crystal forms (cube, octahedron). Resulting crystals consist of the same set of crystal forms, i.e. share the same cubo-octahedral morphology (identical “*Tracht*”), but have different habits. According to [65,78].**

Impurities can be selectively incorporated into the crystal lattice or adsorb onto certain crystallographic faces of the growing crystal, especially if structural similarities between the impurity and the crystal lattice exist [65,67,82]. Clydesdale et al. (1994) classify organic impurities as disruptive or blocker type molecules [82,83]. Structurally similar parts of the molecules can incorporate randomly into the crystal lattice especially if they are smaller than the crystal system [82]. The structurally different moiety of the molecule will disturb the adsorption of a new growth

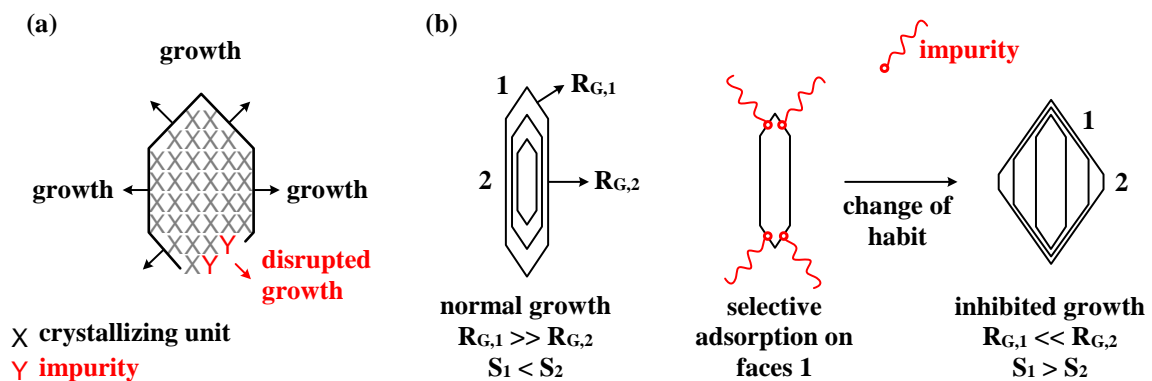


**Figure 2-10: Modification of crystal habit by impurities. (a) Disruptive effect by impurity incorporation and disruption of face growth according to [80] in [67]. (b) Blocking effect by selective adsorption of impurity on crystal face 1 according to [81].  $R_{G,i}$ : growth rate of face  $i$ ,  $S_i$ : Surface  $i$ .**

layer and thereby disrupt normal growth (Figure 2-10a). Molecules larger than the crystal system tend to adsorb onto specific sites on some faces if structurally similar moieties exist [82]. A structurally significantly different end group of the molecule (the blocker) then prevents the adsorption of a new growth layer and blocks the respective crystal face (Figure 2-10b). Distorted growth of a crystal face by incorporation or adsorption of an impurity can change the crystal habit by dominant growth of the remaining unaffected faces (Figure 2-10b).

### 2.2.3 Scale Formation and Mechanisms in Reverse Osmosis Desalination Systems

Supersaturation is the prerequisite for scale formation. During RO desalination, permeate withdrawal leads to an increase of rejected ion concentrations in the remaining feed water. Depending on water recovery ( $\Phi$ ), which is the percent of the feed water converted to fresh water, concentrations of scale-forming ions may increase above their equilibrium concentrations for a given feed water composition at given solution conditions (line A-B-C in Figure 2-6). In addition, rejected solute concentrations are highest directly at the liquid-membrane-surface interface due to concentration polarization (Figure 2-3) and even if the feed bulk solution is unsaturated, supersaturation may exist locally at the membrane surface or at locations of reduced fluid movement. Typical water recoveries and corresponding concentration factors ( $CF$ , with  $CF = c_c/c_f$ ) for different RO applications are displayed in Figure 2-11.

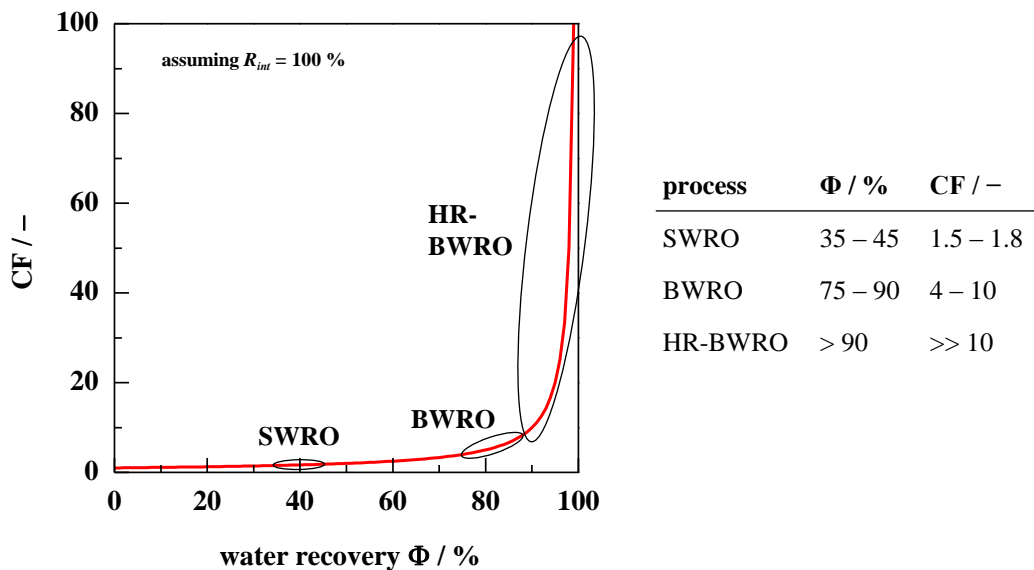


**Figure 2-11: Typical water recoveries  $\Phi$  and resulting concentration factors ( $CF$ , with  $CF = c_c/c_f$ ) of rejected feed water solutes for different RO desalination applications (SWRO: seawater RO, BWRO: brackish water RO, HR-BWRO: high recovery RO). Water recoveries according to [9].**

In seawater reverse osmosis (SWRO), scale formation is generally of inferior concern due to the low typical water recoveries, which are limited by the required osmotic pressure [9]. Contrarily, fouling by particles, colloids and natural organic matter (NOM) as well as biofouling are the major

concerns and challenges during SWRO [9]. The higher typical water recoveries of brackish water RO (BWRO) systems and the resulting higher concentration factors make membrane scaling the principal fouling problem, especially for high recovery BWRO (HR-BWRO) systems [9].

### Scaling mechanisms

Scale formation by sparingly soluble salts during membrane-based desalination has been proposed to occur from two scaling mechanisms: (i) surface and (ii) bulk crystallization [36,38,41,84,85]. While the former mechanism describes heterogeneous nucleation and subsequent lateral crystal growth directly on the membrane surface, the latter mechanism describes nucleation in the feed solution (homogeneously or heterogeneously on particles or colloids), followed by crystal growth and crystal deposition on the membrane surface (Figure 2-12).

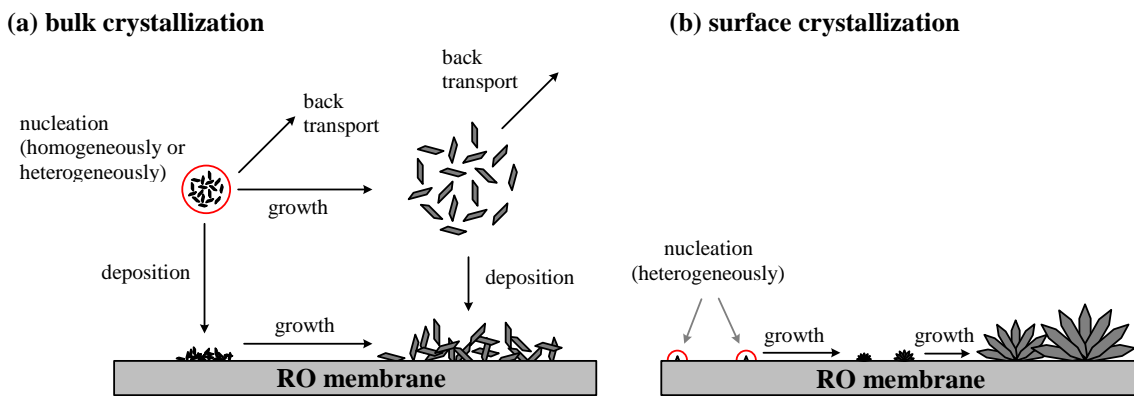


**Figure 2-12: Schematic illustration of scaling mechanisms. (a) Bulk crystallization due to crystal nucleation in the fluid bulk (homogeneously or heterogeneously) followed by deposition, growth and back transport. (b) Surface crystallization due to heterogeneous crystal nucleation on the membrane surface followed by lateral growth. According to [38,84,86].**

Disagreement exists with respect to the occurrence and dominance of the two scaling mechanisms in technical membrane systems. Pervov (1991) suggested that crystal formation takes place in the bulk solution due to high supersaturation reached in deadlocks of the membrane module [87]. Bulk crystallization followed by crystal deposition was also reported to cause gypsum scaling in spiral wound NF modules [84]. Similarly, bench scale NF [88] and RO [89,90] experiments, where supersaturated feed solutions were recycled, gypsum scaling was caused by bulk crystallization as detected permeability declines coincided with fluid turbidity increases which indicated the onset of bulk crystallization. Contrarily, Shih et al. (2005) [19], Uchymiak et al. (2008) [91] and Radu (2014) [92] agree that, unless concentrate solutions are recycled, required induction times for bulk crystallization are significantly longer than the hydraulic residence times of water in spiral wound RO modules even for high supersaturations. They suggest that surface crystallization is the primary contributor to membrane scaling [19,91,92]. According to classical nucleation theory, heterogeneous nucleation on the foreign membrane surface (surface crystallization) is catalyzed

and metastable zone widths as well as induction times are drastically reduced [54,65,67]. Thus, the availability of heteronucleation sites is one of the most relevant factors that governs the formation of scale [93]. Approaches to identify dominant scaling mechanisms in technical RO applications and to develop a model which describes and predicts scale formation by calcium carbonate [94–97] and gypsum [54] in RO systems were made by Karabelas and coworkers. They complemented flux decline measurements with detailed membrane post-analysis by scanning electron microscopy. After conducting stirred and non-stirred dead-end as well as feed spacer-equipped once-through flow RO experiments, they concluded that (i) scaling in RO systems is predominantly caused by heterogeneous crystallization, i.e. heteronucleation and crystal deposition on the membrane surface followed by lateral growth [54,94–97], that (ii) induction times are practically non-existent for heterogeneous nucleation [54,94,97], that (iii) growth rates increase for larger membrane wall supersaturations [96], that (iv) commonly monitored parameters, such as permeability and bulk fluid turbidity and ion concentrations, are too insensitive to detect the early-stage of scaling and remain unaffected even for appreciable degree of scaling [54,94,97] and that (v) scaling parameters, which are related to crystal nucleation, exhibit a distribution dictated by the variability of local membrane properties [95,96]. In addition, experimental studies by Lyster et al. (2010) [98] and Cobry et al. (2011) [99] on gypsum and calcium carbonate membrane scaling do not provide any evidence that significant induction times exist for heterogeneous crystallization on polymeric membranes.

Given the uncertainties regarding relevant scaling mechanisms in technical applications, it is commonly suggested that scaling may be a combination of both mechanisms [10,100] and that the occurrence strongly depends on system design and operating conditions [84,85].

### **Parameters affecting scaling and scaling mechanisms**

Membrane scaling is most commonly investigated using laboratory membrane systems. They provide the major advantage that only small membrane samples are required which can be exchanged cost-efficiently. However, small membrane areas limit the achievable water recoveries in a once-through flow configuration. To overcome this limitation, many scaling studies rely on either continuous permeate withdrawal and concentrate recycling or on full recirculation of permeate and concentrate using supersaturated solutions. In both scenarios, hydraulic residence times of the recycled experimental solution may achieve values which can exceed the induction time of bulk crystallization at the given supersaturation. This mode of operation is significantly different from full scale applications which commonly operate in once-through flow configuration [54]. Therefore, the occurrence and severity of bulk crystallization in technical applications will predominantly depend on the hydraulic residence time in the system and should only occur if concentrates are recycled to achieve higher water recoveries.

For laboratory scale membrane systems, it has been demonstrated that the operating conditions determine the occurrence of the two scaling mechanisms [84,85,95]. During NF experiments,

gypsum surface crystallization was shown to dominate when concentration polarization was high due to high transmembrane pressure and low cross-flow velocity, whereas gypsum bulk crystallization prevailed when concentration polarization was low due to low transmembrane pressure and high cross-flow velocity [84,85]. Dead-end RO experiments with and without agitation support the significance of the degree of concentration polarization with respect to the occurring scaling mechanisms [95].

Further, it has been suggested that the membrane surface chemistry and topography affect scaling mechanisms and kinetics [101]. Shih et al. (2005) observed significant differences in the size of gypsum surface crystals and the overall surface scale coverage among three commercially available RO membranes [19]. Mi and Elimelech (2010) demonstrated that two membranes of different material, polyamide and cellulose acetate, controlled the prevailing gypsum scaling mechanism in laboratory scale RO and FO\* desalination as well as static crystallization experiments [102]. They hypothesize that the carboxyl functional groups of the RO membrane surface form complexes with the calcium ions from solution leading to heterogeneous crystal nucleation [102]. In contrast, the neutral hydroxyl groups of the cellulose acetate FO membrane did not interact with the scale forming species and scaling occurred from deposition of crystals formed in the bulk [102]. A similar study drawing identical conclusions was recently published by Xie and Gray (2016) [103]. Induction of heterogeneous nucleation of calcium phosphate on surfaces with excessive carboxyl groups was also suggested by Rathinam et al. (2017) monitoring crystallization on oligoamide sensors by a quartz crystal microbalance† [104]. Chen et al. (2013) investigated gypsum scaling on FO membranes of different surface charge and topography [105]. Positively charged membrane surfaces and surfaces with a ridge-and-valley structure alleviated gypsum bulk crystal adhesion, while enhanced gypsum scaling was observed on a negatively charged membrane [105]. The importance of surface topography and chemical functionality of different polymeric surfaces on the kinetics of gypsum surface crystallization was also highlighted by Lin et al. (2011) [106]. Mass density on quartz crystal microbalance sensors was higher for rougher surfaces exhibiting the same charge polarity [106]. However, in the same study it was also shown that surface crystal size, morphology and crystal number density varied significantly with the surface type so that the role of surface roughness and chemical functionality could not be discerned [106]. In this regard, Shaffer et al. (2017) reviewed that smoother FO and RO membrane surfaces generally experienced less scaling than rougher surfaces [107]. The authors emphasize that the relative contribution of membrane surface roughness and surface chemistry to the alleviation of scaling is still unknown [107]. Subsequent investigation of different FO membrane polyamide surface chemistries, fabricated by deposition of smooth films with tunable surface

---

\* Desalination by RO and FO underlies identical principles, only the driving forces are different (RO: applied pressure difference, FO: osmotic pressure difference).

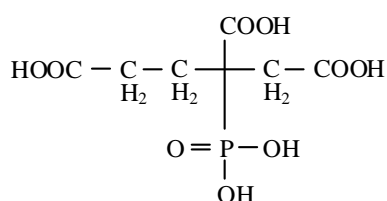
† Quartz crystal microbalances (QCM) are capable of measuring mass changes by surface crystallization or crystal deposition in the nanogram range. Different oligoamide films that mimic NF or RO membrane surfaces can be synthesized on top of the QCM gold sensors. It is important to note that crystallization experiments using QCM techniques are static and that permeation of the polymeric films does not occur.

chemistry, did not show a significant effect on long-term scaling propensity [107]. It was concluded that efforts to develop anti-scaling membranes should focus on the effects of hydrodynamics rather than changes to polyamide surface chemistries [107]. In addition, it has been demonstrated that membrane characteristics [108–110] and performance parameters, such as permeability and salt rejection [111], are not uniform but exhibit significant spatial variability. Just recently, it has been acknowledged that local membrane surface properties, which may be related to crystal nucleation, are expected to vary to an even greater extent [96]. Through experimental and modeling approaches, Mitrouli et al. (2016) [96] and Kostoglou et al. (2017) [95] suggest that heterogeneous calcium carbonate nucleation on RO membranes may be significantly affected by the spatial distribution of energetically favorable nucleation sites on the membrane surface.

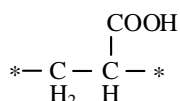
#### 2.2.4 Scale Control by Dosage of Antiscalants

A widely used technique for controlling scale formation in membrane systems is by dosage of an antiscalant [16,17]. When properly selected and applied, an antiscalant can retard scale formation with very low, substoichiometric\* dosages of typically less than 10 mg·l<sup>-1</sup> [16]. Although antiscalants cannot completely prevent crystallization, they effectively retard it until the concentrate leaves the RO plant [112]. Commonly used antiscalants are derived from three chemical families: condensed phosphates and polyphosphates, organophosphates and polyelectrolytes [16]. According to Darton (2000), almost one hundred different antiscalants are used around the world, however, phosphonates and numerous polymers, particularly polyacrylic acid and polymaleic acid, are dominating the market (Figure 2-13) [113].

(a) **phosphonate (PBTCA)**



(b) **polyacrylic acid (PAA)**



(c) **polymaleic acid (PMA)**

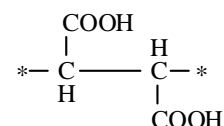


**Figure 2-13: Chemical structures of common antiscalants: (a) example of a phosphonate: 2-phosphono-butane-1,2,4-tricarboxylic acid (PBTCA), (b) polyacrylic acid (PAA) and (c) polymaleic acid (PMA).**

The substoichiometric concentrations required for effective scale suppression indicate that physical rather than chemical reactions are responsible for the inhibitory effect [16,55,112]. An effective scale inhibitor is a compound that interrupts one or more of the stages of the crystallization process [113]. The exact mechanisms of inhibition, however, are poorly understood, especially from their quantitative aspects [55,112]. In general, three closely related mechanisms of inhibition are described, namely the ‘*threshold effect*’, ‘*crystal distortion*’ and ‘*crystal*

\* ‘*substoichiometric*’: less than one mole of antiscalant per one mole of scale-forming anion or cation.

*dispersion*' [113]. The '*threshold effect*' describes the function of an antiscalant to delay the crystallization of a salt by interfering with the nucleation process [113]. It is generally believed that those nucleation inhibitors adsorb onto subcritical nuclei in an early stage, prohibit their growth beyond the critical size and thereby retard the rate of nucleation [55,101]. Alternatively, Gloede and Melin (2007, 2008) hypothesize that nucleation is not inhibited but selectively induced by the antiscalant molecules [112,114]. Selective heteronucleation on the antiscalant molecules leads to the formation of slow-growing metastable nanoparticles which retards the formation of stable nuclei and increases the induction time [112]. '*Crystal distortion*' occurs by adsorption of the antiscalant molecules' negatively charged functional groups [101] on active growth sites of the crystal leading to reduced crystal growth rates, distorted crystal growth and modified crystal habit [16,101,112,113]. In addition, antiscalant adsorption onto crystals may lead to '*dispersive effects*' by giving the crystals a negative, repulsive surface charge thereby preventing their agglomeration and deposition on the membrane surface [113,114].

All polymer inhibitors are effective only within a relatively narrow range of molecular weights, typically around 1,000 – 5,000 Da [55,115–117]. While inhibiting molecules should be sufficiently large to occupy a sufficient area when adsorbed, they should be small enough to feature high mobility and high adsorption rates [55]. Antiscalant effectiveness is generally pronounced at higher dosages [19,76,113,115,116,118–120] and increases with the degree of phosphonic and carboxylic acids [32,55,116,117]. Enhanced effectiveness at higher  $pH$  is attributed to the increased degree of deprotonation of acidic functional groups at increased  $pH$  [55].

Despite the paramount effectiveness of antiscalants, their usage is increasingly associated with several operational and environmental problems. (i) Antiscalants may foul the membrane [121] and enhance biofilm formation [122–124]. (ii) Concentrate streams with rejected antiscalant molecules are commonly released into water bodies and acute and long-term effects on marine and aquatic environments are still uncertain [16,20]. (iii) Recently, 24 commercial phosphonic acid-based antiscalant products, which are approved by § 11 of the German Drinking Water Ordinance, were characterized by advanced analytical techniques [125]. It was found that undeclared phosphonic impurities amounted to up to  $\approx 60\%$  based on the total phosphorus content [125]. Moreover, the study claims that antiscalants were incompletely rejected by current RO membranes during pilot-testing, however, the experimental data have not yet been published [125].

### **2.3 Gypsum Crystallization and Scaling**

The following chapter focuses on gypsum crystallization from supersaturated aqueous solution and gypsum crystallization during high-pressure membrane desalination (NF, RO). First, the relevance of gypsum as a major scale-forming salt during desalination of natural waters is presented in Chapter 2.3.1. Chapters 2.3.2 and 2.3.3 present characteristics of gypsum bulk crystallization and gypsum scaling in membrane systems, respectively, including kinetics,

observed morphology and effects of impurities as well as frequently employed experimental setups and procedures.

### 2.3.1 Relevance of Gypsum Scaling During RO Desalination

The particular risk of scale formation during desalination at high water recoveries was previously demonstrated by Figure 2-11. Scaling is therefore a major concern in brackish water desalination, where high water recoveries are required for economic operation [8]. Brackish water ( $c_{TDS} = 1,000 - 10,000 \text{ mg}\cdot\text{l}^{-1}$  [48]) occurs as brackish groundwater in saline aquifers, as surface water due to erosion, or as a result of seawater mixing with river water or seawater intrusion into groundwater [17]. Major solutes in brackish waters include sodium, chloride, calcium, sulfate and bicarbonate ions [17]. In addition, minor solutes commonly include silicates, iron, strontium, barium, fluoride, selenium, and boron [17]. Different brackish water compositions collected from literature and calculated saturation indices at 75 % water recovery (Table D-1) show that bariumsulfate (barite,  $\text{BaSO}_4$ ), calciumcarbonate (calcite,  $\text{CaCO}_3$ ) and calciumsulfate dihydrate (gypsum,  $\text{CaSO}_4\cdot 2\text{H}_2\text{O}$ ) are the scale-forming salts of major concern. Due to the carbonate system, the solubility of calcite is  $pH$ -dependent and extension of saturation limits can be achieved through  $pH$  adjustment (Figure 2-14). In contrast, barite and gypsum solubilities are  $pH$  insensitive (Figure 2-14) which makes their mitigation and cleaning more problematic. The low concentrations of barium in natural waters make its quantitative contribution to membrane scaling insignificantly small, leaving gypsum as one of the most commonly encountered scale-forming salts in membrane processes for brackish water desalination [9,10,14,15].

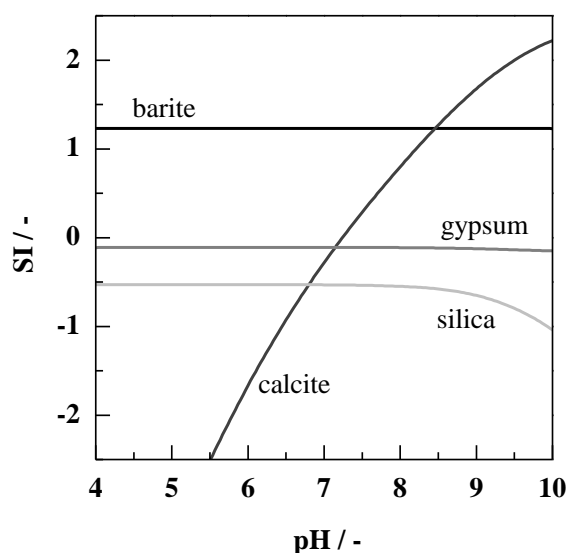


Figure 2-14: Calculated saturation indices ( $SI$ ) as a function of  $pH$  at  $20\text{ }^\circ\text{C}$  for a model brackish water containing  $0.25 \text{ mg}\cdot\text{l}^{-1}$  barium,  $200 \text{ mg}\cdot\text{l}^{-1}$  bicarbonate,  $30 \text{ mg}\cdot\text{l}^{-1}$  silica,  $3,000 \text{ mg}\cdot\text{l}^{-1}$  sulfate,  $400 \text{ mg}\cdot\text{l}^{-1}$  calcium,  $1,500 \text{ mg}\cdot\text{l}^{-1}$  chloride,  $2,000 \text{ mg}\cdot\text{l}^{-1}$  sodium. Concentrations are based on ion concentrations commonly found in natural brackish waters (see Table D-1). Calculations were performed using 'PHREEQC' software, version 3.0.6 and phreeqc.dat database supplied by the US Geological Survey. Solubility products of displayed salts are listed in Table 3-7.

### **2.3.2 Characteristics of Gypsum Bulk Crystallization from Supersaturated Solution**

A great body of literature is available on gypsum bulk crystallization from supersaturated aqueous solution assessing its kinetics and impacts of additives and impurities. Commonly, induction time measurements from stirred laboratory scale glassware crystallization experiments [116,118–120,126–130] or seeded crystal growth experiments [32,77,131] are used to quantify the effects of supersaturation, temperature,  $pH$ , ionic strength and the presence of impurities and additives. Induction time measurements are also frequently used to rank the effectiveness of different additives to retard nucleation. Measurements commonly rely on online monitoring of solution turbidity or ion composition.

Gypsum nucleation from aqueous solution was generally found to strongly depend on kinetic factors and to behave as predicted by classical nucleation theory (Equation 2-11). For example, induction times were observed to be inversely proportional to the supersaturation and temperature [127–129,132–135]. It is established that gypsum crystallization is not affected by  $pH$  over a wide range of  $pH$  values due to the insensitivity of gypsum supersaturation on  $pH$  (Figure 2-14a) [117,136,137]. Alternative pathways of homogeneous and heterogeneous nucleation were identified at high and low supersaturations (transition at  $S \approx 3$  at 25 °C), respectively [127,138]. The fact that all waters, even laboratory model waters, contain colloidal and particulate impurities [67], such as dust particles, heterogeneous nucleation is believed to be the predominant pathway at low supersaturations, i.e. slow nucleation rates. A comprehensive review and experimental study on gypsum nucleation kinetics over a wide range of experimental conditions was published by Reznik (2012) [129]. Gypsum crystal growth rates beyond the induction time are surface controlled and depend on the overall surface area of crystals, on the square of the residual concentration of scale forming ions and follow a second-order dependence upon relative supersaturation [32,128,134,135,139]. It was also reported that gypsum ( $\text{CaSO}_4 \cdot 2\text{H}_2\text{O}$ ) was the only crystallized solid phase, also at higher temperatures where anhydrous calcium sulfate (anhydrite,  $\text{CaSO}_4$ ) is the thermodynamically stable phase [130,140]. Different crystal morphologies have been reported to occur for gypsum crystallized from supersaturated solutions including needles and platelets [139,141] and monoclinic [128] and rhombohedral prisms [36] (Figure 2-15). Gypsum crystal morphology was reported to be affected by the supersaturation ratio [139,142,143], however, no universal trend was observed.

It has been shown that different metal cations, such as  $\text{Cd}^{2+}$ ,  $\text{Cu}^{2+}$ ,  $\text{Fe}^{3+}$  and  $\text{Cr}^{3+}$  [77,144] and  $\text{Zn}^{2+}$  and  $\text{Cu}^{2+}$  [55] retard gypsum crystal nucleation and growth and may affect the crystal habit by incorporation or specific adsorption onto active crystal growth sites. Further, the inhibitory effects of phosphates, phosphonates, amino acids and water-soluble polymers, especially polyacrylic acid, on gypsum bulk crystallization was assessed in several studies [32,116–118,126,145–147]. It was commonly concluded that the dominant mechanism of inhibition is the specific adsorption onto growth site of the developing gypsum crystals leading to retarded nucleation, distorted growth and habit modifications [32,116–118,126,145–147]. In general, a clear dosage-inhibition-efficiency

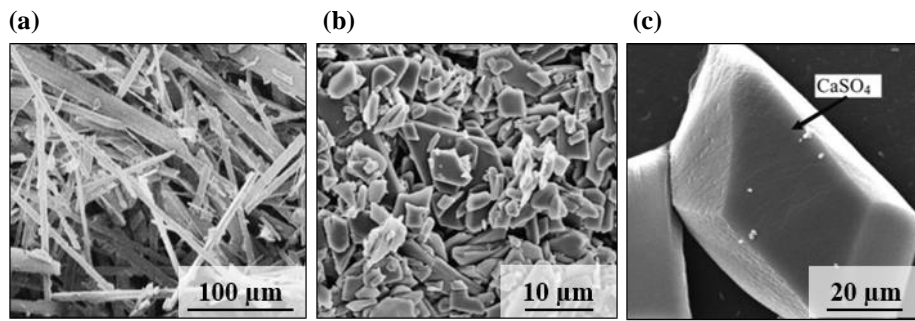


**Figure 2-15: Different morphologies of gypsum bulk crystals crystallized from supersaturated solutions. (a) needles [139], (b) platelets [139] and (c) rhombohedral prisms [36].**

relationship was observed, with enhanced retardation of gypsum nucleation and growth at increased inhibitor dosages [32,76,116,118–120]. Molecular properties of the organic additives have been observed to determine the degree of retardation. Although predictable trends have not yet been identified, certain patterns were repeatedly observed. For polyacrylic acids, threshold inhibition was more efficient at lower molecular weights [116,117,148]. This was also shown for calcite nucleation, where an optimal molecular weight of  $\approx 2,000$  Da was determined [115]. Higher densities of carboxyl groups of the different additives were observed to enhance inhibition [32,116,117]. Also, molecules with sulfonate groups yielded poorer inhibitory effects, likely due to the relatively lower affinity of calcium ions [116,118]. The importance of acidic functional groups is further highlighted by the fact that inhibition is generally pronounced at higher  $pH$  due to deprotonation of carboxyl and phosphonic groups [55].

Limited data is available on the transferability of results obtained from glassware experiments to scaling experiments using membrane systems. Shih et al. (2006) [120] showed that the ranking of antiscalant effectiveness was consistent in membrane scaling and stirred glassware crystallization experiments. From a recent study by Li et al. (2017) [149] it is observable that dissimilar hydrodynamics of different experimental systems limit the comparability and transferability of determined induction times for gypsum bulk crystallization.

### **2.3.3 Characteristics of Gypsum Scaling during Membrane-Based Desalination**

As reviewed in section 2.2.3, scale formation during membrane-based desalination can occur due to bulk or surface crystallization (Figure 2-12). For gypsum, this has been demonstrated using laboratory scale nanofiltration systems [36,84,85]. Depending on the underlying mechanism, different morphologies of gypsum scale have been reported (Figure 2-16). While bulk crystals deposit on the membrane surface and form a dense and homogeneous cake layer of crystals, crystals that nucleated heterogeneously on the membrane surface grow into rosette-like structures [18,19,36,84,85,91,141,150–153].

Different experimental approaches have been used to study gypsum scale development and resulting losses of process performance in laboratory scale cross-flow RO and NF systems. Traditionally, detection of scale formation relied on permeate flux decline and concentrate

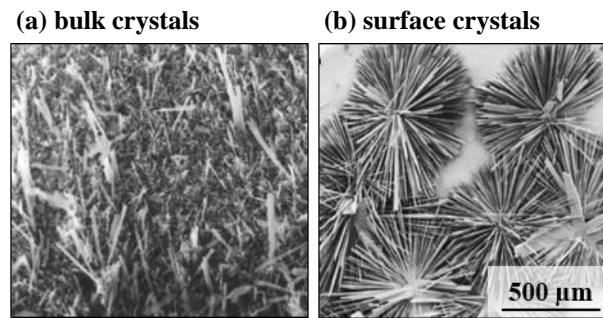


**Figure 2-16: Scanning electron micrographs of membrane surfaces after gypsum scaling by (a) bulk crystallization (no scale or magnification given) [85] and (b) surface crystallization [19].**

turbidity measurements during permeation and concentration of supersaturated solutions. Hasson et al. (2001) first introduced the terms ‘*lower*’ and ‘*upper*’ scaling limit, which describe the supersaturation at which process performance is not deteriorated for a certain period of time (i.e. for as long as the induction time has not been exceeded) and the supersaturation at which spontaneous gypsum bulk crystallization occurs (i.e. the upper end of the metastable zone), respectively [89]. For gypsum scaling due to bulk crystallization, established dependencies of bulk crystallization kinetics on the degree of supersaturation (Chapter 2.3.2) have been confirmed in membrane-based desalination experiments and can be summarized as follows: (i) significant induction times are reported for gypsum bulk crystallization below a critical supersaturation [88–90], (ii) the extent of the induction time is inversely proportional to the degree of supersaturation [88–90], (iii) the achievement of a critical supersaturation, i.e. the ‘*upper*’ scaling limit, triggers spontaneous bulk crystallization [89,90] and (iv) different antiscalants (organo-phosphonate, phosphonic acid sodium salt, polyacrylate and sodium hexametaphosphate) retard the onset of bulk crystallization with increasing effectiveness at higher dosage ( $c_{AS} = 0 - 12 \text{ mg}\cdot\text{l}^{-1}$ ) [89,90]. Strongest retardation of induction time was observed for sodium hexametaphosphate, however, no suggestion with respect to underlying mechanisms was given [89].

Gypsum scaling due to surface crystallization on polymeric membranes and the formation of characteristic rosettes was comprehensively described by Gilron and Hasson (1987) [141]. Since then, extensive research on gypsum surface crystallization has been carried out by Cohen and coworkers by laboratory scale membrane-based desalination experiments [18,19,91,98,154–161]. Shih et al. (2005) investigated axial gypsum surface scale development on RO membranes of different material [19]. Surface coverage and size of rosette-like gypsum surface crystals was observed to increase with axial position along the membrane due to increasing supersaturation. Measurable differences in scale coverage were detected among the different types of RO membranes, which was also shown in a subsequent study by Rahardianto et al. (2006) [18]. Figure 2-17 shows the enhanced inhibition of gypsum scaling due to surface crystallization at increased dosages of a polyacrylic acid-based antiscalant and the effect on crystal morphology [19].

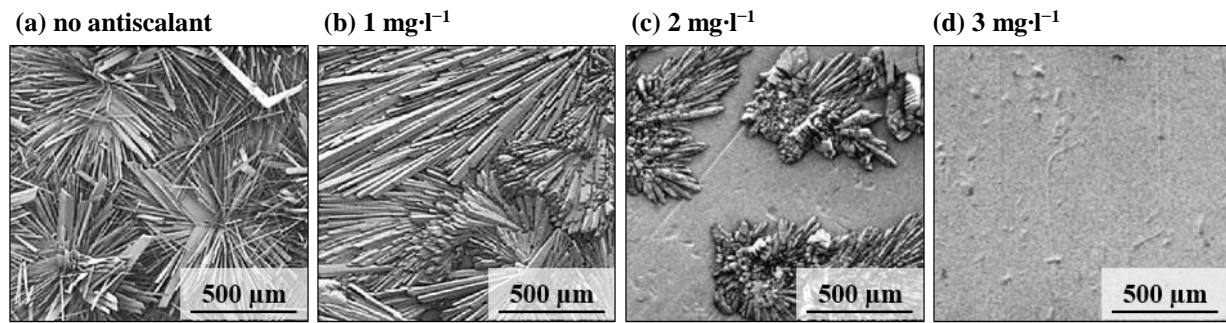


**Figure 2-17: Effect of a polyacrylic acid-based antiscalant on gypsum surface crystal morphology on a reverse osmosis membrane [19].**

Rahardianto et al. (2006) demonstrated that, for a range of gypsum membrane wall supersaturation of  $S_{g,m} = 1.96 - 2.46$  ( $SI_{g,m} = 0.29 - 0.39$ ), flux decline was accelerated and final fraction of the total membrane surface area covered by scale enhanced at higher membrane wall supersaturation [18]. A linear relationship between fractional surface coverage and flux decline was observed [18]. However, fractional flux decline was lower than the fractional surface area covered by scale suggesting incomplete surface blockage by gypsum rosettes [18]. At given membrane wall supersaturation of  $S_{g,m} = 2.46$ , flux decline due to gypsum surface crystallization was alleviated and fractional surface coverage reduced by dosage of a commercial antiscalant ( $c_{AS} = 0.5 - 5 \text{ mg}\cdot\text{l}^{-1}$ ) containing a phosphino-carboxylic acid polymer [18]. Flux decline and surface coverage was lowest at highest antiscalant dosage [18].

It has been acknowledged that monitoring of permeate flux and other global process parameters can only indicate progressed events of scale formation and that those parameters are insensitive to detect the early stages of surficial scale development [54,94,97,156,162]. Advanced experimental methods for early-stage scale detection are reviewed by Karabelas et al. (2014) [54] and Shirazi et al. (2010) [15]. Among the available techniques, direct observation of the membrane surface using real-time imaging by light microscopy is currently the most sensitive method to monitor early-stage development of scale on membrane surfaces [97]. This method was first presented by Cohen and coworkers [156,157]. It consists of a plate-and-frame RO cell with an optical window and operates below gypsum saturation in full recirculation mode, i.e. recycles concentrate and permeate back into the feed reservoir. Supersaturation at the membrane surface is achieved through intensified concentration polarization by operation without a feed channel spacer at constant transmembrane pressure. This mode of operation prevents crystal formation in the fluid bulk and favors the heterogeneous crystallization of gypsum on the membrane surface. With a spatial resolution of  $100 - 150 \mu\text{m}$  [91], the method cannot detect the true onset of crystallization but can provide useful insights into the kinetics of gypsum scaling due to surface crystallization at the single crystal level. The experimental setup has since been used in a variety of studies to investigate heterogeneous gypsum scale formation during RO desalination of synthetic and agricultural drainage waters [91,98,156,158–161]. In general, it was observed that detected gypsum crystals grew continuously into rosette-like structures and that gypsum crystals became visible at different

times, ranging from minutes to hours of operation [91,156]. It was suggested that the most favorable surface nucleation sites were populated first as the time of appearance of crystals increased for each new detected crystal [91]. Lateral crystal growth and increasing gypsum surface crystal density led to increasing surface coverage over time [91,156]. For a range of gypsum membrane wall supersaturations of  $S_{g,m} = 1.30 - 1.72$  ( $SI_{g,m} = 0.11 - 0.24$ ), a more rapid evolution of detected crystal number density and surface coverage was observed at higher membrane wall supersaturations [91]. After modeling hydrodynamics and mass transfer in the employed RO cell [154,155], Lyster et al. (2010) were able to relate observed heterogeneous gypsum crystallization to modelled local supersaturation at the membrane wall ( $SI_{g,m} = 0.11 - 0.36$ ) in single experiments [98]. Calculated intrinsic nucleation rates increased with increasing supersaturation as predicted from classical nucleation theory. Two commercially available antiscalants (carboxylic acid-based and unknown composition) significantly retarded crystal nucleation and growth over the range of investigated supersaturations at a dosage of  $3 \text{ mg}\cdot\text{l}^{-1}$  [98]. The retarding effect of the two antiscalants was confirmed in further studies [158,160,161] using the same experimental setup. Further, the method has been used to demonstrate that growth of gypsum surface crystals was enhanced within a biofilm due to enhanced concentration polarization (CECP, see Chapter 2.4.5 and Figure 2-19) [159] and retarded by adsorption of bicarbonate onto the crystal surface [161].

A non-uniform surficial distribution of gypsum rosettes was repeatedly observed by Cohen and coworkers [91,98,156]. This non-uniformity and the different times of new crystal appearance were explained by either the given randomness [156] and stochastic nature [98] of the nucleation process or the limited availability of energetically favorable heterogeneous surface nucleation sites [91]. The latter suggestion is consistent with recent advances made by Mitrouli et al. (2016) [96] and Kostoglou et al. (2017) [95] who suggest that common polymeric membranes exhibit a spatial distribution of energetically favorable nucleation sites on the membrane surface.

Given this local variability in surface crystallization and the fact that the subarea that can be microscopically monitored by real-time surface imaging is very small, significant data scatter between repeated experiments can be expected. Although this limitation does not conflict with the distinct trends that were observed in previous studies, the assessment of data scatter in repeated experiments (i.e. the reproducibility) would quantify the smallest degree of change that can be detected using this method. To date, the reproducibility of the real-time imaging method has not been documented in literature.

## **2.4 Properties and Effects of Natural Organic Matter**

### **2.4.1 NOM Definition, Properties and Abundance**

The term ‘*natural organic matter*’ (NOM) is used to describe all the organic matter present in a natural water body other than living organisms and compounds of man-made origin [163]. NOM mainly derives from the decomposition of plant and animal residues [164]. Due to the ubiquitous

abundance of NOM in natural waters, it plays a fundamental role in many biological, physical and chemical processes in the environment and in engineered systems [22,23].

NOM possesses a large variety of molecular weights and physical, chemical and structural properties and represents an extremely complex mixture of compounds, most of which have not yet been identified [163]. Molecular weight of dissolved NOM, which is the NOM that passes membrane filtration with a nominal pore size of 0.45  $\mu\text{m}$ , commonly ranges from a few hundred Da to 100 kDa, which is in the colloidal size range\* [22]. NOM is commonly categorized into (i) biopolymers, including primarily proteins and large molecular weight polysaccharides with a long persistence length, (ii) refractory humic substances, including fulvic and humic acids, and (iii) low molecular weight molecules ( $M_w < 1,000$  Da) [21]. NOM molecules generally consist of individual aromatic and aliphatic hydrocarbon structures that have attached amide, carboxyl, hydroxyl, ketone, and various minor functional groups [22]. At the  $pH$  range of natural waters, NOM molecules generally carry a negative charge due to the deprotonation of their distributed carboxyl and hydroxyl groups [164]. The charge character of organic macromolecules is a key property that determines the interactions of NOM with surfaces and divalent cations [165]. NOM terminology and characterization have been comprehensively reviewed by Filella (2009) [163] and Leenheer and Croué (2003) [22].

NOM concentrations of natural waters depend mainly on the water source. For ground waters, the dissolved organic carbon (DOC) concentration typically ranges between 0.5  $\text{mg}\cdot\text{l}^{-1}$  and 4.0  $\text{mg}\cdot\text{l}^{-1}$  [166], however, ground waters associated with coal deposits may have significantly higher concentrations [167]. DOC concentrations of mesotrophic surface waters typically range between 2  $\text{mg}\cdot\text{l}^{-1}$  and 5  $\text{mg}\cdot\text{l}^{-1}$  [166] with significantly higher concentrations found in bog lakes. Shallow seawater (0–300 m depth) typically exhibits a DOC concentration of 0.3–2  $\text{mg}\cdot\text{l}^{-1}$ , while concentrations below 300 m depth are typically below 0.8  $\text{mg}\cdot\text{l}^{-1}$  [167]. Brackish ground waters, which are naturally saline or have become brackish by salt water intrusion, are typically characterized by low organic carbon concentrations comparable to that of ground waters [9]. During desalination of natural waters, NOM concentrations in the feed stream will continuously increase due to pure water extraction. Depending on water recovery ( $\Phi$ ), NOM concentrations in the resulting concentrate stream will be significantly higher compared to the initial NOM concentration of the feed water. For example, NOM concentrations in the concentrate will increase by a factor of 4–10 for typical brackish water desalination applications (see Figure 2-11).

#### **2.4.2 Properties of Different NOM Types**

To represent the different categories of NOM in natural waters, different humic substances, which have been extracted from soil and coal (terrestrial origin [168]) or natural waters (aquatic origin)

---

\* According to IUPAC, the term ‘colloidal’ refers to molecules or polymolecular particles dispersed in a medium which have at least in one direction a dimension roughly between 1 nm and 1  $\mu\text{m}$  [63].

as well as well-defined polysaccharides and proteins are frequently used as surrogate NOM sources in NOM-related research.

Humic substances are found in all aquatic environments and constitute one of the most abundant forms of natural organic matter [169]. The main fractions of humic substances are humic and fulvic acid, which are operational definitions in terms of their solubility in aqueous media as a function of  $pH$ : humic acid is insoluble at acidic conditions whereas fulvic acid is soluble at all  $pH$  values [169]. Humic substances are highly polydisperse with typical molecular weights ranging from several hundred Da to a few hundred kDa [170]. They are negatively charged over a wide  $pH$  range ( $pH > 3$ ) due to the deprotonation of attached carboxyl and hydroxyl groups [168]. Accordingly, charge density increases at higher  $pH$ . At low concentration, low ionic strength and neutral or high  $pH$ , humic substance molecules are flexible linear molecules, however, when any of these conditions are changed, they assume a coiled, globular configuration [171]. Molecular properties of humic substances have been reported to vary according to their source [30,172–174]. Generally, it was found that humic substances from marine and aquatic environments have a more branched aliphatic and less aromatic structure as well as smaller molecular weights than those having terrestrial influence (higher plant and/or soil source).

Compared to humic substances, polysaccharides are significantly larger macromolecules with molecular weights ranging from a few hundred to a few thousand kDa [21]. Polysaccharides typically have a rigid fibrillar- or rod-like structure and exhibit weak negative charges mainly caused by carboxyl groups [175]. Proteins are characterized by well-defined molecular weights and typically represent globular macromolecules with amphoteric charge properties resulting from the presence of both, carboxyl and amide groups [21]. At a  $pH$  below their respective isoelectric point ( $pH_{IEP}$ ), proteins are positively charged and at a  $pH$  greater than  $pH_{IEP}$  negative charges prevail [21].

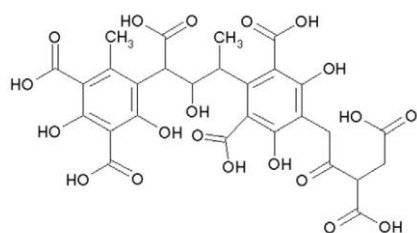
Besides  $pH$ , the charge properties of NOM molecules depend on ionic strength and concentration of divalent cations, which are naturally high in brackish water and seawater. Hong and Elimelech (1997) demonstrated that the charge of different humic acids is significantly reduced due to double layer compression and charge screening at high ionic strengths and in the presence of bivalent cations [25]. Unlike monovalent cations, multivalent cations, especially calcium, have strong affinity to acidic functional groups [21,176]. They can complex with the carboxylic moieties of organic macromolecules, form metal-NOM complexes and partially compensate the NOM negative charge [176–179]. Resulting reduced interchain electrostatic repulsions are responsible for the coiled conformation of humic acids at high ionic strength, high calcium ion concentration and low  $pH$ . Additionally, calcium is able to cross-link organic macromolecules which can lead to the formation of extensive three-dimensional gel-like macromolecular structures [175,177,180–182]. Many polysaccharides, such as alginate, are known to form extensive gel-like structures through calcium ion bringing [175,181,183,184].

Table 2-1 exhibits selected properties of humic acid, alginate and bovine serum albumin (BSA), which are three commonly used examples of model substances that represent different NOM types in natural waters. Figure 2-18 displays corresponding schematic chemical structures.

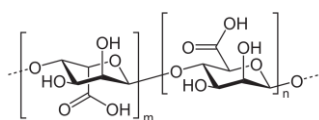
**Table 2-1: Examples and properties of commonly used organic macromolecules in NOM-related membrane research: (a) humic acid, (b) alginate and (c) BSA. Sources: (a) [170], (b) [175], (c) manufacturer's data (Sigma Aldrich Co., MO, USA), (d) [182], (e) [185], (f) [25], (g) [168], (h) [186], (i) [187], (j) [188], (k) [189].**

	(a) humic acid	(b) alginate	(c) BSA
<b>NOM category</b>	humic substances	polysaccharide	protein
<b>molecular weight</b>	few 100 Da – few 100 kDa <sup>(a)</sup>	200 – 2,000 kDa <sup>(b)</sup>	67 kDa <sup>(c)</sup>
<b>functional groups</b>	COOH, C=O, NH <sub>2</sub> , OH	COOH, OH	COOH, C=O, NH <sub>2</sub>
– <b>carboxyl groups</b>	3.3/3.4/10.7 meq·g <sup>-1</sup> <sup>(e/f/g)</sup>	3.0/6 meq·g <sup>-1</sup> <sup>(d/b)</sup>	1.4/1.5 meq·g <sup>-1</sup> <sup>(h/i)</sup>
– <b>phenolic hydroxyl groups</b>	2.5 meq·g <sup>-1</sup> <sup>(e)</sup>	–	–
<b>isoelectric point (pH<sub>IEP</sub>)</b>	< 3 <sup>(a)</sup>	< 3 <sup>(j)</sup>	4.7 – 4.9 <sup>(k)</sup>

(a) humic acid (e.g. C<sub>187</sub>H<sub>186</sub>O<sub>89</sub>N<sub>9</sub>S)



(b) alginate (C<sub>6</sub>H<sub>8</sub>O<sub>6</sub>)<sub>n</sub>



(c) BSA (607 amino acid residues)

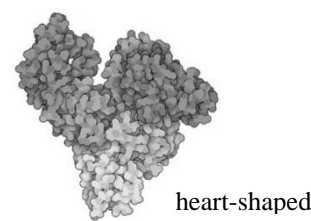


**Figure 2-18: Schematic chemical structures of commonly used organic macromolecules in NOM-related membrane research: (a) humic acid, (b) alginate and (c) BSA.**

### 2.4.3 Effects of NOM on Crystallization Kinetics and Crystal Morphology

Similar to polymeric antiscalants (Chapter 2.2.4), NOM molecules are polyelectrolytes and exhibit different functional groups, particularly carboxyl groups. In contrast, their molecular weight is usually several magnitudes larger. As water constituents, NOM molecules can directly interfere with crystallization processes. Generally, an inhibitory effect and morphological changes, i.e. changes of crystal habit and crystal size, are observed in the coexistence of NOM. For gypsum, this has been shown for the crystallization from supersaturated aqueous solutions [32,33,190] and for the formation of gypsum scale in membrane systems [14,36–39,41]. In general, two mechanisms of interference are discussed: (i) calcium ion complexation by NOM and reduction of supersaturation and (ii) adsorption of NOM molecules onto growth site of developing crystals. Barcelona et al. (1978) investigated gypsum nucleation in natural seawater before and after extraction of NOM [190]. Retarded gypsum nucleation and modification of the normal crystal habit was observed in the presence of NOM and was linked to the adsorption of polar organics onto specific crystal faces [190]. Hamdona et al. (2008) observed reduced gypsum crystal growth rates in the presence of different amino acids ( $M_w = 75 - 174$  Da,  $c = 0 - 20 \mu\text{mol}\cdot\text{l}^{-1}$ ) [32].

Inhibition was stronger at higher amino acid concentration and strongest for the largest molecule [32]. Amino acid adsorption onto crystal faces was assumed to be the underlying mechanism of inhibition [32]. Bock (2017) observed a stronger inhibitory effect of fulvic acid (aquatic origin: Suwannee River, supplied by IHSS) compared to humic acid (terrestrial origin, supplied by Sigma-Aldrich Co., MO, USA) on gypsum nucleation determined from stirred supersaturated model solutions [33]. The author suggested that the smaller molecular weight of the fulvic acid, its higher mobility and higher content of acidic functional groups is responsible for the superior effect [33]. The inhibitory effect was enhanced at higher  $pH$ , presumably due to the deprotonation of acid functional groups [33].

Complementary results are available on the effects of NOM on calcite crystallization from aqueous solution. During seeded calcite crystal growth experiments, Lin et al. (2005) observed different degrees of inhibition by three humic acids ( $c = 0 - 5 \text{ mg}\cdot\text{l}^{-1}$ ) supplied by the IHSS [34]. Strongest inhibition was observed for the humic acid that exhibited the highest molecular weight and highest aromaticity [34]. Hoch et al. (2000) demonstrated that the molecular weight and particularly the aromaticity of humic substances correlated well with growth inhibition of calcite using extracted humic substances from the Florida Everglades (USA) and Lake Fryxell (Antarctica) [35]. The modified morphology of crystals grown in the presence of humic substances suggested that surface growth sites were blocked by adsorbing NOM ligands [35].

A limited number of membrane-related studies is available that investigated the interference of scaling and NOM. Lee et al. (2009) permeated aqueous gypsum solutions ( $c_g = 2 \text{ g}\cdot\text{l}^{-1}$ ) by dead-end RO and achieved higher concentration factors in the presence of humic acid (terrestrial origin, supplied by Sigma-Aldrich Co., MO, USA) and fulvic acid (aquatic origin, Suwannee River, supplied by IHSS) [37]. Humic acid adsorption onto crystal growth sites was claimed responsible for the inhibitory effect and observed morphological changes. An identical experimental approach was employed by Oh et al. (2009) which showed that achievable concentration factors increased in the presence of  $2 \text{ mg}\cdot\text{l}^{-1}$  tannin but remained unaffected by  $2 \text{ mg}\cdot\text{l}^{-1}$  BSA or dextran [38]. Karabelas et al. (2017) performed dead-end RO scaling experiments and observed strong inhibition of gypsum surface crystal development by alginate [39]. At low alginate concentration ( $c = 2 \text{ mg}\cdot\text{l}^{-1}$ ), inhibition was found to originate from growth retardation whereas at higher alginate concentration ( $c = 10 \text{ mg}\cdot\text{l}^{-1}$ ) inhibition was enhanced and caused by the '*threshold effect*', i.e. by adsorption and blockage of subcritical nuclei [39]. In contrast, during forward osmosis desalination, Liu and Mi (2012) observed increased gypsum crystal sizes and higher surface coverage in the presence of alginate ( $c = 200 \text{ mg}\cdot\text{l}^{-1}$ ) [41]. The authors hypothesize that the alginate molecules in solution acted as heteronuclei by attracting calcium ions. However, given the employed high concentration of alginate in their experiments, transferability of effects to natural waters is questionable. Koyuncu and Wiesner (2007) observed morphological variations of gypsum and calcite crystal deposits on nanofiltration membranes using three different natural surface waters of different total organic carbon (TOC), magnesium and sulfate concentrations [36].

Despite the multiple variables, the authors stated that the complexity of crystal morphology increased at higher TOC concentration. Performing scaling experiments during membrane distillation, Curcio et al. (2010) showed that humic acid ( $c = 2 \text{ mg}\cdot\text{l}^{-1}$ ) significantly retarded nucleation and growth of gypsum crystals, presumably by adsorption onto growth sites [40].

In addition to direct interactions between dissolved NOM molecules and the crystallization process during mineral scale formation, desalination of natural waters will inevitably change the intrinsic physicochemical membrane surface properties due to fouling by NOM [42,43]. Interfacial interactions, such as surficial scale formation, may thus be governed by the characteristics of the developing fouling layer [21]. This is further discussed in Chapter 2.4.5.

#### **2.4.4 NOM Fouling During Reverse Osmosis Desalination**

Organic fouling of RO membranes is caused by adsorption and deposition of NOM molecules onto the membrane surface and the progressive formation of a colloidal NOM cake layer. The membrane-foulant and foulant-foulant interactions in aqueous solution are determined by three key interfacial interactions: van der Waals, electrostatic double layer and acid-base interactions [191]. General factors affecting NOM fouling can be classified as (i) chemical composition of the feed water, (ii) characteristics of NOM, (iii) membrane properties and (iv) operational conditions [21,25,192]. Membrane fouling by NOM is comprehensively reviewed by Tang et al. (2011) [21].

##### **Effects of feed water chemical composition**

The role of solution chemistry on colloidal NOM fouling can be explained via electrostatic interaction between colloids and the membrane surface and via specific interaction between the NOM molecules and the background electrolytes [21]. Many physicochemical properties of NOM molecules (functional groups, charge, size, conformation, etc.) and polyamide-based membrane surfaces (functional groups, charge) can be drastically affected by solution chemistry. Double layer compression and charge screening [25,192] as well as protonation of acidic functional groups at low  $pH$  [21,25] reduce electrostatic repulsion of both, NOM molecules and the membrane surfaces, and can lead to increased foulant adsorption and deposition. The surface charge can also be altered by specific adsorption of bivalent cations onto NOM and membrane surface acidic functional groups [25,27,193,194]. In addition, calcium ion bridging between acidic functional groups of NOM molecules and membrane surfaces can cause NOM adsorption [194,195]. Conformal changes of NOM due to charge neutralization by mono- and bivalent ions as well as the formation of cross-linked macromolecular structures mediated by calcium ion bridging were found to form denser fouling layers [25,196].

##### **Effects of NOM character**

As reviewed by Tang et al. (2011) fouling by humic substances was more severe at high foulant concentration and solution chemistries that result in reduced electrostatic repulsive forces, namely

lower  $pH$ , higher ionic strength and higher divalent cation concentration (especially calcium concentration) [21]. Fouling tests using nanofiltration [197,198] and ultrafiltration [199] membranes have shown that the physical adsorption of the hydrophobic NOM fraction onto hydrophobic moieties of the membrane surface by van der Waals forces caused more severe flux decline compared to the hydrophilic NOM fraction. Generally, the hydrophobicity of humic substances is thought to increase with the molecular size [25,198]. Accordingly, Nilson and DiGiano (1996) concluded that the large molecular weight fraction of NOM contributes predominantly to the formation of an NOM cake layer [198]. Polysaccharide fouling of RO membranes was most intensively studied using alginate as a model foulant. Elimelech and coworkers reported that, similar to humic acid, alginate fouling is more severe at lower  $pH$  and higher ionic strength [187,200,201]. The presence of divalent cations, especially calcium, aggravated alginate fouling due to the specific interaction between calcium and the carboxylic moieties of the alginate molecules and due to the formation of extensive gel-like structures [182]. Jin et al. (2009) further reported that alginate became more hydrophobic upon addition of calcium ions [191]. RO membrane fouling was found to be more severe for alginate compared to humic acid, which was explained by the larger molecular size of alginate, its associated lower diffusion coefficient and its lower charge density [201]. Protein fouling studies on RO membranes are virtually limited to using BSA as a model foulant. According to the expected electrostatic interactions, BSA fouling was observed to be most severe at its isoelectric point ( $pH = 4.7 - 4.9$ ), at increased ionic strength and in the presence of calcium ions [28,187].

### **Effects of membranes characteristics**

Membrane surface physicochemical properties such as roughness, present functional groups, charge and hydrophobicity can affect NOM fouling [21,202]. As reviewed by Tang et al. (2011) and Li et al. (2014), smooth and neutral hydrophilic membranes with low carboxylic moieties are less prone to colloidal NOM fouling at the initial stage of permeation [21,202]. However, intrinsic membrane surface properties become less relevant over time as fouling layers will progressively determine surface properties [26,203–205]. Consequently, only the initial phase of membrane fouling is determined by foulant-membrane surface interactions, whereas subsequent fouling is dominated by foulant-deposited-foulant interactions [26,203–205].

### **Effects of operating conditions**

Permeate flux and cross-flow velocity significantly influence mass transfer across the membrane surface and the severity of concentration polarization (see Chapter 2.1.1). Accordingly, membrane fouling is generally enhanced at high permeate flux and low cross-flow velocity, where boundary layer thickness and concentration polarization are high [21]. Higher shear stress at high cross-flow velocities was also found to disrupt the cake layer formation thereby reducing the severity of NOM deposition on an NF membrane [197]. Other parameters, such as water recovery (i.e. effective

NOM concentration at the membrane surface) and temperature, may also significantly affect NOM fouling [21].

#### **2.4.5 Effects of NOM Fouling on Membrane Properties and Scaling**

It was shown that the surfaces of reverse osmosis [26,27] and nanofiltration membranes [25–27] become more negatively charged due to membrane fouling by different model and aquatic humic acids. Hong and Elimelech (1997) observed that the resulting negative charge was found to be directly related to the carboxylic acidity of the humic acids [25]. Similarly, Tang et al. (2007) observed that different RO and NF membranes with considerably different virgin zeta potentials\* all exhibited identical zeta potentials after humic acid fouling [26]. Mo et al. (2008) showed that the zeta potential of an RO membrane fouled with BSA became less negative and that the detected isoelectric point ( $pH_{IEP} = 4.5$ ) was close to that of BSA ( $pH_{IEP} = 4.7 - 4.9$ ) [28]. The increased negative charge of organically fouled membrane surfaces may enhance electrostatic repulsion of anions [29] resulting in an improved salt rejection. At the same time, an increased salt rejection would enhance supersaturation and thus enhance crystallization kinetics in the concentrate stream and boundary layer. Hydrophobicity of NF and RO membranes were found to increase after fouling by humic acid and alginate with resulting contact angles being very similar despite the considerably different virgin hydrophobicity of the two membranes [12]. Increased hydrophobicity of an RO membrane by humic substances of different origin was also shown by Hung et al. (2013) [30].

Although surface properties of polymers and virgin polymeric membranes have been identified to affect the scale formation (Chapter 2.2.3) [19,102–107,107], insights into the effects of existing NOM fouling layers and its properties on the formation of mineral scale by surface crystallization are still limited. Recently, Wang et al. (2016) [43] and Liu and Mi (2012, 2014) [41,42] observed accelerated gypsum scale formation on FO and NF membranes which had been previously fouled with alginate and humic acid. The authors hypothesize that the higher densities of carboxyl groups of alginate and humic acid fouling layers as compared to the virgin membrane attracted calcium ions and thereby acted as heteronucleation sites for crystal development. While Wang et al. (2016) [43] observed enhanced scale formation also after BSA fouling, Liu and Mi (2014) [42] observed an inhibitory effect which is explained by the lower carboxylic acidity of BSA and an additional steric obstruction effect that interferes with interaction between BSA molecules and calcium ions. It is important to note that Wang et al. (2016) [43] and Liu and Mi (2014) [42] used disproportionately high concentrations of organic macromolecules ( $200 \text{ mg}\cdot\text{l}^{-1}$  and  $100 \text{ mg}\cdot\text{l}^{-1}$ , respectively) to enhance NOM fouling. Given the exaggerated thickness of the resulting fouling layers, desorption of NOM from the fouled membranes during subsequent scaling experiments leading to NOM coexistence in the feed solution and to direct interactions between dissolved NOM

---

\* The zeta potential ( $\zeta$ ) describes the charging behavior at the membrane-liquid interface [206]. It is defined as the electrical potential at the shear plane which separates a stationary and a mobile layer of charges [206]. A detailed review on the principles of the zeta potential is provided by Luxbacher (2014) [206].

molecules and crystal nucleation and growth has to be considered. Opposing observations were made by Karabelas et al. (2017), who investigated gypsum scaling on low-pressure RO membranes that had been previously conditioned with alginate [39]. In their investigations, gypsum scale development was significantly inhibited due to the alginate fouling layer [39]. Besides the general tendency of carboxyl groups to adsorb onto and block active sites of growing nuclei and crystals, no explicit explanation for the inhibitory effect of the fouling layer is given [39].

Apart from physicochemical changes of the membrane surface, NOM cake layers can affect mass transfer and enhance concentration polarization at the membrane surface (Figure 2-19). This phenomenon was first described by Hoek and Elimelech (2003) and is referred to as cake-enhanced concentration polarization (CECP) [207]. CECP arises due to the hindered back diffusion of rejected solutes from the fouled membrane surface to the bulk solution through the obstructive cake layer of colloidal matter such as NOM. The absence of tangential shear within the cake layer additionally increases the thickness of the boundary layer. As a consequence, solute concentration and osmotic pressure are greatly enhanced at the membrane surface.

Besides permeability loss [207–211] and deterioration of permeate quality by increased solute passage [12,207,208,212–214], CECP may enhance crystal nucleation and growth by increased supersaturation at the membrane surface [41–43,159].

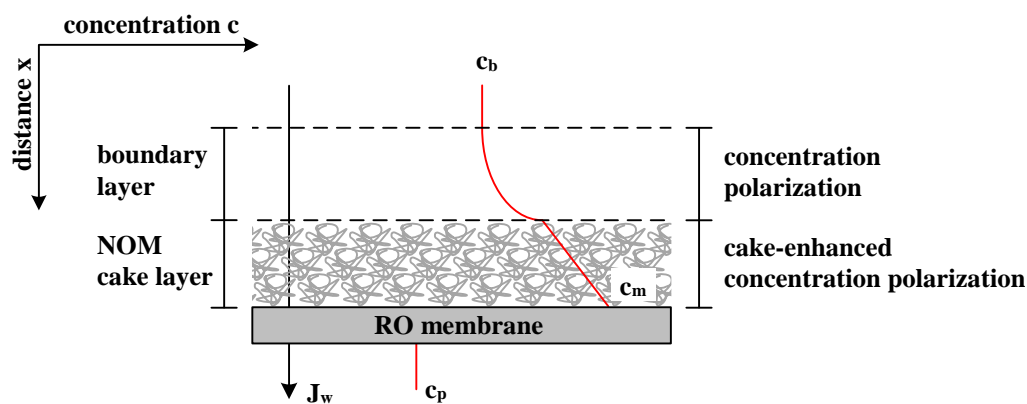


**Figure 2-19: Cake-enhanced concentration polarization (CECP) due to colloidal NOM cake layer formation according to [207,213].**

### 3 Material and Methods

#### 3.1 Chemicals, Solutions and Materials

##### 3.1.1 Natural Organic Matter

Table 3-1 summarizes the NOM sources that were selected to represent three different types of NOM in natural waters. Commercially available substances (Table 3-1a) were obtained in powder or crystalline form and stock solutions were prepared as summarized in Table 3-2. All stock solutions were stored in the dark at 4 °C. Dissolved organic carbon (DOC) concentrations of stock solutions were determined by at least three-fold measurement. The ‘Hohlohsee’ (Table 3-1b) is a bog lake in an upland moor in the Black Forest of Germany. It is located within a preservation area, approximately 1000 m above sea level. ‘Hohlohsee’ water (HSNOM) was sampled by the staff of the Engler-Bunte-Institut Karlsruhe, Germany on June 17, 2015 (sample ID HO29), immediately shipped and stored at 4 °C in the dark. Water composition of HSNOM is summarized in Table 3-3. Pre-filtered (0.45 µm) HSNOM was used as a natural source for aquatic NOM given its high DOC concentration and low electrical conductivity, i.e. low concentration of inorganic constituents. A comprehensive review of ‘Hohlohsee’ water composition and seasonal variation

**Table 3-1: Summary of natural organic matter sources used in this study. (a) Commercially available products obtained in powder or crystalline form. Suppliers: <sup>1</sup> Sigma-Aldrich Co. (MO, USA), <sup>2</sup> Carl Roth GmbH + Co KG (Germany), <sup>3</sup> International Humic Substances Society. (b) Aquatic NOM sampled from lake ‘Hohlohsee’.**

(a)					
NOM category	selected substance	acronym	origin	supplier	product no.
polysaccharide	sodium alginate	SA	synthetic	Sigma-Aldrich <sup>1</sup>	W201502
protein	bovine serum albumin	BSA	animal derived	Sigma-Aldrich <sup>1</sup>	A1933
humic acids	humic acid	RHA	coal extracted [215]	Carl Roth <sup>2</sup>	7824
humic acids	humic acid	SAHA	soil extracted [30]	Sigma-Aldrich <sup>1</sup>	53680
aquatic NOM	Suwannee River NOM	SRNOM	RO isolated	IHSS <sup>3</sup>	2R101N
(b)					
aquatic NOM	Hohlohsee water	HSNOM	surface water	-	HO29

**Table 3-2: Preparation protocol, final DOC concentrations ( $\pm$  SD) and maximum duration of usage (storage life at 4 °C) of NOM stock solutions listed in Table 3-1a. All substances were dissolved in ultrapure water.**

NOM	c / g·l <sup>-1</sup>	procedure	DOC / mg·l <sup>-1</sup>	storage
SA	1	gentle stirring for several hours, 0.45 µm filtration	193 $\pm$ 18	5 days
BSA	1	gentle stirring for several hours, 0.45 µm filtration	322 $\pm$ 14	5 days
RHA	10	ultrasonification for 2 hours, gentle stirring for several days, 0.45 µm filtration	1878 $\pm$ 78	unlimited
SAHA	10	dissolution; precipitation with 1 mol·l <sup>-1</sup> HCl at pH $\approx$ 1; centrifugation, re-suspension, repetition for 4 times, final precipitate dissolved in ultrapure water, 0.45 µm filtration (similar preparation procedure as in [25])	3528 $\pm$ 23	unlimited
SRNOM	1	gentle stirring for several days; 0.45 µm filtration	396 $\pm$ 19	unlimited

is provided by Frimmel et al. (2002) [23]. Prior to the usage of HSNOM, the sample was pre-filtered by 0.45  $\mu\text{m}$  membrane filtration (cellulose nitrate, Sartorius AG, Germany) and DOC concentration determined by at least three-fold measurement. A HSNOM control sample, referred to as ‘*HSNOM after PAC*’ was prepared by removing the organic content of the sample through adsorption onto powdered activated carbon (PHC AZ 1050, Carbon Service & Consulting GmbH & Co. KG, Germany). 5  $\text{g}\cdot\text{l}^{-1}$  of PAC was added to the stirred (300 rpm) sample and equilibrated for 24 h. PAC was subsequently removed from the sample by 0.45  $\mu\text{m}$  filtration. By PAC adsorption, the DOC was reduced from 21.8  $\text{mg}\cdot\text{l}^{-1}$  to 0.31  $\text{mg}\cdot\text{l}^{-1}$ .

**Table 3-3: Composition of the ‘Hohlohsee’ water (HSNOM) after pre-filtration by 0.45  $\mu\text{m}$  (sample ID: HO29). Concentrations of inorganic constituents were determined by ICP-OES or IC and supplied by the Engler-Bunte-Institut Karlsruhe, Germany.**

TOC	DOC	EC	Al	Br	Ca	Cl	F	Fe	K
$\text{mg}\cdot\text{l}^{-1}$	$\text{mg}\cdot\text{l}^{-1}$	$\mu\text{S}\cdot\text{cm}^{-1}$	$\text{mg}\cdot\text{l}^{-1}$						
23.5 $\pm$ 0.7	21.8 $\pm$ 2.6	34.0	0.105	< 0.25	0.791	2.0	< 0.1	0.250	0.007
Mg	Mn	Na	NO <sub>2</sub>	NO <sub>3</sub>	PO <sub>4</sub>	S	Si	SO <sub>4</sub>	Zn
$\text{mg}\cdot\text{l}^{-1}$	$\text{mg}\cdot\text{l}^{-1}$	$\text{mg}\cdot\text{l}^{-1}$	$\text{mg}\cdot\text{l}^{-1}$	$\text{mg}\cdot\text{l}^{-1}$	$\text{mg}\cdot\text{l}^{-1}$	$\text{mg}\cdot\text{l}^{-1}$	$\text{mg}\cdot\text{l}^{-1}$	$\text{mg}\cdot\text{l}^{-1}$	$\text{mg}\cdot\text{l}^{-1}$
0.145	0.084	0.500	< 0.1	< 0.1	< 0.25	0.402	< 0.040	0.4	0.043

### 3.1.2 Chemicals, Reagents and Glassware

**Acids and bases:** For *pH* adjustments and titrations, reagent grade ( $\geq 99\%$ , p.a., ISO) sodium hydroxide (NaOH), potassium hydroxide (KOH) and hydrochloric acid (HCl) supplied by Carl Roth GmbH + Co KG (Germany) in liquid form were used and diluted in ultrapure water.

**Antiscalant:** The commercially available antiscalant ‘*Osmotech<sup>®</sup> 1339*’ based on polyacrylic and phosphonic acid was supplied by BK Giulini GmbH (Germany). The product was supplied in liquid form and stock solutions of 1  $\text{g}\cdot\text{l}^{-1}$  product were prepared by dilution with ultrapure water. Carbon mass content of the liquid product was quantified as 25 % by DOC measurement.

**Salt solutions:** For preparation of scaling and electrolyte solutions, calcium chloride dihydrate ( $\text{CaCl}_2\cdot 2\text{H}_2\text{O}$ ,  $\geq 99\%$ , p.a., ACS), potassium chloride (KCl,  $\geq 99.5\%$ , p.a., ACS, ISO), sodium chloride (NaCl,  $\geq 99.5\%$ , p.a., ACS, ISO) and sodium sulfate ( $\text{Na}_2\text{SO}_4$ ,  $\geq 99\%$ , p.a., ACS, ISO) were obtained in crystalline form from Carl Roth GmbH + Co KG (Germany). Salts were dissolved in ultrapure water and filtered through 0.45  $\mu\text{m}$  cellulose nitrate membrane filters (Sartorius AG, Germany) or polypropylene syringe membrane filters (VWR International GmbH, Germany).

**Ultrapure water:** Ultrapure water was provided by a ‘*Synergy<sup>®</sup>*’ water purification system supplied by Merck Chemicals GmbH (Germany). Purification cartridges were replaced as recommended by the manufacturer. Electrical resistivity at 25  $^\circ\text{C}$  was 18.2  $\text{M}\Omega\cdot\text{cm}$  and total organic carbon (TOC) concentration  $\leq 5$  ppb (manufacturer’s specifications). For cleaning and rinsing procedures, deionized water with an electrical conductivity  $\leq 0.200$   $\mu\text{S}\cdot\text{cm}^{-1}$  was used.

**Cleaning procedure of glassware:** Glassware was cleaned in laboratory dishwashers operated with deionized water and intensive cleaning powder (*‘Roti®-Splish P’*, Carl Roth GmbH + Co KG, Germany) and subsequently dried at 65 °C. Prior to usage, glassware was rinsed with ultrapure water. Any glassware that was used for sampling, sample storage and measurement of TOC, DOC, LC-OCD-UVD, SAC or fluorescence emission was burned at 550 °C or soaked in sodium persulfate solution for 1 h at 60 °C and afterwards thoroughly rinsed with ultrapure water.

### 3.1.3 **Membrane Material**

Table 3-4 summarizes selected properties of the RO membrane used for scaling experiments. Dry membrane material was shipped in coupons of approximately 1 m<sup>2</sup>. In total, two batches of three individual membrane coupons were used. Dry membranes were stored in the dark below 20 °C. For scaling experiments, individual membrane samples were carefully cut from the coupons, soaked individually in 1 l of ultrapure water and stored for a maximum period of 14 days at 4 °C in the dark. Ultrapure water was replaced every other day. Each sample was soaked in at least 3 batches of ultrapure water to wash out any residual solvents. For each set of experiments (i.e. experiments conducted with reverse osmosis system – configuration I and II), all membrane samples were cut adjacent to each other from the same batch of membrane material.

**Table 3-4: Select properties of the employed reverse osmosis membrane.**

<b>manufacturer</b>	Dow Chemical (MI, USA)
<b>product</b>	FILMTEC™ BW30
<b>application</b>	brackish water desalination
<b>structure</b>	thin film composite
<b>active layer material</b>	fully aromatic polyamide (trimesoyl chloride + m-phenylenediamine) [216]
<b>active layer coating</b>	polyvinyl alcohol [216]
<b>water permeability coefficient</b>	3.29 l·m <sup>-2</sup> ·h <sup>-1</sup> ·bar <sup>-1</sup> (product specifications) 3.31 ± 0.38 l·m <sup>-2</sup> ·h <sup>-1</sup> ·bar <sup>-1</sup> (own measurements, n = 59) 3.96 ± 0.31 l·m <sup>-2</sup> ·h <sup>-1</sup> ·bar <sup>-1</sup> [216]
<b>NaCl rejection</b>	99.5 % (product specifications) 97.9 ± 0.4 % [216]
<b>surface roughness (rms)</b>	68.3 ± 12.5 nm [216] 62.6 nm [12]
<b>contact angle</b>	29.0° (own measurements, n = 66, see also Table D-4) 25.9° [216] 55° [12]
<b>zeta potential</b>	-34.9 mV at pH = 9 (own measurements, n = 5, see also Table D-4) -10.1 mV at pH = 9 [216] -25 mV at pH = 9 [12]

## 3.2 Experimental Setups and Procedures

### 3.2.1 Stirred Beaker Crystallization Experiments

**Experimental setup:** The experimental setup consisted of a 1 l glass beaker positioned in a non-transparent temperature controlled water bath ( $T = 25.0 \pm 0.1$  °C,  $\pm$ SD) placed on a magnetic stirrer. Stirring speed was  $\omega = 300$  min<sup>-1</sup> in all experiments using the same magnetic stirrer (PTFE coated, length = 25 mm, diameter = 6 mm). Solution *pH*, electrical conductivity ( $\kappa$ ), temperature (Xylem Analytics Germany Sales GmbH & Co. KG., Germany) and turbidity (model ‘SOLITAX’, Hach Lange GmbH, Germany) were monitored online by handheld probes submerged in the beaker in fixed positions. The glass beaker was continuously purged with nitrogen gas above the liquid surface during experiments to avoid dissolution of carbon dioxide from the atmosphere.

**Experimental procedures:** Tempered (25.0 °C), predetermined volumes of 136 mmol·l<sup>-1</sup> Na<sub>2</sub>SO<sub>4</sub> stock solution, ultrapure water and, if applicable, concentrated NOM or antiscalant (AS) stock solutions were added to the beaker and mixed. The solution was sparged with nitrogen gas for 10 min to remove dissolved inorganic carbon prior to the start of an experiment. Afterwards, *pH* was adjusted to the desired values using diluted HCl or NaOH. The experiment was initiated by adding a tempered (25.0 °C), predetermined volume of 136 mmol·l<sup>-1</sup> CaCl<sub>2</sub>·2H<sub>2</sub>O stock solution. If necessary, *pH* was immediately readjusted. The final volume in the beaker always resulted in 500 ml and the added volumes of 136 mmol·l<sup>-1</sup> Na<sub>2</sub>SO<sub>4</sub> and 136 mmol·l<sup>-1</sup> CaCl<sub>2</sub>·2H<sub>2</sub>O stock solutions were always equal. A list of conducted experiments including solution compositions is provided by Table C-1. The experiments were terminated at a turbidity increase of 200 FNU. Beaker and probes were thoroughly cleaned with a sponge and deionized water. Prior to the next experiment, beaker and probes were thoroughly rinsed with ultrapure water.

**Data evaluation:** Induction time ( $\tau$ ) for gypsum bulk crystallization from supersaturated aqueous solution was determined from the detected turbidity increase of 1 FNU. Turbidity data was therefore corrected by subtracting the initial value at the beginning of an experiment from consecutive values. Crystallization time ( $\Delta t$ ) was defined as the time elapsed between the induction time and the achievement of a solution turbidity of 200 FNU.

### 3.2.2 Reverse Osmosis System – Configuration I

**RO system setup:** All reverse osmosis desalination experiments were performed using an automatically controlled laboratory scale cross-flow RO system (Figure B-1 and Figure B-2). Major system components and specifications are listed in Table B-1. In configuration I (Figure B-1a), the system was operated by continuous withdrawal of permeate and simultaneous recirculation of concentrate. A constant solution volume of 3.0 l was maintained in the temperature-controlled feed water reservoir ( $T = 25.0 \pm 0.1$  °C,  $\pm$ SD) by measurement of the water level and automated refilling with the respective experimental solution. This configuration enabled volumetric concentration of the feed water by factors independent of the feed water reservoir

minimum water level. A rectangular plate-and-frame membrane test cell (SEPA CF II) supplied by Sterlitech Corp. (WA, USA) was used providing a total active membrane area of approximately 140 cm<sup>2</sup> (length: 146 mm, width: 95 mm). A constant transmembrane pressure ( $\Delta p$ ) of  $25.0 \pm 0.1$  bar ( $\pm$  SD) was automatically maintained throughout all experiments. Two different operating modes (Table 3-5) were employed: ‘high’ and ‘low concentration polarization (CP) operating mode’. Average mass transfer coefficients ( $k$ ) at the membrane surface were experimentally determined according to the procedure described by Sutzkover et al. (2000) [217], which is based on the measurement of permeate flux decline induced by NaCl addition to an initially solute-free feed water.

**Table 3-5: Specifications of ‘high’ and ‘low CP operation’ during RO desalination experiments using configuration I. Mass transfer coefficients were experimentally determined according to [217].**

	high CP operation	low CP operation
cross-flow velocity / m·s <sup>-1</sup>	0.12	0.27
type of feed spacer	no spacer used	diamond shaped
feed spacer thickness / mm	–	1.65
feed flow channel height / mm	1.91	1.65
mass transfer coefficient / m·s <sup>-1</sup>	$1.69 \cdot 10^{-5}$	$6.42 \cdot 10^{-5}$

**Experimental procedures:** All experiments were performed using a pre-soaked virgin piece of membrane, which was conditioned for a minimum of 15 hours using a  $46 \text{ mmol}\cdot\text{l}^{-1}$  NaCl solution at a transmembrane pressure of  $\Delta p = 25$  bar. During conditioning, the system was operated in full recirculation mode. After conditioning, the system was rinsed with ultrapure water. Experiments were started immediately afterwards by filling the feed water reservoir (3.0 l) and the feed water tank with the respective experimental solution and switching to permeate withdrawal mode.  $pH$  was adjusted by addition of diluted HCl or NaOH. All experimental solutions were prepared from pre-filtered ( $0.45 \mu\text{m}$ )  $136 \text{ mmol}\cdot\text{l}^{-1}$  Na<sub>2</sub>SO<sub>4</sub>,  $136 \text{ mmol}\cdot\text{l}^{-1}$  CaCl<sub>2</sub>·2H<sub>2</sub>O and NOM or antiscalant (AS) stock solutions diluted in ultrapure water. Scaling solutions were initially unsaturated with respect to gypsum ( $SI = -0.02$ ) and had an initial osmotic pressure of  $\Delta\pi_b = 2.16$  bar, unless otherwise noted. Table C-2 lists all conducted experiments including solution compositions and relevant process parameters. Experiments were terminated after a real permeability loss of greater than 50 % was detected. After termination of an experiment, each membrane piece was recovered for scanning electron microscopy and the RO system thoroughly cleaned by recirculating a mixture of 0.1 weight % NaOH and 0.5 weight % Na<sub>4</sub>EDTA ( $pH = 12$ ) to dissolve any gypsum scale and organic macromolecule depositions.

**Calculations and data evaluation:** The experimentally determined mass transfer coefficients for both operating modes were used to calculate the approximated concentration polarization modulus ( $f_{CP}$ ) according to Equation 3-1, assuming that solute rejection is close to 100 %:

$$f_{CP} = \frac{c_m}{c_b} = \exp\left(\frac{J_w}{k}\right) \quad \text{Equation 3-1}$$

where  $c_m$  is solute concentration at the membrane surface in  $\text{mol}\cdot\text{l}^{-1}$ ,  $c_b$  is the solute concentration in the bulk solution in  $\text{mol}\cdot\text{l}^{-1}$ ,  $J_w$  is permeate water flux in  $\text{l}\cdot\text{m}^{-2}\cdot\text{h}^{-1}$  and  $k$  is the mass transfer coefficient in  $\text{m}\cdot\text{s}^{-1}$ . The volumetric concentration factor (VCF) was calculated according to Equation 3-2:

$$VCF = 1 + \frac{V_p}{V_{reservoir}} = 1 + \frac{V_p}{3.0\text{ l}} \quad \text{Equation 3-2}$$

where  $V_p$  is the cumulative permeate volume and  $V_{reservoir}$  the feed reservoir water volume which was kept constant at 3.0 l. The membrane permeability for water was corrected for the continuously increasing osmotic pressure in the feed water reservoir by calculating the real water permeability  $k_{w,real}$  according to Equation 3-3:

$$k_{w,real} = \frac{J_w}{\Delta p - \Delta\pi} = \frac{J_w}{\Delta p - ((VCF \cdot f_{CP} \cdot \pi_b) - \pi_p)} \quad \text{Equation 3-3}$$

where  $\pi_b$  and  $\pi_p$  are the bulk and permeate osmotic pressures in bar calculated according to Equation 2-2. Membrane real permeability was normalized by the initial real permeability at the beginning of an experiment and subsequently averaged for 5 min intervals.

### 3.2.3 Reverse Osmosis System – Configuration II

**RO system setup:** For RO system configuration II (Figure B-1b), setup and operation of the laboratory scale cross-flow RO system as described in Chapter 3.2.2 was modified. A transparent, acrylic RO membrane test cell (Convergence Industry B.V., Netherlands) with an active membrane area of  $400\text{ cm}^2$  (length: 1 m, width: 40 mm) and a channel height of 4 mm was used in order to microscopically monitor gypsum scale formation on the RO membrane surface in real-time. Experiments were conducted at constant flux of  $30.0 \pm 0.2\text{ l}\cdot\text{m}^{-2}\cdot\text{h}^{-1}$  ( $\pm$  SD), constant cross-flow velocity of  $0.19\text{ m}\cdot\text{s}^{-1}$  ( $\text{SD} < 0.01\text{ m}\cdot\text{s}^{-1}$ ) and constant temperature of  $20.0 \pm 0.1\text{ }^\circ\text{C}$  ( $\pm$  SD) under full recirculation mode. To maintain a constant *pH* value and to avoid any interferences of gypsum crystallization with inorganic carbon [161], the stirred feed solution reservoir was continuously purged with nitrogen gas. Unless otherwise noted, experimental solutions were unsaturated with respect to gypsum ( $SI = -0.02$ ) and local supersaturation at the membrane surface was achieved by operating the cell without a feed spacer. Calculated water recovery over the length of the module was  $\Phi = 0.86\%$ . Thus, the concentrate stream remained unsaturated with respect to gypsum ( $SI = -0.01$ ).

**Experimental procedures:** All experiments were performed using a pre-soaked virgin piece of membrane, which was conditioned with ultrapure water at constant pressure of  $\Delta p = 25\text{ bar}$

overnight (12–14 h) to allow membrane permeability to stabilize. Thereafter, different experimental protocols were resumed as described below and illustrated in Figure B-3. Total volume was 8.0 l for all experiments. Table C-3 lists all conducted experiments including solution compositions and relevant process parameters. *pH* during experiments was adjusted by addition of diluted HCl and NaOH. All experiments were terminated after reaching a  $\Delta p$  of 25 bar or latest after 4.5 h, unless otherwise noted. The RO system was subsequently cleaned by recirculating several batches of ultrapure water over several hours.

*Pure gypsum scaling:* Ultrapure water was replaced by 6.0 l of a  $19.4 \text{ mmol}\cdot\text{l}^{-1}$   $\text{CaCl}_2\cdot 2\text{H}_2\text{O}$  conditioning solution and system operation was commenced at constant flux of  $30 \text{ l}\cdot\text{m}^{-2}\cdot\text{h}^{-1}$ . After 2 h of  $\text{CaCl}_2\cdot 2\text{H}_2\text{O}$  conditioning, gypsum scaling experiments were initiated by addition of  $\text{Na}_2\text{SO}_4$  stock solution and ultrapure water to the feed reservoir, creating an equimolar concentration of  $17 \text{ mmol}\cdot\text{l}^{-1}$   $\text{CaCl}_2\cdot 2\text{H}_2\text{O}$  and  $17 \text{ mmol}\cdot\text{l}^{-1}$   $\text{Na}_2\text{SO}_4$  and a total volume of 8.0 l. Two variations were performed, where scaling was investigated (i) at increased (+4.1 %) feed ion concentrations ( $c_g = 17.7 \text{ mmol}\cdot\text{l}^{-1}$ ,  $SI_{g,b} = 0.00$ ) and (ii) in the presence of inorganic particles using an unintended event of stainless steel grinding from the feed reservoir material (V4A stainless steel) by misalignment of the mechanical feed reservoir stirrer (feed solution turbidity, which was absent in all other experiments, indicated the presence of colloidal and particulate matter in the system, see Table C-3).

*Gypsum crystal re-growth:* Previously scaled membranes were cleaned by in-situ crystal dissolution facilitated by recycling several batches of ultrapure water without applied pressure over night until electrical conductivity remained below  $1 \mu\text{S}\cdot\text{cm}^{-1}$ . Cleaning was completed by a final 2 h ultrapure water permeation step at applied pressure of  $\Delta p = 25$  bar. After cleaning, gypsum crystals had fully dissolved as confirmed by microscopic imaging at 5x magnification. Subsequent scaling experiments were conducted according to the above described experimental protocol for ‘*pure gypsum scaling*’, beginning with  $\text{CaCl}_2\cdot 2\text{H}_2\text{O}$  conditioning for 2 h at constant flux of  $30 \text{ l}\cdot\text{m}^{-2}\cdot\text{h}^{-1}$ .

*Gypsum scaling in the presence of NOM:* Experimental procedure was identical to ‘*pure gypsum scaling*’ experiments, however, after  $\text{CaCl}_2\cdot 2\text{H}_2\text{O}$  conditioning, NOM stock solutions were added simultaneously with the  $\text{Na}_2\text{SO}_4$  stock solution and ultrapure water.

*Pure gypsum scaling after membrane pre-fouling by NOM:* Ultrapure water was replaced by 8.0 l of an NOM-fouling solution containing  $17 \text{ mmol}\cdot\text{l}^{-1}$   $\text{CaCl}_2\cdot 2\text{H}_2\text{O}$  and  $3 \text{ mg C}\cdot\text{l}^{-1}$  of the respective NOM, unless otherwise noted. System operation was commenced at constant pressure of 25 bar. After 24 h, the system was rinsed three times with ultrapure water for 5 min applying no pressure followed by ultrapure water permeation at  $\Delta p = 25$  bar. The intensive rinsing procedure was employed to remove NOM that had not irreversibly adsorbed or deposited on the membrane surface and to guarantee subsequent gypsum crystallization in the absence of dissolved NOM.

Thereafter, scaling experiments were conducted according to the experimental protocol for ‘*pure gypsum scaling*’, beginning with  $\text{CaCl}_2 \cdot 2\text{H}_2\text{O}$  conditioning for 2 h at constant flux of  $30 \text{ l} \cdot \text{m}^{-2} \cdot \text{h}^{-1}$ .

**NOM fouling:** Ultrapure water was replaced by 4.0 l of a conditioning solution containing  $17 \text{ mmol} \cdot \text{l}^{-1}$   $\text{CaCl}_2 \cdot 2\text{H}_2\text{O}$  and  $17 \text{ mmol} \cdot \text{l}^{-1}$   $\text{NaCl}$  and system operation was commenced at constant flux of  $30 \text{ l} \cdot \text{m}^{-2} \cdot \text{h}^{-1}$ . After 12 – 24 h, 4.0 l containing  $17 \text{ mmol} \cdot \text{l}^{-1}$   $\text{CaCl}_2 \cdot 2\text{H}_2\text{O}$ ,  $17 \text{ mmol} \cdot \text{l}^{-1}$   $\text{NaCl}$  and  $6.0 \text{ mg C} \cdot \text{l}^{-1}$  of the respective NOM were added. NOM fouling at a DOC concentration of  $3 \text{ mg} \cdot \text{l}^{-1}$  occurred over a period of 12 – 24 h before experiments were terminated. This procedure was only applied for the humic acids (RHA, SAHA) and aquatic NOM sources (HSNOM, SRNOM).

**Determination of crystal mass by membrane post-analyses:** After termination of an experiment, scaled membranes were carefully extracted from the cell and submerged in an ultrapure water bath for approximately 2 s to prevent further crystallization from residual scaling solution. Membrane samples were then air dried for at least 48 h. For select experiments, dry membrane samples were cut into ten equally sized pieces of  $4 \text{ cm} \times 10 \text{ cm}$ . Cut pieces were stored in a desiccator for at least 24 h. Masses before and after dissolution of crystals in  $1 \text{ mmol} \cdot \text{l}^{-1}$   $\text{NaOH}$  (48 h on shaker at 120 rpm) were determined to calculate the crystal mass ( $\Delta m$ ) of each section as well as total crystal mass ( $\Delta m_{\text{total}}$ ). After dissolution in  $\text{NaOH}$ , each section was again air dried for at least 48 h and afterwards stored in a desiccator for at least 24 h.

**Determination of concentration polarization modulus:** The severity of concentration polarization was calculated according to Equation 3-4:

$$f_{CP} = \frac{c_m}{c_b} = \frac{\Delta p}{\pi_f} - \frac{J_w}{(k_w \cdot \pi_f)} + \frac{\pi_p}{\pi_f} \quad \text{Equation 3-4}$$

where  $f_{CP}$  is the concentration polarization factor,  $\Delta p$  is the transmembrane pressure in bar,  $\pi_f$  is the osmotic pressure of the feed solution in bar,  $J_w$  is the permeate flux in  $\text{l} \cdot \text{m}^{-2} \cdot \text{h}^{-1}$ ,  $k_w$  is the clean water permeability coefficient in  $\text{l} \cdot \text{m}^{-2} \cdot \text{h}^{-1} \cdot \text{bar}^{-1}$ , and  $\pi_p$  is the osmotic pressure of the permeate in bar. For the experiments conducted in this study, the average concentration polarization factor was calculated to be  $f_{CP} = 2.69$ . Accordingly, calculated membrane wall concentrations ( $c_m$ ) of calcium and sulfate ions averaged  $45.7 \text{ mmol} \cdot \text{l}^{-1}$ , which resulted in an average gypsum membrane wall supersaturation of  $SI_{g,m} = 0.51$ .

### **Real-time membrane surface imaging**

**Image acquisition:** Real-time membrane surface imaging was accomplished using a stereomicroscope by Carl Zeiss AG (Germany, model ‘*Stemi 2000*’) equipped with a high resolution digital microscope camera (Olympus K.K., Japan, model ‘*DP73*’) mounted at position  $x/L = 0.86$ . Indirect lighting was realized through both sides of the transparent membrane test cell by ultra-bright custom-made LED lighting. Micrographs were acquired at 5x magnification,

capturing an area of  $14.0 \text{ mm} \times 10.5 \text{ mm} = 147 \text{ mm}^2$ . Micrographs were acquired in 1 min intervals.

**Image analysis:** Images were analyzed using the image processing program ImageJ (version 1.49). Analyses of crystal number density (*CND*) in  $\text{cm}^{-2}$  and fractional surface coverage (*FSC*, ratio of area covered with gypsum scale to total area) at selected points in time were performed semi-automatically. First, the reference image taken at  $t = 0 \text{ min}$  was subtracted from all consecutive images leaving resulting images that only show absolute differences in pixel values. Second, image contrast was enhanced and the number of crystal growth sites was manually counted. Membrane surface scale coverage was quantified by thresholding or by manually cutting the crystal contours from the contrast-enhanced picture after reference image subtraction. After conversion into a binary picture, fractional surface coverage was quantified automatically. The minimum size of reliably detected crystals was  $5 \times 5$  pixels accounting  $43.6 \mu\text{m} \times 43.6 \mu\text{m}$  at 5x magnification. Mean crystal diameter ( $d_p$ ) was calculated from the total scale covered area and the number of crystals and by assuming ideally round gypsum rosette-like crystals. The smallest detectable mean crystal diameter was  $d_{p,min} = 49.3 \mu\text{m}$ .

### 3.3 Analyses

#### 3.3.1 Characterization of Aqueous Solutions

**Sample preparation and storage:** If necessary, pre-filtration of aqueous samples was performed using  $0.45 \mu\text{m}$  cellulose nitrate membrane filters (Sartorius AG, Germany) or polypropylene syringe membrane filters (VWR International GmbH, Germany). Filters were rinsed thoroughly with ultrapure water to wash out residuals. Any sample, which was not immediately analyzed was stored at  $4 \text{ }^\circ\text{C}$  in the dark.

**Dissolved organic carbon analysis:** Dissolved organic carbon (DOC) was quantified using combustion catalytic oxidation at  $680 \text{ }^\circ\text{C}$  coupled with a nondispersive infrared (NDIR) sensor (models 'TOC-V' and 'TOC-L', Shimadzu Corp., Japan). According to DIN EN 1484, samples were pre-filtered by  $0.45 \mu\text{m}$  prior to measurement or had been pre-filtered by  $0.45 \mu\text{m}$  at least once throughout the experimental procedure. Monthly five-point calibration in the range of  $0 - 2 \text{ mg C}\cdot\text{l}^{-1}$  was done using potassium hydrogen phthalate standard solutions as suggested by the manufacturer. Samples were diluted with ultrapure water to a  $\text{DOC} < 2 \text{ mg}\cdot\text{l}^{-1}$ . By default, each sample was analyzed 3 times.

**LC-OCD-UVD:** Size distribution of NOM was determined by size exclusion liquid chromatography (column HW-50S) coupled with organic carbon detection and detection of spectral UV absorbance at  $\lambda = 254 \text{ nm}$  (LC-OCD-UVD, DOC Labor Dr. Huber, Germany). All samples were pre-filtered by  $0.45 \mu\text{m}$  and, if necessary, diluted with ultrapure water to a  $\text{DOC} < 5 \text{ mg}\cdot\text{l}^{-1}$ . Oxidation of DOC is achieved by UV irradiation within the system's Grantzel thin-film reactor. Measurement and subsequent quantification of obtained chromatograms were

performed according to Huber et al. (2011) [218] using ChromCALC Software (DOC Labor Dr. Huber, Germany) for peak integration. The analytical device was periodically calibrated according to the manufacturer's recommendation using potassium hydrogen phthalate standards and humic substance standards supplied by the International Humic Substances Society (IHSS). For further details on the analytical setup it is referred to Huber et al. (2011) [218].

**UV-visible absorption spectroscopy:** Spectral absorption coefficients (SAC) at  $\lambda = 254$  nm ( $SAC_{254}$ ) and  $\lambda = 436$  nm ( $SAC_{436}$ ) of pre-filtered (0.45  $\mu\text{m}$ ) samples were determined according to DIN 38404-3 and DIN EN ISO 7887, respectively, using a 'DR 5000<sup>TM</sup> UV-Vis Spectrophotometer' (Hach Lange GmbH, Germany). Measurements were performed in 5 cm or 1 cm quartz glass cuvettes, depending on intensity of absorbance. For DOC-specific spectral absorbance ( $SUVA_{254}$  and  $SA_{436}$ ), SAC was normalized to the DOC concentration determined by combustion catalytic oxidation.

**Fluorescence spectroscopy:** Fluorescence excitation emission matrices (FEEM) were determined using an 'Aqualog<sup>®</sup>' fluorimeter (Horiba Ltd, Japan). Measurements were done from pre-filtered (0.45  $\mu\text{m}$ ) and blank (ultrapure water) samples at excitations of  $\lambda_{Ex} = 240 - 600$  nm in 3 nm steps. Fluorescence emission between  $\lambda_{Em} = 211 - 621$  nm was simultaneously acquired with a resolution of 0.396 nm. Standardization of emission data was achieved by subtraction of blank emission, Raman stray light removal and correction for inner filter effects as suggested by Goletz et al. (2011) [219] using the 'Aqualog<sup>®</sup>' software. Corrected emission data was normalized by using the area of the Raman scattering peak from 350 nm excitation and fluorescence intensity displayed as Raman units (r.u.) according to Lawaetz and Stedmon (2009) [220].

**Nanoparticle tracking analysis:** Colloidal size distribution and concentration (100 – 1,000 nm) were determined using nanoparticle tracking analysis (NTA) [221]. A 'NanoSight LM10' device equipped with a microscope objective with 20x magnification mounted on a camera (NanoSight Ltd., UK) was used to illuminate nano-scale particles (50 – 2,000 nm) with a laser light source ( $\lambda = 532$  nm). In previous investigations, reliable quantification was achieved for colloids  $\geq 100$  nm. Prior to the measurement of a set of samples, the system's proper operation and settings were confirmed by analysis of a 100 nm colloid standard (PS100) supplied by NanoSight Ltd. (UK).

**Laser obscuration time measurement:** Particle concentration and size distribution (0.1  $\mu\text{m}$  – 300  $\mu\text{m}$ ) were determined by laser obscuration time (LOT) measurement [222] using an 'EyeTech' device and corresponding analysis software supplied by Ankersmid (Netherlands). Analyses were performed in stirred 1 cm quartz glass cuvettes using the laser lens A100 and ACM-101 magnetic stirring cell at high stirring speed. For each analysis, the average of three individual measurements was determined by the software, each lasting until a confidence level of 98 % was reached. Each sample was analyzed two times. Prior to the measurement of a set of samples, the system's proper operation and settings were confirmed by measurement of a 10.25  $\mu\text{m}$  particle standard supplied

by BS-Partikel GmbH (Germany). For determination of particle size distribution and concentration of gypsum crystals during gypsum bulk crystallization tests, samples were taken directly from the stirred beaker, diluted (10-fold) with a saturated and pre-filtered (0.45  $\mu\text{m}$ )  $\text{CaCl}_2$  and  $\text{Na}_2\text{SO}_4$  solution and immediately analyzed to prevent further crystallization. Mean diameters ( $d_p$ ) were calculated by the software using the detected cumulative particle area and particle concentration.

**Direct base titration:** Concentrations of acidic functional groups of NOM solutions were determined by potentiometric titration at a DOC concentration of  $19.15 \text{ mg}\cdot\text{l}^{-1}$  and in the presence of  $10 \text{ mmol}\cdot\text{l}^{-1}$  NaCl as a background electrolyte. 250 ml of the sample solution were acidified to  $pH \approx 3.0$  using  $0.1 \text{ mol}\cdot\text{l}^{-1}$  HCl and sparged with  $\text{N}_2$  gas for 15 min to remove inorganic carbon. The  $pH$  was then adjusted to  $pH = 3.0$  using  $0.1 \text{ mol}\cdot\text{l}^{-1}$  HCl and afterwards titrated to  $pH \approx 10.0$  with  $0.1 \text{ mol}\cdot\text{l}^{-1}$  NaOH. Titrant was added in predefined volumes and equilibration time between titrant addition and  $pH$  reading was constant at 3 min. During titration, the sample solution was continuously sparged with  $\text{N}_2$  gas to maintain absence of inorganic carbon. The sample solution was mixed using a magnetic stirrer for 10 s after titrant addition and then left undisturbed for reliable  $pH$  reading. Blank titration was performed with NOM-free  $10 \text{ mmol}\cdot\text{l}^{-1}$  NaCl solution at the same conditions. Each titration was repeated once. The  $pH$  values achieved during titration of blank samples served to determine the net base consumption for deprotonation of acidic functional groups of the NOM samples. As commonly employed, the net base consumption required to achieve a  $pH$  of 8.0 was used to determine the concentration of carboxyl groups ('*carboxylic acidity*') of the NOM samples assuming that all carboxyl groups are titrated at  $pH = 8.0$  [168,223,224]. The concentration of phenolic hydroxyl groups ('*phenolic acidity*') was determined from titration between  $pH = 8.0 - 10.0$  assuming that one-half of them are titrated and that the concentration is equivalent to two times the net base consumption from  $pH = 8.0 - 10.0$  [168,223,224]. Total acidity was assumed to be the sum of the determined carboxylic and phenolic acidities [168,223,224].

**Fractionation of select humic substances by membrane filtration:** Fractionation of NOM samples by ultrafiltration (UF) and nanofiltration (NF) was performed in collaboration with M. Schulz using membranes with different molecular weight cutoffs (*MWCO*) (Table 3-6) and according to the procedure described by Schulz et al. (2017) [225]. NOM samples were diluted to a DOC concentration of  $5 \text{ mg}\cdot\text{l}^{-1}$  and adjusted to  $pH = 7.0$ . RHA, SAHA and SRNOM samples

**Table 3-6: Overview of membranes used for fractionation of NOM samples.**

MWCO	$\Delta p$ / bar	membrane	material	manufacturer
0,45 $\mu\text{m}$	vacuum	–	cellulose nitrate	Sartorius AG (Germany)
150 kDa	1.0	UP150	polyether-sulfone	Microdyn-Nadir (Germany)
20 kDa	2.0	UP20	polyether-sulfone	Microdyn-Nadir (Germany)
10 kDa	1.0	Ultracel® 10 kDa	regenerated cellulose	EMD Millipore Co. (MA, USA)
5 kDa	1.5	Ultracel® 5 kDa	regenerated cellulose	EMD Millipore Co. (MA, USA)
1 kDa	2.0	Ultracel® 1 kDa	regenerated cellulose	EMD Millipore Co. (MA, USA)
0.4 kDa	5.0	FILMTEC™ NF 270	polyamide TFC	DOW Chemical (MI, USA)

were prepared at  $1 \text{ mmol}\cdot\text{l}^{-1}$   $\text{NaHCO}_3$  and  $1 \text{ mmol}\cdot\text{l}^{-1}$   $\text{CaCl}_2$  to mimic ionic background of natural waters. Filtration of 200 ml sample was performed in stirred dead-end filtration cells. 50 ml of filtrate were collected after wasting the initial 5 ml.

**Electrical conductivity, pH and temperature:** Electrical conductivity (*EC*), *pH* and temperature (*T*) were determined using handheld meters supplied by Xylem Analytics Germany Sales GmbH & Co. KG. (Germany). Adjustment of the EC probe's cell constant was done monthly using a  $0.01 \text{ mol}\cdot\text{l}^{-1}$  KCl standard of  $1,413 \mu\text{S}/\text{cm}$  supplied by Carl Roth GmbH + Co KG (Germany). Calibration of *pH* probes was done at least weekly by a two- or three- point calibration using *pH* standards of *pH* = 4.0, 7.0 and 10.0 supplied by Carl Roth GmbH + Co KG (Germany).

### 3.3.2 Microscopy

**Light microscopy:** Light microscopy of aqueous samples was performed using an 'Axioplan 2' microscope (Carl Zeiss AG, Germany) equipped with a digital microscope camera (Olympus K.K., Japan), model 'DP73'. For light microscopy of dry membrane samples, a stereomicroscope (model 'Stemi 2000', Carl Zeiss AG, Germany) equipped with the same camera was used.

**Scanning electron microscopy and energy-dispersive X-ray spectroscopy:** Scanning electron microscopy (SEM) was performed at a voltage of 2 kV and aperture of  $10 \mu\text{m}$  using a 'Zeiss Supra 55 VP' device (Carl Zeiss AG, Germany). For SEM of membrane surfaces, samples of 10 mm diameter were cut from the dried membrane pieces, mounted on SEM specimen holders and sputtered with 2 – 5 nm gold (model 'SCD 050 sputter coater', Bal-Tec AG, Liechtenstein). For SEM of gypsum bulk crystals from stirred beaker experiments, samples were taken directly from the beaker and a few droplets of aqueous sample were transferred onto a specimen holder. Excess aqueous solution was carefully removed by suction using paper wipes leaving crystals deposited on the specimen holder. Samples were then left to dry in a desiccator and sputtered with 2 – 5 nm gold prior to analysis by SEM. Energy-dispersive x-ray (EDX) spectroscopy was performed during SEM at an accelerating voltage of 20 kV and an aperture of  $20 \mu\text{m}$  using a  $80 \text{ mm}^2$  silicon drift detector and 'Aztec' EDX analysis software supplied by Oxford Instruments PLC (UK).

### 3.3.3 X-ray Diffraction

X-ray diffraction (XRD) analysis was performed using an X-ray diffractometer, model 'D500' (Siemens AG, Germany) equipped with a copper-ceramic anode at  $3^\circ$  2-Theta  $\cdot\text{min}^{-1}$  and  $0.05^\circ$  2-Theta step width. Crystalline matter was identified using 'Diffracplus' software supplied by Bruker Co. (MA, USA) and International Centre for Diffraction Data<sup>®</sup> (ICDD<sup>®</sup>) database.

### 3.3.4 Membrane Surface Characterization

**Contact angle measurement:** Membrane surface contact angle ( $\theta_c$ ) was determined using the captive bubble method in clean water. Membrane samples were mounted on a planar glass specimen holder and reversely submerged in clean water. Individual air bubbles of  $5 \mu\text{l}$  volume

were placed on the membrane surface using a  $\mu\text{l}$ -syringe. Illumination was achieved by indirect lighting and digital photographs were taken planar to the membrane surface. Contact angle was determined using ‘SURFTENS’ software (OEG mbH, Germany). Each measurement was repeated for 3 – 4 times.

**Zeta potential from streaming current measurements:** Zeta potential of membrane surfaces was calculated from the measured streaming current at 300 mbar and  $1 \text{ mmol}\cdot\text{l}^{-1}$  KCl using an electrokinetic analyzer ‘SurPASS<sup>TM</sup>’ equipped with an adjustable gap cell supplied by Anton Paar GmbH (Austria). The electrolyte was initially adjusted to  $pH > 9.0$  and then titrated to  $pH < 3.0$  using  $0.05 \text{ mol}\cdot\text{l}^{-1}$  HCl. Zeta potential was averaged from 4 measurements at each titrated  $pH$ . Calibration of the  $pH$  probe was performed weekly using  $pH$  standards of  $pH = 4.0, 7.0$  and  $10.0$  supplied by Carl Roth GmbH + Co KG (Germany).

### 3.4 Calculations and Statistical Analyses

**Calculation of supersaturation:** Calculation of supersaturation ( $SI$ , Equation 2-8) was performed using ‘PHREEQC’ software, version 3.0.6 and phreeqc.dat database (US Geological Survey). The phreeqc.dat database uses the Debye-Hückel theory and the Davies equation for calculation of activity coefficients. Solubility products ( $K_{sp}$ ) for major scale-forming salts are listed in Table 3-7.

Table 3-7: Solubility products ( $K_{sp}$ ) at 25 °C for major scale-forming salts used by the phreeqc.dat database.

	barite	calcite	gypsum	silica
$\log (K_{sp} / \text{mol}^2\cdot\text{l}^{-2})$	-9.97	-8.48	-4.58	-2.71

**Statistical analyses:** Calculated average values represent arithmetic mean values with corresponding sample standard deviation (SD) or 95 % confidence interval (CI) assuming a t-distribution. Outliers in data sets were identified using the Grubb’s test for outliers at a significance level of  $p = 0.05$ . In order to determine if two sets of data are significantly different from each other, single-sided, unpaired t-tests assuming unequal variances were performed. At a 95 % confidence interval, datasets were claimed significantly different if  $p$  was  $< 0.05$ .



## 4 Characterization of Gypsum Scaling

Gypsum scaling during RO desalination has been reported to occur due to bulk and surface crystallization (Chapter 2.3.3). This chapter investigates the effects of RO operating conditions and antiscalant dosage on the occurrence and dominance of the two reported gypsum scaling mechanisms (Chapter 4.1). Subsequently, both scaling mechanisms are characterized individually. Gypsum bulk crystallization from supersaturated solution is characterized using stirred beaker crystallization experiments (Chapter 4.2) and gypsum surface crystallization on RO membranes is characterized by laboratory scale RO desalination experiments enabling real-time membrane surface imaging (Chapter 4.3).

### 4.1 Gypsum Scaling Mechanisms During RO Desalination

*Selected contents of this chapter have been published in collaboration with J. Rozova and M. Ernst: Separation and Purification Technology 198 (2018), 68–78.*

The following experiments were performed using the laboratory scale RO system in permeate withdrawal mode at constant transmembrane pressure of  $\Delta p = 25$  bar (RO system configuration I with SEPA CF II test cell). All model solutions were initially unsaturated with respect to gypsum ( $SI_{g,b} = -0.02$ ). Operating conditions were tailored in order to create two different degrees of concentration polarization (CP). Corresponding mass transfer coefficients ( $k$ ) during ‘low’ and ‘high CP operation’ were determined experimentally (Table 3-5). Scaling experiments were performed in duplicate to assess the reproducibility of gypsum scale formation and detection. In addition, the effects of antiscalant dosage (polyacrylic and phosphonic acid-based,  $C_{AS,0} = 3 \text{ mg}\cdot\text{l}^{-1}$ ) were assessed. Figure 4-1 displays real permeability and concentrate turbidity as a function of volumetric concentration factor (VCF) for both, pure and antiscalant-spiked gypsum scaling experiments during ‘high’ and ‘low CP operation’. In all experiments an initial decline of real permeability by 8 – 10 % was observed. According to Jin et al. (2009), this initial permeability loss can be attributed to equilibration processes that include membrane compaction and other unknown causes of flux decline inherent to laboratory scale membrane recirculation systems [226]. Subsequent decreases of real permeability either indicate losses of active membrane area by surface crystallization or indicate the adverse effects caused by bulk crystal deposition. Deposited layers of bulk crystals are assumed to reduce the active membrane area by direct coverage, to create an additional hydraulic resistance and to enhance the osmotic pressure at the membrane surface by cake-enhanced concentration polarization (CECP, e.g. [207]). Bulk crystallization during the RO experiments is indicated by increases of concentrate turbidity. The volumetric concentration factors (VCF) achieved at the onset of sudden real permeability losses, sudden concentrate turbidity increases or both determine the critical volumetric concentration factors ( $VCF_{crit}$ ).

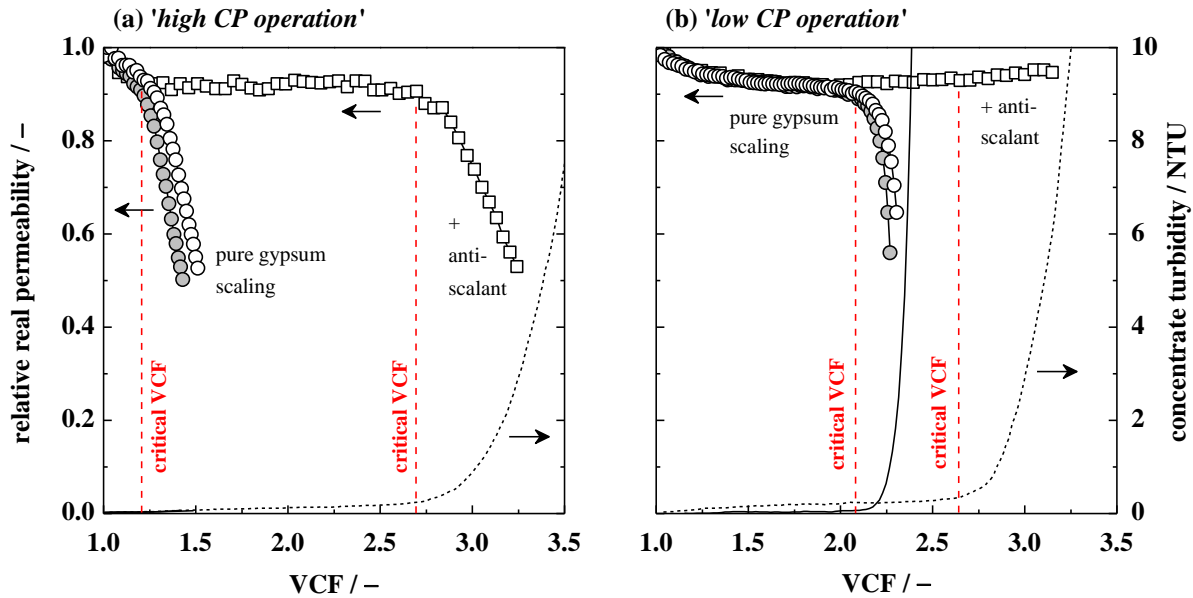


**Figure 4-1:** Development of relative real permeability and concentrate turbidity during gypsum scaling experiments in the absence and presence of  $3 \text{ mg}\cdot\text{l}^{-1}$  antiscalant during (a) ‘*high CP*’ and (b) ‘*low CP operation*’. Real permeabilities are corrected for the continuous increase of osmotic pressure according to Equation 3-3. Experimental conditions:  $SI_{g,b,0} = -0.02$ ,  $\Delta p = 25 \text{ bar}$ ,  $T = 25.0 \pm 0.1 \text{ }^\circ\text{C}$  ( $\pm \text{SD}$ ),  $pH = 6.4 \pm 0.3$  ( $\pm \text{SD}$ ).

During ‘*high CP operation*’, the observed decline in real permeability at  $VCF_{crit} = 1.22$  indicates scaling by surface crystallization as concentrate turbidity was observed to remain low and unaffected (Figure 4-1a). Contrarily, during ‘*low CP operation*’, the observed increase of concentrate turbidity and the coinciding loss of real permeability at  $VCF_{crit} = 2.07$  indicate scaling by bulk crystallization and bulk crystal deposition on the membrane surface. (Figure 4-1b). Antiscalant dosage retarded gypsum crystal formation significantly during both operating modes. It is interesting to note that the scaling mechanism during ‘*high CP operation*’ shifted from surface to bulk crystallization and that permeability during ‘*low CP operation*’ remained unaffected despite the development of bulk crystals in the presence of the dosed antiscalant.

Scanning electron micrographs in Figure 4-2 confirm the dominance of surface and bulk crystallization during ‘*high*’ and ‘*low CP operation*’ in the absence of antiscalant. Surface crystals (Figure 4-2a) exhibited characteristic rosette-like arrangements, which is the commonly reported habit of gypsum surface crystals on polymeric membranes (e.g. [19]). Contrarily, bulk crystals exhibited individual needles that are homogeneously deposited on the membrane surface (Figure 4-2b). Bulk crystals of comparable habit and size were also detected in the recycled concentrate solution (Figure D-1a). Complementary XRD analyses confirmed that gypsum was the only crystalline phase (Figure D-2). Figure 4-2 further demonstrates the effects induced by the dosed antiscalant. Antiscalant dosage resulted in distorted habits of surface and bulk crystals by adsorption of antiscalant molecules onto crystal faces (‘*crystal distortion effect*’ [101], see also Figure D-1b, c) and prevented bulk crystal deposition during ‘*low CP operation*’ by keeping the crystals in suspension (‘*crystal dispersion effect*’ [113,114]).

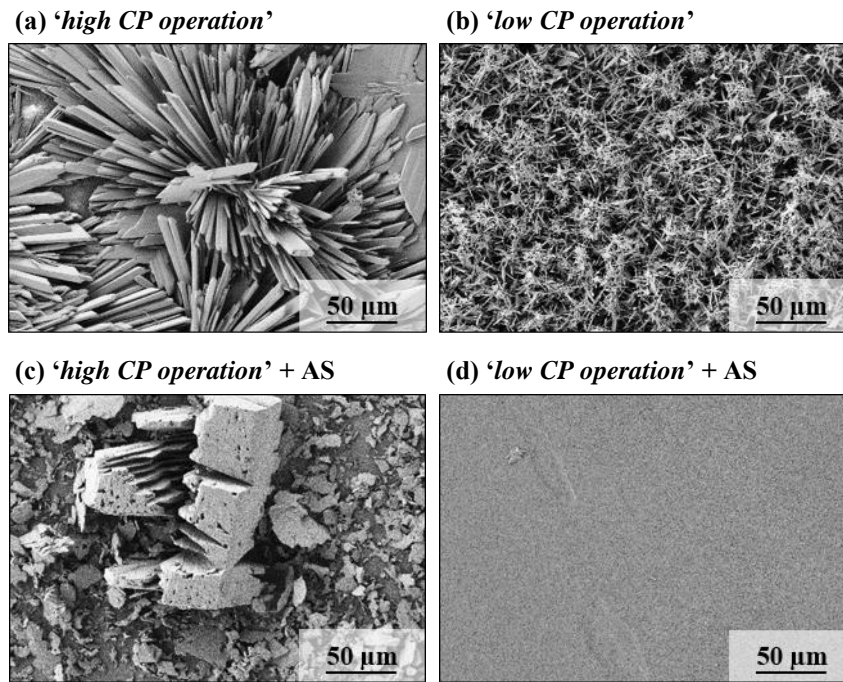


Figure 4-2: Scanning electron micrographs of the membrane surface showing (a) rosette-like gypsum surface crystals after ‘*high CP operation*’, (b) evenly deposited needle-like gypsum bulk crystals after ‘*low CP operation*’, (c) distorted gypsum crystals after ‘*high CP operation*’ in the presence of  $3 \text{ mg}\cdot\text{l}^{-1}$  antiscalant (AS) and (d) the absence of deposited gypsum bulk crystals after ‘*low CP operation*’ in the presence of  $3 \text{ mg}\cdot\text{l}^{-1}$  antiscalant (crystal deposition was prevented by the ‘*crystal dispersion effect*’ of the antiscalant).

Average concentration polarization factors ( $f_{cp} = c_m/c_b$ ) and gypsum saturation indices ( $SI_{g,b}$  and  $SI_{g,m}$ ) at the determined critical *VCF*s are summarized in Table 4-1a. Determined values indicate that surface crystallization was promoted by strong concentration polarization ( $f_{cp} = 2.22$ ) and by a corresponding high gypsum supersaturation at the membrane surface ( $SI_{g,m} = 0.50$ ). Accordingly, the critical operating time of  $t_{crit} = 55 \text{ min}$  was insufficient to exceed the induction time required for bulk crystallization at  $SI_{g,b} = 0.08$ . The relevance of concentration polarization on the prevailing

Table 4-1: (a) Critical volumetric concentration factors ( $VCF_{crit}$ ) and operating times ( $t_{crit}$ ) with corresponding water fluxes ( $J_w$ ), concentration polarization moduli ( $f_{CP}$ ), gypsum saturation indices in the bulk solution ( $SI_{g,b}$ ) and at the membrane surface ( $SI_{g,m}$ ) and dominant gypsum scaling mechanism during ‘*high*’ and ‘*low CP operation*’. (b) Corresponding data for experiments displayed in Figure 4-3 and Figure 4-4. Initial clean water permeability coefficients ( $k_w$ ):  $2.70 - 2.95 \text{ l}\cdot\text{m}^{-2}\cdot\text{h}^{-1}\cdot\text{bar}^{-1}$  (Table C-2).

operating mode	$c_{AS}$ $\text{mg}\cdot\text{l}^{-1}$	$VCF_{crit}$	$t_{crit}$ min	$J_w$ $\text{l}\cdot\text{m}^{-2}\cdot\text{h}^{-1}$	$f_{CP}$	$SI_{g,b}$	$SI_{g,m}$	scaling mechanism
<b>(a)</b>								
‘ <i>high CP</i> ’	0	1.22	55	48.5	2.22	0.08	0.50	surface
	3	2.70	600	30.9	1.66	0.50	0.76	bulk
‘ <i>low CP</i> ’	0	2.07	260	47.1	1.23	0.36	0.47	bulk
	3	2.64	450	43.0	1.20	0.49	0.58	bulk
<b>(b)</b>								
‘ <i>low CP</i> ’, $VCF = 1.5$	0	2.10	140	49.5	1.24	0.37	0.48	bulk
‘ <i>low CP</i> ’, $\Delta p = 0 \text{ bar}$	0	–	120	–	–	0.39	–	bulk

gypsum scaling mechanism is confirmed in previous studies [36,84,85]. Contrarily, the prolonged critical operating time of  $t_{crit} = 260$  min during ‘low CP operation’ exceeded the induction time of gypsum bulk crystallization at  $SI_{g,b} = 0.36$ .

In order to demonstrate the relevance of supersaturation and induction time, two complementary experiments were performed at ‘low CP operation’ where permeation was started at a pre-existing VCF of 1.5 (Figure 4-3) and where a supersaturated gypsum solution ( $SI_{g,b} = 0.39$ ) was recycled in the RO system without applied pressure ( $\Delta p = 0$  bar, Figure 4-4). During permeation and concentration of the pre-concentrated solution ( $VCF_0 = 1.5$ ), bulk crystallization was observed at a supersaturation ( $SI_{g,b} = 0.37$ , Table 4-1b) almost identical to that observed during the experiment that started at  $VCF = 1.0$  ( $SI_{g,b} = 0.36$ ), despite the significantly shorter operating time of  $t_{crit} = 140$  min. This demonstrates that bulk crystallization will occur spontaneously after achieving a system specific bulk supersaturation where induction time is negligibly small [89,90,227]. It is important to consider that the complex hydrodynamics of spacer-filled membrane module flow channels will cause bulk supersaturation to be locally higher than average [92,155]. This was omitted by operating without applied pressure ( $\Delta p = 0$  bar, Figure 4-4) at constant bulk supersaturation of  $SI_{g,b} = 0.39$ . The observed induction time of  $\tau = 120$  min demonstrates that bulk crystallization does not occur spontaneously below a system specific critical supersaturation.

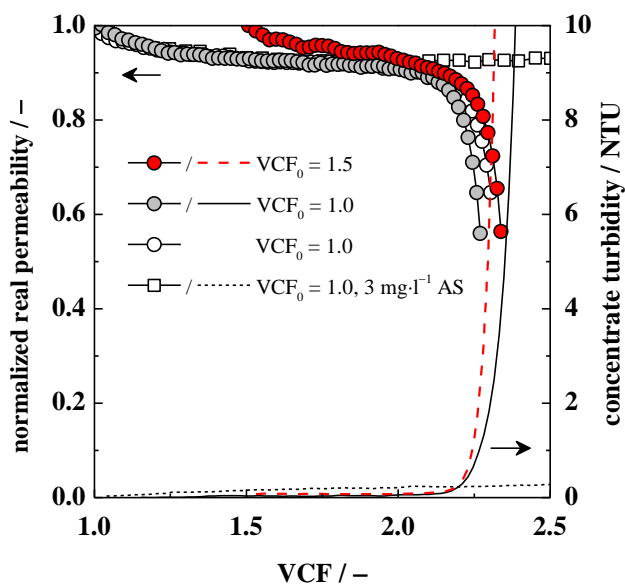


Figure 4-3: Comparison of normalized real permeability and concentrate turbidity development during ‘low CP operation’ starting at a  $VCF_0 = 1.0$  and  $VCF_0 = 1.5$  (previously shown in Figure 4-1b).

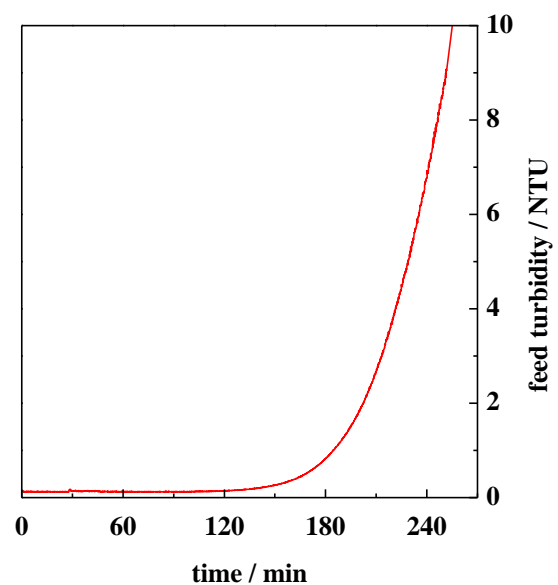


Figure 4-4: Development of concentrate turbidity during recirculation of a supersaturated gypsum solution ( $SI_{g,b} = 0.39$ ) employing low CP operation without permeation ( $\Delta p = 0$  bar).

### **Summary**

It is evident that gypsum scaling during RO desalination will be dominated by bulk crystallization only when operating conditions result in the achievement of (i) a system specific critical bulk supersaturation or (ii) a hydraulic residence time that exceeds the induction time of bulk crystallization at system specific subcritical bulk supersaturations. If bulk crystallization is prevented by operation at short hydraulic residence times and at subcritical supersaturation, scaling will be dominated by surface crystallization, especially at high degrees of concentration polarization. This is expected to be the case in most full scale once-through flow membrane desalination systems, where hydraulic residence times are small and water recoveries and resulting bulk supersaturations are kept below the system specific critical values. In contrast, concentrate recirculation to increase water recovery will favor the occurrence of bulk crystallization.

The results further confirm the commonly described mechanisms of scale inhibition by antiscalant dosage (Chapter 2.2.4). The retardation of bulk crystal nucleation is explained by the '*threshold effect*', which assumes blockage of subcritical nuclei by adsorption of antiscalant molecules [55,101,113]. The adsorption of antiscalant molecules onto crystal faces resulted in distorted crystal growth ('*crystal distortion effect*' [101]) and prevention of bulk crystal deposition by dispersion ('*crystal dispersion effect*' [113,114]).

## **4.2 Gypsum Bulk Crystallization From Supersaturated Solution**

Chapter 4.1 demonstrated that gypsum scale formation in RO systems can be dominated by bulk crystallization which deteriorates RO performance due to crystal deposition on the membrane surface. It was also shown that the induction time at given supersaturation determines the nucleation of bulk crystals. Using stirred beaker experiments, this chapter investigates the effects of supersaturation and *pH* on gypsum bulk crystallization from supersaturated aqueous solution. It presents a prerequisite for subsequent investigations into the effects of NOM on gypsum bulk crystallization kinetics. A complete list of conducted stirred beaker experiments can be found in the appendix (Table C-1).

### **Effects of supersaturation on induction time**

Figure 4-5 displays induction times ( $\tau$ ) of gypsum bulk crystallization from aqueous solution as a function of gypsum bulk supersaturation ( $S_{g,b}$ ). Induction time clearly decreases with increasing supersaturation as expected from classical nucleation theory [65,67]. The relationship between  $\tau$  and  $S$  is well represented by Equation 2-11, which linearly correlates  $\ln(\tau)$  to  $\ln^{-2}(S)$ . Figure 4-5 includes induction times that were observed in previous glassware [127,129,130] and RO desalination [89,90,149] studies. It is important to consider that the induction time is not a fundamental property of the crystallizing system because it depends on the sensitivity of crystal detection and the specific hydrodynamic properties of the experimental system [65]. For example, the influence of hydrodynamics on observed induction times during RO desalination experiments

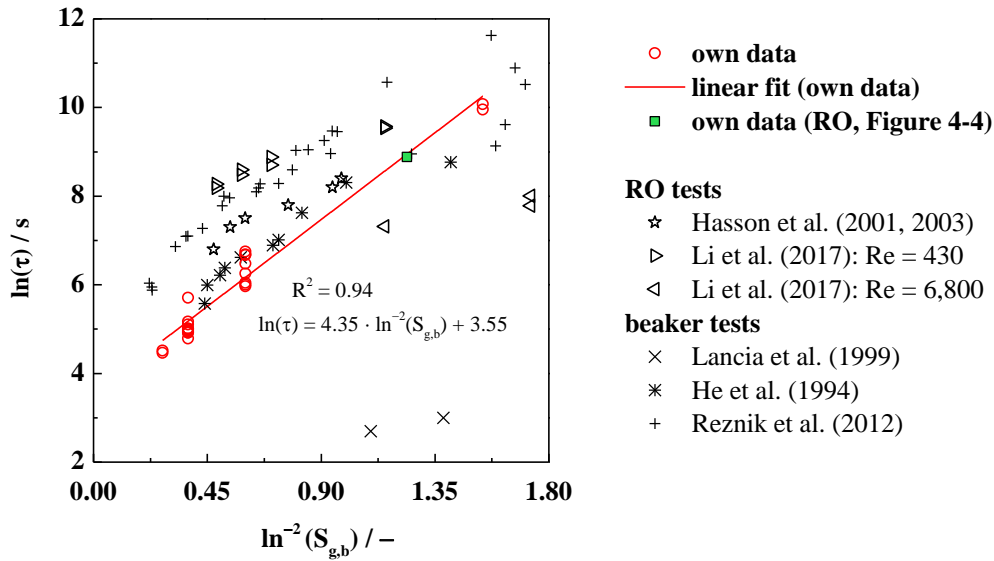


**Figure 4-5: Linear correlation of gypsum supersaturation ( $S_{g,b}$ ) and observed induction time ( $\tau$ ) of the stirred beaker experiments ( $T = 24.9 \pm 0.3$  °C ( $\pm$ SD),  $pH = 7.0 \pm 0.2$  ( $\pm$ SD)), the RO recirculation experiment of Figure 4-4 and reported literature values. Hasson et al. (2001, 2003): RO permeation,  $T = 28 \pm 3$  °C, periodic flux and turbidity measurement [89,90]; Li et al. (2017): RO permeation at different Reynolds numbers,  $T$  not specified, periodic flux and turbidity measurement [149]; Lancia et al. (1999): stirred beaker,  $T = 25$  °C, laser transmittance and scattering [127]; He et al. (1994): stirred beaker,  $T = 25$  °C; turbidity and calcium measurements [130]; Reznik et al. (2012): shaker experiments,  $T = 25$  °C, sulfate measurements [129].**

was previously demonstrated by Hasson and coworkers using different membrane module geometries [89,90,149]. It is therefore expected that each dataset included in Figure 4-5 follows the linear correlation between  $\ln(\tau)$  and  $\ln^2(S)$  but exhibits a different slope and/or intercept. Compared to the data derived in this thesis, the majority of the reported data sets exhibit similar slopes but longer induction times at given supersaturation. Those experiments all relied on periodic measurements of solution turbidity [89,90,149] or ion concentrations [129,130] leading to an inherently lower sensitivity and delayed crystal detection compared to real-time measurements of solution turbidity as employed in this thesis. In contrast, induction times reported by Lancia et al. (1999) were considerably lower given the higher sensitivity of real-time laser transmittance and scattering measurements [127]. Apart from the observed variations, Figure 4-5 shows that the reported induction times and the observed induction times in this work as well as their dependence on supersaturation are in well agreement.

In addition, the observed induction time of the previously presented RO recirculation experiment ( $\Delta p = 0$  bar,  $SI_{g,b} = 0.39$ ,  $\tau = 120$  min, Figure 4-4) fits perfectly to the relationship determined from the stirred beaker experiments (Figure 4-5, green square). It demonstrates that stirred beaker crystallization experiments can supplement resource- and time-consuming RO desalination experiments in order to investigate effects on induction time, such as supersaturation or the presence of antiscalants and natural organic matter (NOM).

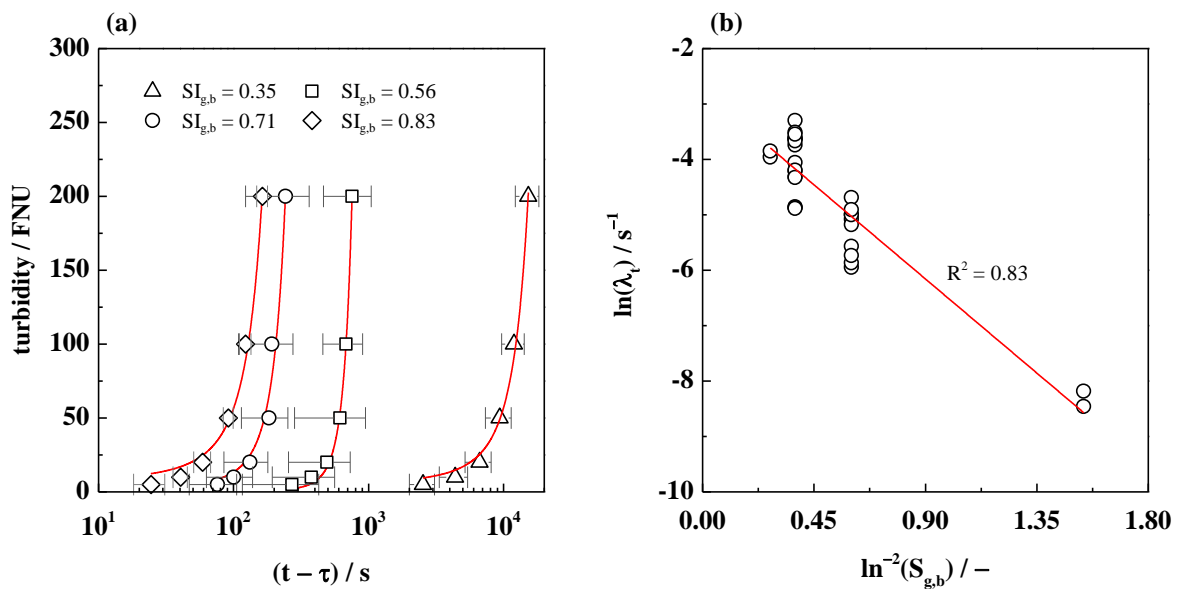
### Effects of supersaturation on crystallization time, turbidity increase and crystal growth

After exceeding the induction time, turbidity increased exponentially with time (Figure 4-6a), which can be estimated by the following exponential function:

$$\kappa = \kappa_0 \cdot e^{(\lambda_t t)} \quad \text{Equation 4-1}$$

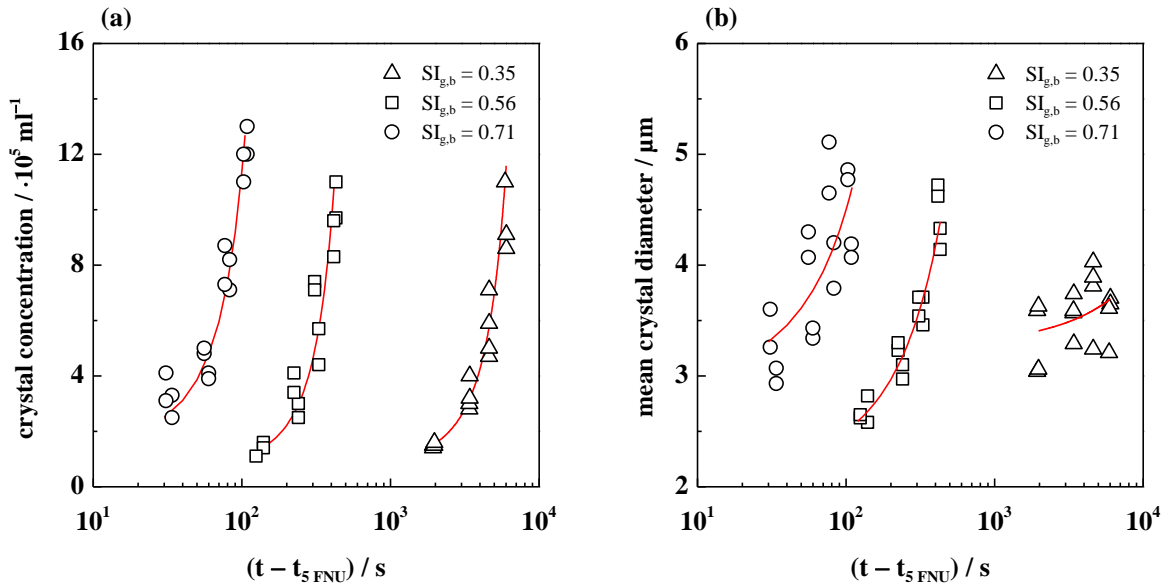
where  $\kappa$  is the turbidity in FNU,  $\kappa_0$  is the initial turbidity in FNU ( $\kappa_0 \approx 1$  FNU),  $\lambda_t$  is the rate constant of turbidity increase in  $s^{-1}$  and  $t$  is the time exceeded after the observed induction time ( $t - \tau$ ) in s. Consistent with observed crystallization times\* ( $\Delta t$ ), fitted rate constants of turbidity increase ( $\lambda_t$ , Table C-1) enhance with increasing supersaturation, which is expressed by the linear relation of  $\ln(\lambda_t)$  and  $\ln^{-2}(S)$  presented in Figure 4-6b. As solution turbidity depends on both, crystal concentration ( $c$ ) and size (i.e. mean diameter,  $d_p$ ) [228], select experiments were periodically sampled and analyzed for both parameters ( $c$  and  $d_p$ ) by laser obscuration time (LOT) measurements. LOT measurements show that for all investigated supersaturations, crystal concentration, after exceeding the induction time, increased exponentially with time (Figure 4-7a). Final crystal concentrations at  $\kappa = 200$  FNU were slightly higher at  $SI_{g,b} = 0.71$  compared to  $SI_{g,b} = 0.56$  and  $SI_{g,b} = 0.35$  ( $p < 0.05$ ).

Figure 4-7b displays the mean crystal diameter as a function of time. After elapse of the induction time, mean crystal diameter ( $d_p$ ) increased exponentially with time and rate constants of gypsum



**Figure 4-6:** (a) Turbidity increase after exceeding the induction time ( $t - \tau$ ) during gypsum bulk crystallization experiments ( $T = 24.9 \pm 0.3$  °C ( $\pm$  SD),  $pH = 7.0 \pm 0.2$  ( $\pm$  SD)). Data points represent mean values  $\pm$  SD ( $n = 2 - 16$ , Table C-1) and lines represent exponential fits according to Equation 4-1. (b) Linear correlation of  $\ln^{-2}(S_{g,b})$  and  $\ln(\lambda_t)$ .

\* Defined as the time elapsed between the induction time and the achievement of a solution turbidity of 200 FNU.



**Figure 4-7:** Development of (a) gypsum crystal concentration and (b) crystal mean diameter during gypsum bulk crystallization experiments ( $T = 25.1 \pm 0.1$  °C ( $\pm$  SD),  $pH = 6.9 \pm 0.1$  ( $\pm$  SD)) determined by laser obscuration time (LOT) measurement of consecutive samples taken at 5, 20, 50, 100 and 200 FNU. Experiments were repeated once and each sample was measured twice. Lines represent exponential fits according to Equation 4-1.

crystal growth ( $\lambda_G$ ) were estimated analogue to Equation 4-1. Fitted rate constants of crystal growth amounted to  $\lambda_G = 4.4 \cdot 10^{-3} \text{ s}^{-1}$  at  $SI_{g,b} = 0.71$ ,  $\lambda_G = 1.7 \cdot 10^{-3} \text{ s}^{-1}$  at  $SI_{g,b} = 0.56$  and  $\lambda_G = 1.9 \cdot 10^{-5} \text{ s}^{-1}$  at  $SI_{g,b} = 0.35$ . Values of  $\lambda_G$  relate linearly to  $S^2$  ( $R^2 > 0.99$ ) as would be predicted from the adsorption-layer theory of crystal growth at low supersaturations [65,67]. Figure 4-8 shows the resulting gypsum bulk crystal morphologies in dependence of supersaturation. Individual gypsum needles were observed at low supersaturation ( $SI_{g,b} = 0.35$ ) and corresponding slow crystallization kinetics whereas the complexity of crystals increased at higher supersaturation and accelerated crystallization kinetics, resulting in platelet-like crystal habits and rosette-like agglomerates.

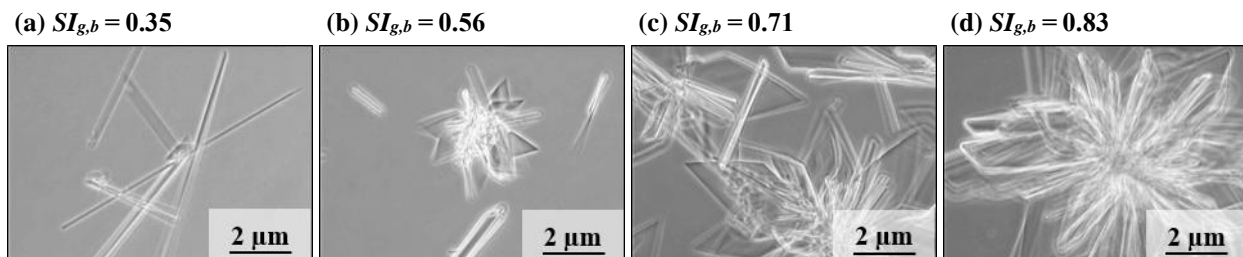


**Figure 4-8:** Impact of supersaturation on gypsum crystal morphology. Samples taken from stirred beaker experiments at a turbidity of 5 FNU ( $T = 24.9 \pm 0.3$  °C ( $\pm$  SD),  $pH = 7.0 \pm 0.2$  ( $\pm$  SD)).

### Effects of pH on induction and crystallization time

Figure 4-9 displays induction times ( $\tau$ ) of gypsum bulk crystallization at constant gypsum supersaturation of  $SI_{g,b} = 0.56$  as a function of  $pH$ . Despite the reported  $pH$ -insensitivity of gypsum

supersaturation [117,136,137], results depicted in Figure 4-9 show that prolonged induction times were observed at  $pH \approx 10.0$  compared to  $pH \leq 8.5$ . In addition, a prolonged mean crystallization time ( $\Delta t$ ) of  $1098 \pm 390$  s compared to  $745 \pm 104$  s ( $\pm 95\%$  confidence intervals) was observed at  $pH \approx 10.0$ . XRD analysis confirmed that gypsum was the only crystalline phase at  $pH$  values of 4.0, 7.0 and 10.0 (Figure D-3). Increases of solution ionic strength and resulting increases of gypsum solubility by acid and base dosage for  $pH$  adjustment were negligible as the addition of an equivalent amount of NaCl ( $0.1 \text{ mmol}\cdot\text{l}^{-1}$ ) at  $pH = 7.0$  left induction time unaffected relative to the reference (Figure 4-9a, red square). Rahardianto et al. (2008) observed that gypsum surface crystal growth was retarded in the presence of bicarbonate ( $\text{HCO}_3^-$ ) and suggested that the retardation was caused by bicarbonate adsorption onto crystal faces [161]. Despite continuous sparging of the experimental solution with  $\text{N}_2$  gas, complete absence of inorganic carbon could not be guaranteed during the stirred beaker experiments given that the experimental design was not entirely closed to the atmosphere. Concluding, at  $pH = 10.0$ , where bicarbonate ( $\text{HCO}_3^-$ ) followed by carbonate ( $\text{CO}_3^{2-}$ ) are the dominant inorganic carbon species\*, direct interactions between bicarbonate or carbonate and gypsum crystal formation may have led to the observed retardation. Further investigations are required to verify this assumption.

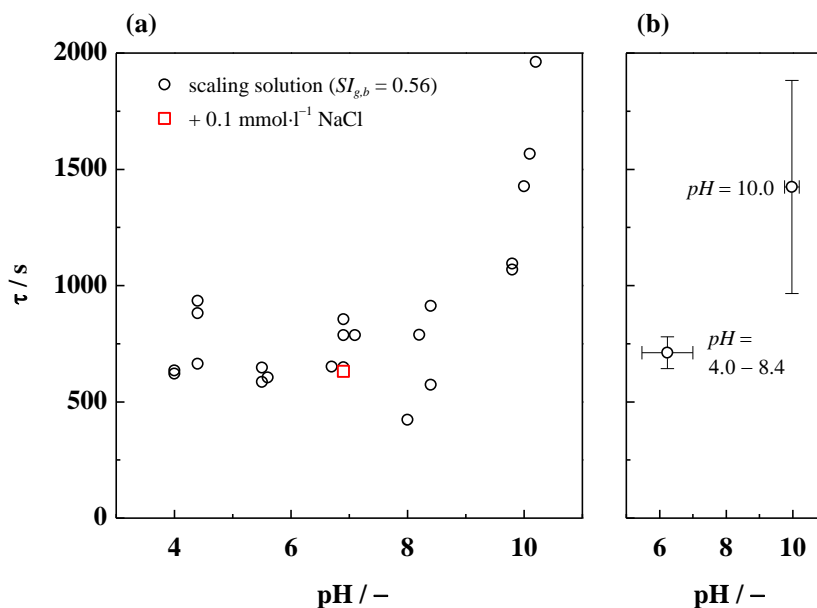


**Figure 4-9: Effects of  $pH$  on observed induction time of gypsum bulk crystallization at  $SI_g = 0.56$  ( $T = 25.1 \pm 0.1$  °C ( $\pm$  SD)). (a) Individual data points; an additional experiment (red square) was spiked with an amount of NaCl equivalent to the amount of NaOH ( $0.1 \text{ mmol}\cdot\text{l}^{-1}$ ) that is required to achieve a  $pH$  of 10.0 in clean water. (b) Mean values for  $pH = 4.0 - 8.4$  and  $pH \approx 10.0$  with error bars indicating the 95 % confidence interval.**

\* Acidity constants ( $K_a$ ) of the carbonate system are  $pK_a = -\log(K_a) = 6.35$  and  $10.33$ .

### **Summary**

Observed induction times of gypsum bulk crystallization decreased with increasing supersaturation ( $\ln(\tau) \propto \ln^{-2}(S)$ ) and were in well agreement with reported induction times of previous studies. It was also demonstrated that stirred beaker experiments can supplement RO desalination experiments in order to investigate effects on induction time. Similarly, the time required to achieve a solution turbidity of 200 FNU ( $\Delta t$ ) decreased with increasing supersaturation as was expressed by the linear correlation of the rate constant of turbidity increase ( $\lambda_t$ ) and supersaturation ( $\ln(\lambda_t) \propto \ln^{-2}(S)$ ). Crystal concentration ( $c$ ) and mean crystal diameter ( $d_p$ ) during the phase of increasing turbidity increased exponentially with increased rate constants at increased supersaturation. Gypsum crystals grew into individual needles at low supersaturation and platelet-like and rosette-like arrangements at increased supersaturation. Indication was given that crystallization kinetics may be indirectly decelerated at high  $pH$  due to the adsorption of trace inorganic carbon species onto subcritical nuclei and crystal faces. The results represent an important prerequisite for the following investigations into the effects of natural organic matter (NOM) on gypsum bulk crystallization kinetics at different  $pH$  values.

### **4.3 Gypsum Surface Crystallization on RO Membranes**

*Selected contents of this chapter have been published in collaboration with M. Haas, F. Baur and M. Ernst: Desalination 428 (2018), 161–171.*

Chapter 4.1 demonstrated that gypsum scaling during RO desalination can be dominated by surface crystallization, which results in deterioration of RO process performance due to heterogeneous crystal nucleation and growth on the membrane surface (in the following referred to as ‘*surface scaling*’). Severe degrees of surface scaling can be detected by permeate flux decline, however, this method proved insensitive to monitor the early-stages of surface scale formation and small degrees of scale coverage [54,94,97,156,162]. This chapter investigates the development and reproducibility of gypsum surface scaling on RO membrane samples using real-time membrane surface imaging by light microscopy (RO setup – configuration II, Chapter 3.2.3), which at present represents the most sensitive method to monitor early-stage scale development on membrane surfaces during permeation [97]. To date, the expectable variability of identically performed gypsum scaling experiments has not been documented. In addition, effects of small variations of supersaturation, effects of increased feed water turbidity and effects of repeated scaling and subsequent cleaning on gypsum surface scaling behavior are assessed in this chapter. A complete list of conducted scaling experiments can be found in Table C-3.

#### **Development of heterogeneous gypsum scale on RO membranes**

A total number of 11 identical pure gypsum scaling experiments were performed to assess the reproducibility of gypsum surface scaling behavior on virgin RO membrane samples. As

commonly observed (e.g. [19]), detected gypsum crystals grew into three-dimensional rosette-like structures by lateral growth and secondary nucleation in the vicinity of existing crystalline matter (Figure 4-10). In addition to large gypsum rosettes, which are reliably detected by the employed real-time imaging method ( $d_{p,min} = 49.3 \mu\text{m}$ ), small crystals with diameters below  $d_{p,min}$  are visible on the scanning electron micrograph shown in Figure 4-10 (arrows). It is uncertain, whether these crystals nucleated heterogeneously on the membrane surface or represent detached crystal fragments from existing rosettes which broke off during operation or post-treatment. Despite careful handling, crystal fragmentation and random deposition of fragments during membrane cell disassembly and sample preparation for scanning electron microscopy (SEM) is likely. Given that the bulk solution remained below supersaturation with respect to gypsum ( $SI_{g,b} = -0.02$ ), bulk crystal nucleation, growth and subsequent deposition on the membrane surface is unlikely. The absence of bulk crystals was confirmed by low concentrate turbidity, which averaged  $0.05 \pm 0.03$  NTU ( $\pm 95\%$  confidence interval) throughout all reference gypsum scaling experiments ( $n = 11$ ). Complementary analysis of concentrate solution by nanoparticle tracking analysis (NTA) did not indicate the presence of gypsum bulk crystals (Figure D-4).

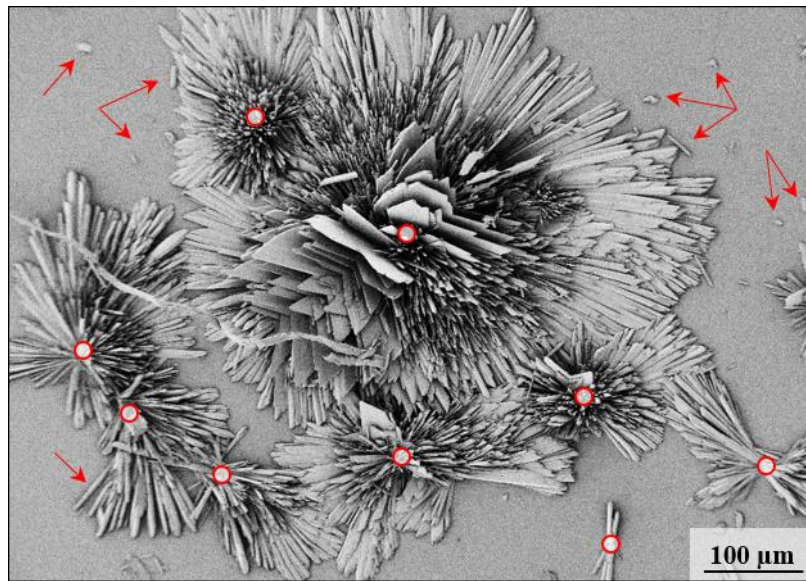


**Figure 4-10: Scanning electron micrograph (200x magnification) showing three-dimensional rosette like gypsum crystals on the RO membrane surface after termination of the experiments at  $t = 270$  min. Red circles indicate individual rosettes detectable by the real-time imaging method ( $d_p > 49.3 \mu\text{m}$ ), whereas red arrows indicate crystals or crystal fragments that are smaller than the detection limit.**

Real-time images were analyzed for the detectable crystal number density ( $CND$ ) and the fractional surface coverage ( $FSC$ ). Additionally, the mean crystal diameter ( $d_p$ ) was calculated. Temporal evolution of the determined parameters is presented in Figure 4-11. Although significant scatter around the corresponding mean values is observed, each experiment followed the general trend observable for the average temporal evolution. First crystals ( $d_p > 49.3 \mu\text{m}$ ) were detected after 4 – 18 min (mean:  $9.5 \pm 2.6$  min,  $\pm 95\%$  confidence interval,  $n = 11$ ). Thereafter,  $CND$  developed

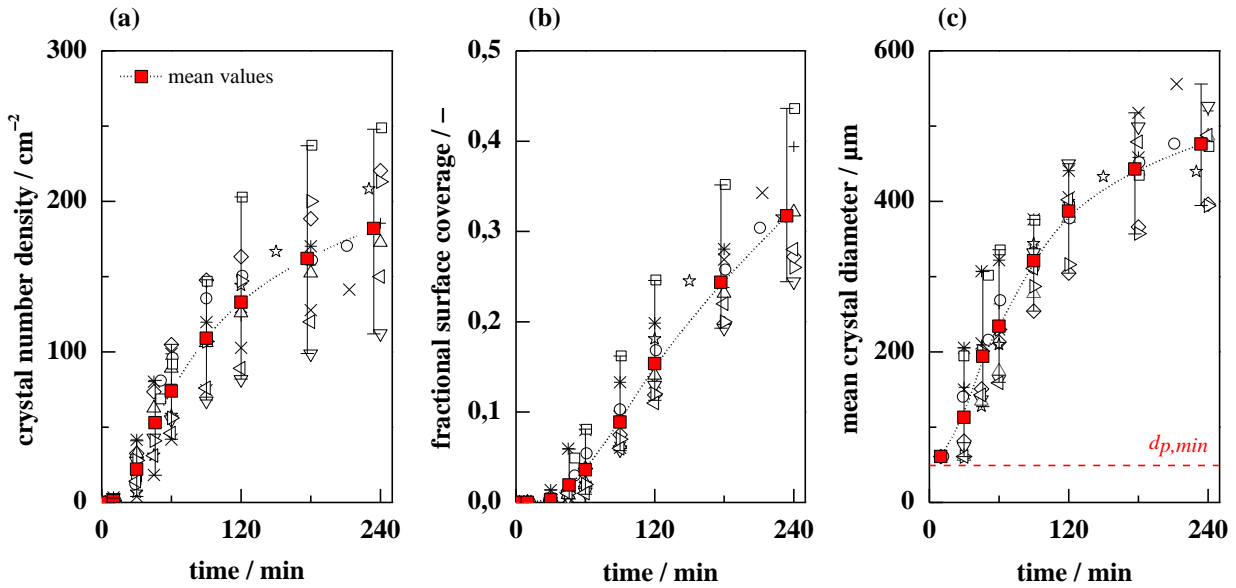


Figure 4-11: Temporal development of (a) gypsum surface crystal number density ( $CND$ ) ( $d_p > 49.3 \mu\text{m}$ ), (b) fractional membrane surface coverage ( $FSC$ ) and (c) mean crystal diameter ( $d_p > 49.3 \mu\text{m}$ ) on 11 virgin RO membrane samples detected by real-time membrane surface imaging. Error bars of mean values represent determined minimal and maximal values of individual experiments.

logarithmic ( $\log_{10}(t) \propto CND$ ) with a decreasing detection rate of new crystals (Figure 4-11a). Given the method's lower detection limit of  $d_{p,min} = 49.3 \mu\text{m}$ , it is clear that true heterogeneous nucleation rates cannot be observed and that the true  $CND$  is higher, as previously shown in Figure 4-10. However, as all heterogeneous critical nuclei are expected to grow into detectable size within reasonably short time periods, true nucleation is assumed to behave analogue to the detected  $CND$  and is assumed to decrease according to the decreasing rate of crystal detection. Similar assumptions were previously drawn by Uchymiak et al. (2008) [91]. Further, the observed short latent periods indicate that, for the chosen experimental conditions, true induction periods for heterogeneous gypsum nucleation on the employed RO membrane were not existing or insignificant. The non-existence of induction times for heterogeneous gypsum scaling on RO membranes is supported by previous studies [54,98]. Despite the absence of induction times for initial crystal nucleation, the continuous appearance of new crystals throughout the experiment indicates that induction periods experience a temporal distribution. As previously suggested [91,95,96], it is assumed that the available heterogeneous nucleation sites on the membrane surface exhibit different nucleation affinities. Accordingly, nucleation occurs first and preferentially on energetically favorable nucleation sites of highest affinity. The effective nucleation affinity of the membrane is therefore continuously reduced and crystal nucleation and detection rates decrease accordingly.

Fractional surface coverage increased consistently due to lateral growth of gypsum surface crystals (Figure 4-11b). After 234 min of operation, an average of 31.7 % ( $n=11$ ) of the monitored membrane area was covered by gypsum scale. Unlike crystal number density, which is likely

underestimated due to the method's detection limit, fractional surface coverage is virtually unaffected by undetected crystals ( $d_p < 49.3 \mu\text{m}$ ) as their total area is negligibly small. In Figure 4-10, for example, only 0.31 % of the total area is covered by crystals smaller than  $49.3 \mu\text{m}$ . Mean crystal growth decelerated during the course of the experiments as exhibited by the decreasing slope of the temporal evolution of the mean crystal diameter (Figure 4-11c). With increasing crystal size, an increased amount of crystal-forming ions is required for further growth and diffusional transport of ions from the bulk solution towards the crystallizing layer may become limiting [55]. Additionally, crystal growth is governed by supersaturation [65,67], which diminishes gradually as, for the given experimental procedure, the inventory of scale-forming ions is limited. Further, the development of three-dimensional scale will alter hydrodynamics in the feed flow channel, possibly enhance mass transfer at the membrane surface by promoting turbulence and in turn decrease the degree of concentration polarization. These considerations may explain the decreasing rate of crystal growth and the expected asymptotic attainment of constant values at prolonged experimental durations.

#### Reproducibility of gypsum surface scale development

Crystal parameters ( $CND$ ,  $FSC$ ,  $d_p$ ) determined for the individual experiments experienced significant scatter around the calculated mean values (Figure 4-11). After 234 min of operation, values for crystal number density, fractional surface coverage and mean crystal diameter varied between  $CND = 112 - 249 \text{ cm}^{-2}$ ,  $FSC = 0.24 - 0.44$  and  $d_p = 394 - 556 \mu\text{m}$ . Among the three parameters, the crystal number density experienced greatest scatter in terms of percent deviation. Real-time images in Figure 4-12 show three different membrane samples at  $t = 180 \text{ min}$ . Significant differences can be identified with respect to the size and the distribution of gypsum surface crystals. In general, large areas remained free of detectable crystals or exhibited crystals

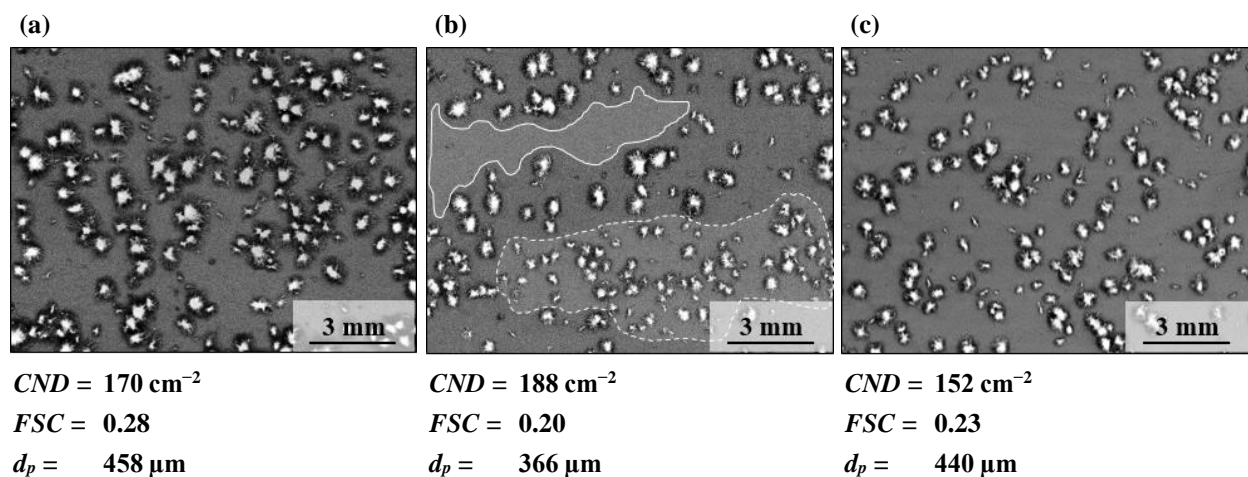


**Figure 4-12: Real-time images ( $t = 180 \text{ min}$ ) and determined crystal number density ( $CND$ ), fractional surface coverage ( $FSC$ ) and mean crystal diameter ( $d_p$ ) of three identically performed experiments. In (b), areas with comparably small crystals (dashed line) and areas free of detectable crystals (solid line) are highlighted.**

of comparably small size. In all experiments, crystals that exhibited largest sizes at the end of an experiment were also detected first and vice versa.

Non-uniform spatial distributions of heterogeneous gypsum crystals on RO membranes have been previously reported in literature [91,98,156]. This non-uniform distribution and the different times of crystal detection were explained by either the given randomness [156] and the inherent stochastic nature [98] of the nucleation process or the limited availability of energetically favorable surface nucleation sites [91]. The latter explanation is consistent with recent advances made by Mitrouli et al. (2016) [96] and Kostoglou et al. (2017) [95], who suggest that polymeric membranes exhibit a spatial distribution of energetically favorable nucleation sites on the membrane surface. This assumption, rather than stoichiometry alone, may explain the observed spatial non-uniformity, the absence or delayed appearance of detectable crystals in large areas of the membrane sample as well as the temporal distribution of new crystal detection. Given the uncertainty whether the imaged area exhibits higher or lower nucleation affinity relative to the overall behavior of the entire membrane sample and due to the fact that the monitored membrane area accounts to less than 1 % of the total active membrane area, increased data scatter of determined crystal parameters is expectable. It emphasizes the inherent tradeoff between the acquirable detail and the size of the imaged area depending on magnification, which are two competing parameters.

Reliable parameters to assess the degree of scaling on a global scale are the gravimetrically determined total crystal mass and the crystal mass distribution on the membrane surface. As expected [19], crystal mass on each 10 cm membrane subsection increased axially towards the concentrate outlet as ion concentration and supersaturation increased (Figure 4-13). Despite the

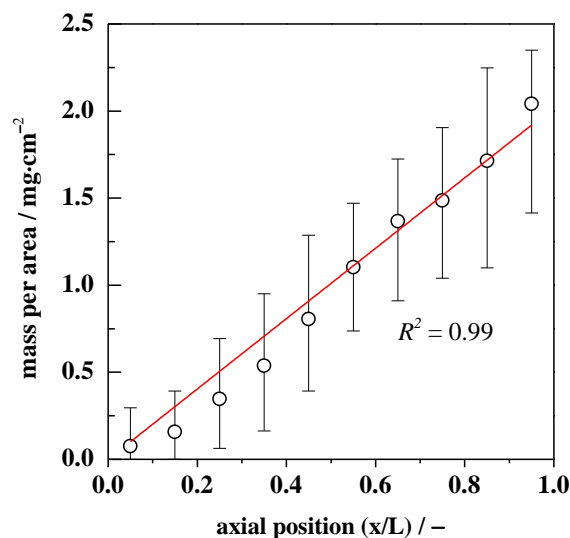


**Figure 4-13: Axial gypsum crystal mass distribution on the membrane surface (determined from 40 cm<sup>-2</sup> membrane subsections). L: length of the feed flow channel (L=100 cm). Mean values (n=7) with corresponding determined minimal and maximal values of individual experiments as error bars.**

fact that individually analyzed membrane subsections ( $A_i = 40 \text{ cm}^2$ ) represent 10 % of the entire active membrane area ( $A_{active} = 400 \text{ cm}^2$ ), the observed variations are still high. Total crystal mass ( $\Delta m_{total}$ ) varies between  $\Delta m_{total} = 248 - 588 \text{ mg}$  (mean:  $412 \pm 86 \text{ mg}$ ,  $\pm 95 \%$  confidence interval,  $n = 9$ ). Concluding, the distribution of heterogeneous gypsum scale was highly variable not only on the imaged membrane subarea of  $1.47 \text{ cm}^2$  during real-time imaging, but also on the entire membrane area of  $400 \text{ cm}^2$ . The assessment of the non-uniform spatial distribution of gypsum scale and the resulting limited reproducibility of repetitive gypsum surface scaling experiments is an important prerequisite for the evaluation of influencing parameters on gypsum surface scaling on RO membranes as it determines the sensitivity of the method and the minimal degree of detectable variations.

It is reasonable to assume that the total crystal mass ( $\Delta m_{total}$ ) and the fractional surface coverage ( $FSC$ ) correlate with the detected increase of applied transmembrane pressure ( $\Delta p$ ) as surface crystals reduce the active membrane area (Figure 4-14). Both parameters,  $\Delta m_{total}$  and  $FSC$ , correlate well to the increase of  $\Delta p$ . However, significant data scatter is observed for the latter correlation ( $FSC$  vs.  $\Delta p$ ) as the fractional surface coverage is determined from the small imaged subarea and correlated to a global parameter that characterizes the entire membrane sample.

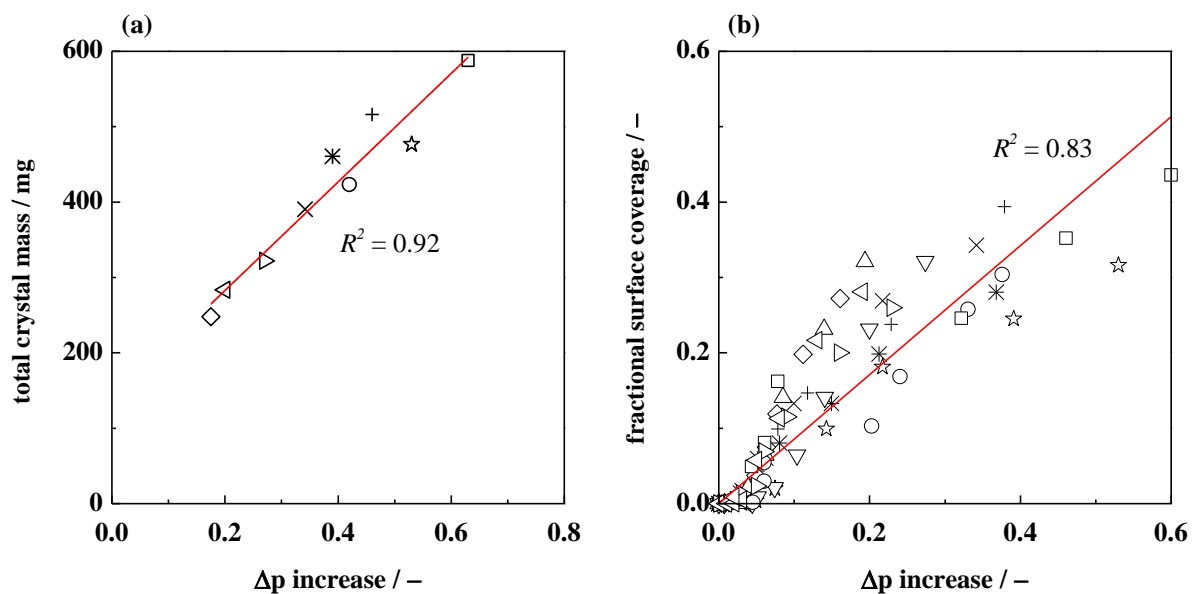
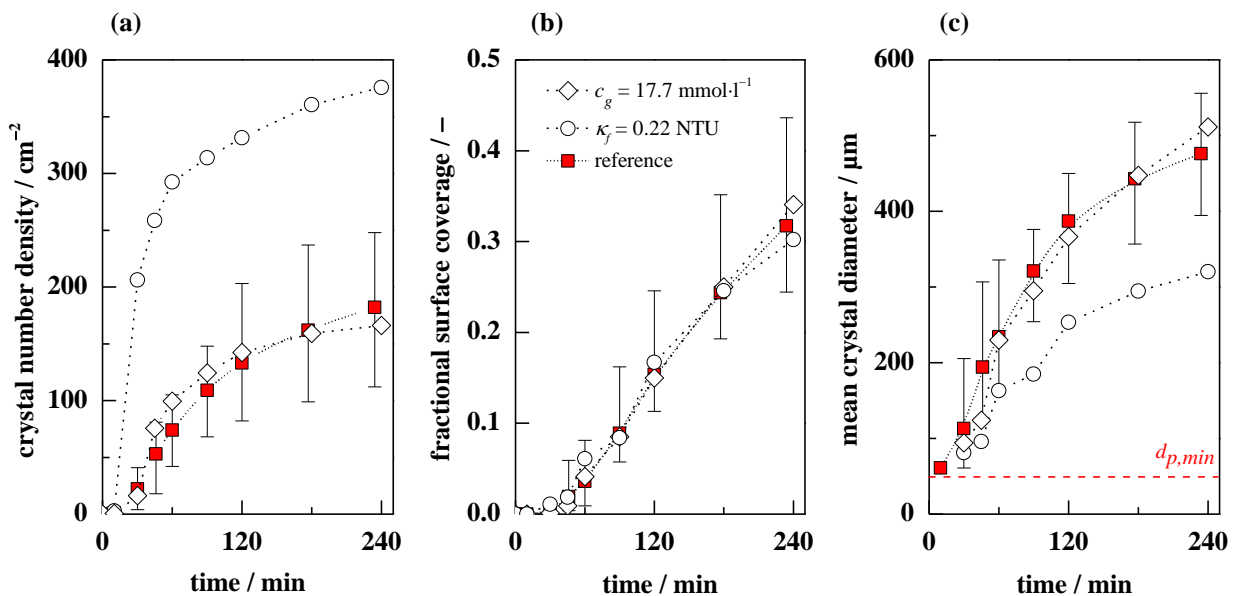


Figure 4-14: Correlations between increase of applied transmembrane pressure ( $\Delta p$ ) and (a) total gypsum crystal mass ( $\Delta m_{total}$ ) and (b) fractional surface coverage ( $FSC$ ).

#### Effects of small variations of gypsum bulk supersaturation

Despite identical experimental protocols, feed ion concentrations during individual experiments varied slightly as indicated by the initial feed solution electrical conductivity ( $EC_f$ , Table C-3).  $EC_f$  varied between  $5625 \mu\text{S}\cdot\text{cm}^{-1}$  and  $5742 \mu\text{S}\cdot\text{cm}^{-1}$  (mean:  $5674 \pm 31 \mu\text{S}\cdot\text{cm}^{-1}$ ,  $\pm 95 \%$  confidence interval,  $n = 11$ ). It is well established that crystal nucleation and growth depends on supersaturation, i.e. scale-forming ion concentration. For heterogeneous gypsum scaling on RO

membranes, this was repeatedly demonstrated by Cohen and coworkers using a similar real-time membrane surface imaging method and a relatively broad range of membrane wall supersaturations ( $SI_{g,m} = 0.11 - 0.24$ ) [91,98,154–156,161]. However, it remains uncertain, whether small variations of supersaturation as experienced in this study, result in detectable variations of scaling behavior, i.e. affect the determined scaling parameters. Therefore, the initial feed solution electrical conductivity was linearly related to total crystal mass ( $EC_f$  vs.  $\Delta m_{total}$ ,  $R^2 = 0.40$ ) and final fractional surface coverage ( $EC_f$  vs.  $FSC$ ,  $R^2 = 0.54$ ). In both cases, correlations were only weak. Therefore, feed ion concentration was increased by 4.1 % in an additional experiment, resulting in a gypsum-saturated solution ( $SI_{g,b} = 0.00$ ,  $SI_{g,m} = 0.53$ ) exhibiting a feed solution electrical conductivity of  $EC_f = 5825 \mu\text{S}\cdot\text{cm}^{-1}$ . Determined crystal parameters ( $CND$ ,  $FSC$  and  $d_p$ ) all lay within the previously observed data scatter of reference experiments (Figure 4-15). Resulting correlation coefficients ( $R^2$ , Figure D-5) between feed solution electrical conductivity and total crystal mass ( $EC_f$  vs.  $\Delta m_{total}$ ,  $R^2 = 0.17$ ) and fractional surface coverage ( $EC_f$  vs.  $FSC$ ,  $R^2 = 0.37$ ) reduced significantly. Total crystal mass amounted to  $\Delta m_{total} = 393 \text{ mg}$  and compares well the mean of previous reference scaling experiments ( $\Delta m_{total} = 412 \pm 86 \text{ mg}$ ,  $\pm 95 \%$  confidence interval,  $n = 9$ ). Concluding, small variations in supersaturation due to differences in scale-forming ion concentrations or inhomogeneous flow regimes were not the primary cause for the previously observed data scatter. In turn, this supports the hypothesis that spatially varying membrane surface properties and corresponding nucleation affinities determine gypsum scaling behavior in addition to supersaturation and other known influ-



**Figure 4-15: Temporal development of (a) gypsum surface crystal number density ( $CND$ ) ( $d_p > 49.3 \mu\text{m}$ ), (b) fractional membrane surface coverage ( $FSC$ ) and (c) mean crystal diameter ( $d_p > 49.3 \mu\text{m}$ ) during RO desalination at (i) increased feed ion concentration ( $c_g = 17.7 \text{ mmol}\cdot\text{l}^{-1}$  compared to  $c_g = 17.0 \text{ mmol}\cdot\text{l}^{-1}$  during reference experiments) and at (ii) increased feed solution turbidity ( $\kappa_f = 0.22 \text{ NTU}$  compared to  $\kappa_f = 0.05 \text{ NTU}$  during reference experiments) caused by stainless steel colloids and particles. Reference experiments are displayed as mean values ( $n = 9$ ) with minimal and maximal values represented as error bars.**

ences. It further portrays the inherent limitation of the employed real-time imaging method, which is the insensitivity to detect any effects on gypsum surface scaling behavior that lie within the existing data scatter of reference experiments.

#### **Effects of increased feed solution turbidity by suspended colloids and particles**

An increased feed solution turbidity of  $\kappa_f = 0.22$  NTU due to suspended stainless steel colloids and particles resulted in significantly higher crystal number density (Figure 4-15a). It is well known that suspended matter initiates and catalyzes heterogeneous nucleation [65,67,229]. Therefore, it is assumed that deposited colloids and particles acted as energetically favorable heteronucleation sites and enhanced the effective membrane surface nucleation affinity. Despite enhanced crystal number density, fractional membrane surface coverage (Figure 4-15b) and total crystal mass ( $\Delta m_{total} = 392$  mg) remained unaffected relative to the reference scaling experiments ( $\Delta m_{total} = 412 \pm 86$  mg,  $\pm 95\%$  confidence interval,  $n=9$ ). Individual gypsum rosettes were significantly smaller in diameter (Figure 4-15c), which shows that an increased rate of heterogeneous nucleation decelerates individual crystal growth. Accordingly, neither total crystal mass nor fractional surface coverage were notably affected by the increased crystal number density. It implies that any efforts to reduce the membrane effective heteronucleation affinity may not be effective in alleviating the overall propensity of surface scale formation and corresponding deterioration of RO process performance during long-term operation. Nevertheless, the observations highlight the significance of the effective membrane nucleation affinity as an additional parameter which determines the surface scaling behavior on RO membranes.

#### **Effects of repeated scale formation and in-situ membrane cleaning**

Consecutive scaling experiments were conducted on a repeatedly scaled and subsequently in-situ cleaned membrane sample. In-situ crystal dissolution was achieved by recycling and permeating ultrapure water as described in Chapter 3.2.3. Subsequent membrane conditioning and scaling experiments were performed identical to the initial pure gypsum reference experiment. Real-time images at  $t = 240$  min (Figure 4-16) show that crystal number density increased significantly and

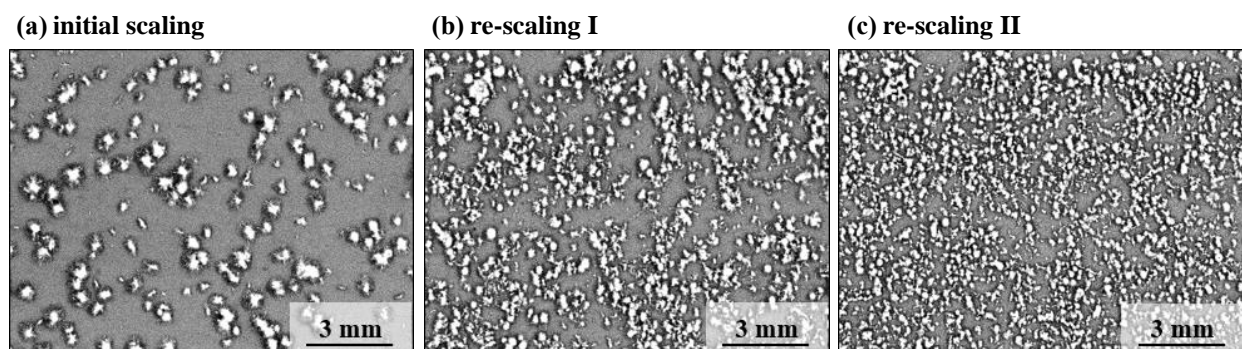


**Figure 4-16: Real-time micrographs showing gypsum crystals at  $t = 240$  min for three consecutive gypsum scaling experiments reusing the same membrane sample after in-situ membrane cleaning according to the cleaning procedure described in Chapter 3.2.3.**

that gypsum crystals regrew preferentially in areas where crystals had previously existed. These observations are supported by complementary non-agitated dead-end RO gypsum surface scaling experiments conducted at constant flux of  $J_w = 30 \text{ l}\cdot\text{m}^{-2}\cdot\text{h}^{-1}$  using the same RO membrane material (Figure D-6).

Analyses of real-time images (Figure 4-17) show that, despite the significantly increased crystal number density ( $CND$ ), fractional surface coverage ( $FSC$ ) was only marginally affected. Although an increase of final  $FSC$  by approximately 8 % was observed after the first re-scaling experiment (re-scaling I), a further increase of final  $FSC$  was not observed during the second re-scaling experiment (re-scaling II) despite the significantly higher  $CND$ . Figure 4-17c shows that mean crystal diameters in re-scaling experiments (I and II) were significantly reduced. Likewise, total crystal mass after the second re-scaling experiment amounted to  $\Delta m_{total} = 382 \text{ mg}$  and lies within the expectable variation of reference experiments ( $\Delta m_{total} = 412 \pm 86 \text{ mg}$ ,  $\pm 95 \%$  confidence interval,  $n = 9$ ), despite significantly increased  $CND$ . It supports the previous observation that neither final fractional surface coverage nor total crystal mass are notably affected by increased final crystal number densities. Concluding, fractional surface coverage and total crystal mass approached similar values independent of effective membrane nucleation affinity. Although the effective membrane nucleation affinity affected gypsum surface scaling behavior on the RO membrane, it did not significantly affect the overall propensity of surface scaling. This is further supported by the nonexistent linear correlation between the crystal number density and the required increase of applied transmembrane pressure (Figure 4-18).

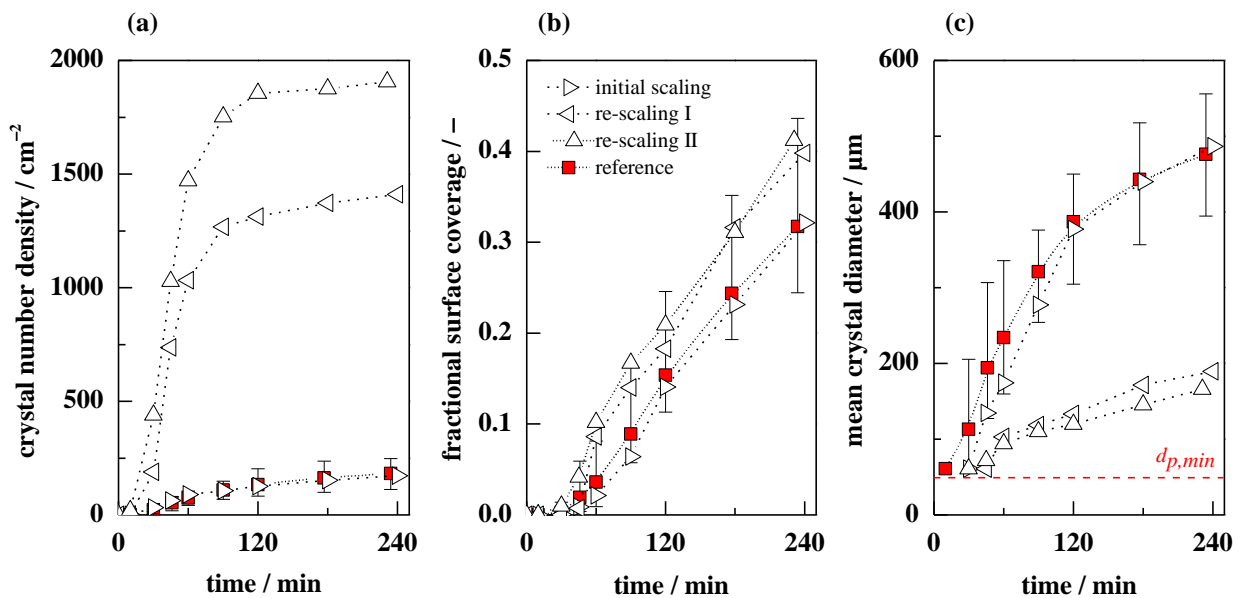


**Figure 4-17:** Temporal development of (a) gypsum surface crystal number density ( $CND$ ) ( $d_p > 49.3 \mu\text{m}$ ), (b) fractional membrane surface coverage ( $FSC$ ) and (c) mean crystal diameter ( $d_p > 49.3 \mu\text{m}$ ) during repeated pure gypsum scaling experiments using an in-situ cleaned membrane sample. Reference experiments are displayed as mean values ( $n = 9$ ) with minimal and maximal values represented as error bars.

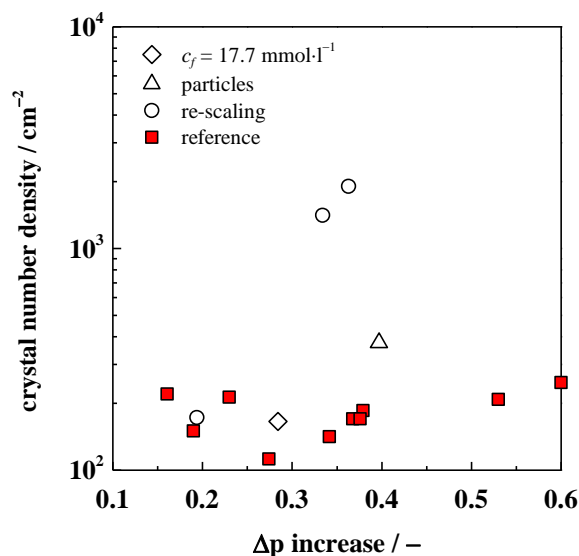


**Figure 4-18: Relationship between transmembrane pressure increase ( $\Delta p$ ) and crystal number density.**

Increased gypsum crystal number densities on cleaned RO membranes were previously reported by Uchymiak et al. (2007) and explained by the initiation of new crystallization sites due to incomplete dissolution of gypsum crystals embedded in the membrane matrix [156]. Scanning electron micrographs of a virgin and a cleaned RO membrane surface (Figure 4-19) show that individual rosette-like gypsum surface crystals mechanically altered the membrane surface leaving behind the characteristic rosette pattern after dissolution (Figure 4-19b). The characteristic and commonly reported ‘*ridge-and-valley*’ structure [6] of the RO membrane (Figure 4-19a) appears to be flattened and to be deeply perforated in various locations (Figure 4-19c). Complementary EDX analyses did not detect calcium and indicated that the gypsum rosette initially present in Figure 4-19b had fully dissolved after dissolution in ultrapure water for 48 h (Figure D-7). Concluding, the observed increased effective nucleation affinity after in-situ cleaning may have primarily resulted from the physical alteration of the membrane surface, which generated additional energetically favorable heteronucleation sites for surface crystal development in areas of previous scale.

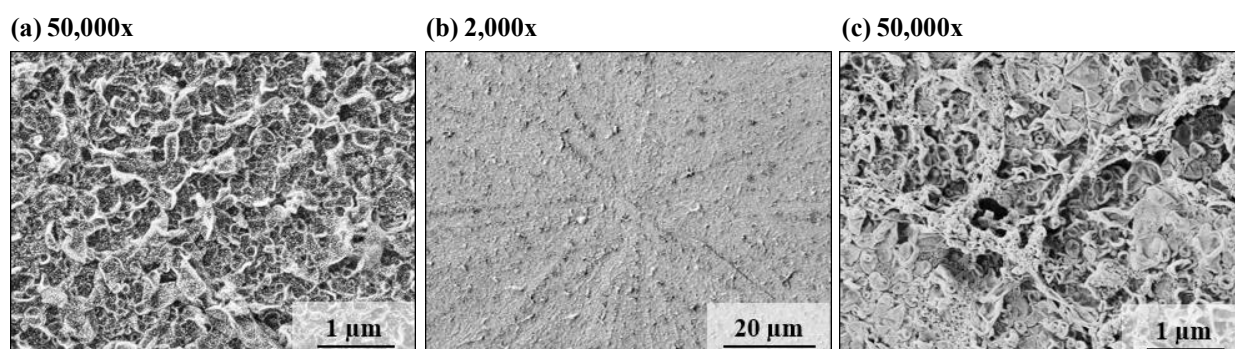


**Figure 4-19: Scanning electron micrographs showing (a) a virgin RO membrane sample rinsed with ultrapure water, (b) an RO membrane sample after dissolution of a heterogeneous gypsum crystal leaving behind the characteristic rosette pattern and (c) the physically altered membrane surface after gypsum crystal dissolution.**

### Summary

Repeated gypsum scaling experiments demonstrated that the polyamide RO membrane surface exhibited a non-uniform spatial distribution of intrinsic heteronucleation affinities, which resulted in considerable variations of surface scaling behavior on a global (crystal mass and  $\Delta p$  increase) and local ( $CND$ ,  $FSC$ ,  $d_p$ ) basis. The observed variation of surface scaling determines the sensitivity of the real-time imaging method and represents a required prerequisite for subsequent investigations into the effects of natural organic matter (NOM) on gypsum surface scaling behavior. It further emphasizes the significance of membrane heteronucleation affinity as an additional parameter determining the surface scaling behavior on RO membranes. Effective membrane heteronucleation affinity may be enhanced by deposited particulate matter, embedded crystals and nuclei after cleaning as well as physical membrane surface alterations. However, the overall loss of RO performance ( $FSC$ , crystal mass and  $\Delta p$  increase), i.e. the overall propensity of surface scaling, was not significantly affected by increased effective nucleation affinities because crystal growth was observed to be decelerated at higher heteronucleation rates. The relationship between the final crystal number density (i.e. effective heteronucleation affinity) and the final crystal diameter (i.e. crystal growth) is further discussed in Chapter 7.1 (Figure 7-3).

## 5 Characterization of the Selected NOM Sources

Different natural organic matter sources were selected to represent different types of NOM in natural waters as previously summarized in Table 3-1. To represent polysaccharides and proteins, sodium alginate (SA) and bovine serum albumin (BSA) were selected due to their commercial availability and their common use in membrane related fouling studies. As representatives for humic substances, the following three commercially available sources were selected: coal-extracted humic acid (RHA) supplied by Carl Roth GmbH + Co KG (Germany), soil-extracted humic acid (SAHA) supplied by Sigma-Aldrich Co. (MO, USA) and RO-isolated Suwannee River NOM (SRNOM) supplied by the International Humic Substance Society (IHSS). In addition, a DOC-rich bog lake water sample taken from the ‘*Hohlohsee*’ (HSNOM) was selected. In this thesis, HSNOM is considered the most representative source for NOM of natural waters due to its availability in aqueous form and because it was not treated for isolation purposes. HSNOM contains humic and fulvic acids and has been comprehensively characterized by Frimmel and coworkers [23]. This chapter characterizes the different NOM sources with respect to their molecular size distributions and their colloidal content (Chapter 5.1), their spectral absorbance and fluorescent characteristics (Chapter 5.2) and their acidic functional group contents (Chapter 5.3).

### 5.1 Molecular Size Distribution

#### Size exclusion chromatography

Molecular size distributions were determined by size exclusion chromatography coupled with organic carbon and UV detection (LC-OCD-UVD) (Figure 5-1). According to the literature values of molecular weight (Table 2-1), elution time was shortest for SA ( $M_w = 200 - 2000$  kDa) followed by BSA ( $M_w = 67$  kDa) and humic substances ( $M_w$ : several hundred Da to a few hundred kDa). The nomenclature established by Huber et al. (2011) [218], characterizes SA and BSA as the biopolymer fraction of NOM. The remaining NOM sources eluted as humic substances and smaller molecules (building blocks and low molecular acids and neutrals). A clear order of average molecular size is obtained: SA > BSA >> RHA > SAHA > HSNOM > SRNOM. The larger average molecular size of coal- (RHA) and soil-extracted (SAHA) humic acids relative to the aquatic NOM sources (SRNOM and HSNOM) may be attributed to their different origin (terrestrial vs. aquatic). As summarized by Repeta et al. (2002), humic substances are unique products of the environments in which they are formed or transformed [174]. For example, it has been repeatedly shown that humic substances from terrestrial sources have higher molecular weights than those from marine origin [30,172–174].

It is important to note that the average molecular size of NOM molecules will likely increase at higher ionic strength and in the presence of bivalent cations, specifically calcium ions, due to cross-linkage of individual NOM molecules [175,177,180–182]. Although LC-OCD-UVD analysis of NOM in saline solution would better represent the effective molecular size in RO feed

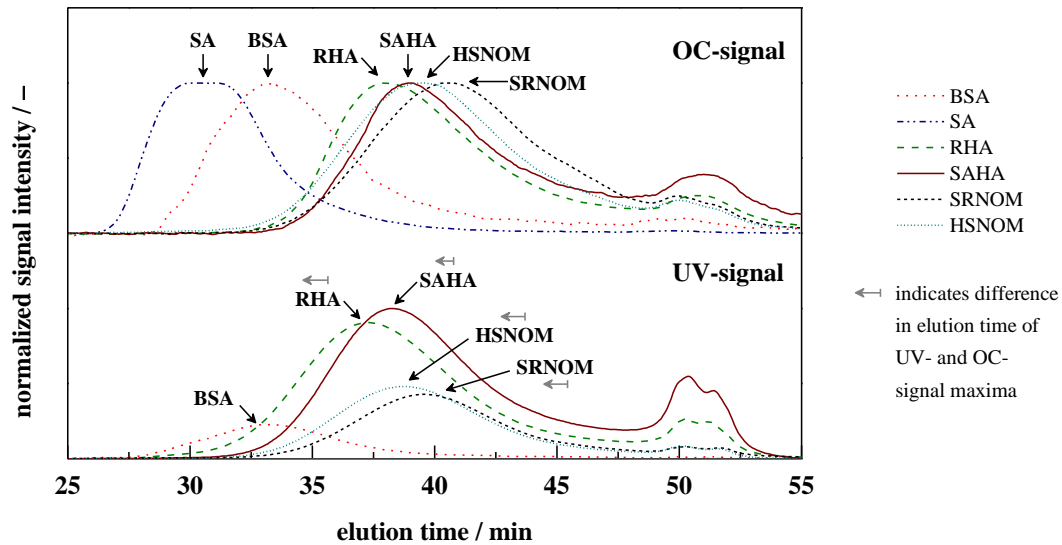


**Figure 5-1: LC-OCD-UVD chromatograms of the selected NOM samples.** All samples were diluted with ultrapure water to a DOC concentration of  $3.0 \text{ mg}\cdot\text{l}^{-1}$  as quantified by combustion catalytic oxidation after  $0.45 \mu\text{m}$  filtration and adjusted to  $\text{pH}=7.0$ . OC signal intensities were normalized by the sample maximum signal. UV signal intensities were multiplied by the corresponding normalization factor to display the relative differences in UV absorbance of the individual NOM samples.

waters, the LC-OCD-UVD method is only validated for fresh water analysis and would require advanced modification and validation for analysis of saline aqueous NOM samples [230].

Supplemental quantification results of LC-OCD-UVD chromatograms are summarized in Table D-2. Oxidation yields ( $\Phi_{UV}$ ), which are the ratios between the DOC concentration quantified from the LC column bypass signal and the DOC concentration quantified by combustion catalytic oxidation, are remarkably low for BSA ( $\Phi_{UV}=43.8\%$ ), SAHA ( $\Phi_{UV}=55.2\%$ ) and RHA ( $\Phi_{UV}=67.3\%$ ) (Table D-2a). They imply that the DOC of these NOM samples was incompletely oxidized within the UV oxidation vessel of the LC-OCD-UVD system ('Grüntzel' thin-film reactor). As reported by the manufacturer [218], oxidation yields are generally above  $\Phi_{UV}=90\%$  for most low and high molecular weight organic compounds. In contrast, Lankes et al. (2009) observed that up to about 70% of certain OC components of natural surface water samples are not detected by the LC-OCD system [231]. It is therefore concluded that BSA, SAHA and RHA molecules were incompletely oxidized given the limited hydraulic residence time of the sample inside the UV oxidation thin-film reactor and given the limited intensity of the UV irradiation.

Hydrophobic OC fractions ( $\Phi_{HOC}$ ), which are the %-fractions of the OC retained in the LC column by strong hydrophobic interactions [218] or sieving effects (i.e. rejection due to molecular sizes larger than the pore structure), were detected for BSA ( $\Phi_{HOC}=51.9\%$ ) and SAHA ( $\Phi_{HOC}=15.8\%$ ). It indicates that, in addition to the low oxidation yields, considerable DOC fractions of the BSA and SAHA samples were retained within the LC column.

### **Fractionation of humic substances by membrane filtration (UF/NF)**

Humic acids (RHA, SAHA) and aquatic NOM sources (SRNOM, HSNOM) were fractionated by membrane filtration (UF/NF) using membranes of different molecular weight cut-off\* ( $MWCO = 0.4 \text{ kDa} - 150 \text{ kDa}$ ). Filtrates were subsequently analyzed for DOC concentration (Figure 5-2), for spectral absorbance at  $\lambda = 254 \text{ nm}$  ( $SAC_{254}$ ) and  $\lambda = 436 \text{ nm}$  ( $SAC_{436}$ ) (Figure 5-2) and for molecular size distribution by LC-OCD-UVD analysis (Figure D-8). DOC rejections by membrane filtration at different  $MWCOs$  show that RHA and SAHA are characterized by significantly larger molecular size distributions as compared to HSNOM and SRNOM. For example, DOC rejections by 150 kDa ultrafiltration amounted to 52 % and 72 % for RHA and SAHA, whereas DOC rejection by 150 kDa UF of SRNOM and HSNOM was only 2 % and 5 %.

Overall, SRNOM is characterized by the smallest molecular size distribution with 63 % of the DOC passing the 1 kDa ultrafiltration membrane. This ranking of relative molecular sizes is supported by previous results of LC-OCD-UVD analyses.

Compared to DOC %-removal, spectral absorbance at  $\lambda = 254 \text{ nm}$  and  $\lambda = 436 \text{ nm}$  experienced higher %-removals by membrane filtration at defined  $MWCOs$ . This is likely related to the generally observed higher aromaticity of larger molecular weight humic substances [218,225,233]. Supplemental LC-OCD-UVD analyses of the filtrates confirm that DOC %-removal was greater for RHA and SAHA compared to HSNOM and SRNOM at defined  $MWCOs$  and that %-removal of UV absorbance ( $\lambda = 254 \text{ nm}$ ) was generally greater compared to DOC %-removal (Figure D-8).

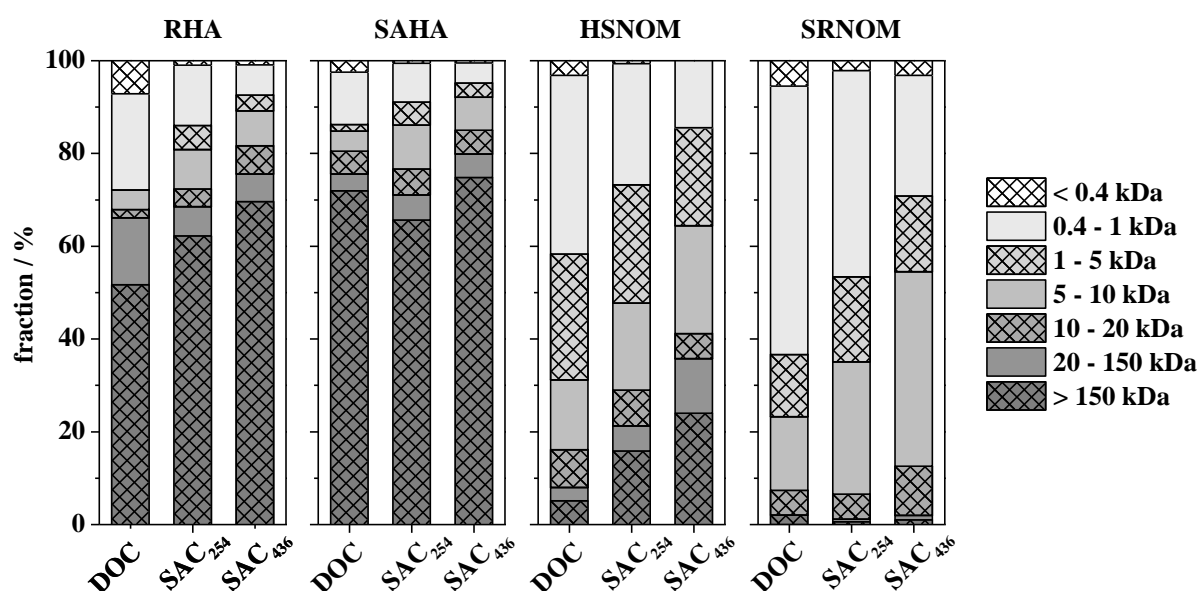


**Figure 5-2: Size distribution of organic bulk parameters ( $DOC$ ,  $SAC_{254}$  and  $SAC_{436}$ ) of the selected humic substances determined by fractionation using ultrafiltration and nanofiltration membranes with different molecular weight cutoffs (0.4 kDa – 150 kDa).**

\*  $MWCO$ : molecular weight of a molecule (e.g. a globular protein) that is rejected by 90% [232].

### Colloid concentration and colloidal size distribution

Colloid concentration ( $c$ ) (Figure 5-3a), mean colloid diameter ( $d_c$ ) (Figure 5-3b) and colloidal size distribution (Figure D-9) were determined by nanoparticle tracking analysis (NTA) from pre-filtered (0.45  $\mu\text{m}$ ) NOM samples diluted in either ultrapure water or 17  $\text{mmol}\cdot\text{l}^{-1}$   $\text{CaCl}_2$  solution. DOC-specific colloid concentrations were relatively small in SA, BSA and aquatic NOM samples ( $d_c \leq 0.27 \cdot 10^{11} \cdot \text{mg C}^{-1}$ , Figure 5-3a). Contrarily, colloid concentrations in RHA and particularly SAHA samples were more than a magnitude higher. Estimated minimal diameters\* of SA and BSA molecules are within a range of  $d_{\text{min}} = 5.4 - 16.6$  nm and considerably smaller than the NTA's lower limit of detection ( $d_{c,\text{min}} = 100$  nm). Given that humic substances are even smaller, as previously confirmed by size exclusion chromatography and membrane fractionation, detected colloids therefore represent molecular agglomerates rather than individual NOM molecules. Thus, RHA and SAHA stock solutions contained a large fraction of agglomerated humic acids of considerable size. This was previously indicated by the observed low oxidation yields ( $\Phi_{\text{UV}}$ ) of the LC-OCD-UVD analyses. The presence of calcium ions significantly increased the concentration of colloids in the SAHA sample ( $p < 0.05$ ). Apparently, humic acid molecules smaller than the method's detection limit agglomerated by calcium-ion bridging [175,177,180–182] and became accessible to detection.

Determined mean colloid diameters ( $d_c$ ) in Figure 5-3b have to be interpreted with care given the detected small colloid concentrations of all NOM samples except RHA and SAHA and given the

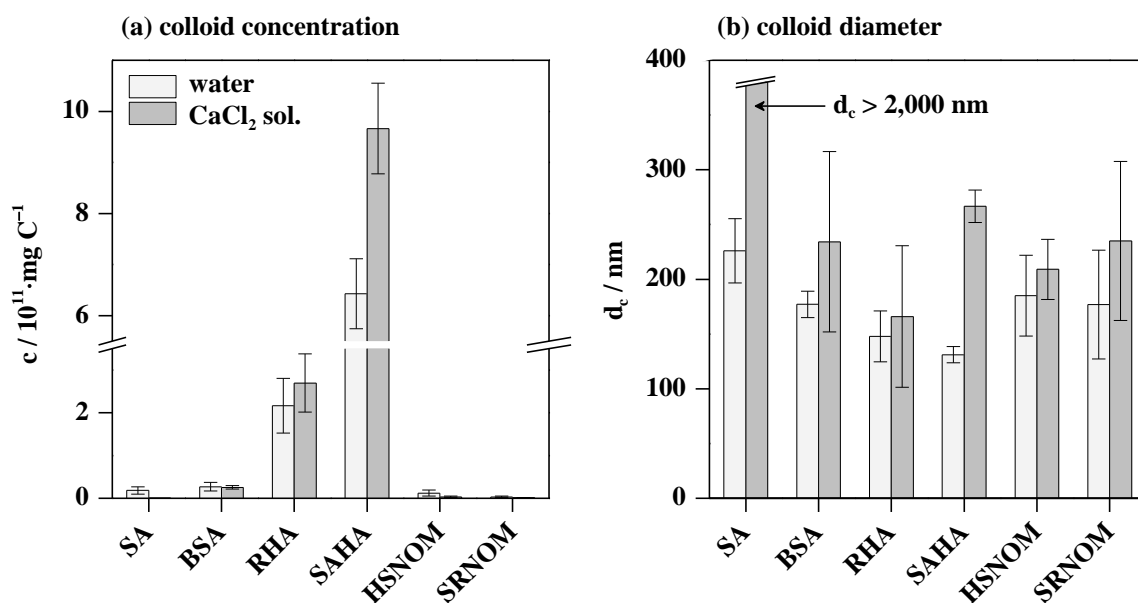


**Figure 5-3:** Nanoparticle tracking analysis (NTA) of NOM samples dissolved in ultrapure water and 17  $\text{mmol}\cdot\text{l}^{-1}$   $\text{CaCl}_2$  solution after 0.45  $\mu\text{m}$  pre-filtration at  $\text{pH} = 7.0$  ( $n = 4 - 5$ ,  $\pm 95\%$  confidence interval). (a) DOC-specific colloid concentration and (b) mean colloid diameter ( $d_c$ ).

\*  $d_{\text{min}} = 2 \cdot r_{\text{min}} = 2 \cdot 0.066 \cdot M_w^{1/3}$  with  $r_{\text{min}}$  being the minimal radius of a sphere that could contain the given mass of a protein [234].

underlying statistical uncertainty. A significant increase of mean colloid diameter ( $p < 0.05$ ) by calcium ion bridging was only observed for the SAHA and SA samples. The calcium ion bridging effect was most severe for SA, where final diameters of cross-linked agglomerates exceeded the NTA's upper detection limit of  $d_{c,max} = 2,000$  nm. SA, in particular, is known to form extensive cross-linked gel-like structures in the presence of calcium ions [175,181–184,200].

It is important to note that ultrafiltration with a *MWCO* of 150 kDa effectively eliminated any colloids detectable by NTA. Given the NTA method's detection limit, it is further important to remember that all NOM samples will contain colloidal NOM with diameters below  $d_{c,min} = 100$  nm.

## 5.2 Spectral Absorbance and Fluorescence Emission

### Spectral absorbance at $\lambda = 254$ nm and $\lambda = 436$ nm

Light absorption of NOM is assigned to the aromatic chromophores with conjugated C=C and C=O double bonds [166]. The typical yellow to brown color of humic substances, which is a result of light absorption, can be clearly seen in the photograph displayed in Figure D-10. It is also visible that the color intensity at identical DOC concentration is different among the four humic substance samples (Figure D-10). The visual appearance was confirmed by spectrophotometric analysis of DOC-specific spectral absorbance at  $\lambda = 254$  nm ( $SUVA_{254}$ ) and at  $\lambda = 436$  nm ( $SA_{436}$ ) (Table 5-1). Significantly higher values for  $SUVA_{254}$  and  $SA_{436}$  of coal- and soil-extracted humic acids (RHA and SAHA) indicate a higher aromaticity relative to the aquatic NOM samples (SRNOM and HSNOM). It has been shown that larger molecular weight humic substances generally exhibit a higher aromaticity and corresponding higher specific spectral absorbance [218,225,233]. In contrast to the humic substances, BSA exhibited only low  $SUVA_{254}$  while SA showed almost full light transmittance due to the lack of light absorbing chromophores [235] (Table 5-1).

Spectral UV absorbance at  $\lambda = 254$  nm was detected online during LC-OCD-UVD analyses (Figure 5-1). For the selected humic substances, maximal LC-UVD signal intensities were detected prior to maximal LC-OCD signal intensities (as indicated by arrows in Figure 5-1). Thus, larger humic substance molecules, which eluted first, exhibited higher UV absorbance and accordingly higher aromaticity. This was previously observed during membrane fractionation where  $SUVA_{254}$  and  $SA_{436}$  % rejections were higher compared to DOC % rejection at given *MWCO*.

**Table 5-1: DOC-specific spectral absorbance at  $\lambda = 254$  nm ( $SUVA_{254}$ ) and  $\lambda = 436$  nm ( $SA_{254}$ ) of the selected NOM sources diluted in ultrapure water to a DOC concentration of  $3.0 \text{ mg}\cdot\text{l}^{-1}$  and a *pH* of 7.0.**

		SA	BSA	RHA	SAHA	HSNOM	SRNOM
$SUVA_{254}$	$\text{l}\cdot\text{mg}^{-1}\cdot\text{m}^{-1}$	BDL	0.18	10.17	10.30	4.87	3.87
$SA_{436}$	$\text{l}\cdot\text{mg}^{-1}\cdot\text{m}^{-1}$	BDL	BDL	1.77	1.91	0.40	0.21

### **Fluorescence emission**

Fluorescence excitation emission matrices (FEEM) were obtained by fluorescence spectroscopy at a DOC concentration of 3.0 mg·l<sup>-1</sup> and a *pH* of 7.0 (Figure D-11). Except for alginate, which is not excited by UV and visible light [235], each NOM sample exhibits a distinct FEEM, also referred to as fluorescence fingerprint [22]. Positions and intensities of fluorescence peaks are summarized in Table 5-2. A single distinct peak is observed for BSA which is characteristic for tryptophan-like proteins [22,236,237]. Humic acids and aquatic NOM samples show a single, distinct peak of high intensity (referred to as ‘*primary peak*’) and a second, overlapping peak of lower intensity (referred to as ‘*secondary peak*’), which are characteristic for humic substances [22,236,237]. Higher overall fluorescence intensities are observed for RHA and SAHA relative to aquatic NOM (SRNOM, HSNOM) and originate from the higher DOC-specific spectral absorbance of larger humic acid samples and their higher aromaticity and higher content of fluorophores. Primary fluorescence peak excitation wavelengths are similar for all four humic substances ( $\lambda_{Ex} \approx 250$  nm) whereas corresponding ranges of emission wavelengths are broader and shifted towards larger wavelengths for RHA and SAHA indicating larger humic substances [238]. The secondary peak excitation and emission wavelengths are different for RHA and SAHA as compared to aquatic NOM. The difference in secondary peak position may indicate the different origin of the NOM (terrestrial vs. aquatic origin) and the abundance of fulvic acids in the HSNOM [23] and SRNOM [239] samples. Further structure-related interpretation is limited due to the limited understanding of relaxation mechanisms in complex aquatic systems [166] and due to the fact that typically less than 1 % of the aromatic moieties in NOM emit light as fluorophores [22,236].

**Table 5-2: Position and intensity of fluorescence peaks in the selected NOM sample’s excitation emission matrices. Samples were diluted in ultrapure water to a DOC of 3.0 mg·l<sup>-1</sup> and adjusted to *pH* = 7.0.**

		SA	BSA	RHA	SAHA	HSNOM	SRNOM
primary peak	$\lambda_{Ex}$ / nm	–	280	250	260	250	250
	$\lambda_{Em}$ / nm	–	335	480	525	455	455
	intensity / r.u.	–	40.0	13.1	23.0	7.1	10.9
secondary peak	$\lambda_{Ex}$ / nm	–	–	430	440	330	325
	$\lambda_{Em}$ / nm	–	–	520	525	455	450
	intensity / r.u.	–	–	3.4	7.8	3.9	6.5

### **5.3 Concentration of Acidic Functional Groups**

Direct base (NaOH) titration between *pH* = 3.0 – 10.0 was used to estimate the concentrations of acidic functional groups of the selected NOM sources (Figure D-12). The carboxylic acidity was quantified from the net NaOH consumption required to achieve a *pH* of 8.0, assuming that all carboxyl groups are titrated at *pH* = 8.0 [168,223,224]. Similarly, the phenolic acidity was quantified from two times the net NaOH consumption between *pH* = 8.0 – 10.0, assuming that one-

half of the phenolic hydroxyl groups are titrated by  $pH = 10.0$  [168,223,224]. The total acidity was calculated from the sum of carboxylic and phenolic acidities [168,223,224]. Determined acidities are summarized in Table 5-3 together with collected values from literature. BSA exhibited the lowest carboxylic and total acidities among the selected NOM sources. Highest carboxylic acidity was exhibited by SA while moderate carboxylic acidities were exhibited by the humic substances. Due to the considerable presence of phenolic hydroxyl groups, highest total acidities were determined for the soil- and coal-extracted humic acids SAHA and RHA.

As comprehensively reviewed by Santos et al. (1999) [240], comparison of titration results among different studies is limited due to the multiple sources of error, including hysteresis phenomena, which is the tendency for  $pH$  values to drift downward after additions of base titrant [168,240,241], and due to the inaccuracy of  $pH$  measurements at high  $pH$  values [240]. For example, reported carboxylic acidities of SRNOM are  $8.6 \text{ mmol}\cdot\text{g C}^{-1}$  [182] and  $11.2 \text{ mmol}\cdot\text{g C}^{-1}$  [242]. In addition, considerable differences of total acidities were reported for SA ( $10.9 \text{ mmol}\cdot\text{g C}^{-1}$  [187] and  $18.1 \text{ mmol}\cdot\text{g C}^{-1}$  [175]). Despite the observed variations in determined acidities, the determined acidities and the observed relative ranking of carboxylic acidities (BSA < humic substances < SA) are in general agreement with previous studies.

**Table 5-3: Summary of carboxylic, phenolic and total acidities of the selected NOM sources. (a) Values quantified by direct base titration performed with  $0.1 \text{ mol}\cdot\text{l}^{-1}$  NaOH from  $pH = 3.0$  to  $pH = 10.0$  in the background of  $0.1 \text{ mol}\cdot\text{l}^{-1}$  NaCl at a DOC concentration of  $19.15 \text{ mg}\cdot\text{l}^{-1}$  and at  $T = 22.2 \pm 0.6 \text{ }^\circ\text{C}$  ( $\pm$ SD). (b) Values collected from different literature sources.**

**(a) Quantification by direct base titration**

		SA	BSA	RHA	SAHA	SRNOM	HSNOM
carboxylic acidity	$\text{mmol}\cdot\text{g C}^{-1}$	8.5	3.4	5.6	5.6	5.9	5.3
phenolic acidity	$\text{mmol}\cdot\text{g C}^{-1}$	1.3	4.2	7.0	8.0	5.6	5.4
total acidity	$\text{mmol}\cdot\text{g C}^{-1}$	9.8	7.6	12.6	13.6	11.5	10.7

**(b) Literature values**

		SA	BSA	RHA	SAHA	SRNOM	HSNOM
carboxylic acidity	$\text{mmol}\cdot\text{g C}^{-1}$	9.7	3.4	–	8.3	8.6	–
		[187]	[187]	–	[185]	[182]	–
		–	–	–	8.5	11.2	–
phenolic acidity	$\text{mmol}\cdot\text{g C}^{-1}$	–	–	–	[25]	[242]	–
		1.2	0.5	–	6.3	3.2	–
		[187]	[187]	–	[185]	[182]	–
total acidity	$\text{mmol}\cdot\text{g C}^{-1}$	–	–	–	–	2.5	–
		–	–	–	–	[242]	–
		10.9	3.9	–	14.5	11.8	–
total acidity	$\text{mmol}\cdot\text{g C}^{-1}$	[187]	[187]	–	[185]	[182]	–
		18.1	3.6	–	–	13.7	–
		[175]	[186]	–	–	[242]	–



## 6 Effects of NOM on Gypsum Bulk Crystallization

This chapter investigates the effects of dissolved NOM on the kinetics of gypsum bulk crystallization from supersaturated aqueous solution. Using stirred beaker experiments, effects were assessed at gypsum bulk supersaturations of  $SI_{g,b} = 0.71$  and  $SI_{g,b} = 0.56$  at varying concentrations of the selected NOM sources ( $c_{NOM} = 0 - 12 \text{ mg C}\cdot\text{l}^{-1}$  at  $SI_{g,b} = 0.71$ ,  $c_{NOM} = 0 - 5 \text{ mg C}\cdot\text{l}^{-1}$  at  $SI_{g,b} = 0.56$ , Chapter 6.1) and at varying  $pH$  ( $pH = 4 - 10$ , Chapter 6.2). In addition, effects of NOM were compared to the effects induced by a polyacrylic and phosphonic acid-based antiscalant (Chapter 6.3). A complete list of conducted stirred beaker experiments including experimental conditions and complementary parameters can be found in Table C-1. The chapter concludes with an assessment of NOM effects on gypsum bulk crystallization during laboratory scale RO desalination and a subsequent discussion of transferability to beaker experiments (Chapter 6.4).

### 6.1 Effects of NOM Character and NOM Concentration

*Selected contents of this chapter have been published in collaboration with J. Rozova and M. Ernst: Separation and Purification Technology 198 (2018), 68–78.*

#### Effects of NOM on induction time of gypsum bulk crystallization

Figure 6-1 shows induction times ( $\tau$ ) for gypsum bulk crystallization from supersaturated solution at  $SI_{g,b} = 0.71$  (Figure 6-1a) and  $SI_{g,b} = 0.51$  (Figure 6-1b) in the presence of varying NOM concentrations as relative values compared to the respective values of reference experiments in the absence of NOM. At both supersaturations, prolonged induction times were observed in the presence of dissolved NOM. In addition, the degree of retardation enhanced with increasing NOM concentration. However, significant differences regarding the relative retardation capability of the selected NOM sources were observed. Weakest retardation was consistently observed in the presence of bovine serum albumin (BSA,  $SI_{g,b} = 0.71$  and  $0.56$ ) whereas strongest retardations were observed in the presence of sodium alginate (SA,  $SI_{g,b} = 0.71$ ) and the ‘Hohlohsee’ aquatic humic substances (HSNOM,  $SI_{g,b} = 0.56$ ).

It is important to recognize that determined induction times in repeated experiments varied considerably. This limited reproducibility is attributed to the manifold influences on the process of bulk crystallization, such as (i) the presence of dust particles, (ii) slight differences in local hydrodynamics or (iii) minor temperature variations, and the resulting difficulty of reliable induction times measurements [65,67,90]. Given the considerable data scatter, it is difficult to obtain a general ranking of the retardation capability exhibited by the different NOM sources. Except for BSA, which induced weakest retardation, the retardation capabilities of the remaining NOM sources have to be rated comparable given the experienced data scatter.

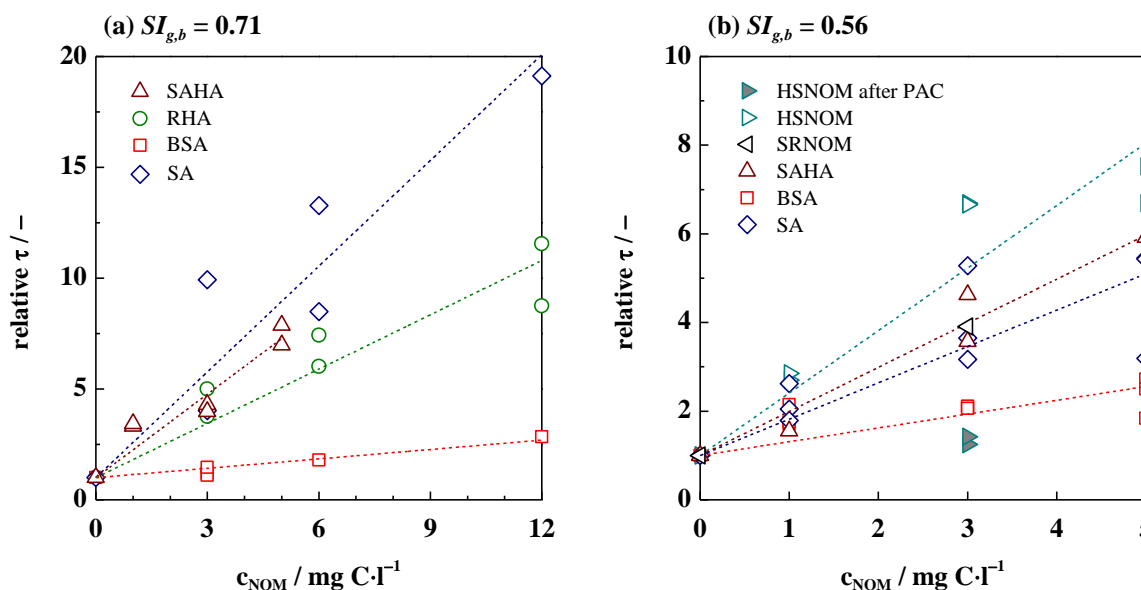


**Figure 6-1: Relative induction times ( $\tau$ ) of gypsum bulk crystallization obtained from stirred beaker experiments at (a)  $SI_{g,b} = 0.71$  and (b)  $SI_{g,b} = 0.56$  in the presence of NOM at varying concentrations. ‘*HSNOM after PAC*’ was previously treated by powdered activated carbon to remove NOM by adsorption (Chapter 3.1.1). Experimental conditions:  $T = 25.0 \pm 0.1$  °C ( $\pm$  SD),  $pH = 6.8 \pm 0.2$  ( $\pm$  SD).**

### Mechanisms of retarded gypsum crystal nucleation

XRD analyses of solid phases collected from the experiments performed in the presence of 3 mg C·l<sup>-1</sup> NOM at  $SI_{g,b} = 0.56$  confirmed that gypsum was the only detectable crystalline phase (Figure D-13). It was also shown that induction times of gypsum bulk crystallization in the presence of the inorganic (Table 3-3) and non-adsorbable NOM fraction (1.4 % of the total DOC) of HSNOM (‘*HSNOM after PAC*’, see Chapter 3.1.1) remained unaffected relative to the reference experiments. This clearly demonstrates that the adsorbable NOM fraction (98.6 % of the total DOC) of the HSNOM sample rather than any inorganic background impurities induce the retarding effect.

As the underlying mechanisms of retardation, (i) complexation of calcium ions through carboxylic acid moieties of the NOM molecules [176–179] and a resulting reduction of solution supersaturation and (ii) adsorption of NOM molecules onto subcritical gypsum nuclei [32,33,190] have to be considered. The relevance of the former mechanism (i) is theoretically assessed by the following considerations. Strongest retardation of gypsum nucleation was observed in the presence of 12 mg C·l<sup>-1</sup> SA at a supersaturation of  $SI_{g,b} = 0.71$  (Figure 6-1a). Total acidity of SA was previously determined to be 9.8 mmol·g C<sup>-1</sup>, (Table 5-3a). Assuming that two acidic groups can stoichiometrically complex one calcium ion, a maximal concentration of 58.8  $\mu$ mol·l<sup>-1</sup> calcium ions can be theoretically complexed in the presence of 12 mg C·l<sup>-1</sup> SA. Given the considerably higher bulk concentration of calcium ions ( $c_b = 68 \cdot 10^3$   $\mu$ mol·l<sup>-1</sup>), this would only reduce the free calcium ion concentration by less than 0.1 %. In turn, a reduction of supersaturation from originally  $SI_{g,b} = 0.71$  to  $SI_{g,b} = 0.42$  would be required to achieve the observed retardation according to the

previously determined relationship between the induction time ( $\tau$ ) of gypsum bulk crystallization and gypsum supersaturation ratio ( $S_{g,b}$ ) (Figure 4-5). Therefore, it can be concluded that calcium ion complexation by NOM molecules and the resulting reduction of gypsum supersaturation and gypsum nucleation rate is negligible. Accordingly, the latter mechanism (ii) of NOM adsorption onto subcritical nuclei has to be considered as the underlying mechanism of retardation. This mechanism is commonly described as the ‘*threshold effect*’ [55,101,112,114] and suggests that organic molecules adsorb onto subcritical nuclei and decelerate their growth beyond the critical size [55,101]. Alternatively, selective heteronucleation on the NOM molecules could lead the formation of slow-growing metastable nanoparticles which decelerates the formation of stable nuclei and enhances the observed induction time [112,114]. Retardation of gypsum nucleation by NOM has been previously observed and was attributed to NOM adsorption onto crystal faces given that the observed size or habit of subsequently developed gypsum crystals was modified [32,33,190]. In order to confirm if gypsum bulk crystallization was affected by adsorption of NOM onto crystal faces, crystal growth beyond the induction time is important to consider and will be investigated in the following section.

### Effects of NOM on crystallization time, turbidity increase and crystal growth

Crystallization times ( $\Delta t$ ), which were defined as the time elapsed between the induction time and the achievement of a solution turbidity of  $\kappa = 200$  FNU, are presented in Figure 6-2. A clear extension of gypsum crystallization time was observed in the presence of all NOM sources. Again, retardation clearly enhanced with increasing NOM concentration and the degree of retardation was

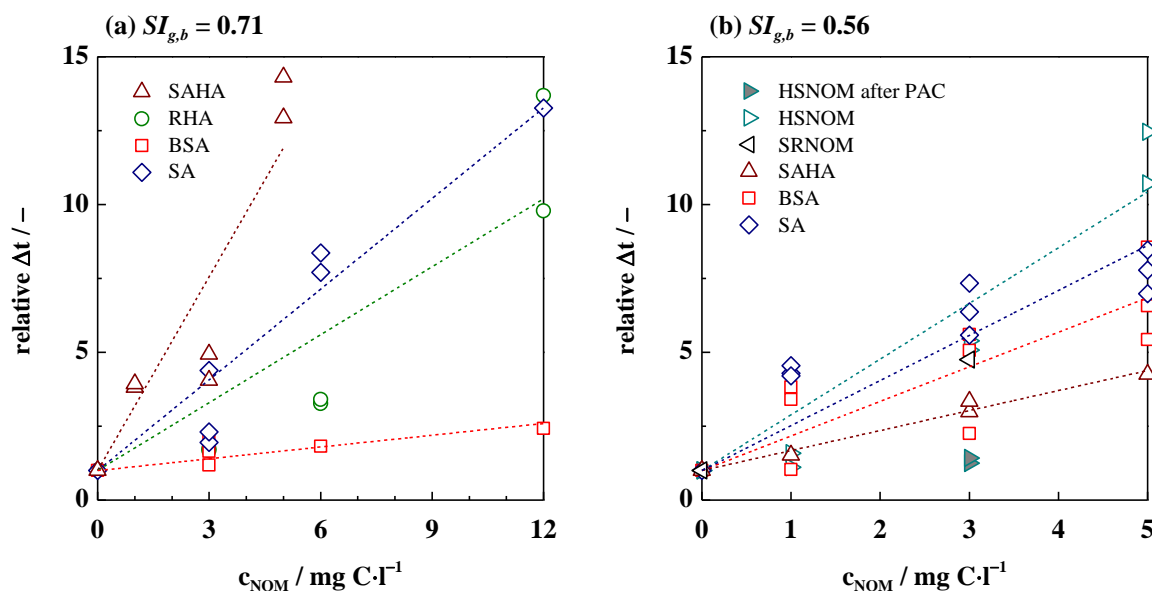


**Figure 6-2:** Relative crystallization times ( $\Delta t$ ) of gypsum bulk crystallization obtained from stirred beaker experiments at (a)  $SI_{g,b} = 0.71$  and (b)  $SI_{g,b} = 0.56$  in the presence of NOM at varying concentrations. ‘*HSNOM after PAC*’ was previously treated by powdered activated carbon to remove NOM by adsorption (Chapter 3.1.1). Experimental conditions:  $T = 25.0 \pm 0.1$  °C ( $\pm$  SD),  $pH = 6.8 \pm 0.2$  ( $\pm$  SD).

depending on the NOM source. These observations are also evident from comparison of fitted rate constants of turbidity increase  $\lambda_t$  (Table C-1), which show that the rate of turbidity increase was significantly reduced in the presence of all NOM sources. It is important to recognize that the relative ranking among the retardation capabilities of the different NOM sources changed with supersaturation. For example, BSA was least efficient at  $SI_{g,b} = 0.71$  but competitive to the remaining NOM sources at  $SI_{g,b} = 0.56$ . Further, retardation by SAHA was strong at  $SI_{g,b} = 0.71$  but considerably low at  $SI_{g,b} = 0.56$ . The different retardation capabilities at different supersaturations imply that the rate of turbidity increase and the associated rate of crystal growth, which enhance at higher supersaturation, affect the NOM-crystal-interaction. Assuming that NOM adsorption is the underlying mechanism of retardation, the time which is required for NOM molecules to diffuse from the bulk solution towards the crystal-solution interface and to adsorb onto the crystal surface may become limited at increasing supersaturations. In turn, this would affect the retardation capabilities at different supersaturations of different NOM sources with different diffusional properties. Given the experienced data scatter and the manifold influences on gypsum bulk crystallization, an overall ranking of the retardation capabilities of the different NOM sources with general validity cannot be made.

#### **Mechanisms of retarded crystallization time, turbidity increase and crystal growth**

Extended crystallization times (Figure 6-2) and decreased rate constants of turbidity increase ( $\lambda_t$ , Table C-1) in the presence of NOM indicate that nucleation and growth of gypsum crystals are decelerated in the presence of NOM. Reduced gypsum crystal growth in the presence of NOM was previously observed and attributed to NOM adsorption onto actively growing gypsum crystal faces [32,37,38]. This effect, known as '*crystal distortion*' [16,101,112,113,190], was previously shown to affect crystal size and habit in seeded gypsum crystal growth experiments due to NOM adsorption [32,37,190].

Crystal habit and size were assessed by light microscopy of crystal suspensions sampled from stirred beaker experiments conducted at gypsum supersaturation of  $SI_{g,b} = 0.71$  and in the presence of 12 mg C·l<sup>-1</sup> RHA, BSA and SA (Figure D-14a – d). The micrographs show that the platelet- and partially rosette-like crystals of the reference experiment became disturbed and that the mean crystal size decreased in the presence of NOM. Quantification of DOC concentrations at the beginning ( $\kappa = 0$  FNU) and end ( $\kappa \approx 1,000$  FNU) of the crystallization experiments conducted at gypsum supersaturation of  $SI_{g,b} = 0.71$  in the presence of RHA, BSA and SA ( $c_{NOM} = 3$  mg C·l<sup>-1</sup>, 6 mg C·l<sup>-1</sup> and 12 mg C·l<sup>-1</sup>) confirmed considerable removals of DOC during bulk crystallization (Table 6-1). The consistent DOC-removal in all nine experiments support the assumption that NOM adsorption and incorporation was the relevant mechanism of crystal growth distortion.

For selected experiments performed at  $SI_{g,b} = 0.56$  and in the presence of SAHA, HSNOM, BSA and SA ( $c_{NOM} = 3$  mg C·l<sup>-1</sup> and 5 mg C·l<sup>-1</sup>), samples of crystal suspension were taken from the stirred beaker at a solution turbidity of  $\kappa = 200$  FNU and analyzed by LOT measurement for crystal

**Table 6-1: DOC removal as absolute values during select stirred beaker experiments in the presence of varying NOM concentrations. Samples were taken at the beginning ( $\kappa = 0$  FNU) and end of an experiment ( $\kappa \approx 1,000$  FNU) and immediately filtered by  $0.45 \mu\text{m}$ . Experimental conditions:  $SI_{g,b} = 0.71$ ,  $T = 25.0^\circ\text{C}$ ,  $pH = 7.0$ .**

$c_{NOM,0} / \text{mg C}\cdot\text{l}^{-1}$	absolute DOC removal / mg		
	RHA	BSA	SA
3	0.41	1.29	0.69
6	0.44	2.20	0.94
12	0.95	2.41	1.65

concentration ( $c$ ) and mean crystal diameter ( $d_p$ ). Given that samples were analyzed at constant turbidity, decreased mean crystal diameters should coincide with higher crystal concentrations and vice versa given that turbidity depends on both, size and concentration of suspended particles and colloids [228]. Decreased crystal diameters associated with increased crystal concentrations were observed in the presence of the two employed humic substances, i.e. terrestrial humic acid (SAHA) and the aquatic ‘Hohlohsee’ NOM (HSNOM) at  $3 \text{ mg C}\cdot\text{l}^{-1}$  and  $5 \text{ mg C}\cdot\text{l}^{-1}$  (Figure 6-3a). It supports the assumption of NOM adsorption as a mechanism of retardation leading to reduced rates of crystal growth with resulting smaller mean crystal diameters at given solution turbidity.

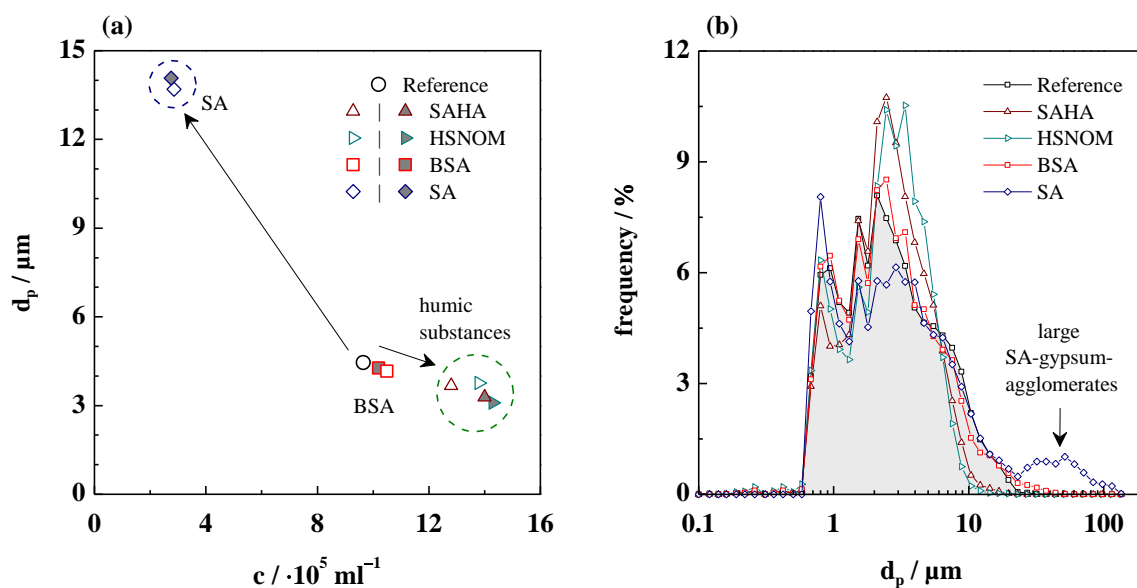


**Figure 6-3: (a) Mean crystal diameter ( $d_p$ ) and crystal concentration ( $c$ ) determined by LOT measurement of crystal suspensions taken from stirred beaker experiments at a solution turbidity of  $\kappa = 200$  FNU in the absence (‘Reference’) and presence of NOM (open symbols:  $3 \text{ mg C}\cdot\text{l}^{-1}$ , solid grey symbols:  $5 \text{ mg C}\cdot\text{l}^{-1}$ ). (b) Corresponding crystal size distribution (number distribution) in the presence of  $5 \text{ mg C}\cdot\text{l}^{-1}$  NOM. The area below the reference curve is shaded grey. Experimental conditions:  $SI_{g,b} = 0.56$ ,  $T = 25.0 \pm 0.1^\circ\text{C}$  ( $\pm$ SD),  $pH = 6.8 \pm 0.2$  ( $\pm$ SD).**

Marginal effects on crystal diameter and concentration were observed in the presence of BSA (Figure 6-3a), which supports the previously observed weak retardations of induction time and crystallization time by BSA. Contrarily, in the presence of SA, increased crystal diameters associated with decreased crystal concentrations were detected by LOT measurements. The corresponding crystal size distribution in the presence of  $5 \text{ mg C}^{-1}$  SA (Figure 6-3b) shows an additional distinct peak with mean crystal diameters in the range of  $d_p = 30 - 150 \mu\text{m}$ , whereas gypsum crystallization in the absence of NOM (*Reference*) and in the presence of the remaining investigated NOM sources only resulted in a single broad peak with diameters smaller than  $30 \mu\text{m}$ . It indicates that gypsum crystals in the presence of SA formed large agglomerates due to cross-linkage by SA molecules, which was further confirmed by scanning electron microscopy of crystal suspensions (Figure 6-4). Additionally, the SEM images in Figure 6-4 show that the sizes of individual gypsum crystals of the SA-gypsum-agglomerate (Figure 6-4c, d) were in fact significantly smaller compared to the reference (Figure 6-4a, b) which confirms crystal growth distortion in the presence of SA. It is well described in literature that SA has great affinity to calcium ions which can lead to the formation of extensive gel-like structures through calcium ion bringing [175,181,183,184]. This phenomenon was previously observed during NTA measurements of SA in the absence and presence of calcium ions (Figure 5-3). Here, it is clearly shown that alginate is also capable of cross-linking gypsum crystals presumably due to cross-linkage of calcium ions on the gypsum crystal surface.

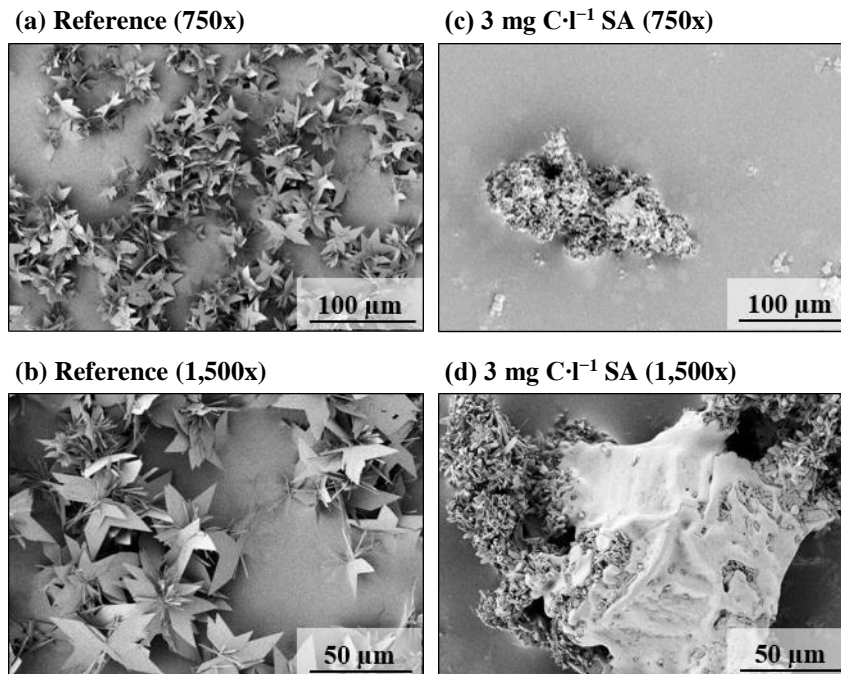


**Figure 6-4:** Scanning electron micrographs of gypsum crystals developed in the (a) absence of NOM (*Reference*) and (b) presence of  $3 \text{ mg C}^{-1}$  SA. Samples were taken from the stirred beaker at the end of the experiment. Experimental conditions:  $SI_{g,b} = 0.56$ ,  $T = 25.0 \text{ }^\circ\text{C}$ ,  $pH = 7.0$ .

As indicated by Figure 6-3a, deceleration of crystal growth in the presence of NOM is supported by rate constants of crystal growth ( $\lambda_G$ ) fitted from the temporal evolution of the mean crystal diameter (Table 6-2), which decreased in the presence of NOM. However, determined values have to be regarded with care as crystal agglomeration by NOM (e.g. in the presence of SA) restricts their accuracy.

**Table 6-2: Rate constants of crystal growth ( $\lambda_G$ ) of gypsum bulk crystallization in the presence of selected NOM sources. Values for  $\lambda_G$  were obtained from the temporal evolution of the mean crystal diameter (LOT measurements analogue to the procedure described in Chapter 4.2) during stirred beaker experiments at  $SI_{g,b} = 0.51$ . A complete list including supplemental experimental conditions and Pearson correlation coefficients can be found in Table D-3.**

$c_{NOM,0} / \text{mg C}\cdot\text{l}^{-1}$	$\lambda_G / \cdot 10^{-3} \text{ s}^{-1}$				
	Reference	HSNOM	SAHA	BSA	SA
0	1.72	–	–	–	–
3	–	0.26	0.56	1.14	0.71
5	–	0.09	0.37	1.29	0.44

### **Summary and discussion**

Induction ( $\tau$ ) and crystallization time ( $\Delta t$ ) of gypsum bulk crystallization from supersaturated solution ( $SI_{g,b} = 0.56$  and  $SI_{g,b} = 0.71$ ) were significantly prolonged in the presence of all NOM sources. A clear NOM concentration-retardation relationship was observed, with enhanced retardation of both parameters,  $\tau$  and  $\Delta t$ , at increased NOM concentration ( $c_{NOM} = 0 - 12 \text{ mg C}\cdot\text{l}^{-1}$ ). Microscopic analyses of suspended crystals, DOC depletion during the crystallization experiments and quantification of crystal concentration and mean crystal diameter by LOT measurements confirmed that regular crystal growth was distorted in the presence of dissolved NOM, which resulted in decelerated crystal growth and smaller mean crystal diameters. It is therefore concluded that the adsorption and incorporation of NOM on and into developing gypsum crystals was the underlying mechanism of distorted and retarded crystal growth (*'crystal distortion effect'*). Accordingly, it is concluded that NOM adsorption onto subcritical nuclei was the relevant mechanism that delayed the development of stable nuclei and thereby extended the observed induction times in the presence of NOM (*'threshold effect'*).

Due to the relatively large variations of determined induction and crystallization times in repeated experiments and the different NOM-specific retardation capabilities at different supersaturations, a generally valid ranking of NOM-specific retardation capability could not be identified. However, the following trends were observed and may be linked to the respective NOM properties:

- (i) Weakest retardation of gypsum bulk crystal nucleation was consistently observed in the presence of BSA. BSA was previously shown to have the lowest carboxylic and total acidities among the investigated NOM sources (Table 5-3). The carboxylic acidity of organic

polyelectrolytes was repeatedly reported to be responsible for the retarding effect on bulk crystallization of sparingly soluble salts [32,33,55,116,117]. In addition, BSA has a globular heart-shaped structure at neutral  $pH$  [187,243] whereas the remaining NOM sources are characterized by rather linear configurations. In previous studies, BSA's globular configuration was assumed to sterically interfere with the complexation of calcium ions [42].

- (ii) Strong retardation of gypsum bulk crystal nucleation and growth was repeatedly observed for sodium alginate. The strong affinity of SA towards calcium ions due to its high carboxylic acidity (Table 5-3) is well described in literature [175,181,183,184] and was previously confirmed by NTA measurements (Figure 5-3). By LOT measurements and SEM analyses, it was shown that individual gypsum crystals exhibited smaller sizes and distorted habits in the presence of SA. The observed formation of larger gypsum-SA-agglomerates indicates that SA has a high affinity not only for aqueous calcium ions but also for calcium ions on the gypsum crystal surface. Similarly, Hoch et al. (2000) suggested that deprotonated carboxyl groups which have a high affinity for aqueous calcium ions should have an affinity for calcium ions on calcite crystal surfaces [35]. The SA molecule is further characterized by an aliphatic, linear configuration and a large molecular size which may enable adsorption onto more than one growth site on a crystal surface [244]. The above characteristics may explain the superior retardation capability of SA.
- (iii) No clear and generally valid ranking between the terrestrial humic acids (RHA, SAHA) and the aquatic NOM sources (SRNOM, HSNOM) could be made. NOM characterization in Chapter 5 showed that carboxylic acidities were similar for all humic substances despite significant differences in size, colloid content, aromaticity and fluorescent character. The manifold differences in characteristics make it unfeasible to relate the determined humic substance properties to their retardation capability.

Previous studies have tried to determine relationships between NOM chemistry and retardation capability and have delivered interesting but inconsistent results. Bock (2017) showed that fulvic acids exhibited a superior retardation effect on gypsum crystallization compared to larger, less aromatic and less acidic humic acids [33]. Enhanced retardation of gypsum crystal growth with increasing molecular weight of different amino acids was observed by Hamdona et al. (2008) [32]. Retardation of calcite crystallization was repeatedly observed to increase with higher NOM aromaticity [34,245,246]. Similarly, Hoch et al. (2000) studied calcite growth in the presence of isolated aquatic NOM and showed greater retardation at higher NOM molecular weight and higher aromaticity [35]. Interestingly, the authors observed that the carboxylic acidity of the NOM related least systematically to the growth rate reduction [35]. This is in contrast to the fact that the inhibitory effect of commercial antiscalants increases with the density of acidic functional groups [32,55,116,117]. However, it was also shown that the affinity for calcium ions alone does not make a molecule with a high density of carboxyl groups a strong sorbent on a crystal surface [190]. For example, ethylenediaminetetraacetic acid (EDTA) is a very strong complexing agent with aqueous

calcium ions but a poor inhibitor of gypsum [190] and aragonite ( $\text{CaCO}_3$ ) [247] growth. It implies that the stereochemical character and the molecular size of organic compounds and NOM molecules are critical parameters that determine the inhibitory effect. For calcite growth this was concluded in a number of previous studies [247–249]. From the above findings and the effects observed in this thesis, it is reasonable to assume that the retardation capability of NOM cannot be limited to a single NOM property, such as the carboxylic acidity, the molecular weight or the aromaticity but is determined by a combination of the relevant characteristics.

## 6.2 Effects of $pH$ on Gypsum Bulk Crystallization in the Presence of NOM

Effects of  $pH$  variation ( $pH \approx 4, 7$  and  $10$ ) on the retardation capability of selected NOM sources (BSA, SA, SAHA and HSNOM) were investigated at a gypsum supersaturation of  $SI_{g,b} = 0.56$  and a dissolved NOM concentration of  $c_{NOM} = 3 \text{ mg C}\cdot\text{l}^{-1}$  (Figure 6-5). Strongest effects of  $pH$  were observed in the presence of HSNOM, where relative induction time increased from  $\tau_{rel} = 1.5$  at  $pH = 4.0$  to  $\tau_{rel} = 12.1$  at  $pH = 9.5$ . Similarly, relative crystallization time increased from  $\Delta t_{rel} = 1.1$  at  $pH = 4.0$  to  $\Delta t_{rel} = 16.6$  at  $pH = 9.5$ . A clear enhancement of retardation was also observed in the presence of SAHA, however, the effect was significantly less pronounced compared to HSNOM. Relatively marginal and insignificant effects of  $pH$  were observed in the presence of BSA and SA, respectively. Complementary rate constants for crystal growth ( $\lambda_G$ ) determined from LOT measurement can be found in Table D-3 and show enhanced retardation of crystal growth particularly for HSNOM and SAHA with increasing  $pH$ .

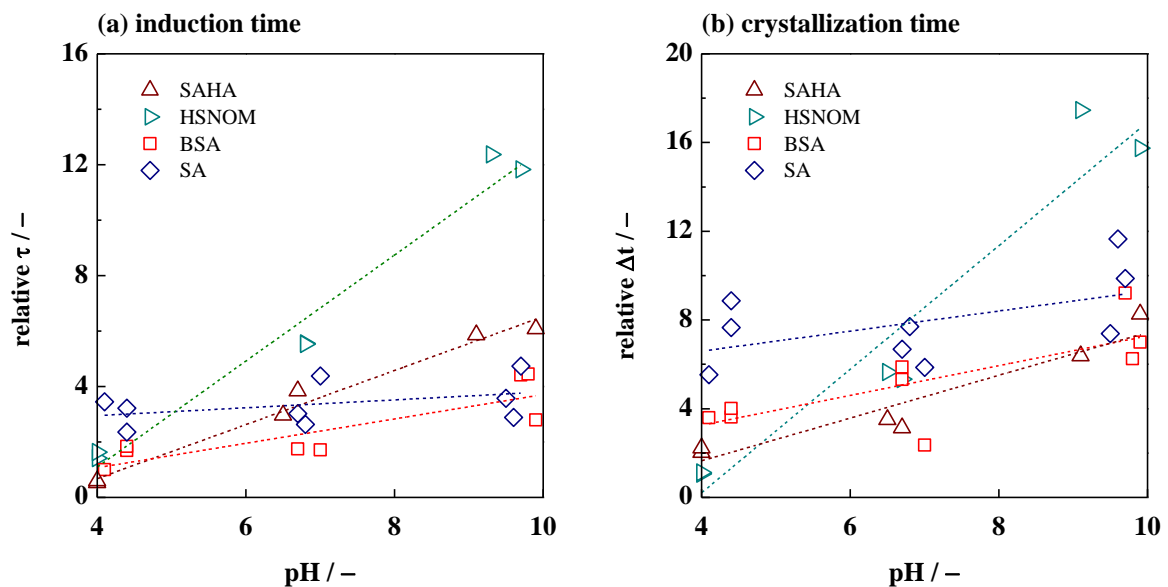


Figure 6-5: Effects of  $pH$  on (a) relative induction times ( $\tau_{rel}$ ) and (b) relative crystallization times ( $\Delta t_{rel}$ ) of gypsum bulk crystallization obtained from stirred beaker experiments at  $SI_{g,b} = 0.56$ ,  $T = 25.0 \pm 0.1 \text{ }^\circ\text{C}$  ( $\pm$  SD) and  $3 \text{ mg C}\cdot\text{l}^{-1}$  NOM. Prior to calculation of relative values ( $\tau_{rel}$  and  $\Delta t_{rel}$ ), absolute values of  $\tau$  and  $\Delta t$  obtained at  $pH \approx 10$  were corrected for the previously observed higher values during reference experiments at  $pH \approx 10$  (Chapter 4.2 and Figure 4-9).

A limited number of previous studies investigated the effects of  $pH$  on the retardation capability of humic substances [33,37] and polymeric antiscalants [55,250] and observed enhanced retardation of gypsum crystallization at increased  $pH$ . In all cases, the observed enhancement was attributed to the increased deprotonation of acidic functional groups and the resulting increased charge density of the organic molecules which enhanced their affinity for calcium ions [33,37,55,250]. The dissociation behavior of humic substances is a multi-step mechanism due to the complex molecular structure, the different acidic functional groups and the according distribution of dissociation constants ( $pK_a$ ) of acidic moieties [251]. Thus, deprotonation and charge density of HSNOM and SAHA molecules are expected to continuously increase with increasing  $pH$  over the studied range of  $pH = 4 - 10$ . This assumption is supported by titration data (Figure D-12), which showed increasing deprotonation of acidic functional groups with increasing  $pH$  and quantified significant contents of phenolic hydroxyl groups by titration between  $pH = 8$  and  $pH = 10$  (Table 5-3). However, retardation at  $pH = 10$  was significantly lower for SAHA compared to HSNOM, despite comparable carboxylic acidity and higher total acidity of SAHA (Table 5-3). It indicates that other molecular properties, in addition to the content of acidic functional groups, determine the effective retardation capability of NOM. This assumption is further supported by the fact that retardation by BSA and SA were comparable at  $pH = 10$ , despite lower carboxylic and total acidities of BSA (Table 5-3). For humic substances it is known that the coiled and globular configuration at low  $pH$  changes to a more flexible and linear configuration at increased  $pH$  [171]. Similarly,  $pH$ -induced structural transitions and a looser configuration were also reported for BSA at higher  $pH$  [252]. It emphasizes that the stereochemical properties and the molecular size of an organic compound together with the acidities, rather than the carboxylic or total acidities by themselves, determine the retardation capabilities. For both, humic substances and BSA,  $pH$ -induced stereochemical changes may enhance the interaction of acidic moieties of the molecules with aqueous calcium ions and calcium ions on crystal surfaces. For example, molecular configurations with enhanced linearity or looser structure can be capable of adsorbing to more than one growth site on a crystal surface [244] and thereby enhance the retardation capability.

In contrast to humic substances and BSA, SA only contains carboxylic groups and is an aliphatic, linear molecule. SA has a reported  $pK_a$  value of 3.4 – 4.4 [253] and showed little increase of acidity by titration between  $pH = 8$  and  $pH = 10$  (Table 5-3). It explains the comparable retardation capability of SA at  $pH = 7$  and  $pH = 10$ . Interestingly, retardation by SA was also comparable at  $pH = 4$  (Figure 6-5), where a larger fraction of the carboxylic groups should be protonated. Consequently, the increased acidity at higher  $pH$  values did not enhance the retardation capability of SA, which may be linked to the linear configuration and the inherently strong calcium ion affinity. Kuntze (1966) studied the effects of aliphatic polycarboxylic acids on gypsum growth and found that the arrangement of carboxylic groups in the aliphatic chain rather than the total carboxylic acidity determined the optimal inhibition behavior [248].

Concluding, variation of solution  $pH$  indicated that both, the content of deprotonated acidic functional groups and the stereochemical properties of the selected NOM sources are relevant molecular properties that determine the retardation capability. It supports the previously drawn conclusion (Chapter 6.1) that the retardation capability of different NOM sources cannot be limited to a single molecular property but is affected by a set of molecular properties that determine the effective retardation capability at given experimental conditions.

### 6.3 Comparison of NOM Effects to Antiscalant Dosage

A series of gypsum bulk crystallization experiments ( $SI_{g,b} = 0.71$ ) was conducted in the presence of a commercial polymeric antiscalant (polyacrylic and phosphonic acid-based) in order to compare the retardation capability of antiscalant and NOM. Relative induction ( $\tau_{rel}$ ) and crystallization times ( $\Delta t_{rel}$ ) in Table 6-3 show enhanced retardation capabilities, i.e. enhanced ‘*threshold inhibition*’ and ‘*growth distortion*’ at increased antiscalant dosage as would be expected from previous studies [32,76,116,118–120]. In addition, the micrograph in Figure D-14e displays significantly smaller gypsum crystals in the presence of the antiscalant. Compared to the retardation capabilities of NOM (Figure 6-1 and Figure 6-2), the antiscalant showed significantly higher efficiencies with  $\tau_{rel}$  and  $\Delta t_{rel}$  being magnitudes higher. For example, strongest retardation at  $SI_{g,b} = 0.71$ , neutral  $pH$  and  $c_{NOM} = 3 \text{ mg C}\cdot\text{l}^{-1}$  was previously observed in the presence of SA with an estimated relative induction time  $\tau_{rel} = 5.9$  according to the linear fit in Figure 6-1a. Retardation by the antiscalant at equivalent carbon concentration was more than 27-fold higher.

**Table 6-3: Relative induction ( $\tau_{rel}$ ) and crystallization ( $\Delta t_{rel}$ ) times of gypsum bulk crystallization from supersaturated solution ( $SI_{g,b} = 0.71$ ,  $T = 25.0 \pm 0.2 \text{ }^\circ\text{C}$  ( $\pm \text{SD}$ ),  $pH = 6.8 \pm 0.3$  ( $\pm \text{SD}$ ) in the presence of antiscalant at varying dosage ( $c_{AS} = 1.5 - 12 \text{ mg}\cdot\text{l}^{-1}$ ).**

$c_{AS} / \text{mg}\cdot\text{l}^{-1}$	1.5	3.0	12
$c_{AS} / \text{mg C}\cdot\text{l}^{-1}$	0.4	0.8	3.0
$\tau_{rel} / -$	18.8	45.3	162.7
$\Delta t_{rel} / -$	7.8	19.0	57.1

The following considerations may explain the superior retardation capability of the employed antiscalant. (i) Molecular weights of polymeric antiscalants are typically around 1 kDa to 5 kDa [55,115–117]. Therefore, molar concentration at equivalent carbon mass concentration is expected to be significantly higher for the antiscalant resulting in a significantly higher number of molecules compared to NOM. (ii) The smaller molecular size of the antiscalant molecules will result in higher diffusion constants and higher mobility in the water phase [254] which may enhance adsorption rates onto crystal phases [55]. (iii) The antiscalant molecules are expected to exhibit higher carboxylic acidities compared to the studied NOM sources. For example, the theoretical carboxylic acidity of polyacrylic acid ( $28 \text{ mmol}\cdot\text{g C}^{-1}$ ) is more than 2-fold higher than those determined for the studied NOM sources ( $\leq 13.6 \text{ mmol}\cdot\text{g C}^{-1}$ , Table 5-3). In addition, antiscalant molecules have

less complex molecular structures which may enhance the accessibility of acidic functional groups for interaction with aqueous calcium ions and those on the gypsum crystal surface.

## 6.4 Effects of NOM on Gypsum Scaling by Bulk Crystallization During RO Desalination

*Selected contents of this chapter have been published in collaboration with J. Rozova and M. Ernst: Separation and Purification Technology 198 (2018), 68–78.*

Chapter 4.1 demonstrated that RO operating conditions can favor bulk crystallization and the subsequent deposition of gypsum crystals on the membrane surface. The induction time of bulk crystallization and its sufficient retardation is therefore of crucial importance during RO operation under such operating conditions of high recoveries and high hydraulic residence times. Preceding crystallization experiments have demonstrated that the presence of dissolved NOM can enhance the observed induction time. Thus, it is expected that NOM will delay the onset of scaling by bulk crystallization during RO desalination. However, water permeation, fouling by NOM and surface crystallization on the RO membrane represent additional phenomena that may occur during RO desalination.

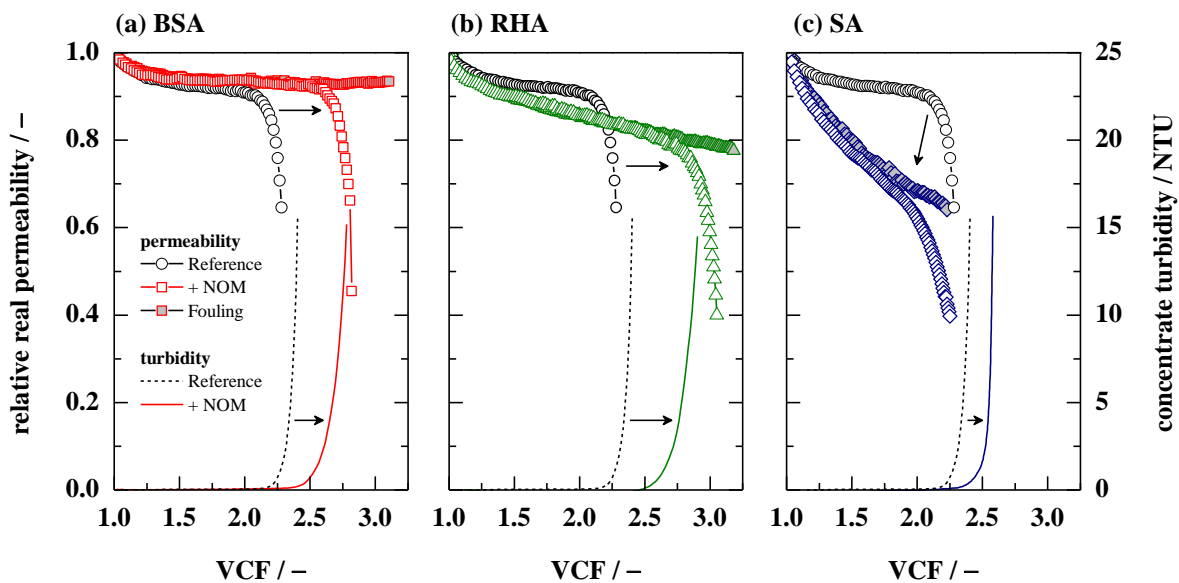


**Figure 6-6:** Development of relative real permeability (symbols, left axis) and concentrate turbidity (lines, right axis) during gypsum scaling experiments in the absence (*Reference*) and presence of (a) BSA, (b) RHA and (c) SA at  $3 \text{ mg C}\cdot\text{l}^{-1}$  (*+NOM*) and during pure NOM fouling experiments (*Fouling*, substitution of  $\text{Na}_2\text{SO}_4$  by  $\text{NaCl}$ ). Experiments were performed using RO system configuration I (permeate withdrawal mode) at *low CP operation*. Real permeability was normalized to the initial real permeability at  $t = 0 \text{ min}$  and averaged for 5 min intervals. Experimental conditions:  $T = 25.0 \pm 0.1 \text{ }^\circ\text{C}$  ( $\pm \text{SD}$ ),  $\Delta p = 25.0 \pm 0.1 \text{ bar}$  ( $\pm \text{SD}$ ),  $pH = 6.9 \pm 0.4$  ( $\pm \text{SD}$ ),  $k_{w,real} = 2.71 \pm 0.09 \text{ l}\cdot\text{m}^{-2}\cdot\text{h}^{-1}\cdot\text{bar}^{-1}$  ( $\pm \text{SD}$ ),  $SI_{g,b,0} = -0.02$ .

RO experiments under permeate withdrawal mode using the RO system in configuration I and ‘low CP operating mode’ (Chapter 3.2.2) were performed in the presence of selected NOM sources (SA, BSA, RHA) to assess the effect of NOM on achievable volumetric concentration factors (*VCFs*). Complementary fouling experiments were conducted to assess the degree of real permeability decline due to NOM fouling. Figure 6-6 shows relative real permeabilities during gypsum scaling and pure NOM fouling experiments with respective concentrate turbidities as a function of *VCF*. While sudden increases of concentrate turbidity during scaling experiments indicate bulk crystallization, losses of real permeability can be attributed to fouling or to gypsum scale formation by either bulk crystal deposition or surface crystallization. Table 6-4 summarizes obtained critical *VCFs* based on (a) turbidity increase and (b) real permeability decline. Complementary, Table 6-4 includes the data obtained during experiments in the presence of the polyacrylic and phosphonic acid-based antiscalant, which were previously presented in Figure 4-1 and Table 4-1 of Chapter 4.

Turbidity data show that the onset of bulk crystallization occurred at higher *VCFs* and longer operating times in the presence of NOM (Figure 6-6, Table 6-4). Accordingly, higher water recoveries  $\Phi$  ( $\Phi = 1 - VCF^{-1}$ ) were achieved in the presence of NOM before spontaneous gypsum bulk crystallization was initiated. The order of retardation was AS > RHA > BSA > SA. Interestingly, the order of retardation is different as would be expected from previous stirred beaker

**Table 6-4: Critical volumetric concentration factors ( $VCF_{crit}$ ), critical operating time ( $t_{crit}$ ) and gypsum bulk supersaturation ( $SI_{g,b}$ ) determined at the onset of gypsum scaling during RO desalination (‘low CP operation’) in the presence of NOM (Figure 6-6) by (a) bulk crystallization based on turbidity increase and (b) bulk and surface crystallization based on real permeability decline. Data in the presence of antiscalant (AS) was extracted from Figure 4-1. From complementary NOM fouling experiments, concentrate DOC concentrations ( $c_{DOC,c}$ ) for the critical *VCFs* were quantified and corresponding total masses of DOC that were adsorbed or deposited on the membrane surface ( $\Delta m_{DOC}$ ) were calculated. Experimental conditions:  $T = 25.0 \pm 0.1$  °C ( $\pm$  SD),  $\Delta p = 25.0 \pm 0.1$  bar ( $\pm$  SD),  $pH = 6.9 \pm 0.4$  ( $\pm$  SD),  $k_{w,real} = 2.71 \pm 0.09$  l·m<sup>-2</sup>·h<sup>-1</sup>·bar<sup>-1</sup> ( $\pm$  SD),  $SI_{g,b,0} = -0.02$ ,  $c_{NOM,0} = 3$  mg C·l<sup>-1</sup>.**

<b>(a) based on turbidity increase</b>					
	$VCF_{crit} / -$	$t_{crit} / \text{min}$	$SI_{g,b} / -$	$c_{DOC,c} / \text{mg C} \cdot \text{l}^{-1}$	$\Delta m_{DOC} / \text{mg C}$
Reference	2.10	270	0.37	–	–
+ BSA	2.36	355	0.43	7.5	0
+ RHA	2.47	405	0.45	3.4	11.3
+ SA	2.24	445	0.40	2.3	14.2
+ AS	2.64	450	0.49	–	–
<b>(b) based on permeability decline</b>					
	$VCF_{crit} / -$	$t_{crit} / \text{min}$	$SI_{g,b} / -$		
Reference	2.07	260	0.36		
+ BSA	2.52	400	0.46		
+ RHA	2.60	445	0.48		
+ SA	1.87	270	0.31		
+ AS	no decline detected				

experiments, where SA showed superior and BSA showed inferior retardation capabilities relative to RHA (Figure 6-1a and Figure 6-2a). Here, the different degrees of fouling caused by the NOMs have to be taken into consideration. A clear order of permeability loss due to organic fouling was observed ( $SA > RHA > BSA$ ) with strongest permeability decline caused by SA and no observable permeability loss in the presence of BSA. This fouling behavior is in agreement with previous RO and NF fouling studies using BSA, SA and different humic substances as organic foulants [182,201,255]. DOC mass balances at the critical  $VCFs$  show that total DOC masses of  $\Delta m_{DOC} = 14.2 \text{ mg C}$  and  $11.3 \text{ mg C}$  were adsorbed or deposited on the RO membrane surface during SA and RHA fouling experiments, while no DOC depletion was quantified for BSA (Table 6-4a). Strong fouling by SA is frequently reported and is a result of the specific interactions between the SA molecules and calcium ions and the corresponding formation of extensive cross linked gel-like structures [175,181–184,200]. The adsorption and deposition of DOC due to fouling affected residual concentrations of DOC in the feed solution as exhibited in Table 6-4a. Relative to RHA and SA, the concentration of BSA at the onset of bulk crystallization was significantly higher, which may explain the observed ranking of retardation capabilities. Further, BSA exhibits a comparably instable protein structure [256,257]. A study by Haberkamp (2008) showed that fragmentation of the globular BSA molecule can occur by mechanical shear forces, which can make inner parts of the original BSA molecule available for adsorptive interactions [258].

As previously discussed for stirred beaker crystallization experiments, the mechanism of retarded gypsum bulk crystallization can be attributed to the adsorption of NOM onto developing gypsum bulk crystals, which is supported by microscopic changes of gypsum bulk crystal size and habit in the presence of the three investigated NOM sources (Figure D-15). Despite the fact that bulk crystallization was retarded in the presence of all NOM sources, evaluation of permeability data (Figure 6-6, Table 6-4b) clearly shows that permeability decline due to scale formation was accelerated in the presence of SA. The scanning electron micrograph displayed in Figure 6-7c shows individual, large crystals beneath a layer of deposited bulk crystals. The large crystals likely originated from surface crystallization, which reduced active membrane area and consequently reduced effective real permeability prior to the onset of bulk crystallization. This is also observed for RHA-gypsum scaling (Figure 6-7b), however, the effect appears to be considerably less pronounced. In contrast, for BSA (Figure 6-7d), only bulk crystals are visible, which are evenly distributed across the membrane surface. The observed shift of scaling mechanisms from bulk to surface crystallization in the presence of SA may be attributed to the following considerations.

- (i) The SA fouling layer may supply heteronucleation sites on the membrane surface resulting from the strong attraction of calcium ions by the SA fouling layer, which was previously observed by Wang et al. (2016) and Liu et al. (2014) during NF [43] and FO [42] scaling experiments.
- (ii) Concentration polarization and consequently heteronucleation and crystal growth may be

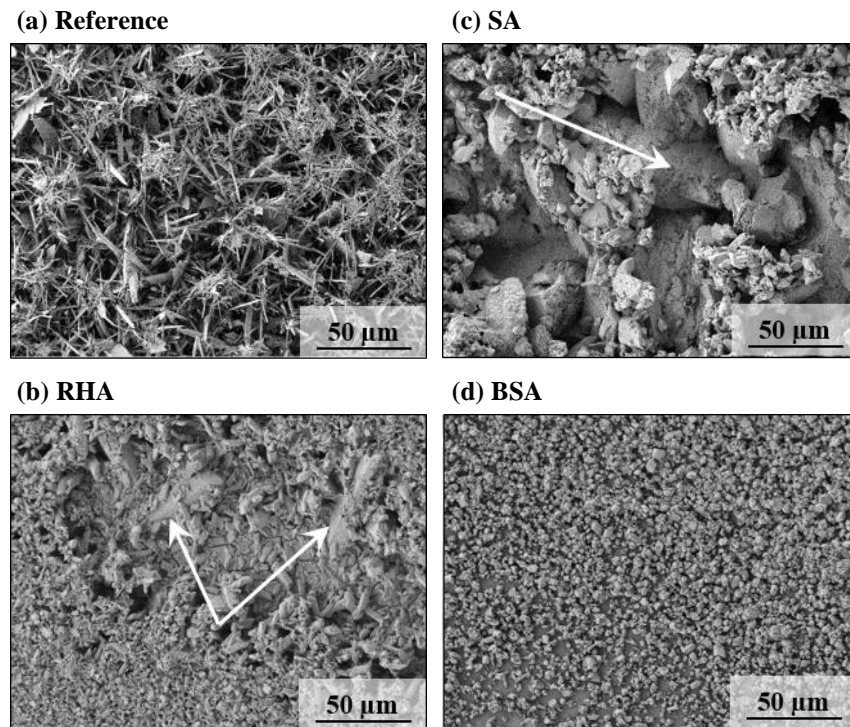


**Figure 6-7:** Scanning electron micrographs (1,000x magnification) of membrane surfaces after RO scaling experiments displayed in Figure 6-6. Arrows highlight gypsum surface crystals underneath deposited bulk crystals.

enhanced due to hindered back diffusion of rejected ions within the thick SA fouling layer [41–43,213], a phenomenon referred to as cake-enhanced concentration polarization [207].

Concluding, as expected from stirred beaker crystallization experiments, gypsum bulk crystallization during RO operation was significantly retarded in the presence of the selected NOM sources (SA, BSA, RHA) and led to increased critical volumetric concentration factors. In addition, the retardation capability of the antiscalant was superior to that of NOM (Table 6-4) as critical volumetric concentration factors were higher and bulk crystals were kept in suspension by the antiscalant's dispersing properties (*'dispersing effect'*). The additional phenomena that can occur during RO desalination, such as water permeation, concentration polarization, surface crystallization and membrane fouling, limit the transferability of NOM retardation capabilities obtained from stirred beaker experiments to RO operation. This was clearly indicated by the observed shift of scaling mechanism from bulk to surface crystallization due to the strong fouling by SA. Any assessment of the retardation capability of NOM and organic additives should therefore include an assessment of their membrane fouling potential and the effects of fouling on surface crystallization and bulk crystal deposition. If fouling is negligible, as was observed for BSA, stirred beaker crystallization experiments may aid in identifying potential organic substances suitable for scale inhibition due to bulk crystallization.



## 7 Effects of NOM on Gypsum Surface Crystallization on RO Membranes

This chapter investigates the effects of selected NOM sources on gypsum scaling during RO desalination due to surface crystallization on the membrane surface. Effects are assessed using the RO setup in configuration II (full recirculation mode, Chapter 3.2.3), which facilitates real-time membrane surface imaging by light microscopy. Experimental results are evaluated relative to the results obtained in Chapter 4.3, which investigated the development and reproducibility of gypsum surface scaling on virgin RO membrane samples in the absence of NOM. Chapter 7.1 assesses the effects of NOM fouling on gypsum surface scaling during RO desalination in the absence of dissolved NOM (pure gypsum scaling on ‘pre-fouled’ membranes). Subsequently, Chapter 7.2 investigates the effects of dissolved NOM on gypsum surface crystallization. Concluding, Chapter 7.3 compares the effects of dissolved aquatic HSNOM to the effects induced by a commercial polyacrylic and phosphonic acid-based antiscalant. A complete list of conducted RO experiments and relevant process parameters can be found in Table C-3.

### 7.1 Effects of Membrane Pre-Fouling by NOM

#### 7.1.1 Effects of NOM Pre-Fouling on Membrane Characteristics

NOM pre-fouling was observed to affect the zeta potential ( $\zeta$ ) and contact angle ( $\theta_c$ ) of the membrane surface (Table D-4). For membrane samples that were pre-fouled with SA, humic acids (RHA, SAHA) and aquatic NOM (SRNOM, HSNOM), zeta potential and contact angle measurements resulted in decreased values and indicate an increased surface charge and increased hydrophilicity. This is in agreement with previous studies concluding that polymeric membranes become more negatively charged due to the adsorption of humic substances [25–27,57]. Marginally increased zeta potential was observed after pre-fouling by BSA, which has also been reported in literature [28]. It is generally concluded that NOM fouling layers and particularly the NOM’s functional groups rather than the intrinsic membrane characteristics determine the membrane surface properties [25–28,57].

While zeta potential and contact angle measurements show that pre-fouling by NOM affects membrane surface properties, they do not indicate the severity of fouling. Scanning electron micrographs in Figure D-16 exhibit the membrane surfaces after NOM fouling. After pre-fouling by BSA, the membrane surface still exhibited the characteristic ‘ridge and valley’ structure of the virgin membrane material, whereas after pre-fouling by HSNOM and SAHA, homogenous but comparably loose fouling layers are visible. A dense and thick fouling layer is visible after pre-fouling by SA. Observed flux declines during pre-fouling experiments (Figure D-17a) indicate the following order of fouling severity: BSA < HSNOM < SAHA < SA, which is in well agreement

with the visual observations (Figure D-16) and the previous observations made during fouling experiments using BSA, RHA and SA in Chapter 6.4.

Previous studies have shown that fouling layers can enhance concentration polarization (CECP, Figure 2-19) at the membrane surface and thereby reduce the observed solute rejection [12,207,208,212–214]. Table C-3b exhibits the  $\text{CaCl}_2$  rejections during the membrane conditioning step. Observed rejections of SA ( $R_{obs} = 95.6\%$ ) and SAHA ( $R_{obs} = 96.7\%$ ) pre-fouled membranes were lower relative to the membranes pre-fouled by BSA ( $R_{obs} = 97.6\%$ ) and HSNOM ( $R_{obs} = 97.8\%$ ). This observation indicates the increasing relevance of CECP with increasing fouling severity. However, given the high variation of virgin membrane  $\text{CaCl}_2$  rejections ( $R_{obs} = 92.8 - 97.8\%$ , Table C-3), long-term fouling experiments at stabilized salt rejections should be performed in future studies to verify the relevance of CECP after NOM pre-fouling.

### 7.1.2 Effects of NOM Pre-Fouling on Gypsum Surface Scaling

Gypsum surface scaling behavior on NOM pre-fouled membranes (24 h at  $3 \text{ mg C}\cdot\text{l}^{-1}$  NOM, Figure B-3: ‘pure gypsum scaling after NOM pre-fouling’) was monitored by real-time imaging (Figure 7-1). Corresponding increases of transmembrane pressure are presented in Figure D-17b and axial distributions of crystal mass as well as total crystal masses are summarized in Table D-5. It is important to note that pre-fouling according to the protocol described in Chapter 3.2.3 was followed by thorough rinsing with ultrapure water. This was necessary in order to remove the hydraulically reversible fraction of NOM fouling and to thereby guarantee that subsequent gypsum surface scaling was not affected by NOM in solution. DOC measurements during subsequent

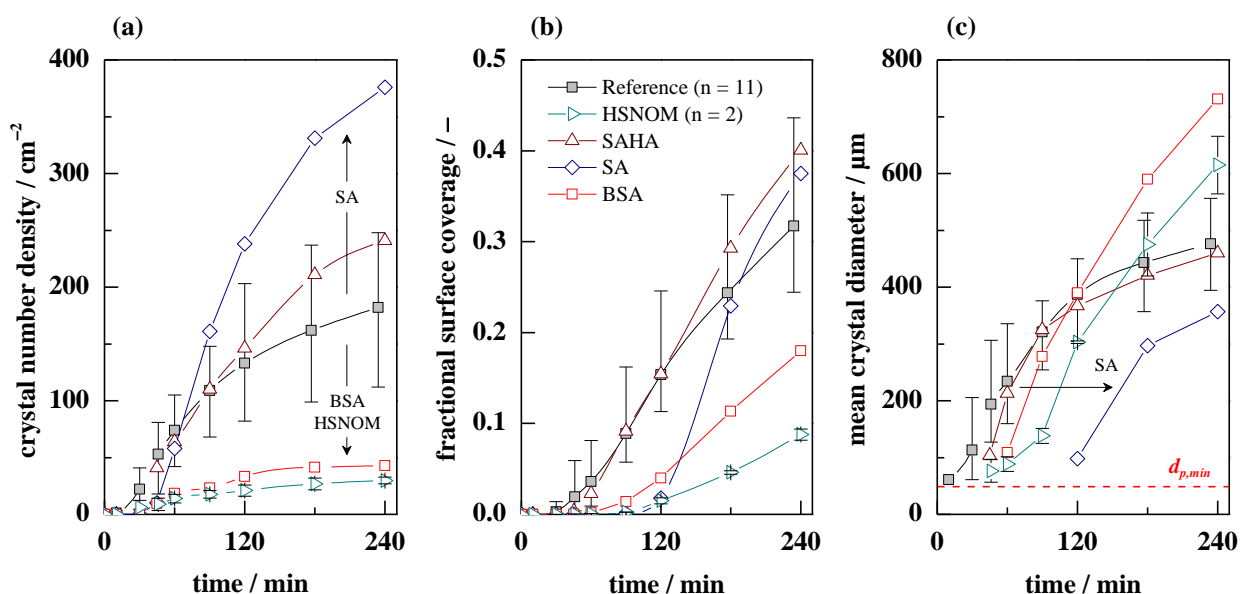
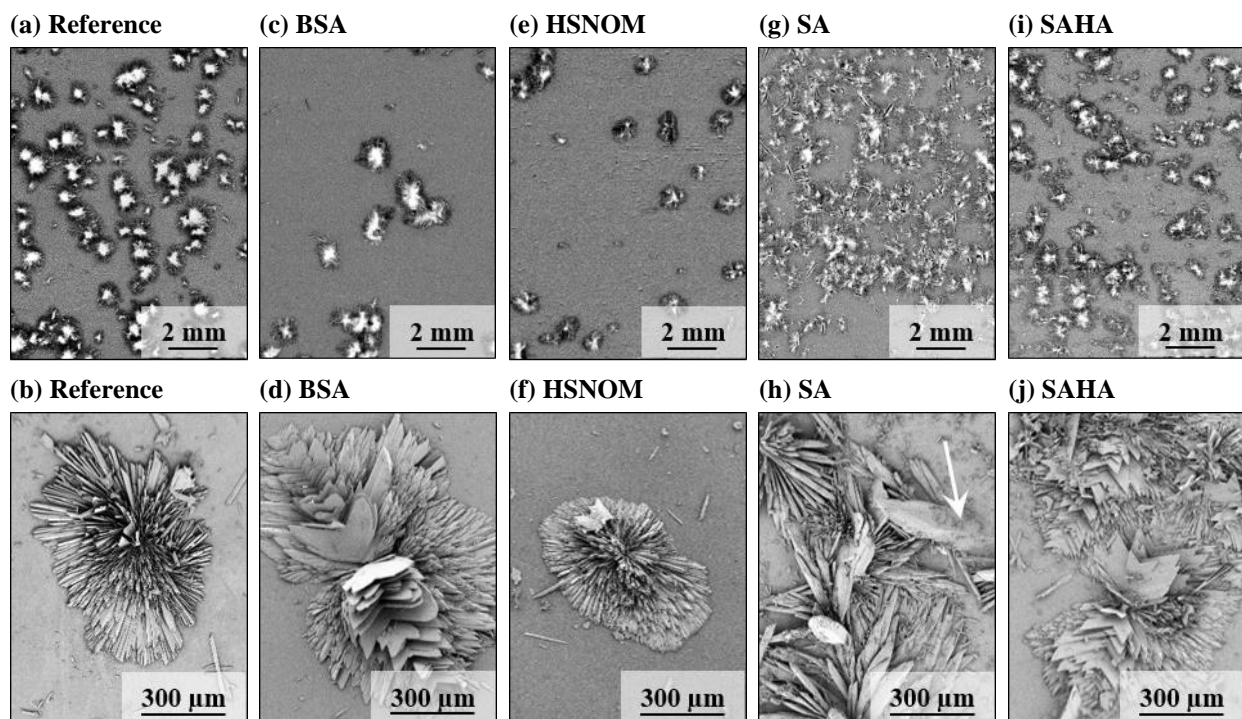


Figure 7-1: Temporal development of (a) gypsum surface crystal number density (CND) ( $d_p > 49.3 \mu\text{m}$ ), (b) fractional membrane surface coverage (FSC) and (c) mean crystal diameter ( $d_p > 49.3 \mu\text{m}$ ) on virgin and NOM-pre-fouled RO membrane samples. For repeated experiments ( $n > 1$ ), mean values are presented with error bars representing determined minimal and maximal values.

scaling experiments (Table D-6) show that NOM concentrations in solution were negligible relative to the background DOC concentrations quantified during reference experiments.

Membrane pre-fouling by BSA and HSNOM significantly reduced the rate of crystal detection (Figure 7-1a) and the fractional surface coverage (Figure 7-1b) relative to the reference experiments on virgin membranes. The lower fractional surface coverage after gypsum scaling on BSA and HSNOM pre-fouled membranes is supported by significantly slower transmembrane pressure increases (Figure D-17b) and lower final total crystal masses (Table D-5). Micrographs in Figure 7-2 (a – f) show that individual gypsum surface crystals grew undisturbed into regular rosette-like structures on the BSA and HSNOM pre-fouled membranes. Accordingly, regular gypsum crystal growth was unaffected by the negligible concentration of dissolved NOM in solution (Table D-6).



**Figure 7-2: Real-time membrane surface images (5x magnification, top row) and scanning electron micrographs (200x magnification, bottom row) showing gypsum surface crystals on (a, b) virgin and (c – j) NOM pre-fouled membranes after 240 – 270 min of operation. Arrow in (h) indicates a crystal that grew within SA fouling layer.**

Despite the alleviated propensity of gypsum surface scaling on the BSA and HSNOM pre-fouled membranes (slower  $\Delta p$  increase and smaller total crystal mass), it is important to note that the growth of gypsum surface crystals was accelerated, which resulted in larger observed mean crystal diameters relative to the reference (Figure 7-1c). It indicates that heteronucleation and growth of gypsum surface crystals on the RO membrane surface are dependent processes, where reduced heteronucleation, i.e. a smaller crystal number density, enhances individual crystal growth. This observation is supported and complemented by previous results of Chapter 4.3, which showed that

growth of gypsum surface crystals was slower on RO membranes which exhibited enhanced effective heteronucleation affinities, i.e. which had higher final crystal number densities (Figure 4-15 and Figure 4-17). The repeatedly observed relationship between crystal number density ( $CND$ ) and mean crystal diameter ( $d_p$ ) is summarized by Figure 7-3 ( $d_p \propto -\log(CND)$ ). A similar behavior can be extracted from the data provided by Uchymiak et al. (2008) [91]. Using real-time membrane (RO) surface imaging, the authors observed that gypsum surface crystal number density was higher at higher supersaturation ( $SI_{g,m}$ ) [91]. The higher crystal number densities (at higher  $SI_{g,m}$ ) coincided with smaller mean crystal diameters (Fig. 5 in [91]). Supersaturation at the membrane surface can be released by crystal nucleation or crystal growth. Given that the local supersaturation and the inventory of available scale-forming ions are limited, reduced heteronucleation and a reduced number of growing crystals leave a higher amount of scale-forming ions available for growth of the existing crystals. This higher effective supersaturation is assumed to stimulate enhanced crystal growth at lower crystal number densities. Figure 7-3 additionally displays the fractional surface coverage ( $FSC$ ) as a function of  $\log(CND)$ . The data suggest the linear relationship  $FSC \propto \log(CND)$  ( $R^2 = 0.60$ ). Assuming that gypsum surface crystals under conditions of undisturbed growth (i.e. in the absence of dissolved NOM or additives) grow into ideal rosette-like hemispheres, the ratio of the hemisphere's volume and its base area increases as the hemisphere (i.e. crystal) grows. Given that the observed correlation of  $FSC \propto \log(CND)$  is relatively weak, further verification of this relationship is required during long-term scaling experiments on RO membranes where crystal growth may not be ideal.

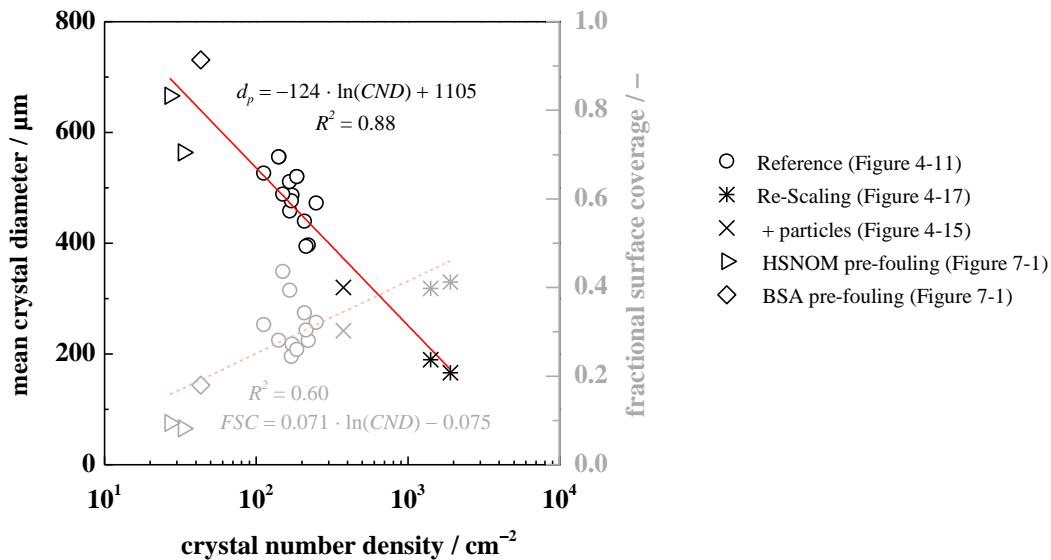


**Figure 7-3: Relationships between (i) mean crystal diameter ( $d_p$ ) and crystal number density ( $CND$ ) and (ii) fractional surface coverage ( $FSC$ ) and crystal number density ( $CND$ ) observed in pure gypsum experiments, i.e. all experiments where growth of regular rosette-like gypsum surface crystals was not distorted by dissolved NOM in solution. Based on final values at  $t = 240$  min.**

If confirmed, membrane surfaces with reduced effective heteronucleation affinity would alleviate the propensity of gypsum surface scaling ( $FSC \downarrow$ ). Nevertheless, the potential of this anti-scaling measure would be limited due to the acceleration of crystal growth ( $d_p \uparrow$ ) at lower  $CND$ .

Gypsum surface scaling behavior on the SA pre-fouled membrane resulted in an enhanced rate of crystal detection (Figure 7-1a) and a delayed growth of crystals (Figure 7-1c). Final surface coverage (Figure 7-1b) was comparable to that of the reference experiment. Interestingly, the transmembrane pressure increase (Figure D-17b) was significantly lower compared to the reference experiments despite comparable surface coverage (Figure 7-1b) and comparable total crystal mass (Table D-5). The enhanced rate of crystal detection (Figure 7-1a) indicates that the SA fouling layer itself supplied energetically favorable heteronucleation sites in addition to those available on the virgin membrane material. Micrographs in Figure 7-2 (g, h) show distorted crystal growth and partial crystal growth within the SA fouling layer. Heteronucleation on or within the SA fouling layer may explain a slower loss of RO performance ( $\Delta p$  increase) despite comparable fractional surface coverage and crystal mass as the detected crystals may not have reduced the active membrane area by direct contact.

After SAHA pre-fouling, indistinguishable differences were observed relative to the reference (Figure 7-1), although determined crystal parameters ( $CND$ ,  $FSC$ ,  $d_p$ ) lay within the upper data scatter of the reference experiments. Detected transmembrane pressure increase (Figure D-17b) and total crystal mass (Table D-5) indicate a slightly increased gypsum surface scaling propensity relative to the reference experiment. Micrographs in Figure 7-2 (i, j) show that individual gypsum surface crystals grew undisturbed into regular rosette-like structures on the SAHA pre-fouled membranes.

### **Mechanisms of interference**

Effects of NOM pre-fouling on gypsum scaling were recently investigated by Liu et al. (2012, 2014) during forward osmosis (FO) [41,42] and by Wang et al. (2016) during nanofiltration (NF) [43]. The above studies [41–43] relied on scale detection by monitoring of global process parameters and used intensive pre-fouling protocols of 48 h pre-fouling with  $200 \text{ mg}\cdot\text{l}^{-1}$  NOM [41,42] and 24 h pre-fouling with  $100 \text{ mg}\cdot\text{l}^{-1}$  NOM [43]. Further, supersaturated gypsum scaling solutions ( $SI_{g,b} = 0.18$ ) were used and the membrane systems were operated in permeate withdrawal mode at continuously increasing gypsum supersaturation [41–43]. During FO experiments, Liu et al. (2012, 2014) observed that flux decline after BSA pre-fouling was marginally delayed whereas it was accelerated after SA and SAHA pre-fouling [41,42]. The authors concluded that the carboxyl groups of the SA and SAHA fouling layers acted as heteronucleation sites and that the dense fouling layers contributed to cake-enhanced concentration polarization (CECP) [41,42]. For BSA pre-fouling, it was concluded that the lower carboxylic density and the heart-shaped structure of the BSA molecule, which causes a steric effect, limit the interaction between BSA molecules and calcium ions. Interestingly, Wang et al. (2016) observed

accelerated flux decline for all three selected NOM sources (SA, SAHA and BSA) during NF gypsum scaling experiments [43]. The authors concluded that gypsum scaling on NOM pre-fouled membranes is determined by the NOM calcium ion binding capacity and the resulting membrane surface charge as well as the fouling layer structure [43]. Due to the intensive NOM pre-fouling protocol in above studies [41–43] and given that the scaling protocol clearly favored gypsum bulk crystallization, transferability to the results of this thesis may be limited.

The two mechanisms of interference, namely the ‘*provision of heteronucleation sites (I)*’ and ‘*cake-enhanced concentration polarization (II)*’ (CECP) by NOM fouling layers, which were proposed by Liu et al. (2012, 2014) [41,42] and Wang et al. (2016) [43] may explain the enhanced crystal number density observed on the SA pre-fouled membrane. First, heteronucleation was enhanced by the inherently strong affinity of SA towards calcium ions and the supply of energetically favorable heteronucleation sites (*I*). In addition, SA pre-fouling alleviated RO performance loss which indicated that the SA fouling layer inhibited crystal growth directly on the membrane surface by providing a secondary layer (i.e. the NOM fouling layer) with distributed heteronucleation sites. Second, CECP (*II*) due to the strong fouling layer formation by SA may have contributed to enhanced heteronucleation (i.e. increased *CND*) by enhancing scale-forming ion concentrations at the membrane surface. However, the relevance of CECP (*II*) requires further verification (as discussed in Chapter 7.1.1). Third, heteronucleation and growth of gypsum crystals within the SA fouling layer would explain the observed distorted crystal morphology observed in Figure 7-2e and represents a third (*III*) mechanism of interference, which is the capability of individual molecules of the three dimensional fouling layer network to distort regular crystal growth by adsorption onto crystal faces. ‘*Crystal distortion by fouling layer NOM molecules (III)*’ could also lead to the complete inactivation of subcritical nuclei, which would inhibit crystal nucleation by the ‘*threshold effect*’.

While the above mechanisms of interference (*I – III*) may explain the scaling behavior observed on the SA pre-fouled membrane, they lack to explain the reduced crystal number densities observed on the BSA and HSNOM pre-fouled membranes. As extensively discussed in Chapter 4.3, there is clear indication that polymeric membranes exhibit a spatial distribution of energetically favorable heterogeneous nucleation sites where crystal heteronucleation preferentially occurs. These heteronucleation sites may include local areas of high carboxyl group density which attract calcium ions and initiate heteronucleation as suggested by Mi and Elimelech (2010) [102] and Xie and Gray (2016) [103]. At the same time, those active nucleation sites may be favorable for NOM complexation through calcium ion bridging [21,202]. Accordingly, ‘*inactivation of membrane heteronucleation sites (IV)*’ is proposed as a fourth mechanism of interference, which may explain the observed reduced rate of crystal development on the BSA and HSNOM pre-fouled membranes and the inhibition of crystal growth directly on the SA pre-fouled membrane. The proposed mechanisms of interference (*I – IV*) are schematically illustrated in Figure 7-4. It is important to recognize that the individual mechanisms are simplified and that

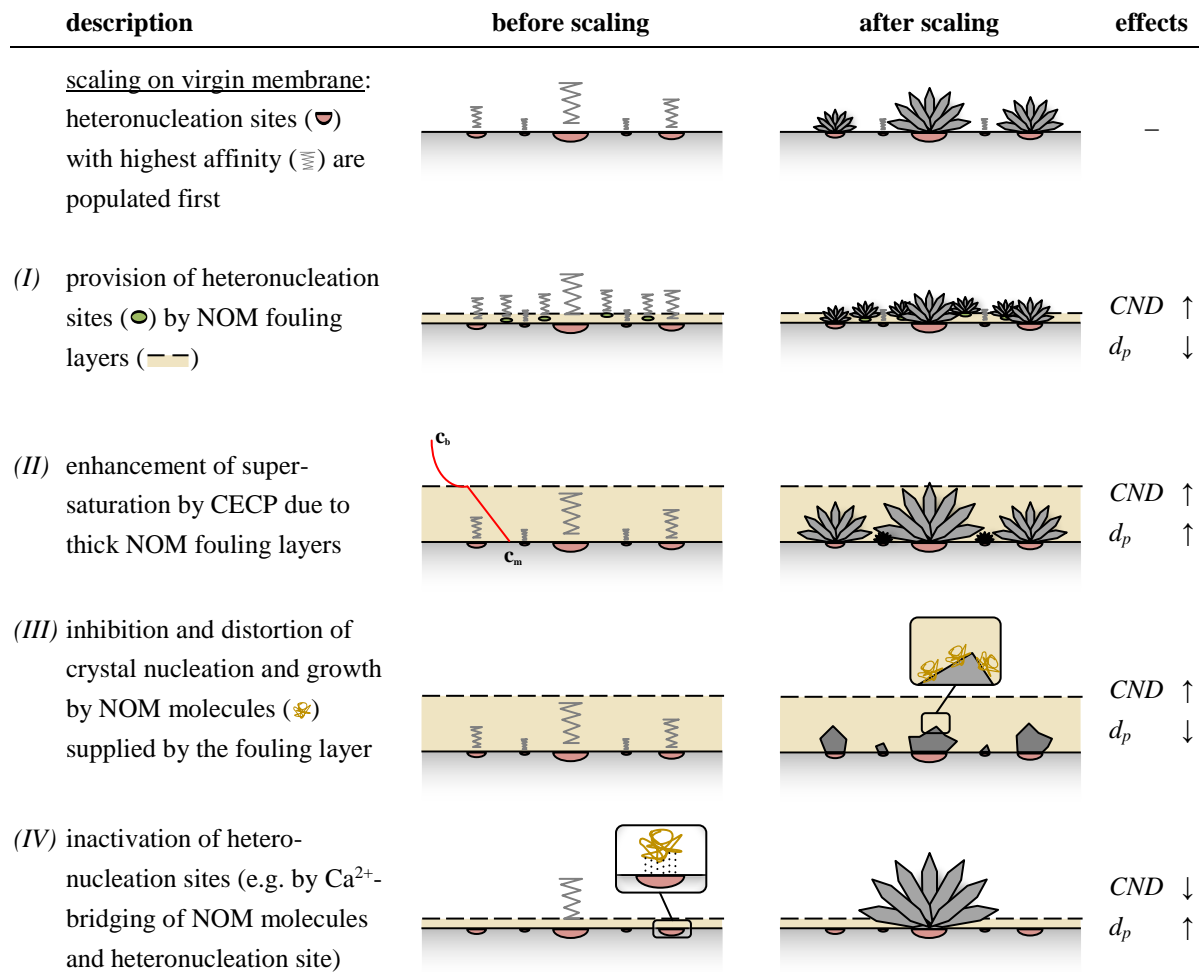


**Figure 7-4: Schematic illustration of proposed mechanisms of interaction (I – IV) between NOM fouling and gypsum surface scaling on RO membrane surfaces including proposed effects on scaling behavior (CND: crystal number density,  $d_p$ : mean crystal diameter,  $\uparrow$ : indicates increase,  $\downarrow$ : indicates decrease). It is important to note that the four mechanisms are simplified and will likely occur simultaneously. Fundamentals of ‘cake-enhanced concentration polarization (CECP)’ by NOM fouling (II) are described in Chapter 2.4.5.**

multiple mechanisms can occur simultaneously depending on the fouling layer structure and the molecular NOM properties.

Interestingly, gypsum surface scaling behavior was unaffected on the SAHA pre-fouled membrane. This is in contrast to observations made by Liu et al. (2012, 2014) [41,42] and Wang et al. (2016) [43] where heteronucleation was enhanced. However, the pre-fouling protocol adapted in this thesis was significantly less intensive. While Liu et al. (2012, 2014) [41,42] and Wang et al. (2016) [43] suggested that CECP due to the severe fouling layer formation played a relevant role in their studies, this could not be confirmed in this thesis where NOM pre-fouling procedure was adapted to low NOM concentrations found in natural waters and was limited to hydraulically irreversible fouling (due to the pre-fouling procedure which included intensive hydraulic rinsing, Chapter 3.2.3). However, the slightly accelerated transmembrane pressure increase (Figure D-17b) and the increased total crystal mass (Table D-5) indicate increased scaling

propensity on the SAHA pre-fouled membrane assumingly caused by CECP due to the fouling layer formation by the relatively large fraction (72 % of the total DOC) of colloidal humic acids ( $\geq 150$  kDa, Figure 5-2) of the SAHA sample.

### Summary

The results show that membrane pre-fouling by NOM at moderate NOM concentrations (24 h at  $3 \text{ mg C}\cdot\text{l}^{-1}$  NOM) can alleviate the severity of gypsum scaling due to surface crystallization and alleviate the loss of RO performance. This was observed after pre-fouling by aquatic HSNOM and BSA and is in contrast to previous studies [41–43] that investigated the effects of severe NOM fouling layers. Both NOM sources, HSNOM and BSA, were observed to inactivate membrane intrinsic heteronucleation sites by fouling, which reduced heteronucleation on the membrane surface ( $CND \downarrow$ ) and reduced membrane fractional surface coverage ( $FSC \downarrow$ ) despite accelerated individual crystal growth ( $d_p \uparrow$ ). By summarizing these and previous observations, a negative linear relationship between  $d_p$  and  $\log(CND)$  and a positive linear relationship between  $FSC$  and  $\log(CND)$  were identified for conditions of undisturbed crystal growth in the absence of dissolved NOM or additives ( $d_p \propto -\log(CND)$  and  $FSC \propto \log(CND)$ ).

SA pre-fouling provided additional heteronucleation sites on and within the fouling layer (i.e. increased  $CND$ ). The provision of nucleation sites can be attributed to the strong specific interactions of SA with calcium ions due to the long aliphatic structure and high carboxylic acidity of SA. Both, the capability of SA to attract calcium ions (Chapters 5.1 and 6.1) and to enhance heteronucleation on the membrane surface (Chapter 6.4) were previously observed in this thesis and find support in previous studies [41–43]. Despite enhanced  $CND$  and a final fractional surface coverage that was comparable to the reference experiments on virgin membrane samples, the increase of transmembrane pressure was decelerated. It indicated that crystal growth directly on the membrane surface was partially inhibited, presumably due to nucleation and growth on or within the SA fouling layer. Crystal growth within the fouling layer was observed on SEM images and confirm that thick fouling layers can partially or fully enclose developing surface crystals and thereby distort crystal growth (*'crystal distortion effect'*) or even prevent crystal development (*'threshold effect'*). In addition, cake-enhanced concentration polarization (CECP) may play an additional role in surface scale formation on pre-fouled RO membranes, however, further investigations are required to confirm the relevance of CECP.

An aggravation of gypsum surface scaling by SAHA fouling, as was previously observed after exaggerated SAHA pre-fouling [41–43], could not be confirmed under the given experimental conditions, where the NOM pre-fouling procedure was adapted to low NOM concentrations commonly found in natural waters and was limited to hydraulically irreversible fouling.

It is important to note that membrane surface properties, namely zeta potential ( $\zeta$ ) and contact angle ( $\theta_c$ ), determined after NOM pre-fouling could not be linked to the observed gypsum surface scaling behavior. For example, SAHA and HSNOM pre-fouling resulted in almost identical values

for zeta potential and contact angle, but scaling behavior was significantly different. Similarly, zeta potential and contact angle after BSA and HSNOM pre-fouling were considerably different whereas effective heteronucleation affinity decreased in both cases.

### 7.1.3 Effects of NOM Pre-Fouling Intensity on Gypsum Surface Scaling

A series of scaling experiments was conducted on HSNOM pre-fouled membranes where pre-fouling intensity was varied according to the following 24 h pre-fouling protocols: ‘*low*’: 3 mg C·l<sup>-1</sup> HSNOM diluted in ultrapure water, ‘*medium*’: 3 mg C·l<sup>-1</sup> HSNOM diluted in 17 mmol·l<sup>-1</sup> CaCl<sub>2</sub> solution and ‘*intensive*’: 10 mg C·l<sup>-1</sup> HSNOM diluted in 17 mmol·l<sup>-1</sup> CaCl<sub>2</sub> solution. Flux decline during pre-fouling (Figure D-18a) as well as scanning electron micrographs (Figure 7-5c, f, i, m) confirm an increasing fouling layer formation with intensification of HSNOM

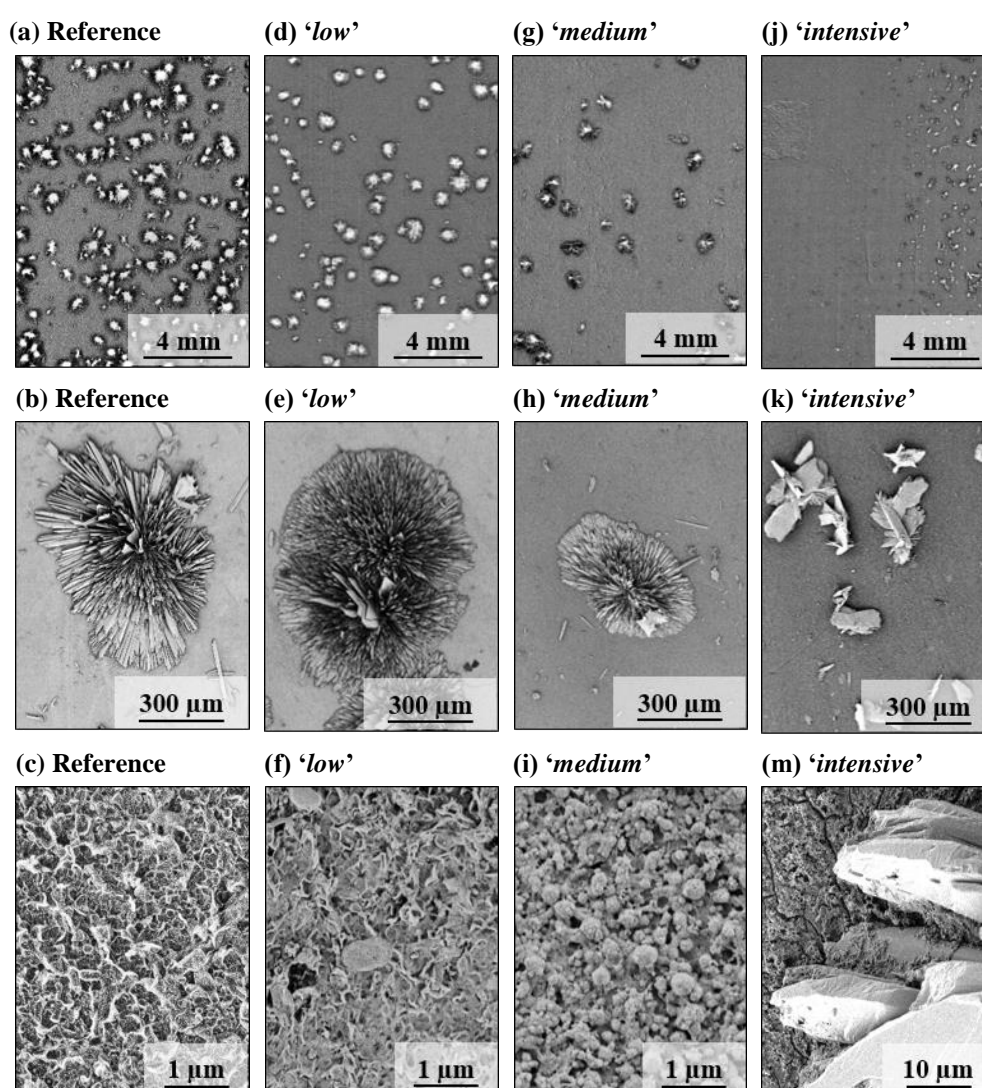


**Figure 7-5:** Real-time (5x, top row) and scanning electron (middle row: 200x magnification, bottom row: 5,000x – 50,000x magnification) micrographs of membrane surfaces showing gypsum surface crystals and fouling layers after different intensities of HSNOM pre-fouling. ‘*low*’: 3 mg C·l<sup>-1</sup> HSNOM diluted in ultrapure water, ‘*medium*’: 3 mg C·l<sup>-1</sup> HSNOM diluted in 17 mmol·l<sup>-1</sup> CaCl<sub>2</sub> solution, ‘*intensive*’: 10 mg C·l<sup>-1</sup> HSNOM diluted in 17 mmol·l<sup>-1</sup> CaCl<sub>2</sub> solution.

pre-fouling. After ‘*intensive*’ pre-fouling, characteristic drying cracks visualize the relative thickness of the dehydrated HSNOM fouling layer (Figure 7-5m). Comparison of the severity of membrane fouling by ‘*low*’ and ‘*medium*’ fouling protocols demonstrates the effect of calcium ions by intensifying fouling through NOM charge neutralization [25,27,193,194], calcium ion bridging of individual NOM molecules [25,196] and calcium ion bridging of NOM molecules and the carboxyl groups of the membrane surface [194,195].

The trends observable in Figure 7-5 are temporally resolved by analysis of real-time imaging (Figure 7-6). Severity of gypsum surface scale formation, in terms of fractional surface coverage (Figure 7-6b), was significantly reduced with increasing HSNOM fouling intensity. This is supported by monitored transmembrane pressure increases (Figure D-18b) and total crystal masses (Table D-5b), which were both lowest after ‘*intensive*’ HSNOM pre-fouling. Relative to the reference experiments, the rate of crystal detection (Figure 7-6a) decreased after ‘*low*’ and ‘*medium*’ HSNOM pre-fouling while mean crystal growth (Figure 7-6c) was slightly accelerated. In contrast, the rate of crystal detection increased after ‘*intensive*’ HSNOM pre-fouling while mean crystal growth was significantly decelerated. After ‘*intensive*’ pre-fouling, a clear distortion of the regular gypsum rosette-like surface crystals is visible in Figure 7-5 (j – m). As previously discussed (Chapter 6), crystal distortion is generally attributed to the adsorption of NOM onto growing crystal faces [32,37,190]. However, as DOC measurements during scaling experiments (Table D-6) were insignificantly different from the background DOC concentrations during reference experiments, it is assumed that gypsum crystal nucleation and growth took place within

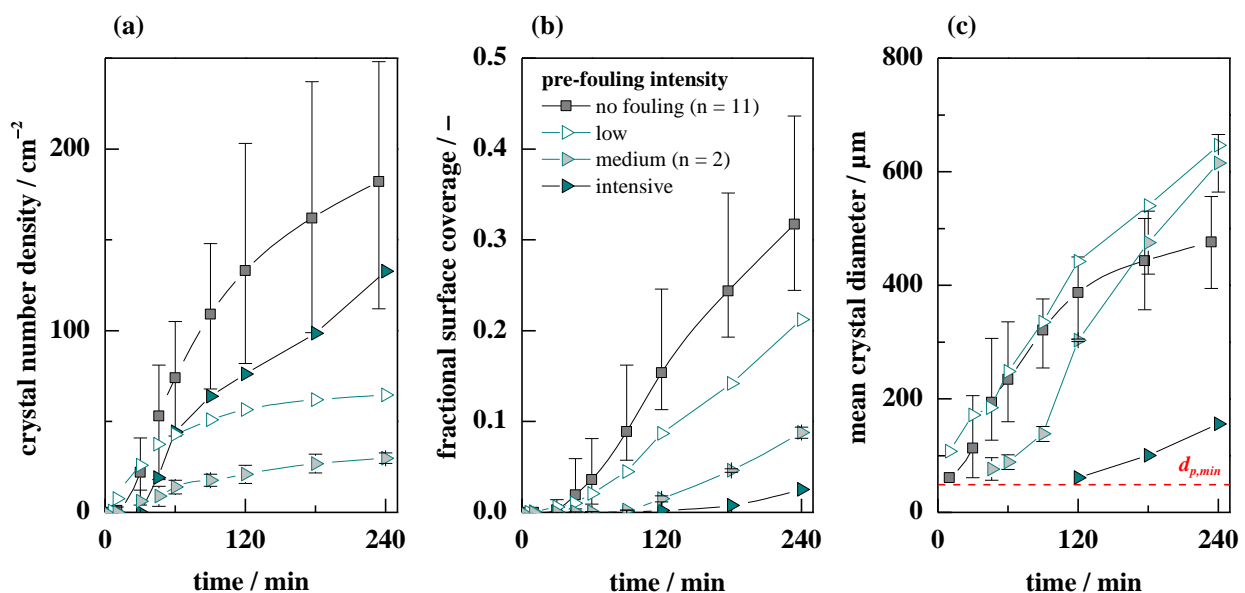


Figure 7-6: Temporal development of (a) gypsum surface crystal number density (CND) ( $d_p > 49.3 \mu\text{m}$ ), (b) fractional membrane surface coverage (FSC) and (c) mean crystal diameter ( $d_p > 49.3 \mu\text{m}$ ) on virgin membrane samples (‘*no fouling*’) and membrane samples after different intensities of HSNOM pre-fouling. For repeated experiments ( $n > 1$ ), mean values are presented with error bars representing determined minimal and maximal values. ‘*low*’:  $3 \text{ mg C}\cdot\text{l}^{-1}$  HSNOM diluted in ultrapure water; ‘*medium*’:  $3 \text{ mg C}\cdot\text{l}^{-1}$  HSNOM diluted in  $17 \text{ mmol}\cdot\text{l}^{-1}$   $\text{CaCl}_2$  solution; ‘*intensive*’:  $10 \text{ mg C}\cdot\text{l}^{-1}$  HSNOM diluted in  $17 \text{ mmol}\cdot\text{l}^{-1}$   $\text{CaCl}_2$  solution.

the three-dimensional HSNOM fouling layer of the '*intensively*' pre-fouled membrane. Accordingly, individual HSNOM molecules of the fouling layer adsorbed onto developing gypsum crystals and decelerated their growth (mechanism (III) in Figure 7-4). Growth of gypsum crystals within the fouling layer and partial crystal coverage by NOM on the '*intensively*' pre-fouled membrane is visible in the micrograph presented in Figure 7-5m. In addition, it is assumed that although the fouling layer was hydraulically irreversible, individual NOM molecules are capable of desorbing from the membrane surface and to interact directly with the crystal development.

### **Summary**

While passivation of intrinsic membrane heteronucleation sites was the dominating mechanism of reduced gypsum surface scaling after '*low*' and '*medium*' fouling, decelerated crystal growth by adsorption of NOM molecules of the dynamic fouling layer was the dominant mechanism after '*intensive*' fouling. In the latter case, decelerated crystal growth stimulated heteronucleation and led to higher crystal number densities relative to '*low*' and '*medium*' pre-fouling given that the release of supersaturation due to crystal growth was limited. The results show that the retardation of crystal growth by dissolved impurities is a far stronger and more effective way to inhibit surface crystallization on membranes compared to a reduction of effective heteronucleation affinity by chemical surface modification. It emphasizes that the three-dimensional structure of the fouling layer and its capability to supply NOM molecules that adsorb onto crystal faces is an important mechanism of interference (mechanism (III) in Figure 7-4). Importantly, the results show that fouling by aquatic NOM did not aggravate gypsum scaling due to surface crystallization even after intensified pre-fouling.

## **7.2 Effects of Dissolved NOM**

### **7.2.1 Effects of NOM Character**

During operation of RO desalination systems, NOM will unavoidably foul the membrane but NOM will also be present as dissolved molecules in the feed stream. Gypsum surface scaling behavior was therefore assessed in the presence of different dissolved NOM sources at a concentration of  $3 \text{ mg C}\cdot\text{l}^{-1}$ . Analysis of real-time images shows that the presence of all dissolved NOM sources, except SAHA, significantly decelerated individual gypsum surface crystal growth resulting in significantly smaller mean crystal diameters relative to the reference (Figure 7-7c). In addition, fractional surface coverage (Figure 7-7b) was significantly reduced by all NOM sources, except SAHA. In the presence of SAHA crystal growth and the rate of surface coverage were accelerated. These observations are supported by the monitored transmembrane pressure increases (Figure D-19a) and the final crystal masses (Figure D-19b), which were higher for SAHA and significantly lower for the remaining NOM sources relative to the reference. Controversial results were observed with respect to the detected crystal number densities (Figure 7-7a), which were significantly higher in the presence of BSA and HSNOM, unaffected in the presence of SAHA,

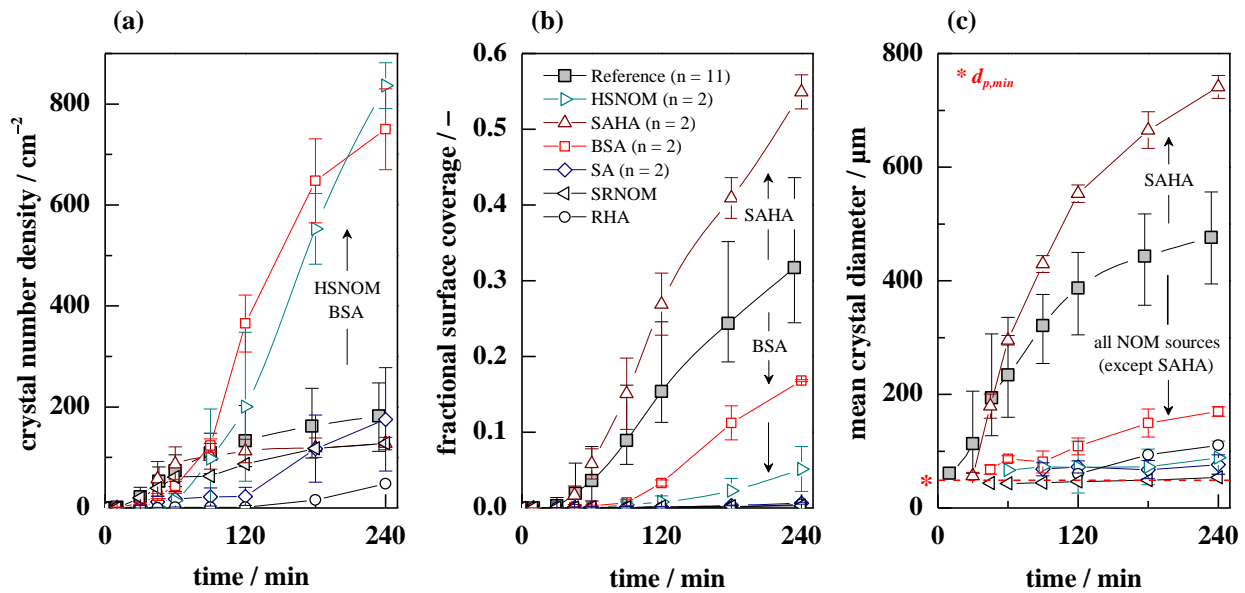


**Figure 7-7:** Temporal development of (a) gypsum surface crystal number density (CND) ( $d_p > 49.3 \mu\text{m}$ ), (b) fractional membrane surface coverage (FSC) and (c) mean crystal diameter ( $d_p > 49.3 \mu\text{m}$ ) during RO desalination in the absence ('Reference') and presence of different NOM sources at  $3 \text{ mg C}\cdot\text{l}^{-1}$ . For repeated experiments ( $n > 1$ ), mean values are presented with error bars representing determined minimal and maximal values.

delayed in the presence of SA and significantly reduced in the presence of RHA. At this point, the detection limit of the real-time imaging method ( $d_{p,min} = 49.3 \mu\text{m}$ ) has to be considered. Under conditions, where individual crystal growth is significantly retarded (all NOM sources except for SAHA) and crystal sizes remain below the detectable size, reliable determination of true crystal number densities is clearly unfeasible. While this limits the reliability of detected crystal number densities, it does not affect the reliable determination of fractional surface coverage, which is marginally affected by small crystals as was previously assessed in Chapter 4.3.

### Mechanisms of interference

Scanning electron micrographs in Figure 7-8 show distorted gypsum surface crystal growth in the presence of all NOM sources. In the presence of SAHA (Figure 7-8b), surface crystals still exhibit the typical rosette-like habit but show increased lateral expansion with a decreased number and an increased thickness of individual needles. At higher magnification (Figure 7-8c), distorted growth of individual crystal planes is visible. Gypsum rosettes were also the dominating habit in the presence of BSA (Figure 7-8d), however as indicated by real-time imaging (Figure 7-7c), their mean size is considerably smaller compared to the reference. Additionally, individual planes of BSA-distorted crystals exhibit discrete steps and kinks. In the presence of the aquatic humic substances (HSNOM, SRNOM) and the coal-extracted humic acid (RHA), development of rosette-like crystals was completely inhibited resulting in laterally discontinuous planes and distinct kinks.

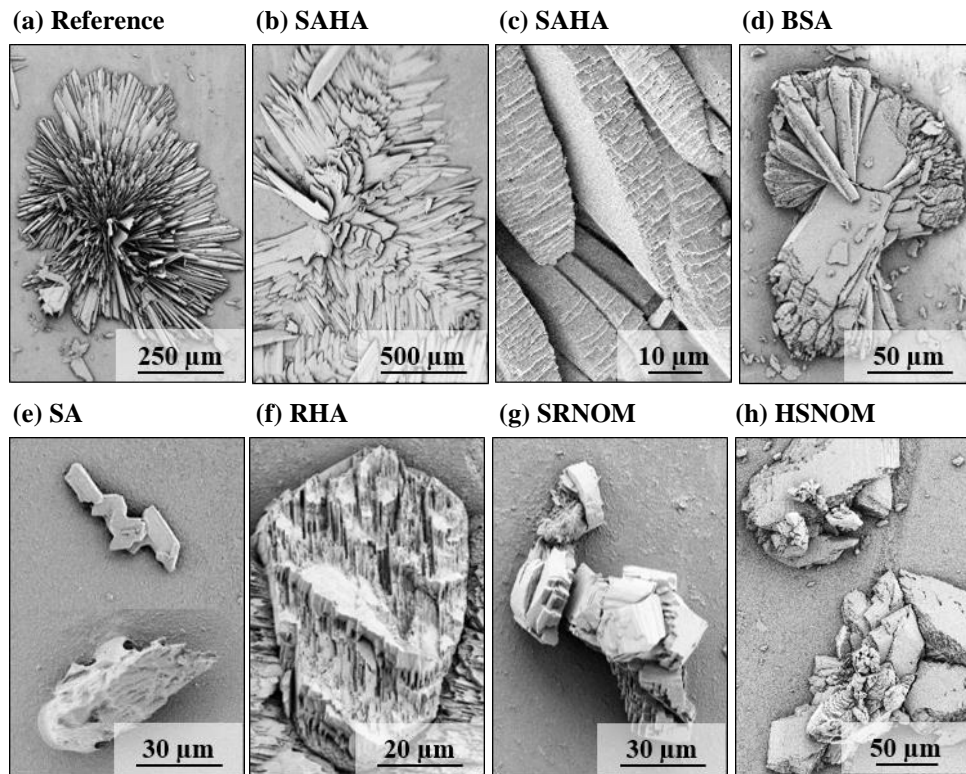


**Figure 7-8: Scanning electron micrographs (150x–3,500x magnification) of membrane surfaces showing gypsum surface crystals after scaling experiments in the presence of different NOMs.**

Gypsum surface crystals that grew in the presence of SA appear to be enclosed within the developed SA fouling layer. The above observations show that the adsorption of NOM onto growing crystal faces was the relevant mechanism that led to the distortion of regular gypsum surface crystal growth (*'crystal distortion effect'* [32,37,190]).

Significant differences were observed with respect to the degree of distortion caused by the different NOM sources. Weakest distortion, in terms of crystal habit modification, was exhibited by SAHA, however, SAHA was also the only NOM source that aggravated surface scaling. Despite the observed distortion by SAHA, individual crystal growth was enhanced. This is in contradiction to observations made during previous bulk crystallization experiments, where induction and crystallization time were prolonged and crystal growth decelerated in the presence of SAHA (Chapter 6). Characterization of SAHA (Chapter 5.1) identified a considerable fraction of large colloidal humic acids or humic acid agglomerates with molecular weights  $\geq 150$  kDa (Figure 5-2). In addition, SAHA was visually observed to cause hydraulically reversible fouling layers during permeation, which were quickly disintegrated after termination of the experiments and by gentle water flushing (Figure D-20). Considerable depletion of solution DOC confirms the strong fouling layer formation by SAHA (Table D-7). These observations indicate that SAHA formed a colloidal cake layer on the membrane surface, assumingly by the  $\geq 150$  kDa fraction (72% of the total DOC, Figure 5-2). It is assumed that the enhancement of concentration polarization by the colloidal SAHA fouling layer contributed to the accelerated lateral growth of

gypsum surface crystals (according to mechanism (II) in Figure 7-4). Effects of the  $\geq 150$  kDa fraction of SAHA are further investigated in Chapter 7.2.3.

Among the remaining NOM sources (all except for SAHA), weakest growth retardation was induced by BSA. This is in agreement with previous results from stirred beaker experiments, where BSA exhibited weak capabilities to retard observed induction (Figure 6-1) and crystallization times (Figure 6-2). The low carboxylic acidity (Table 5-3) and the globular molecular structure of BSA may limit its interactions with gypsum crystal growth [42]. Interestingly, BSA pre-fouling was observed to reduce heteronucleation affinity in Chapter 7.1.2, whereas the simultaneous presence of BSA in solution enhanced the observed effective rate of heteronucleation (Figure 7-7a). It indicates that the enhanced effective heteronucleation affinity observed in the presence of BSA was not a result of BSA fouling. Further, it supports the previous observation that surface crystal growth and heteronucleation are dependent parameters (Figure 7-3). While the relationship in Figure 7-3 exhibits that undisturbed crystal growth relates to the crystal number density (faster growth at lower *CND* and vice versa), the results of this chapter show that distortion of crystal growth by BSA stimulates heteronucleation. Similar effects were observed in the presence of HSNOM, however, growth distortion by HSNOM was stronger as compared to BSA.

Retardation of gypsum surface crystal growth was strongest in the presence of SA, the coal-extracted humic acid (RHA) and the aquatic NOM (SRNOM). The strong distortion of crystal growth in the presence of SA may be linked to the inherently strong affinity of the linear SA molecule to calcium ions and gypsum crystals. Given that the observed retardation of gypsum surface crystal growth was strong for all humic substances, except for SAHA, a direct linkage between molecular properties of the humic substances and the exhibited retardation capability cannot be extracted from the derived data.

### **Summary**

All investigated NOM sources distorted regular gypsum surface crystal growth by adsorption of dissolved NOM molecules onto crystal faces. However, the strong colloidal cake layer formation by SAHA, assumingly caused by the  $\geq 150$  kDa colloidal humic acid fraction, enhanced lateral crystal growth. It was concluded that cake-enhanced concentration polarization (CECP) may have been responsible for the observed behavior. Interestingly, this behavior was not observed in the presence of RHA, which also contains a significant fraction of humic substances with molecular weights  $\geq 150$  kDa (Chapter 5.1). However, NTA analyses showed that calcium-ion bringing was less pronounced for RHA compared to SAHA (Figure 5-3) and that resulting RHA-Ca<sup>2+</sup>-agglomerates were smaller compared to SAHA-Ca<sup>2+</sup>-agglomerates.

Deterioration of RO process performance (increase of  $\Delta p$ , Figure D-19a) due to gypsum surface scaling was significantly alleviated in the presence of all NOM sources, except SAHA, which was further supported by total crystal masses (Figure D-19b). Weakest distortion of crystal growth was observed in the presence of BSA, whereas strong distortion was exhibited by the remaining NOM

sources. While the relatively weak effects of BSA can be attributed to its low acidity and globular molecular structure, which may limit its adsorption affinity towards gypsum crystals, the indistinguishably strong effects of the remaining NOM sources, namely SA, RHA, HSNOM and SRNOM, did not allow to relate the retardation capability to their molecular properties.

Observations made during NOM pre-fouling scaling experiments (Chapter 7.1) and scaling experiments in the presence of dissolved NOM implicate that membrane surface and fouling layer properties become irrelevant under conditions where individual crystal growth is significantly distorted and decelerated by dissolved NOM from solution. For example, HSNOM and BSA pre-fouling were observed to reduce the effective heteronucleation affinity of the membrane, however, as dissolved feed solution constituent, HSNOM and BSA decelerated gypsum surface crystal growth which enhanced the observed heteronucleation. It demonstrates that the enhanced heteronucleation in the presence of HSNOM and BSA was not a consequence of NOM fouling but resulted from the limited release of supersaturation through crystal growth. It is assumed that the limited release of supersaturation by crystal growth results in a higher effective concentration of scale-forming ions at the membrane surface which stimulates heteronucleation. However, this effect was only observed in the presence of HSNOM and BSA but not for the remaining NOM sources that strongly retarded crystal growth (SA, RHA and SRNOM). In this regard, it is important to consider the detection limitation of the employed real-time imaging method ( $d_{p,min} = 49.3 \mu\text{m}$ ), which prevents the reliable detection of true crystal number densities under conditions where crystal growth is significantly decelerated and crystal sizes remain below the limit of detection. This effect becomes more important as regular crystal growth is retarded by adsorption of impurities.

### 7.2.2 Effects of HSNOM Concentration

The effects of NOM concentration on the retardation of gypsum surface scaling was exemplarily assessed in the presence of different HSNOM concentrations ( $0.5 - 5.0 \text{ mg C}\cdot\text{l}^{-1}$ ). The common rosette-like habit of gypsum surface crystals (Figure 7-9a) was still partially existing in the presence of  $0.5 \text{ mg C}\cdot\text{l}^{-1}$  HSNOM (Figure 7-9b) but diminished at higher HSNOM concentrations

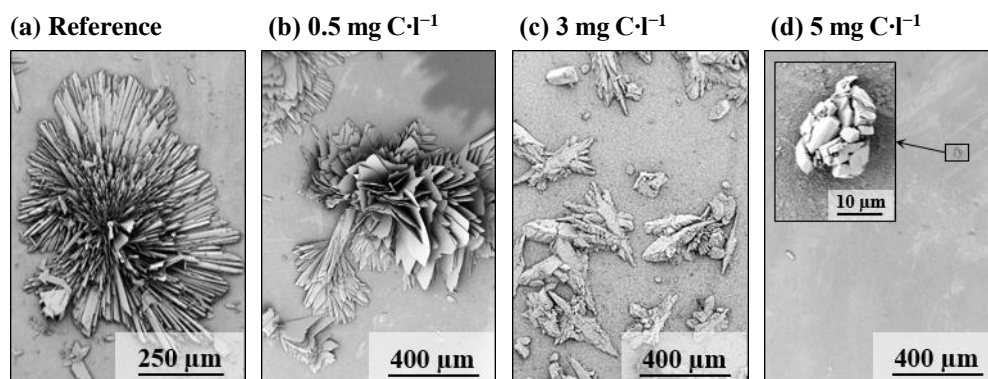
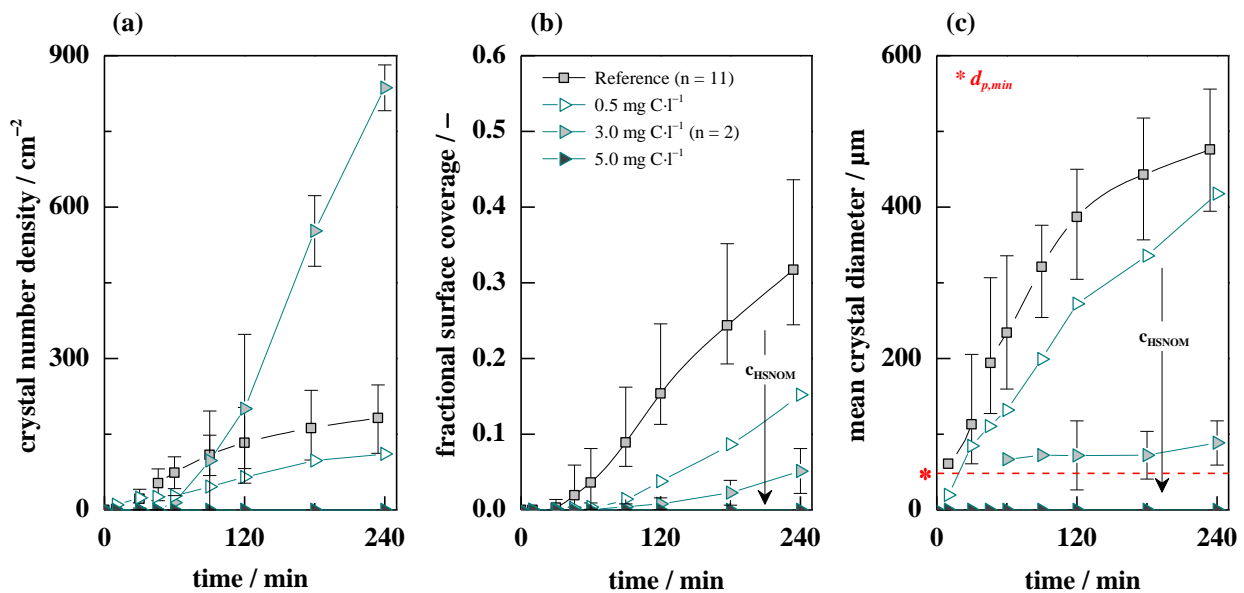


Figure 7-9: Scanning electron micrographs (200x – 5,000x magnification) of membrane surfaces showing gypsum surface crystals after scaling experiments in the presence of different HSNOM concentrations.

(Figure 7-9c,d). A concentration-retardation relationship is supported by real-time image analyses (Figure 7-10), monitored transmembrane pressure increases (Figure D-21) and determined final crystal masses (Table D-5). An NOM concentration-retardation relationship was previously observed for gypsum bulk crystallization in the presence of different NOM concentrations (Chapter 6.1) and was previously described in literature for NOM [32,34,35,190] and polymeric antiscalants [18,19,76,113,115,116,118–120].



**Figure 7-10:** Temporal development of (a) gypsum surface crystal number density ( $CND$ ) ( $d_p > 49.3 \mu\text{m}$ ), (b) fractional membrane surface coverage ( $FSC$ ) and (c) mean crystal diameter ( $d_p > 49.3 \mu\text{m}$ ) during RO desalination in the absence ('Reference') and presence of different HSNOM concentrations (0.5 – 5 mg C·l<sup>-1</sup>). For repeated experiments ( $n > 1$ ), mean values are presented with error bars representing determined minimal and maximal values.

It is important to note that the strong inhibitory effect at high HSNOM concentration (5 mg C·l<sup>-1</sup>) resulted in surface crystals (Figure 7-9d) that were below the detection limit of the real-time imaging method ( $d_{p,min} = 49.3 \mu\text{m}$ ). Thus, no crystals were detected during the respective experiment and longer operating times would have been required to attain detectable crystal sizes.

### 7.2.3 Effects of Different SAHA and HSNOM Fractions

#### Effects of the $\geq 150$ kDa colloidal SAHA fraction

SAHA was the only NOM source that exacerbated gypsum surface scaling. It was assumed that the colloidal SAHA fraction with molecular weights  $\geq 150$  kDa (based on ultrafiltration with a  $MWCO$  of 150 kDa, Figure 5-2) caused this detrimental effect. Therefore, complementary scaling experiments were conducted using the  $\leq 150$  kDa fraction of the SAHA stock solution after ultrafiltration. As expected, ultrafiltration with a  $MWCO$  of 150 kDa completely rejected the colloidal SAHA fraction that is detectable by nanoparticle tracking analysis (Table D-8).

Complementary LC-OCD analysis of both, SAHA and the  $\leq 150$  kDa SAHA fraction at  $3 \text{ mg C}\cdot\text{l}^{-1}$  (Figure D-22a), revealed that the  $\leq 150$  kDa fraction exhibited a higher oxidation yield ( $\Phi_{UV}$ , Table D-8), indicating that the colloidal fraction  $\geq 150$  kDa is incompletely oxidized by the UV irradiation and not fully quantified by the LC-OCD system. This also explains the considerably higher DOC-specific fluorescence intensity of the  $\leq 150$  kDa fraction (Figure D-23) as large humic substances are known to exhibit lower fluorescence intensity due to internal quenching, i.e. deactivation of excited states by internal self-absorbance [238,259].

Gypsum surface scaling behavior in the presence of the  $\leq 150$  kDa SAHA fraction was first investigated at a DOC concentration equivalent to the original DOC concentration of this fraction prior to ultrafiltration ( $0.5 \text{ mg C}\cdot\text{l}^{-1}$ ). Second, DOC concentration of the  $\leq 150$  kDa SAHA fraction was increased to  $3.0 \text{ mg C}\cdot\text{l}^{-1}$  for comparison to the effects observed for the other NOM sources (previous Chapter 7.2.1). Real-time imaging during scaling experiments (Figure 7-11) showed that the adverse effects caused by the original SAHA source were no longer observed in the presence of the  $\leq 150$  kDa SAHA fraction at  $0.5 \text{ mg C}\cdot\text{l}^{-1}$  and that gypsum surface crystal growth was completely inhibited or that crystals remained below the detectable size ( $d_{p,min} = 49.3 \mu\text{m}$ ) in the presence of the  $\leq 150$  kDa SAHA fraction at  $3.0 \text{ mg C}\cdot\text{l}^{-1}$ . Micrographs in Figure 7-12 confirm that the enhanced lateral growth of gypsum rosettes, which was previously observed in the presence of SAHA (Figure 7-12b), did not occur in the absence of the colloidal  $\geq 150$  kDa SAHA fraction (Figure 7-12c,d). Consequently, the colloidal DOC fraction with a molecular weight  $\geq 150$  kDa was responsible for the previously observed enhanced lateral growth, presumably due to cake

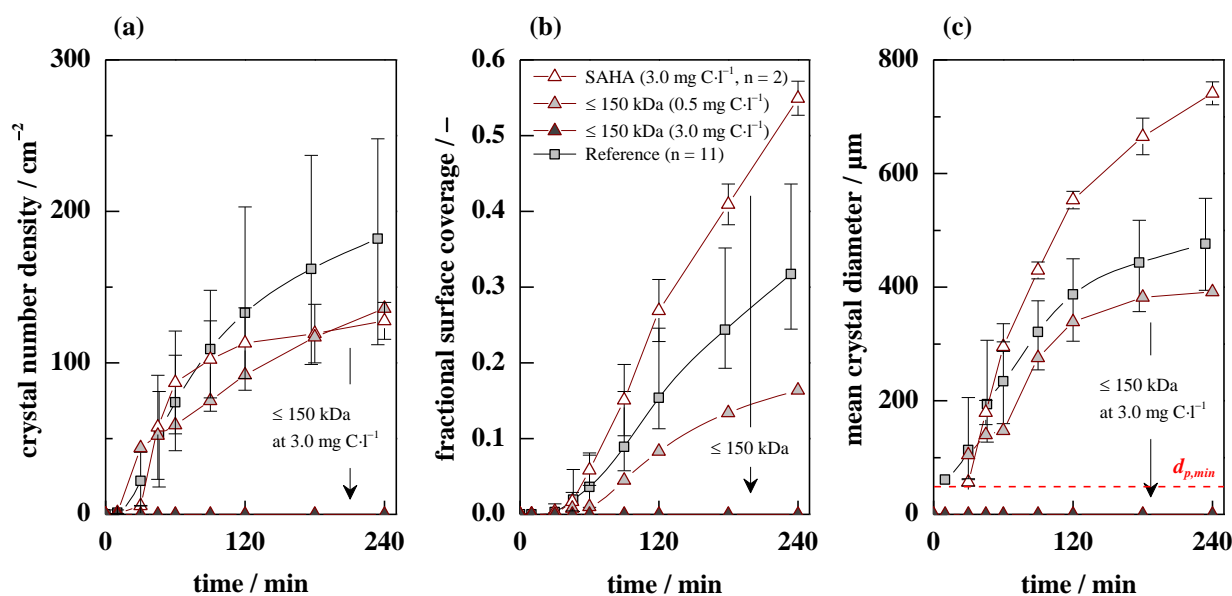
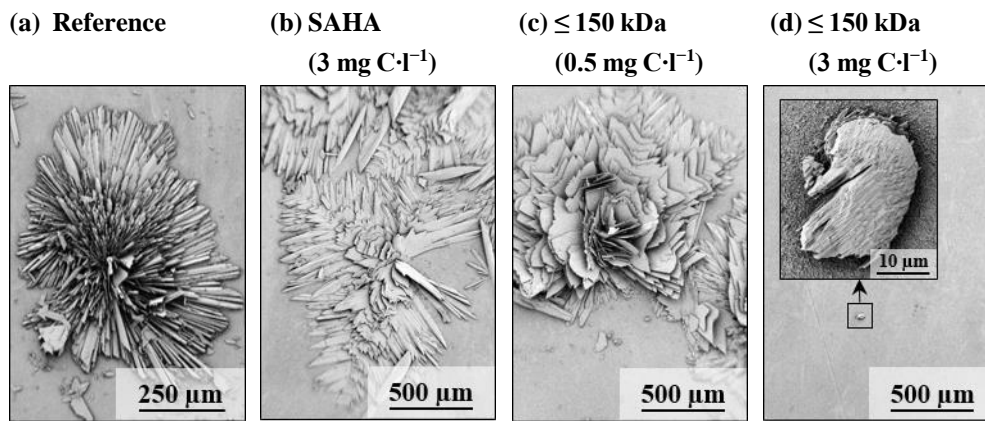


Figure 7-11: Temporal development of (a) gypsum surface crystal number density ( $CND$ ) ( $d_p > 49.3 \mu\text{m}$ ), (b) fractional membrane surface coverage ( $FSC$ ) and (c) mean crystal diameter ( $d_p > 49.3 \mu\text{m}$ ) during RO desalination in the absence ('Reference') and presence of SAHA and  $\leq 150$  kDa SAHA fraction. For repeated experiments ( $n > 1$ ), mean values are presented with error bars representing determined minimal and maximal values.



**Figure 7-12: Scanning electron micrographs (200x – 5,000x magnification) of membrane surfaces showing gypsum surface crystals after (a) reference scaling experiments and experiments in the presence of (b) 3 mg C·l<sup>-1</sup> SAHA and (c) 0.5 mg C·l<sup>-1</sup> ≤ 150 kDa SAHA fraction and (d) 3.0 mg C·l<sup>-1</sup> ≤ 150 kDa SAHA fraction.**

formation by colloidal humic acids and resulting cake-enhanced concentration polarization (CECP, mechanism (II) in Figure 7-4). At an adapted DOC concentration of 3.0 mg C·l<sup>-1</sup>, only small crystals with distorted habit and diameters below the detection limit were observed by SEM (Figure 7-12d). Development of transmembrane pressure (Figure D-25a) and final crystal masses (Table D-5) support the inhibitory effect exhibited by the ≤ 150 kDa SAHA fraction. Thus, at equivalent DOC concentration of 3.0 mg C·l<sup>-1</sup>, deceleration and distortion of crystal growth by the ≤ 150 kDa SAHA fraction appeared to be similar or superior to the effect exhibited by the other investigated humic substances (Chapter 7.2.1).

#### **Effects of the ≤ 5 kDa HSNOM fraction and the HSNOM inorganic background**

Fractionation of HSNOM by membrane filtration (Chapter 5.1) showed that only 16 % of the sample DOC was rejected by an ultrafiltration membrane with a *MWCO* of 10 kDa, whereas a significantly higher fraction of 31 % was rejected by ultrafiltration with a *MWCO* of 5 kDa (Figure 5-2). The HSNOM ≤ 5 kDa was subsequently chosen for additional gypsum surface scaling experiments because it represents a fraction of HSNOM with significantly smaller overall molecular size distribution. It has to be noted that a relatively large volume of this fraction was required for the conduction of the experiments and that the corresponding fractionation procedure required longer filtration times as compared to the fractionation displayed in Figure 5-2. Observed DOC rejection was considerably higher (74.3 %, Table D-8) assumingly due to cake layer formation by rejected HSNOM fractions and enhanced DOC rejection by this secondary membrane on top of the virgin UF membrane. The reduction of the specific UV absorbance at  $\lambda = 254$  nm from 4.91 to 3.04 l·m<sup>-1</sup>·mg C<sup>-1</sup> (Table D-8) indicates the predominant rejection of large aromatic humic substances by 5 kDa UF. This is supported by LC-OCD analysis, showing significantly longer retention times, i.e. smaller molecular weights, of the ≤ 5 kDa HSNOM fraction (Figure D-22b). The LC-OCD chromatogram indicates that large humic substances were rejected by UF and that predominantly small humic substances, building blocks as well as low

molecular weight acids and neutrals are remaining in the sample according to nomenclature introduced by Huber et al. (2011) [218]. The narrowing and the slight shift of fluorescence peaks towards smaller wavelengths (Figure D-23) further indicates the rejection of large and aromatic molecular weight humic substances [238].

In addition, the HSNOM sample was treated with powdered activated carbon as described in Chapter 3.1.1 (*'HSNOM after PAC'*) in order to assess the effects of the HSNOM inorganic background on gypsum surface scaling. LC-OCD analysis (Figure D-22b) as well as UV-vis (Table D-8) and fluorescence spectroscopy (Figure D-24) confirmed that the residual non-adsorbable NOM was negligibly small.

Gypsum surface scaling behavior in the presence of the  $\leq 5$  kDa HSNOM fraction was first investigated at a DOC concentration equivalent to the original DOC concentration of this fraction prior to ultrafiltration ( $0.8 \text{ mg}\cdot\text{l}^{-1}$ ). Second, DOC concentration of the  $\leq 5$  kDa HSNOM fraction was increased to  $3.0 \text{ mg}\cdot\text{l}^{-1}$  for comparison to the effects observed for the other NOM sources. Real-time imaging during scaling experiments showed that the scaling behavior in the presence of HSNOM after PAC and in the presence of the HSNOM  $\leq 5$  kDa fraction at both concentrations,  $0.8 \text{ mg}\cdot\text{C}\cdot\text{l}^{-1}$  and  $3.0 \text{ mg}\cdot\text{C}\cdot\text{l}^{-1}$ , was insignificantly different relative to the reference experiments (Figure 7-13). Insignificant effects on scaling propensity are further supported by the monitored transmembrane pressure increases (Figure D-25b) and the determined final crystal masses (Table D-5c). Micrographs in Figure 7-14 show that even at adapted concentration of  $3.0 \text{ mg}\cdot\text{C}\cdot\text{l}^{-1}$ , the  $\leq 5$  kDa HSNOM fraction did not inhibit the formation of typical gypsum rosette-like surface

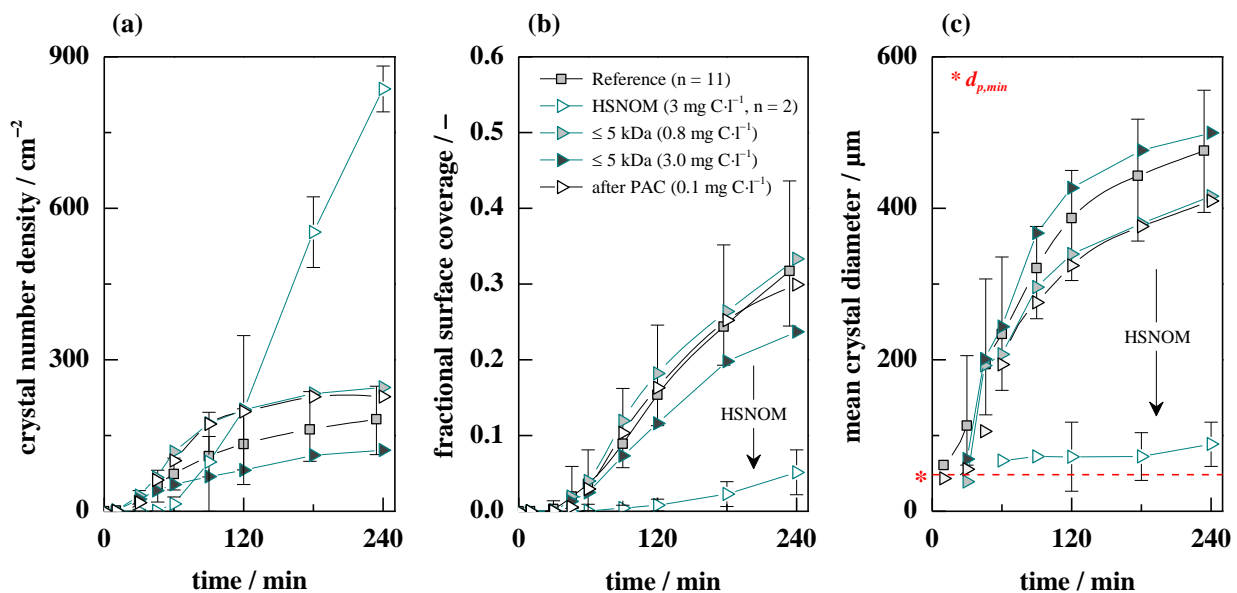
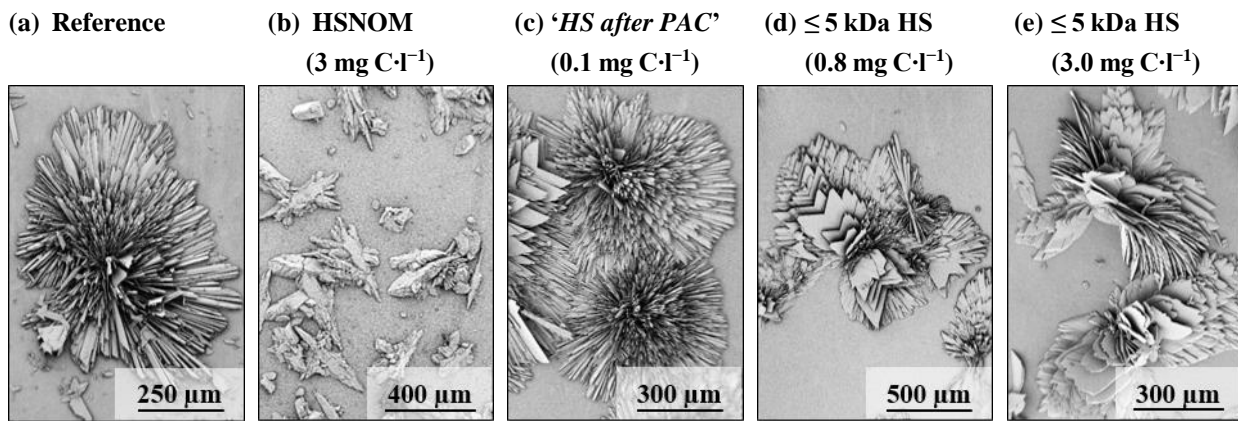


Figure 7-13: Temporal development of (a) gypsum surface crystal number density ( $CND$ ) ( $d_p > 49.3 \mu\text{m}$ ), (b) fractional membrane surface coverage ( $FSC$ ) and (c) mean crystal diameter ( $d_p > 49.3 \mu\text{m}$ ) during RO desalination in the absence (*'Reference'*) and presence of HSNOM and HSNOM fractions after 5 kDa UF filtration and PAC adsorption. For repeated experiments ( $n > 1$ ), mean values are presented with error bars representing determined minimal and maximal values.



**Figure 7-14:** Scanning electron micrographs (150x–250x magnification) of membrane surfaces showing gypsum surface crystals after scaling experiments (a) without NOM (reference) and in the presence of (b) 3.0 mg C·l<sup>-1</sup> HSNOM (HS), (c) ‘HSNOM after PAC’ fraction (0.1 mg C·l<sup>-1</sup>), (d) 0.8 mg C·l<sup>-1</sup> ≤ 5 kDa HSNOM fraction and (e) 3.0 mg C·l<sup>-1</sup> ≤ 5 kDa HSNOM fraction.

crystals. However, some degree of crystal distortion is visible as individual crystal needles are significantly thicker compared to the reference. In the presence of ‘HSNOM after PAC’, no distortion of regular crystal growth is observed (Figure 7-14c).

The results show that neither the inorganic background nor the ≤ 5 kDa UF fraction of the HSNOM sample affected gypsum surface scaling behavior and RO process performance significantly. Concluding, the ≥ 5 kDa HSNOM fraction, i.e. the large HSNOM humic substance molecules with molecular weights ≥ 5 kDa and high aromaticity rather than smaller ( $M_w \leq 5$  kDa), low aromatic humic substances, building blocks and low molecular weight substances, are responsible for the retardation of gypsum surface crystal growth. This is in agreement with previous results which indicated that RHA (Figure 7-7) and the SAHA ≤ 150 kDa fraction (Figure 7-11), both humic substances with relatively large molecular weight distributions and high aromaticity, exhibited very strong retarding effects of gypsum surface crystal growth. Contrarily, it is interesting to note that polymeric inhibitors (antiscalants) are effective only within a relatively narrow range of molecular weights, typically around 1 kDa to 5 kDa [55,115–117]. It shows that the retarding effect exhibited by the chemically complex humic substances underlies a different regularity compared to that exhibited by the less complex antiscalant molecules. Assuming that the retarding effect of both, antiscalants and NOM, is of adsorptive nature (*‘crystal distortion effect’*), the adsorption affinity onto gypsum nuclei and crystal faces will, among other parameters, determine the retarding effect. For antiscalant molecules, which are relatively small and exhibit low structural complexity, the functionality and the density of functional groups may determine the complexation and adsorption behavior. For NOM molecules, additional molecular properties, such as the aromaticity and the hydrophobicity, which will generally increase with increasing molecular weight of humic substances [170,260,261], may determine the adsorption affinity and the corresponding retardation capability. Compared to small NOM molecules ( $M_w \leq 5$  kDa), larger humic substances ( $M_w = 5 - 150$  kDa) appeared to be more effective in adsorbing onto gypsum

crystals and in disrupting or blocking regular growth of crystal faces. A superior retardation capability of larger humic substances was observed in several previous studies [32,34,35,245,246]. However, it is important to consider that this trend may only be valid for similar types of NOM molecules, for example humic substances. A combination of different molecular properties, such as stereochemical properties, functionality and content of acidic functional groups of different types of NOM (proteins, polysaccharides, humic substances) are additional parameters that will affect the retardation capability of an NOM molecule, as was previously discussed in Chapter 6.

### **Summary**

Gypsum surface scaling was previously observed to be exacerbated in the presence of SAHA. This detrimental effect was completely omitted by removing the  $\geq 150$  kDa fraction of the SAHA sample. The  $\geq 150$  kDa SAHA fraction was previously identified to consist of large humic acid agglomerates with mean diameters in the few hundred nm range (Chapter 5.1). It is assumed that the fouling layer by the  $\geq 150$  kDa SAHA fraction enhanced crystal growth due to enhanced concentration polarization (mechanism (II) in Figure 7-4). At adapted DOC concentration of  $3 \text{ mg C}\cdot\text{l}^{-1}$ , retardation exhibited by the  $\leq 150$  kDa SAHA fraction was very strong and only few crystals with sizes below the real-time imaging's detection limit ( $d_{p,min} = 49.3 \text{ }\mu\text{m}$ ) were subsequently detected by SEM. Given that SAHA is characterized by a larger molecular size distribution compared to the aquatic NOM (HSNOM and SRNOM), it is assumed that larger humic substances, except for fractions with molecular weights  $\geq 150$  kDa, are more effective in inhibiting gypsum surface crystallization. This is supported by the previously observed strong retardation capability of RHA (Figure 7-7 and Figure 7-8f), which exhibited the largest molecular size distribution of the investigated humic substances, and by the insignificant retardation capability exhibited by the  $\leq 5$  kDa HSNOM fraction. As opposed to unfractionated HSNOM, the  $\leq 5$  kDa HSNOM fraction, even at  $3.0 \text{ mg C}\cdot\text{l}^{-1}$ , did not prevent the formation of rosette-like gypsum crystals and did not alleviate RO performance losses due to gypsum surface scaling. Similarly, the inorganic background of the HSNOM source exhibited no observable effects.

It is concluded that large humic substances with molecular weights of 5 – 150 kDa and with inherently higher aromaticity are effective inhibitors of gypsum crystal growth. This is consistent with the limited number of previous studies which investigated gypsum or calcite growth retardation by NOM [32,34,35,245,246] and which observed a greater retardation of growth at increased molecular weight and aromaticity of NOM molecules of the same type. While this regularity may be valid for similar types of NOM, e.g. humic substances [34,35,245,246] or amino acids [32], it may not apply to the entirety of NOM. For example, retardation by BSA was observed to be considerably lower (Figure 7-7) despite the significantly higher molecular weight distribution compared to the humic substances (Figure 5-1).

### 7.3 Comparison of NOM Effects to Antiscalant Dosage

The retardation capability of HSNOM ( $c_{NOM} = 3 \text{ mg C}\cdot\text{l}^{-1}$ ) was evaluated against the dosage of a polyacrylic and phosphonic acid-based antiscalant ( $c_{AS} = 3 \text{ mg l}^{-1} \approx 0.75 \text{ mg C}\cdot\text{l}^{-1}$ ) during gypsum surface scaling experiments over an experimental duration of 24 h. Analyses of real-time images (Figure 7-15) show that gypsum surface scaling behavior in the presence of HSNOM and antiscalant was affected in very similar ways. The rate of crystal detection was significantly accelerated and crystal number densities ( $CND$ ) significantly higher relative to the reference (Figure 7-15a). As previously, determined values for  $CND$  should be evaluated only indicatively as true  $CNDs$  may be considerably higher given the lower limit of crystal detection ( $d_{p,min} = 49.3 \text{ }\mu\text{m}$ ). Despite increased  $CNDs$ , final fractional surface coverages (Figure 7-15b) were reduced due to decelerated gypsum surface crystal growth (Figure 7-15c). As expected from previous comparisons (Chapters 6.3 and 6.4), observed effects induced by the dosed antiscalant were stronger compared to those induced by the presence of HSNOM.

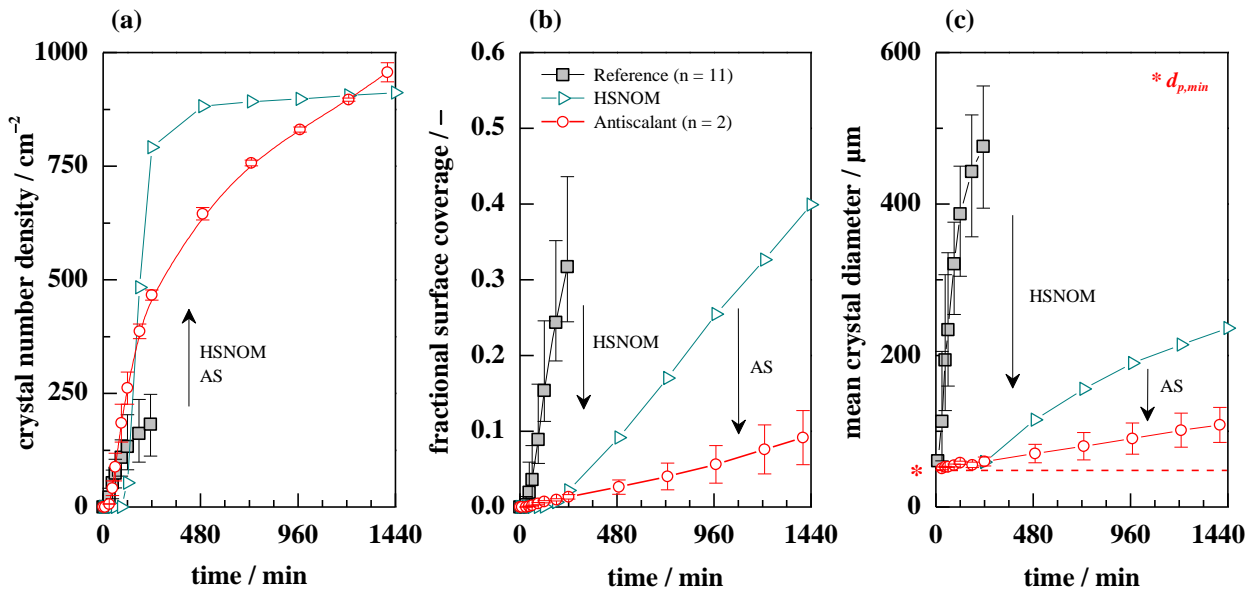


**Figure 7-15:** Temporal development of (a) gypsum surface crystal number density ( $CND$ ) ( $d_p > 49.3 \text{ }\mu\text{m}$ ), (b) fractional membrane surface coverage ( $FSC$ ) and (c) mean crystal diameter ( $d_p > 49.3 \text{ }\mu\text{m}$ ) during RO desalination in the absence ('Reference') and presence of  $3 \text{ mg}\cdot\text{l}^{-1}$  antiscalant (AS) and  $3 \text{ mg C}\cdot\text{l}^{-1}$  HSNOM. For repeated experiments ( $n > 1$ ), mean values are presented with error bars representing determined minimal and maximal values. Note that reference experiments were always terminated after 240 min due to severe increases of transmembrane pressure.

Micrographs in Figure 7-16 show that the formation of rosette-like gypsum surface crystals was inhibited in the presence of both additives, HSNOM and antiscalant. Resulting surface crystals exhibit distorted habits which indicates that 'crystal distortion' by adsorption of HSNOM and antiscalant molecules onto crystal faces was the underlying mechanism of crystal growth retardation. As previously observed (Chapter 7.2), retardation of crystal growth stimulated

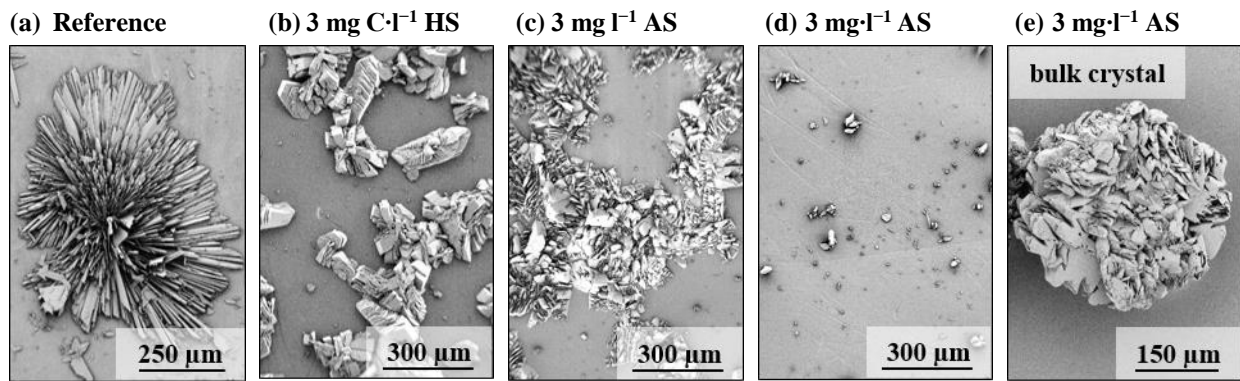


**Figure 7-16:** (a – d) Scanning electron micrographs (200x – 500x magnification) of membrane surfaces showing gypsum surface crystals after scaling experiments (a) without additive (*‘Reference’*), (b) in the presence of  $3 \text{ mg C}\cdot\text{l}^{-1}$  HSNOM (HS) and (c, d) in the presence of  $3 \text{ mg}\cdot\text{l}^{-1}$  antiscalant (AS). (e) Detached crystal agglomerate captured from the recycled concentrate stream during operation in the presence of  $3 \text{ mg}\cdot\text{l}^{-1}$  antiscalant (AS).

heteronucleation. This can be attributed to the limited release of supersaturation by crystal growth which results in higher effective scale-forming ion-concentrations at the membrane surface. It was also observed that the spatial distribution of surface crystals was inhomogeneous after dosage of antiscalant with few local areas exhibiting larger surface crystals (Figure 7-16c) and remaining areas with only smaller crystals (Figure 7-16d). In addition, the antiscalant was observed to repel crystals from the membrane surface, which resulted in partial crystal detachment and in the appearance of larger crystal agglomerates in the recycled concentrate solution (Figure 7-16e). This *‘dispersing effect’* of the antiscalant was previously observed in Chapter 4.1 and may be related to the presence of phosphonic acids in the antiscalant product [262].

Relative to the reference experiments, gypsum scaling propensity in terms of RO performance loss was reduced in the presence of both additives as demonstrated by the slower increases of transmembrane pressure (Figure 7-17). It confirms the previously observed lower fractional surface coverages. The slower increase of  $\Delta p$  in the presence of the antiscalant confirms and highlights the superior retardation capability of the employed antiscalant relative to aquatic NOM. This is further emphasized by the fact that carbon based antiscalant dosage ( $0.75 \text{ mg C}\cdot\text{l}^{-1}$ ) was significantly smaller than that of HSNOM ( $3.0 \text{ mg C}\cdot\text{l}^{-1}$ ). The superior effectiveness of the antiscalant was previously observed in Chapters 6.3 and 6.4 and can be explained by the smaller molecular size of the antiscalant molecules, which results in a higher mobility in the water phase and a significantly higher number of molecules at equivalent mass concentration, and the higher density of acidic functional groups of the antiscalant molecules. Despite the higher effectiveness of the antiscalant, the results emphasize that the aquatic NOM acts as a natural antiscalant.

Concluding, it is important to recognize that the antiscalant did not completely inhibit gypsum scale formation and corresponding RO performance loss at the given operational conditions and dosage. Complete inhibition of gypsum surface scaling by antiscalants was previously observed to require a specific minimum dosage at given operational conditions [18,19]. A concentration-

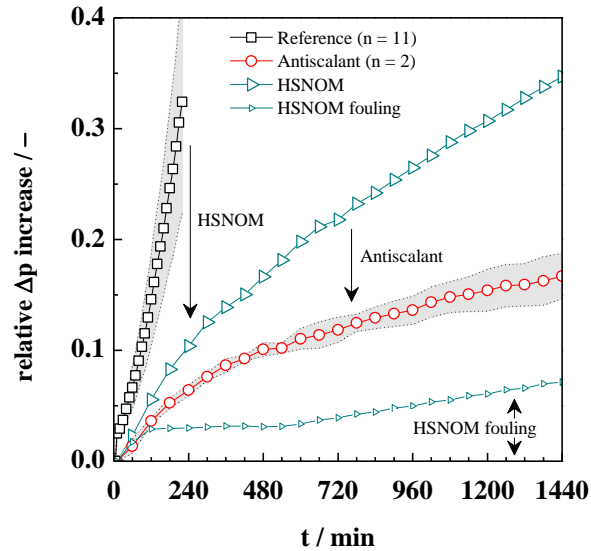


**Figure 7-17:** Transmembrane pressure ( $\Delta p$ ) increase during gypsum surface scaling experiments in the presence of  $3 \text{ mg}\cdot\text{l}^{-1}$  antiscalant and  $3 \text{ mg C}\cdot\text{l}^{-1}$  HSNOM. Grey areas identifies standard deviation of reference ( $n = 11$ ) and antiscalant-spiked ( $n = 2$ ) experiments.

inhibition relationship was demonstrated for HSNOM in Chapter 7.2.2. It can be assumed that gypsum surface scaling may be fully prevented during RO desalination of natural waters with higher NOM concentrations. Nevertheless, RO performance loss due to organic membrane fouling by NOM would need to be considered and would need to be evaluated against the beneficial anti-scaling effects.

## 8 Conclusion

This final chapter summarizes the major conclusions drawn in the individual chapters of this thesis and highlights future research directions (Chapter 8.1). Concluding, final remarks and implications for practice are provided (Chapter 8.2).

### 8.1 Conclusions and Future Directions

#### Characterization of gypsum scaling (Chapter 4)

Chapter 4.1 investigated gypsum scaling mechanisms during laboratory scale reverse osmosis (RO) desalination (permeate withdrawal,  $SI_{g,b} > 0$ ,  $\Delta p = 25$  bar,  $pH = 7$ ,  $T = 25$  °C) in dependence of operating conditions and antiscalant dosage. The following conclusions were drawn:

- Gypsum scaling will be dominated by bulk crystallization during operation above the system-specific critical supersaturation, i.e. above a critical water recovery ( $\Phi$ ), or at hydraulic residence times ( $HRT$ ) that exceed the induction time of gypsum bulk crystallization. In all other cases and at high degrees of concentration polarization, gypsum scaling will be dominated by surface crystallization.
- Thus, during large scale once-through flow RO desalination (short  $HRT$ , limited  $\Phi$ ) gypsum scaling will be dominated by surface crystallization whereas concentrate recirculation (long  $HRT$ , high  $\Phi$ ) will promote bulk crystallization.
- Antiscalant dosage (commercial polyacrylic and phosphonic acid-based product) effectively retards gypsum scaling by ‘*threshold inhibition*’ and ‘*distortion of crystal growth*’. Further, its ‘*dispersing*’ properties keep bulk crystals in suspension and inhibits their deposition.

Chapter 4.2 investigated kinetic aspects of gypsum bulk crystallization from supersaturated solution in stirred beaker crystallization experiments. The following characteristics were identified for the chosen experimental conditions ( $SI_{g,b} = 0.35 - 0.83$ ,  $pH = 7$ ,  $T = 25$  °C):

- Induction time ( $\tau$ ) decreases with increasing gypsum supersaturation ( $S$ ). The obtained data correlate well with reported values (glassware and RO experiments) and with the commonly reported behavior of  $\ln(\tau) \propto \ln^{-2}(S)$ . Similarly, the crystallization time ( $\Delta t$ , time elapsed between  $\kappa = 1$  FNU and  $\kappa = 200$  FNU) increases with decreasing supersaturation.
- During crystallization ( $\kappa = 1 - 200$  FNU), crystal concentration and mean crystal diameter increase exponentially with enhanced rate constants at higher supersaturation.
- Gypsum bulk crystallization was not affected by variations of  $pH$  between  $pH = 4.0 - 8.5$ . However,  $\tau$  and  $\Delta t$  were prolonged at  $pH = 10.0$ , which was assumed to be due the adsorption of inorganic carbon species ( $HCO_3^-$  or  $CO_3^{2-}$ ) onto subcritical gypsum nuclei and crystal faces. This assumption requires further verification in future experiments. It is recommended to perform future crystallization experiments under closed nitrogen atmosphere.

Chapter 4.3 characterized gypsum surface crystallization on RO membrane samples during laboratory scale desalination ( $J_w = 30 \text{ l}\cdot\text{m}^{-2}\cdot\text{h}^{-1}$ ,  $\text{pH} = 7$ ,  $T = 20 \text{ }^\circ\text{C}$ ). Experiments were conducted under full recirculation of permeate and concentrate using unsaturated experimental solutions ( $SI_{g,b} = -0.02$ ) and the following characteristics were obtained:

- Real-time membrane surface imaging revealed that rates of gypsum surface crystal detection and growth decreased over the experimental duration of 240 min. Resulting fractional surface coverage increased linearly and correlated with the monitored increase of transmembrane pressure ( $\Delta p$ ). It was further observed that first crystals appeared without the elapse of significant induction times.
- Significant data scatter on the local and global scale was observed in repeated experiments ( $n = 11$ ). It was suggested that polymeric RO membrane surfaces exhibit a non-uniform spatial distribution of energetically favorable heteronucleation sites and that the intrinsic membrane nucleation affinity, among other parameters, controls surface scaling behavior.
- This suggestion was further supported by observed higher effective membrane nucleation affinities in the presence of turbidity, i.e. colloids/particles that acted as heteronucleation sites after deposition, and on a repeatedly scaled and cleaned membrane. Nonetheless, deterioration of RO performance ( $\Delta p$  and final crystal mass) was not significantly affected as crystal growth was observed to be decelerated at higher crystal number densities.
- The non-uniform spatial distribution of membrane heteronucleation affinities determines the sensitivity of the employed real-time imaging method. This was highlighted by an experiment conducted at slightly increased scale-forming ion concentration (+ 4.1 %), which resulted in undetectable changes of surface scaling behavior. Therefore, it is strongly advised to assess the variability of surface scaling behavior and to verify observations through repeated experiments.

Future research should investigate the nature of membrane heteronucleation affinity in order to evaluate the relevance of chemical and physical membrane surface properties on heteronucleation. This would enable modification of membrane surfaces to reduce intrinsic nucleation affinity. If successful, long-term scaling experiments will be required to evaluate the effectiveness of reduced membrane heteronucleation affinity on long-term scaling propensity and RO performance loss.

#### **Characterization of the selected natural organic matter sources (Chapter 5)**

Sodium alginate (SA, polysaccharide), bovine serum albumin (BSA, protein), two humic acids of terrestrial origin (RHA, SAHA) and two aquatic NOM sources (HSNOM, SRNOM) were selected to represent NOM molecules in natural waters. Characterization obtained the following results:

- Size exclusion chromatography confirmed the expected molecular weights of NOM sources ( $\text{SA} > \text{BSA} > \text{humic substances}$ ). Complementary membrane (UF/NF) fractionation showed that the humic acids RHA and SAHA (terrestrial origin) exhibit larger molecular size distributions compared to the aquatic NOM sources HSNOM and SRNOM. Nanoparticle

tracking analysis showed that the terrestrial humic acids (RHA, SAHA) contain a considerable fraction of large humic acid molecules / agglomerates with molecular weights  $\geq 150$  kDa. Detected NOM colloid diameters increased in the presence of calcium ions assumingly due to calcium ion bringing of NOM molecules. This effect was most pronounced for SA and SAHA.

- The humic acids (RHA, SAHA) exhibited higher UV-vis absorbance and higher fluorescence emissions compared to aquatic humic substances (HSNOM, SRNOM). The higher aromaticity (i.e. higher light absorbance) and difference in fluorophoric character is assumed to result from the larger molecular size, the different origin (terrestrial vs. aquatic) and the absence of fulvic acids in the RHA and SAHA sources.
- Carboxylic and total acidities were determined to be lowest for BSA. SA exhibits the highest carboxylic acidity but a lower total acidity compared to the humic substances (RHA, SAHA, HSNOM, SRNOM), which exhibit comparable acidities.

Due to their commercial availability and cost efficiency, humic acids of terrestrial origin (i.e. soil- or coal-extracted) are frequently used as surrogate NOM for aquatic environments. The above characterization shows that terrestrial humic acids and aquatic NOM exhibit different properties which should be considered in future NOM-related research. Further, it is advised to establish a standard procedure for the preparation of aqueous stock solutions from humic substances supplied in dry form (e.g. RHA, SAHA and SRNOM). To date, the different preparation procedures used by researchers are not consistent. Most importantly, the molecular weight cut-off of the membrane used to reject undissolved residues will affect the final size distribution of the prepared NOM stock solution. A standard procedure would guarantee better comparability of results.

### **Effects of NOM on gypsum bulk crystallization (Chapter 6)**

Effects of selected NOM sources on the kinetics of gypsum bulk crystallization from supersaturated solution was investigated using stirred beaker crystallization experiments ( $SI_{g,b} = 0.56$  and  $0.71$ ,  $pH = 7$ ,  $T = 25$  °C). Chapter 6.1 identified the following characteristics at NOM concentrations commonly found in natural waters ( $c_{NOM} = 0 - 12$  mg C·l<sup>-1</sup>):

- All NOM sources significantly prolong observed induction ( $\tau$ ) and crystallization time ( $\Delta t$ ). Retardation capabilities increase at higher NOM concentration. Observed modified crystal habits, DOC depletions as well as smaller individual crystal diameters indicated that NOM adsorption onto crystal faces and NOM incorporation into growing crystals were the underlying mechanisms of crystal growth distortion and retardation ('*crystal distortion effect*'). Accordingly, retardation of gypsum nucleation was attributed to NOM adsorption onto subcritical nuclei ('*threshold effect*'). However, detailed analyses at molecular level are still required to verify the latter assumption.
- Retardation capabilities were observed to be NOM-specific at given DOC concentration and to be affected by gypsum supersaturation. The following trends between NOM character and retardation capability are suggested:

- Weakest retardation was exhibited by BSA due to its low carboxylic and total acidity, which limits its interaction with calcium ions, and due to its globular heart-shaped structure, which may cause an additional steric interference.
  - Strong retardation was exhibited by SA due to its high carboxylic acidity and intrinsically strong affinity for aqueous calcium ions and calcium ions on the gypsum surface. The long and aliphatic structure of SA may enhance retardation by enabling adsorption onto more than one crystal growth site and by coverage of large crystal areas. The strong affinity of SA for gypsum crystals leading to the formation of large SA-gypsum agglomerates was confirmed by microscopy and by particle size analyses.
  - Retardation capabilities of the selected humic substances were insignificantly different despite the previously identified differences in characteristics. It was concluded that the retardation capability cannot be linked to a single NOM molecule's property but is determined by a set of molecular properties, such as acidity, molecular structure, stereochemical character, molecular size and aromaticity.
- Retardation capabilities of the selected NOM sources increase with increasing  $pH$  (investigated values:  $pH = 4, 7, \text{ and } 10$ , Chapter 6.2). Enhanced retardations at high  $pH$  were attributed to the increased deprotonation of acidic functional groups at high  $pH$ . However, different degrees of  $pH$ -dependency indicated that the  $pH$ -dependent molecular structures and the stereochemical character of NOM molecules rather than acidity alone affect the retardation capability. It supports the previous assumption that NOM retardation capability is determined by a set of molecular properties.
  - A commercial polyacrylic and phosphonic acid-based antiscalant exhibited significantly higher retardation capability compared to NOM, ( $>27$ -fold higher at  $c_{DOC} = 3 \text{ mg}\cdot\text{l}^{-1}$  and  $SI_{g,b} = 0.71$ , Chapter 6.3). The high carboxylic acidity ( $>2$ -fold higher) and the less complex molecular structure is assumed to determine the superior effect of the antiscalant.

During laboratory scale RO desalination at operating conditions that favor bulk crystallization (permeate withdrawal mode,  $SI_{g,b} > 0$ ,  $\Delta p = 25 \text{ bar}$ ,  $v_{cf} = 0.27 \text{ m}\cdot\text{s}^{-1}$ ,  $pH = 7$ ,  $T = 25 \text{ }^\circ\text{C}$ ), the following observations were made in the presence of SA, BSA and RHA at an initial DOC concentration of  $3 \text{ mg}\cdot\text{l}^{-1}$  (Chapter 6.4):

- Gypsum crystallization in the recycled bulk solution was significantly retarded resulting in higher critical volumetric concentration factors, i.e. higher water recoveries before bulk crystallization is spontaneously initiated. As expected from stirred beaker crystallization experiments, retardation of NOM was inferior compared to that exhibited by the antiscalant.

To investigate effects on gypsum scaling by bulk crystallization, stirred beaker experiments can be used to supplement time- and resource-consuming RO scaling experiments. However, transferability may be limited given that hydrodynamic conditions are different and that membrane fouling during RO desalination represents an additional phenomenon. For example, the strong fouling caused by SA promoted gypsum surface crystallization on the RO membrane surface prior

to the onset of bulk crystallization. The promotion of surface crystallization was explained by the strong affinity of SA for calcium ions and gypsum crystals and by cake-enhanced concentration polarization (CECP) induced by the SA fouling layer. The relevance of CECP requires verification in further experiments. Concluding, the assessment of retardation capabilities of additives (e.g. NOM or antiscalants) should always include an assessment of their membrane fouling potential and their effects on surface crystallization and on bulk crystal deposition.

Future research should aim at identifying fractions of NOM and corresponding molecular properties that are responsible for the retarding effect on bulk crystallization of gypsum and other scale-forming salts. This may be achieved by determination of adsorption isotherms during crystal growth experiments coupled with identification of incorporated and adsorbed NOM fractions by advanced analytical techniques (e.g. fluorescence spectroscopy, LC-OCD-UVD). Fractionation of aquatic NOM sources by membrane filtration or solid-phase extraction techniques and the subsequent determination of the individual fractions' retardation capabilities represent an alternative approach. Given that aquatic NOM represents a complex mixture of organic substances, identification of relevant molecular properties that determine the retardation capability may be most feasible by using well-defined model substances, such as amino acids, polysaccharides or polycarboxylic acids. The possibility of estimating the anti-scaling effects of NOM by determination of molecular properties could lead to the reduction of water-specific antiscalant dosages and to the optimization of antiscalant design. In this regard, emphasis should also be placed upon the assessment of synergistic effects between aquatic NOM and commercial antiscalants.

### **Effects of NOM on gypsum surface crystallization on RO membranes (Chapter 7)**

Effects of NOM on gypsum surface scaling were assessed in laboratory scale RO desalination experiments ( $J_w = 30 \text{ l}\cdot\text{m}^{-2}\cdot\text{h}^{-1}$ ,  $pH = 7$ ,  $T = 20 \text{ }^\circ\text{C}$ ) that favor surface crystallization (full recirculation at  $SI_{g,b} = -0.02$ ) that enabled real-time membrane surface imaging. NOM concentrations were adapted to those expected in natural waters (i.e. few  $\text{mg C}\cdot\text{l}^{-1}$ ). First, effects of NOM pre-fouling (24 h at  $3 \text{ mg C}\cdot\text{l}^{-1}$  SA, BSA, SAHA or HSNOM) on gypsum surface scaling (in the absence of dissolved NOM) were assessed (Chapter 7.1):

- Under the given experimental conditions, NOM pre-fouling either alleviated the severity of gypsum surface scaling and the loss of RO performance ( $\Delta p$  and total crystal mass) or resulted in insignificant changes. Four simplified mechanisms of interference, which may occur simultaneously, were proposed: (I) provision of heteronucleation sites by NOM fouling layers, (II) cake-enhanced concentration polarization (CECP) due to thick NOM fouling layers, (III) inhibition and distortion of crystal nucleation and growth by NOM molecules supplied by the NOM fouling layer and (IV) inactivation of heteronucleation sites by NOM molecules.
- The latter mechanism (IV) dominated after BSA and HSNOM pre-fouling and resulted in significantly reduced final crystal number densities ( $CND \downarrow$ ) but accelerated gypsum surface

crystal growth ( $d_p \uparrow$ ). Complemented by previous observations (Chapter 4.3), a strong negative linear relationship between  $d_p$  and  $\log(CND)$  and a weak positive linear relationship between  $FSC$  and  $\log(CND)$  were identified for conditions of undisturbed crystal growth in the absence of dissolved NOM or additives. It indicates that reduced membrane heteronucleation affinity can alleviate scaling propensity ( $FSC \propto \log(CND)$ ) despite an enhancement of crystal growth ( $d_p \propto -\log(CND)$ ). Further research is needed to evaluate the effectiveness of reduced heteronucleation affinity on long-term scaling propensity.

- Interestingly, zeta potential ( $\zeta$ ) and contact angle ( $\theta_c$ ) were significantly affected by NOM pre-fouling but could not be linked to the observed gypsum surface scaling behavior under the given experimental conditions.

Second, the effects of dissolved NOM on gypsum surface scaling were assessed (Chapter 7.2):

- All NOM sources ( $3 \text{ mg C}\cdot\text{l}^{-1}$ ) except SAHA significantly decelerated gypsum surface crystal growth and distorted regular crystal habit assumingly due to adsorption and incorporation of NOM. Accordingly, RO performance loss ( $\Delta p$  and total crystal mass) was decelerated. Weakest retardation was observed for BSA, which was expected given the previously observed weak retardation of gypsum bulk crystallization by BSA. A clear NOM concentration-retardation relationship was exemplarily shown for HSNOM ( $0.5 - 5 \text{ mg C}\cdot\text{l}^{-1}$ ). The strong retardation of crystal growth by NOM ( $d_p \downarrow$ ) was observed to stimulate heteronucleation in the presence of BSA and HSNOM ( $CND \uparrow$ ). For the remaining NOM sources except SAHA, mean crystal diameters ( $d_p$ ) remained below the real-time imaging's lower detection limit of  $d_{p,min} = 49.3 \text{ }\mu\text{m}$ . In contrast, under the given experimental conditions, the presence of SAHA exacerbated gypsum surface scaling presumably due to CECP by the strong hydraulically reversible fouling layer formation of the  $\geq 150 \text{ kDa}$  SAHA fraction. Removal of this fraction by ultrafiltration ( $MWCO = 150 \text{ kDa}$ ) showed that the retardation capability of the  $\leq 150 \text{ kDa}$  SAHA fraction was competitive or even superior to that of the remaining NOM sources.
- In addition, the  $\leq 5 \text{ kDa}$  HSNOM fraction (after ultrafiltration with a  $MWCO$  of  $5 \text{ kDa}$ ) at  $3 \text{ mg C}\cdot\text{l}^{-1}$  did not retard surface crystallization, which indicates that large and aromatic humic substances with molecular weights between  $5 - 150 \text{ kDa}$  are effective crystal growth retardants compared to smaller and less aromatic humic substances.

The independent investigation of the effects induced by NOM fouling (Chapter 7.1) and those induced by dissolved NOM (Chapter 7.2) demonstrate that surface scaling behavior under experimental conditions that provide dissolved NOM is determined by direct interactions between crystal growth and NOM in solution, unless NOM fouling layer formation is severe. It implicates that membrane surface properties may be irrelevant under conditions where crystal growth is significantly distorted by NOM adsorption onto crystal faces and that adverse effects by NOM fouling are only expectable for NOM fractions that exhibit a high RO membrane fouling potential (e.g. alginate or large humic acids). Accordingly, any efforts to reduce membrane heteronucleation affinity by chemical surface modifications may be ineffective in alleviating the propensity of

surface scaling under real conditions where dissolved growth-interfering substances, such as NOM or antiscalants are present. In addition, intrinsic membrane surface properties and corresponding heteronucleation affinity will be unavoidably altered by membrane fouling. Consequently, the fouling layer properties rather than the intrinsic membrane surface properties will dominate the interfacial interactions at the membrane-liquid interface. Therefore, it is suggested that any efforts to alleviate scaling should focus on system hydrodynamics, for example optimized module and feed spacer geometries to reduce the degree of supersaturation at the membrane surface, rather than chemical membrane surface modifications.

Third, the retardation capability of HSNOM ( $3 \text{ mg C}\cdot\text{l}^{-1}$ ) was compared to that induced by a commercial phosphonic and polyacrylic acid-based antiscalant ( $3 \text{ mg}\cdot\text{l}^{-1}$ ). In agreement to previous observations, retardation by the antiscalant was superior. Besides the retardation and distortion of crystal growth, the antiscalant additionally repelled crystals from the membrane surface, which resulted in partial crystal detachment and in the appearance of larger crystal agglomerates in the recycled concentrate solution.

Analogue to the previously provided directions, future research should aim at identifying relevant fractions of NOM and according molecular properties. NOM fractionation by membrane filtration and subsequent investigation of the retarding effects induced by the individual fractions was shown to be a successful procedure to achieve this aim. Further, the quantification of synergistic effects between NOM and antiscalants would be of great practical relevance.

## **8.2 Final Remarks and Implications for Practice**

The thesis demonstrates that gypsum scaling during RO desalination by both, bulk and surface crystallization is considerably retarded in the presence of dissolved NOM. Accordingly, losses of RO process performance due to gypsum scaling are alleviated in the presence of dissolved NOM. At the same time, NOM fouling, which is unavoidable during desalination of natural waters, does not adversely affect surface scaling behavior unless fouling layer formation is strong. Given the relatively low NOM concentrations of most natural brackish waters, enhanced concentration polarization which would enhance the effective degree of supersaturation at the membrane surface and thereby enhance surface crystal nucleation and growth is not expected. Severe NOM fouling was only observed for the selected polysaccharide sodium alginate and the large colloidal humic acid (SAHA) fraction with molecular weights  $\geq 150 \text{ kDa}$ . Natural ground waters will only contain small or negligible concentrations of both, large polysaccharides and large colloidal humic acids. It emphasizes that antiscalant-free operation or operation at reduced antiscalant dosage may be implemented during desalination of natural waters with high NOM concentrations. Alternatively, water recovery at high NOM feed water concentrations may be increased.

In contrast, some natural surface waters, especially those with high microbiological activity, and waters that are strongly affected by human use (e.g. municipal and industrial wastewaters) may contain increased concentrations of critical NOM compounds with high membrane fouling

potential. Adverse effects are, however, still unlikely as feed water pretreatment typically includes low-pressure membrane filtration (MF or UF) as well as flocculation or adsorption processes, which will predominantly remove large NOM fractions and thereby remove any critical compounds. NOM fractions that remain after pretreatment are expected to effectively retard membrane scaling by gypsum and by other mineral salts.

NOM-assisted scale control appears to be a promising approach in membrane-based desalination applications where discharge requirements or other concerns (e.g. incomplete rejection of antiscalant molecules) would limit or restrict the dosage of commercial antiscalants. In those cases, feed water pretreatment, if required, should focus on removal of suspended matter (particles and large colloids) and should not target the removal of NOM with molecular weights below 150 kDa. Nevertheless, the long-term effects of membrane fouling by NOM and the potential for enhanced biofouling at high NOM concentrations need to be assessed. Required membrane cleaning intervals to remove NOM fouling and biofouling together with the associated costs and productivity losses would need to be evaluated against the beneficial anti-scaling effects of higher NOM concentrations.

The thesis also shows that effective inhibition of scaling during membrane-based desalination processes should be guaranteed at all times. Even if removable by in-situ cleaning, preceding gypsum surface scale can physically alter the membrane surface and thereby damage the active separation layer of the RO membrane and it can enhance the effective membrane heteronucleation affinity. Similarly, feed water turbidity should be low as suspended matter will likely enhance heteronucleation.

Regarding RO membrane material and module design, the results implicate that intrinsic membrane surface properties and their modification may not be successful in alleviating the propensity of scaling under operating conditions where NOM fouling occurs and where crystal growth is retarded by dissolved impurities, such as NOM or antiscalant molecules. It is therefore suggested that efforts to alleviate the propensity of scaling during RO desalination should focus on hydrodynamic aspects, such as the development of RO module designs that reduce the overall and local degrees of concentration polarization, on the optimization of conventional anti-scaling measures and on the development of alternative anti-scaling approaches.

## A. Appendix I – References and Lists

### References

- [1] M. Elimelech, W.A. Phillip, The Future of Seawater Desalination: Energy, Technology, and the Environment, *Science* 333 (6043) (2011) 712–717. DOI: 10.1126/science.1200488.
- [2] M. Elimelech, The global challenge for adequate and safe water, *Journal of Water Supply: Research and Technology - Aqua* 55 (1) (2006) 3–10. DOI: 10.2166/aqua.2005.064.
- [3] M.A. Shannon, P.W. Bohn, M. Elimelech, J.G. Georgiadis, B.J. Marinas, A.M. Mayes, Science and technology for water purification in the coming decades, *Nature* 452 (7185) (2008) 301–310. DOI: 10.1038/nature06599.
- [4] P.S. Goh, T. Matsuura, A.F. Ismail, N. Hilal, Recent trends in membranes and membrane processes for desalination, *Desalination* 391 (2016) 43–60. DOI: 10.1016/j.desal.2015.12.016.
- [5] N. Voutchkov, Desalination – Past, Present and Future, available at <http://www.iwa-network.org/desalination-past-present-future/> (accessed on January 30, 2018).
- [6] J.R. Werber, C.O. Osuji, M. Elimelech, Materials for next-generation desalination and water purification membranes, *Nature Reviews Materials* 1 (5) (2016) 16018. DOI: 10.1038/natrevmats.2016.18.
- [7] S. Lattemann, M.D. Kennedy, J.C. Schippers, G. Amy, Chapter 2: Global Desalination Situation, in: I.C. Escobar (Ed.), *Sustainable water for the future: Water recycling versus desalination*, 1st ed., Elsevier, Amsterdam, 2010, pp. 7–39. DOI: 10.1016/S1871-2711(09)00202-5.
- [8] C.J. Gabelich, P. Xu, Y. Cohen, Chapter 10: Concentrate Treatment for Inland Desalting, in: I.C. Escobar (Ed.), *Sustainable water for the future: Water recycling versus desalination*, 1st ed., Elsevier, Amsterdam, 2010, pp. 295–326. DOI: 10.1016/S1871-2711(09)00210-4.
- [9] L.F. Greenlee, D.F. Lawler, B.D. Freeman, B. Marrot, P. Moulin, Reverse osmosis desalination: water sources, technology, and today's challenges, *Water Research* 43 (9) (2009) 2317–2348. DOI: 10.1016/j.watres.2009.03.010.
- [10] A. Antony, J.H. Low, S. Gray, A.E. Childress, P. Le-Clech, G. Leslie, Scale formation and control in high pressure membrane water treatment systems: A review, *Journal of Membrane Science* 383 (1-2) (2011) 1–16. DOI: 10.1016/j.memsci.2011.08.054.
- [11] C. Bellona, J.E. Drewes, The role of membrane surface charge and solute physico-chemical properties in the rejection of organic acids by NF membranes, *Journal of Membrane Science* 249 (1-2) (2005) 227–234. DOI: 10.1016/j.memsci.2004.09.041.
- [12] K.L. Tu, A.R. Chivas, L.D. Nghiem, Effects of membrane fouling and scaling on boron rejection by nanofiltration and reverse osmosis membranes, *Desalination* 279 (1-3) (2011) 269–277. DOI: 10.1016/j.desal.2011.06.019.
- [13] E. Arkhangelsky, F. Wicaksana, S. Chou, A.A. Al-Rabiah, S.M. Al-Zahrani, R. Wang, Effects of scaling and cleaning on the performance of forward osmosis hollow fiber membranes, *Journal of Membrane Science* 415-416 (2012) 101–108. DOI: 10.1016/j.memsci.2012.04.041.
- [14] Y. Le Gouellec, M. Elimelech, Calcium sulfate (gypsum) scaling in nanofiltration of agricultural drainage water, *Journal of Membrane Science* 205 (1-2) (2002) 279–291. DOI: 10.1016/S0376-7388(02)00128-X.
- [15] S. Shirazi, C.-J. Lin, D. Chen, Inorganic fouling of pressure-driven membrane processes — A critical review, *Desalination* 250 (1) (2010) 236–248. DOI: 10.1016/j.desal.2009.02.056.
- [16] D. Hasson, H. Shemer, A. Sher, State of the Art of Friendly “Green” Scale Control Inhibitors: A Review Article, *Industrial & Engineering Chemistry Research* 50 (12) (2011) 7601–7607. DOI: 10.1021/ie200370v.

- [17] S. Gray, R. Semiat, M. Duke, A. Rahardianto, Y. Cohen, 4.04 - Seawater Use and Desalination Technology, in: P. Wilderer (Ed.), *Treatise on Water Science: Volume 3: Aquatic Chemistry and Biology*, Elsevier, Oxford, 2011, pp. 73–109. DOI: 10.1016/B978-0-444-53199-5.00077-4.
- [18] A. Rahardianto, W.-Y. Shih, R.-W. Lee, Y. Cohen, Diagnostic characterization of gypsum scale formation and control in RO membrane desalination of brackish water, *Journal of Membrane Science* 279 (1–2) (2006) 655–668. DOI: 10.1016/j.memsci.2005.12.059.
- [19] W.-Y. Shih, A. Rahardianto, R.-W. Lee, Y. Cohen, Morphometric characterization of calcium sulfate dihydrate (gypsum) scale on reverse osmosis membranes, *Journal of Membrane Science* 252 (1-2) (2005) 253–263. DOI: 10.1016/j.memsci.2004.12.023.
- [20] S. Lattemann, T. Höpner, Environmental impact and impact assessment of seawater desalination, *Desalination* 220 (1-3) (2008) 1–15. DOI: 10.1016/j.desal.2007.03.009.
- [21] C.Y. Tang, T.H. Chong, A.G. Fane, Colloidal interactions and fouling of NF and RO membranes: a review, *Advances in colloid and interface science* 164 (1-2) (2011) 126–143. DOI: 10.1016/j.cis.2010.10.007.
- [22] J.A. Leenheer, J.-P. Croué, Characterizing Aquatic Dissolved Organic Matter: Understanding the unknown structures is key to better treatment of drinking water, *Environmental Science and Technology* 37 (1) (2003) 18A-26A. DOI: 10.1021/es032333c.
- [23] F.H. Frimmel, G. Abbt-Braun, K.G. Heumann, B. Hock, H.-D. Lüdemann, M. Spiteller, *Refractory organic substances in the environment*, Wiley-VCH, Weinheim, Cambridge, 2002.
- [24] A.E. Childress, S.S. Deshmukh, Effect of humic substances and anionic surfactants on the surface charge and performance of reverse osmosis membranes, *Conference Membranes in Drinking and Industrial Water Production* 118 (1–3) (1998) 167–174. DOI: 10.1016/S0011-9164(98)00119-2.
- [25] S. Hong, M. Elimelech, Chemical and physical aspects of natural organic matter (NOM) fouling of nanofiltration membranes, *Journal of Membrane Science* 132 (2) (1997) 159–181. DOI: 10.1016/S0376-7388(97)00060-4.
- [26] C.Y. Tang, Y.-N. Kwon, J.O. Leckie, Characterization of Humic Acid Fouled Reverse Osmosis and Nanofiltration Membranes by Transmission Electron Microscopy and Streaming Potential Measurements, *Environmental Science and Technology* 41 (3) (2007) 942–949. DOI: 10.1021/es061322r.
- [27] A.E. Childress, M. Elimelech, Effect of solution chemistry on the surface charge of polymeric reverse osmosis and nanofiltration membranes, *Journal of Membrane Science* 119 (2) (1996) 253–268. DOI: 10.1016/0376-7388(96)00127-5.
- [28] H. Mo, K.G. Tay, H.Y. Ng, Fouling of reverse osmosis membrane by protein (BSA): Effects of pH, calcium, magnesium, ionic strength and temperature, *Journal of Membrane Science* 315 (1-2) (2008) 28–35. DOI: 10.1016/j.memsci.2008.02.002.
- [29] C.Y. Tang, Y.-N. Kwon, J.O. Leckie, Fouling of reverse osmosis and nanofiltration membranes by humic acid – Effects of solution composition and hydrodynamic conditions: Effects of solution composition and hydrodynamic conditions, *Journal of Membrane Science* 290 (1-2) (2007) 86–94. DOI: 10.1016/j.memsci.2006.12.017.
- [30] P.V.X. Hung, B.-S. Oh, B.X. Tung, S.-G. Oh, K.-S. Kim, S.-J. Kim, S.-H. Moon, I.S. Kim, A. Jang, Reflection of the structural distinctions of source - different humic substances on organic fouling behaviors of SWRO membranes, *Desalination* 318 (2013) 72–78. DOI: 10.1016/j.desal.2013.03.019.
- [31] M.J. Barcelona, T.R. Tosteson, D.K. Atwood, Study of organic-calcium interactions: gypsum precipitation in tropical surface waters, *Marine Chemistry* 4 (1) (1976) 89–92. DOI: 10.1016/0304-4203(76)90038-4.
- [32] S.K. Hamdona, O.A. Al Hadad, Influence of additives on the precipitation of gypsum in sodium chloride solutions, *Desalination* 228 (1) (2008) 277–286. DOI: 10.1016/j.desal.2007.11.008.
- [33] H. Bock, The effects of humic substances on the crystallization of gypsum. Master thesis. Stellenbosch University, Stellenbosch, South Africa, 2017.

- [34] Y.-P. Lin, P.C. Singer, G.R. Aiken, Inhibition of calcite precipitation by natural organic material - kinetics, mechanism, and thermodynamics // Inhibition of Calcite Precipitation by Natural Organic Material: Kinetics, Mechanism, and Thermodynamics, *Environmental Science and Technology* 39 (17) (2005) 6420–6428. DOI: 10.1021/es050470z.
- [35] A.R. Hoch, M.M. Reddy, G.R. Aiken, Calcite crystal growth inhibition by humic substances with emphasis on hydrophobic acids from the Florida Everglades, *Geochimica et Cosmochimica Acta* 64 (1) (2000) 61–72. DOI: 10.1016/S0016-7037(99)00179-9.
- [36] I. Koyuncu, M.R. Wiesner, Morphological Variations of Precipitated Salts on NF and RO Membranes, *Environmental Engineering Science* 24 (5) (2007) 602–614. DOI: 10.1089/ees.2006.0114.
- [37] S. Lee, J.-S. Choi, C.-H. Lee, Behaviors of dissolved organic matter in membrane desalination, *Desalination* 238 (1-3) (2009) 109–116. DOI: 10.1016/j.desal.2008.01.041.
- [38] H.-J. Oh, Y.-K. Choung, S. Lee, J.-S. Choi, T.-M. Hwang, J.H. Kim, Scale formation in reverse osmosis desalination: model development, *Desalination* 238 (1-3) (2009) 333–346. DOI: 10.1016/j.desal.2008.10.005.
- [39] A.J. Karabelas, A. Karanasiou, D.C. Sioutopoulos, Experimental study on the effect of polysaccharides on incipient membrane scaling during desalination, *Desalination* 416 (2017) 106–121. DOI: 10.1016/j.desal.2017.04.009.
- [40] E. Curcio, X. Ji, G. Di Profio, A.O. Sulaiman, E. Fontananova, E. Drioli, Membrane distillation operated at high seawater concentration factors: Role of the membrane on CaCO<sub>3</sub> scaling in presence of humic acid, *Journal of Membrane Science* 346 (2) (2010) 263–269. DOI: 10.1016/j.memsci.2009.09.044.
- [41] Y. Liu, B. Mi, Combined fouling of forward osmosis membranes: Synergistic foulant interaction and direct observation of fouling layer formation, *Journal of Membrane Science* 407-408 (2012) 136–144. DOI: 10.1016/j.memsci.2012.03.028.
- [42] Y. Liu, B. Mi, Effects of organic macromolecular conditioning on gypsum scaling of forward osmosis membranes, *Journal of Membrane Science* 450 (2014) 153–161. DOI: 10.1016/j.memsci.2013.09.001.
- [43] J. Wang, L. Wang, R. Miao, Y. Lv, X. Wang, X. Meng, R. Yang, X. Zhang, Enhanced gypsum scaling by organic fouling layer on nanofiltration membrane: Characteristics and mechanisms, *Water Research* 91 (2016) 203–213. DOI: 10.1016/j.watres.2016.01.019.
- [44] National Research Council, *Desalination: A National Perspective*, National Academies Press, Washington, D.C., 2008. DOI: 10.17226/12184.
- [45] C. Fritzmann, J. Löwenberg, T. Wintgens, T. Melin, State-of-the-art of reverse osmosis desalination, *Desalination* 216 (1-3) (2007) 1–76. DOI: 10.1016/j.desal.2006.12.009.
- [46] R. Semiat, *Energy Issues in Desalination Processes*, *Environmental Science and Technology* 42 (22) (2008) 8193–8201. DOI: 10.1021/es801330u.
- [47] J. MacHarg, T.F. Seacord, B. Sessions, ADC baseline tests reveal trends in membrane performance, *Desalination & Water Reuse* 18 (2008) 30–39.
- [48] S.N. Davis, R.J.M. DeWriest, *Hydrogeology*, John Wiley & Sons, New York, 1966.
- [49] J.C. Crittenden, R.R. Trussell, D.W. Hand, K.J. Howe, G. Tchobanoglous, *MWH's water treatment: Principles and design*, 3rd ed., John Wiley and Sons, Hoboken, N.J, 2012.
- [50] R.W. Baker, *Membrane technology and applications*, 3rd ed., Wiley, Chichester, UK, 2012. DOI: 10.1002/9781118359686.
- [51] A.G. Fane, C.Y. Tang, R. Wang, *Membrane Technology for Water: Microfiltration, Ultrafiltration, Nanofiltration, and Reverse Osmosis*, in: P. Wilderer (Ed.), *Treatise on Water Science: Volume 3: Aquatic Chemistry and Biology*, Elsevier, Oxford, 2011, pp. 301–335. DOI: 10.1016/B978-0-444-53199-5.00091-9.
- [52] R.D. Cohen, R.F. Probstein, Colloidal fouling of reverse osmosis membranes, *Journal of Colloid and Interface Science* 114 (1) (1986) 194–207. DOI: 10.1016/0021-9797(86)90252-3.

- [53] P. Bacchin, P. Aimar, V. Sanchez, Model for colloidal fouling of membranes, *AIChE Journal* 41 (2) (1995) 368–376. DOI: 10.1002/aic.690410218.
- [54] A.J. Karabelas, A. Karanasiou, S.T. Mitrouli, Incipient membrane scaling by calcium sulfate during desalination in narrow spacer-filled channels, *Desalination* 345 (2014) 146–157. DOI: 10.1016/j.desal.2014.04.020.
- [55] D. Hasson, R. Semiat, Scale Control in Saline and Wastewater Desalination, *Israel Journal of Chemistry* 46 (1) (2006) 97–104. DOI: 10.1560/BM6M-01UJ-CNP2-W0E3.
- [56] B. Mi, O. Coronell, B. Marinas, F. Watanabe, I. Petrov, Physico-chemical characterization of NF/RO membrane active layers by Rutherford backscattering spectrometry, *Journal of Membrane Science* 282 (1-2) (2006) 71–81. DOI: 10.1016/j.memsci.2006.05.015.
- [57] A.E. Childress, M. Elimelech, Relating Nanofiltration Membrane Performance to Membrane Charge (Electrokinetic) Characteristics, *Environmental Science and Technology* 34 (17) (2000) 3710–3716. DOI: 10.1021/es0008620.
- [58] M.J. Ariza, J. Benavente, E. Rodríguez-Castellón, L. Palacio, Effect of hydration of polyamide membranes on the surface electrokinetic parameters: surface characterization by x-ray photoelectronic spectroscopy and atomic force microscopy, *Journal of Colloid and Interface Science* 247 (1) (2002) 149–158. DOI: 10.1006/jcis.2001.8071.
- [59] C.R. Bartels, K.L. Kreuz, A. Wachtel, Structure-performance relationships of composite membranes: Porous support densification, *Journal of Membrane Science* 32 (2-3) (1987) 291–312. DOI: 10.1016/S0376-7388(00)85013-9.
- [60] S.D. Arthur, Structure-property relationship in a thin film composite reverse osmosis membrane, *Journal of Membrane Science* 46 (2-3) (1989) 243–260. DOI: 10.1016/S0376-7388(00)80338-5.
- [61] V. Freger, J. Gilron, S. Belfer, TFC polyamide membranes modified by grafting of hydrophilic polymers: An FT-IR/AFM/TEM study, *Journal of Membrane Science* 209 (1) (2002) 283–292. DOI: 10.1016/S0376-7388(02)00356-3.
- [62] S.-Y. Kwak, Relationship of relaxation property to reverse osmosis permeability in aromatic polyamide thin-film-composite membranes, *Polymer* 40 (23) (1999) 6361–6368. DOI: 10.1016/S0032-3861(98)00842-8.
- [63] D.H. Everett, Manual of Symbols and Terminology for Physicochemical Quantities and Units, Appendix II: Definitions, Terminology and Symbols in Colloid and Surface Chemistry, *Pure and Applied Chemistry* 31 (4) (1972). DOI: 10.1351/pac197231040577.
- [64] T. Tran, B. Bolto, S. Gray, M. Hoang, E. Ostarcevic, An autopsy study of a fouled reverse osmosis membrane element used in a brackish water treatment plant, *Membranes* 41 (17) (2007) 3915–3923. DOI: 10.1016/j.watres.2007.06.008.
- [65] J.W. Mullin, *Crystallization*, 4th ed., Butterworth-Heinemann, Oxford, 2001.
- [66] J.B. Clarke, J.W. Hastie, L.H.E. Kihlborg, R. Metselaar, M.M. Thackeray, Definitions of terms relating to phase transitions of the solid state (IUPAC Recommendations 1994), *Pure and Applied Chemistry* 66 (3) (1994). DOI: 10.1351/pac199466030577.
- [67] W. Beckmann, *Crystallization*, Wiley-VCH Verlag GmbH & Co. KGaA, Weinheim, Germany, 2013. DOI: 10.1002/9783527650323.
- [68] S. Karthika, T.K. Radhakrishnan, P. Kalaichelvi, A Review of Classical and Nonclassical Nucleation Theories, *Crystal Growth & Design* 16 (11) (2016) 6663–6681. DOI: 10.1021/acs.cgd.6b00794.
- [69] D. Gebauer, A. Völkel, H. Cölfen, Stable prenucleation calcium carbonate clusters, *Science* 322 (5909) (2008) 1819–1822. DOI: 10.1126/science.1164271.
- [70] E.M. Pouget, P.H.H. Bomans, J.A.C.M. Goos, P.M. Frederik, G. de With, N.A.J.M. Sommerdijk, The initial stages of template-controlled CaCO<sub>3</sub> formation revealed by cryo-TEM, *Science* 323 (5920) (2009) 1455–1458. DOI: 10.1126/science.1169434.

- [71] M. Volmer, *Kinetik der Phasenbildung*, J. W. Edwards, 1939.
- [72] A. Mersmann, *Crystallization Technology Handbook*, 2nd ed., Marcel Dekker Inc, Hoboken, 2001.
- [73] A. Mersmann, K. Bartosch, How to predict the metastable zone width, *Journal of Crystal Growth* 183 (1-2) (1998) 240–250. DOI: 10.1016/S0022-0248(97)00417-X.
- [74] J. Nývlt, J. Ulrich, *Admixtures in crystallization*, VCH, Weinheim, New York, 1995. DOI: 10.1002/9783527615315.
- [75] V. Babić-Ivančić, H. Füredi-Milhofer, B. Purgarić, N. Brničević, Z. Despotović, Precipitation of calcium oxalates from high ionic strength solutions III. the influence of reactant concentrations on the properties of the precipitates, *Journal of Crystal Growth* 71 (3) (1985) 655–663. DOI: 10.1016/0022-0248(85)90374-4.
- [76] S. He, J.E. Oddo, M.B. Tomson, The inhibition of gypsum and barite nucleation in NaCl brines at temperatures from 25 to 90 °C, *Applied Geochemistry* 9 (5) (1994) 561–567. DOI: 10.1016/0883-2927(94)90018-3.
- [77] S.K. Hamdona, U.A. Al Hadad, Crystallization of calcium sulfate dihydrate in the presence of some metal ions, *Journal of Crystal Growth* 299 (1) (2007) 146–151. DOI: 10.1016/j.jcrysgro.2006.11.139.
- [78] K.-W. Benz, W. Neumann, A. Mogilatenko, *Introduction to crystal growth and characterization*, Wiley-VCH, Weinheim, 2014.
- [79] I. Sunagawa, *Growth and Morphology of Crystals*, Forma 14 (1999) 147–166.
- [80] J. Ulrich, S. Niehörster, Additive für die Kristallisation: Maßgeschneidert und multifunktionell, *Chemische Industrie* 11 (1994) 46–47.
- [81] I. Weissbuch, L.J.W. Shimon, E.M. Landau, R. Popovitz-Biro, Z. Berkovitch-Yellin, L. Addadi, M. Lahav, L. Leiserowitz, 'Tailormade' auxiliaries for nucleation, growth and dissolution of organic crystals, *Pure and Applied Chemistry* 58 (6) (1986) 107. DOI: 10.1351/pac198658060947.
- [82] G. Clydesdale, K.J. Roberts, R. Docherty, Modelling the morphology of molecular crystals in the presence of disruptive tailor-made additives, *Journal of Crystal Growth* 135 (1-2) (1994) 331–340. DOI: 10.1016/0022-0248(94)90760-9.
- [83] G. Clydesdale, K.J. Roberts, K. Lewtas, R. Docherty, Modelling the morphology of molecular crystals in the presence of blocking tailor-made additives, *Journal of Crystal Growth* 141 (3-4) (1994) 443–450. DOI: 10.1016/0022-0248(94)90250-X.
- [84] S. Lee, J. Kim, C.-H. Lee, Analysis of CaSO<sub>4</sub> scale formation mechanism in various nanofiltration modules, *Journal of Membrane Science* 163 (1) (1999) 63–74. DOI: 10.1016/S0376-7388(99)00156-8.
- [85] S. Lee, C.-H. Lee, Effect of operating conditions on CaSO<sub>4</sub> scale formation mechanism in nanofiltration for water softening, *Water Research* 34 (15) (2000) 3854–3866. DOI: 10.1016/S0043-1354(00)00142-1.
- [86] M. Kostoglou, A.J. Karabelas, Modeling scale formation in flat-sheet membrane modules during water desalination, *AIChE Journal* 59 (8) (2013) 2917–2927. DOI: 10.1002/aic.14045.
- [87] A.G. Pervov, Scale formation prognosis and cleaning procedure schedules in reverse osmosis systems operation, *Desalination* 83 (1-3) (1991) 77–118. DOI: 10.1016/0011-9164(91)85087-B.
- [88] P. Dydo, M. Turek, J. Ciba, K. Wandachowicz, J. Misztal, The nucleation kinetic aspects of gypsum nanofiltration membrane scaling, *Desalination* 164 (1) (2004) 41–52. DOI: 10.1016/S0011-9164(04)00154-7.
- [89] D. Hasson, A. Drak, R. Semiat, Inception of CaSO<sub>4</sub> scaling on RO membranes at various water recovery levels, *Desalination* 139 (1-3) (2001) 73–81. DOI: 10.1016/S0011-9164(01)00296-X.
- [90] D. Hasson, A. Drak, R. Semiat, Induction times induced in an RO system by antiscalants delaying CaSO<sub>4</sub> precipitation, *Desalination* 157 (1-3) (2003) 193–207. DOI: 10.1016/S0011-9164(03)00399-0.
- [91] M. Uchymiak, E. Lyster, J. Glater, Y. Cohen, Kinetics of gypsum crystal growth on a reverse osmosis membrane, *Journal of Membrane Science* 314 (1-2) (2008) 163–172. DOI: 10.1016/j.memsci.2008.01.041.
- [92] A.I. Radu, *Modeling fouling in spiral wound membrane systems*. Dissertation. TU Delft, Delft, NL, 2014. DOI: 10.4233/uuid:e5b8ff75-73dd-444f-8213-0b4acfd2378e.

- [93] P.S. Goh, W.J. Lau, M.H.D. Othman, A.F. Ismail, Membrane fouling in desalination and its mitigation strategies, *Desalination* 425 (2018) 130–155. DOI: 10.1016/j.desal.2017.10.018.
- [94] A.J. Karabelas, M. Kostoglou, S.T. Mitrouli, Incipient crystallization of sparingly soluble salts on membrane surfaces: The case of dead-end filtration with no agitation, *Desalination* 273 (1) (2011) 105–117. DOI: 10.1016/j.desal.2010.10.057.
- [95] M. Kostoglou, S.T. Mitrouli, A.J. Karabelas, Model Development and Experimental Data Analysis for Calcium Carbonate Membrane Scaling during Dead-End Filtration with Agitation, *Industrial & Engineering Chemistry Research* 56 (2) (2017) 603–613. DOI: 10.1021/acs.iecr.6b04063.
- [96] S.T. Mitrouli, M. Kostoglou, A.J. Karabelas, Calcium carbonate scaling of desalination membranes: Assessment of scaling parameters from dead-end filtration experiments, *Journal of Membrane Science* 510 (2016) 293–305. DOI: 10.1016/j.memsci.2016.02.061.
- [97] S. Mitrouli, A.J. Karabelas, A. Karanasiou, M. Kostoglou, Incipient calcium carbonate scaling of desalination membranes in narrow channels with spacers—experimental insights, *Journal of Membrane Science* 425–426 (2013) 48–57. DOI: 10.1016/j.memsci.2012.09.025.
- [98] E. Lyster, M.-m. Kim, J. Au, Y. Cohen, A method for evaluating antiscalant retardation of crystal nucleation and growth on RO membranes, *Journal of Membrane Science* 364 (1-2) (2010) 122–131. DOI: 10.1016/j.memsci.2010.08.020.
- [99] K.D. Cobry, Z. Yuan, J. Gilron, V.M. Bright, W.B. Krantz, A.R. Greenberg, Comprehensive experimental studies of early-stage membrane scaling during nanofiltration, *Desalination* 283 (2011) 40–51. DOI: 10.1016/j.desal.2011.04.053.
- [100] N. Her, G. Amy, C. Jarusutthirak, Seasonal variations of nanofiltration (NF) foulants: identification and control, *Desalination* 132 (1-3) (2000) 143–160. DOI: 10.1016/S0011-9164(00)00143-0.
- [101] M. Gloede, T. Melin, Potentials and limitations of molecular modelling approaches for scaling and scale inhibiting mechanisms, *Desalination* 199 (1-3) (2006) 26–28. DOI: 10.1016/j.desal.2006.03.012.
- [102] B. Mi, M. Elimelech, Gypsum scaling and cleaning in forward osmosis: Measurements and mechanisms, *Environmental Science and Technology* 44 (6) (2010) 2022–2028. DOI: 10.1021/es903623r.
- [103] M. Xie, S.R. Gray, Gypsum scaling in forward osmosis: Role of membrane surface chemistry, *Journal of Membrane Science* 513 (2016) 250–259. DOI: 10.1016/j.memsci.2016.04.022.
- [104] K. Rathinam, Y. Oren, W. Petry, D. Schwahn, R. Kasher, Calcium phosphate scaling during wastewater desalination on oligoamide surfaces mimicking reverse osmosis and nanofiltration membranes, *Water Research* (2017). DOI: 10.1016/j.watres.2017.10.055.
- [105] S.C. Chen, J. Su, F.-J. Fu, B. Mi, T.-S. Chung, Gypsum ( $\text{CaSO}_4 \cdot 2\text{H}_2\text{O}$ ) Scaling on Polybenzimidazole and Cellulose Acetate Hollow Fiber Membranes under Forward Osmosis, *Membranes* 3 (4) (2013) 354–374. DOI: 10.3390/membranes3040354.
- [106] N.H. Lin, W.-Y. Shih, E. Lyster, Y. Cohen, Crystallization of calcium sulfate on polymeric surfaces, *Journal of Colloid and Interface Science* 356 (2) (2011) 790–797. DOI: 10.1016/j.jcis.2011.01.042.
- [107] D.L. Shaffer, M.E. Tousley, M. Elimelech, Influence of polyamide membrane surface chemistry on gypsum scaling behavior, *Journal of Membrane Science* 525 (2017) 249–256. DOI: 10.1016/j.memsci.2016.11.003.
- [108] C.Y. Tang, Y.-N. Kwon, J.O. Leckie, Effect of membrane chemistry and coating layer on physiochemical properties of thin film composite polyamide RO and NF membranes, *Desalination* 242 (1-3) (2009) 149–167. DOI: 10.1016/j.desal.2008.04.003.
- [109] C.Y. Tang, Y.-N. Kwon, J.O. Leckie, Probing the nano- and micro-scales of reverse osmosis membranes – A comprehensive characterization of physiochemical properties of uncoated and coated membranes by XPS, TEM, ATR-FTIR, and streaming potential measurements, *Journal of Membrane Science* 287 (1) (2007) 146–156. DOI: 10.1016/j.memsci.2006.10.038.
- [110] V. Freger, Nanoscale Heterogeneity of Polyamide Membranes Formed by Interfacial Polymerization, *Langmuir* 19 (11) (2003) 4791–4797. DOI: 10.1021/la020920q.

- [111] S.T. Mitrouli, A.J. Karabelas, N.P. Isaias, Polyamide active layers of low pressure RO membranes: Data on spatial performance non-uniformity and degradation by hypochlorite solutions, *Desalination* 260 (1-3) (2010) 91–100. DOI: 10.1016/j.desal.2010.04.061.
- [112] M. Gloede, T. Melin, Physical aspects of membrane scaling, *Desalination* 224 (1-3) (2008) 71–75. DOI: 10.1016/j.desal.2007.02.081.
- [113] E.G. Darton, Membrane chemical research: Centuries apart, *Desalination* 132 (1-3) (2000) 121–131. DOI: 10.1016/S0011-9164(00)00141-7.
- [114] M. Gloede, T. Melin, Entwicklung von Prozessen zur Steigerung der Wasserausbeute von Membranverfahren bei der Brackwasseraufbereitung in Entsalzungsanlagen: Abschlussbericht zum BMBF-Vorhaben 02WT0537, 2007.
- [115] Z. Amjad, J.P. Hooley, Effect of antiscalants on the precipitation of calcium carbonate in aqueous solutions, *Tenside, Surfactants, Detergents* 31 (1) (1994) 12–17.
- [116] M.G. Lioliou, C.A. Paraskeva, P.G. Koutsoukos, A.C. Payatakes, Calcium sulfate precipitation in the presence of water-soluble polymers, *Journal of Colloid and Interface Science* 303 (1) (2006) 164–170. DOI: 10.1016/j.jcis.2006.07.054.
- [117] M. Öner, Ö. Doğan, G. Öner, The influence of polyelectrolytes architecture on calcium sulfate dihydrate growth retardation, *Journal of Crystal Growth* 186 (3) (1998) 427–437. DOI: 10.1016/S0022-0248(97)00518-6.
- [118] Z. Amjad, R.T. Landgraf, J.L. Penn, Calcium sulfate dihydrate (gypsum) scale inhibition by PAA, PAPEMP, and PAA/PAPEMP blend, *International Journal of Corrosion and Scale Inhibition* 3 (1) (2014) 35–47. DOI: 10.17675/2305-6894-2014-3-1-035-047.
- [119] W.-Y. Shih, K. Albrecht, J. Glater, Y. Cohen, A dual-probe approach for evaluation of gypsum crystallization in response to antiscalant treatment, *Desalination* 169 (3) (2004) 213–221. DOI: 10.1016/j.desal.2003.12.008.
- [120] W.-Y. Shih, J. Gao, A. Rahardianto, J. Glater, Y. Cohen, C.J. Gabelich, Ranking of antiscalant performance for gypsum scale suppression in the presence of residual aluminum, *Desalination* 196 (1–3) (2006) 280–292.
- [121] A. Sweity, Z. Ronen, M. Herzberg, Induced organic fouling with antiscalants in seawater desalination, *Desalination* 352 (2014) 158–165. DOI: 10.1016/j.desal.2014.08.018.
- [122] A. Sweity, Y. Oren, Z. Ronen, M. Herzberg, The influence of antiscalants on biofouling of RO membranes in seawater desalination, *Water Research* 47 (10) (2013) 3389–3398. DOI: 10.1016/j.watres.2013.03.042.
- [123] A. Sweity, T.R. Zere, I. David, S. Bason, Y. Oren, Z. Ronen, M. Herzberg, Side effects of antiscalants on biofouling of reverse osmosis membranes in brackish water desalination, *Journal of Membrane Science* 481 (2015) 172–187. DOI: 10.1016/j.memsci.2015.02.003.
- [124] J.P. van der Hoek, J.A.M.H. Hofman, P.A.C. Bonn e, M.M. Nederlof, H.S. Vrouwenvelder, RO treatment: Selection of a pretreatment scheme based on fouling characteristics and operating conditions based on environmental impact, *Desalination* 127 (1) (2000) 89–101. DOI: 10.1016/S0011-9164(99)00195-2.
- [125] O. Happel, D. Armbruster, U. M uller, H.-J. Brauch, Reinheitspr ufung phosphonathaltiger Antiscalants, *energie | wasser-praxis* 69 (04) (2018) 25–29.
- [126] E.A. Abdel-Aal, M.M. Rashad, H. El-Shall, Crystallization of calcium sulfate dihydrate at different supersaturation ratios and different free sulfate concentrations, *Crystal Research and Technology* 39 (4) (2004) 313–321. DOI: 10.1002/crat.200310188.
- [127] A. Lancia, D. Musmarra, M. Prisciandaro, Measuring induction period for calcium sulfate dihydrate precipitation, *AIChE Journal* 45 (2) (1999) 390–397. DOI: 10.1002/aic.690450218.
- [128] A. Packter, The precipitation of calcium sulphate dihydrate from aqueous solution, *Journal of Crystal Growth* 21 (2) (1974) 191–194. DOI: 10.1016/0022-0248(74)90004-9.

- [129] I.J. Reznik, J. Ganor, C. Gruber, I. Gavrieli, Towards the establishment of a general rate law for gypsum nucleation, *Geochimica et Cosmochimica Acta* 85 (2012) 75–87. DOI: 10.1016/j.gca.2012.02.002.
- [130] S. He, J.E. Oddo, M.B. Tomson, The Nucleation Kinetics of Calcium Sulfate Dihydrate in NaCl Solutions up to 6 m and 90°C, *Journal of Colloid and Interface Science* 162 (2) (1994) 297–303. DOI: 10.1006/jcis.1994.1042.
- [131] S. Halevy, E. Korin, J. Gilron, Kinetics of Gypsum Precipitation for Designing Interstage Crystallizers for Concentrate in High Recovery Reverse Osmosis, *Industrial & Engineering Chemistry Research* 52 (41) (2013) 14647–14657. DOI: 10.1021/ie400977p.
- [132] D.M. Keller, R.E. Massey, O.E. Hileman Jr., Studies on nucleation phenomena occurring in aqueous solutions supersaturated with calcium sulfate. II. The induction time, *Canadian Journal of Chemistry* 56 (1978) 3096–3103. DOI: 10.1139/v78-506.
- [133] D.M. Keller, R.E. Massey, O.E. Hileman Jr., Studies on nucleation phenomena occurring in aqueous solutions supersaturated with calcium sulfate, *Canadian Journal of Chemistry* 56 (1978) 831–838. DOI: 10.1139/v78-138.
- [134] B.R. Smith, F. Sweett, The crystallization of calcium sulfate dihydrate, *Journal of Colloid and Interface Science* 37 (3) (1971) 612–618. DOI: 10.1016/0021-9797(71)90339-0.
- [135] S.-T. Liu, G.H. Nancollas, Linear crystallization and induction-period studies of the growth of calcium sulphate dihydrate crystals, *Talanta* 20 (2) (1973) 211–216. DOI: 10.1016/0039-9140(73)80268-1.
- [136] S.-T. Liu, G.H. Nancollas, The crystal growth of calcium sulfate dihydrate in the presence of additives, *Journal of Colloid and Interface Science* 44 (3) (1973) 422–429. DOI: 10.1016/0021-9797(73)90318-4.
- [137] P.G. Klepetsanis, P.G. Koutsoukos, Precipitation of calcium sulfate dihydrate at constant calcium activity, *Journal of Crystal Growth* 98 (3) (1989) 480–486. DOI: 10.1016/0022-0248(89)90164-4.
- [138] M. Prisciandaro, A. Lancia, D. Musmarra, Gypsum nucleation into sodium chloride solutions, *AIChE Journal* 47 (4) (2001) 929–934. DOI: 10.1002/aic.690470415.
- [139] S. Seewoo, R. van Hille, A. Lewis, Aspects of gypsum precipitation in scaling waters, *Hydrometallurgy* 75 (1-4) (2004) 135–146. DOI: 10.1016/j.hydromet.2004.07.003.
- [140] P.G. Klepetsanis, P.G. Koutsoukos, Spontaneous precipitation of calcium sulfate at conditions of sustained supersaturation, *Journal of Colloid and Interface Science* 143 (2) (1991) 299–308. DOI: 10.1016/0021-9797(91)90263-8.
- [141] J. Gilron, D. Hasson, Calcium sulphate fouling of reverse osmosis membranes: Flux decline mechanism, *Chemical Engineering Science* 42 (10) (1987) 2351–2360. DOI: 10.1016/0009-2509(87)80109-4.
- [142] M.R. Christoffersen, J. Christoffersen, M.P.C. Weijnen, G.M. van Rosmalen, Crystal growth of calcium sulphate dihydrate at low supersaturation, *Journal of Crystal Growth* 58 (3) (1982) 585–595. DOI: 10.1016/0022-0248(82)90145-2.
- [143] J.M. Deckers, J.E. Lash, G. Burns, Heats of Crystallization of CaSO<sub>4</sub>·2H<sub>2</sub>O, *Bulletin des Sociétés Chimiques Belges* 93 (4) (1984) 271–280. DOI: 10.1002/bscb.19840930402.
- [144] S. Muryanto, The role of impurities and additives in the crystallisation of gypsum. Ph.D. thesis. Curtin University of Technology, Perth, Australia, 2002.
- [145] D. Bosbach, J.L. Junta-Rosso, U. Becker, M.F. Hochella, Gypsum growth in the presence of background electrolytes studied by Scanning Force Microscopy, *Geochimica et Cosmochimica Acta* 60 (17) (1996) 3295–3304. DOI: 10.1016/0016-7037(96)00147-0.
- [146] M.P.C. Weijnen, G.M. van Rosmalen, Adsorption of phosphonates on gypsum crystals, *Journal of Crystal Growth* 79 (1-3) (1986) 157–168. DOI: 10.1016/0022-0248(86)90431-8.
- [147] B.R. Smith, A.E. Alexander, The effect of additives on the process of crystallization II. Further studies on calcium sulphate (1), *Journal of Colloid and Interface Science* 34 (1) (1970) 81–90. DOI: 10.1016/0021-9797(70)90261-4.

- [148] E.R. McCartney, A.E. Alexander, The effect of additives upon the process of crystallization, *Journal of Colloid Science* 13 (4) (1958) 383–396. DOI: 10.1016/0095-8522(58)90047-3.
- [149] X. Li, D. Hasson, H. Shemer, Flow conditions affecting the induction period of CaSO<sub>4</sub> scaling on RO membranes, *Desalination* (2017). DOI: 10.1016/j.desal.2017.08.014.
- [150] A. Jawor, E.M.V. Hoek, Effects of feed water temperature on inorganic fouling of brackish water RO membranes, *Desalination* 235 (1-3) (2009) 44–57. DOI: 10.1016/j.desal.2008.07.004.
- [151] A.P. Mairal, A.R. Greenberg, W.B. Krantz, Investigation of membrane fouling and cleaning using ultrasonic time-domain reflectometry, *Desalination* 130 (1) (2000) 45–60. DOI: 10.1016/S0011-9164(00)00073-4.
- [152] M. Brusilovsky, J. Borden, D. Hasson, Flux decline due to gypsum precipitation on RO membranes, *Desalination* 86 (2) (1992) 187–222. DOI: 10.1016/0011-9164(92)80033-6.
- [153] M. Shmulevsky, X. Li, H. Shemer, D. Hasson, R. Semiat, Analysis of the onset of calcium sulfate scaling on RO membranes, *Journal of Membrane Science* 524 (2017) 299–304. DOI: 10.1016/j.memsci.2016.11.055.
- [154] E. Lyster, Y. Cohen, Numerical study of concentration polarization in a rectangular reverse osmosis membrane channel: Permeate flux variation and hydrodynamic end effects, *Journal of Membrane Science* 303 (1-2) (2007) 140–153. DOI: 10.1016/j.memsci.2007.07.003.
- [155] E. Lyster, J. Au, R. Rallo, F. Giralt, Y. Cohen, Coupled 3-D hydrodynamics and mass transfer analysis of mineral scaling-induced flux decline in a laboratory plate-and-frame reverse osmosis membrane module, *Journal of Membrane Science* 339 (1-2) (2009) 39–48. DOI: 10.1016/j.memsci.2009.04.024.
- [156] M. Uchymiak, A. Rahardianto, E. Lyster, J. Glater, Y. Cohen, A novel RO ex situ scale observation detector (EXSOD) for mineral scale characterization and early detection, *Journal of Membrane Science* 291 (1-2) (2007) 86–95. DOI: 10.1016/j.memsci.2006.12.038.
- [157] Y. Cohen, M. Uchymiak Patent: WO2007087578 A3, 2007.
- [158] A.R. Bartman, E. Lyster, R. Rallo, P.D. Christofides, Y. Cohen, Mineral scale monitoring for reverse osmosis desalination via real-time membrane surface image analysis, *Desalination* 273 (1) (2011) 64–71. DOI: 10.1016/j.desal.2010.10.021.
- [159] J. Thompson, N. Lin, E. Lyster, R. Arbel, T. Knoell, J. Gilron, Y. Cohen, RO membrane mineral scaling in the presence of a biofilm, *Journal of Membrane Science* 415-416 (2012) 181–191. DOI: 10.1016/j.memsci.2012.04.051.
- [160] J. Thompson, A. Rahardianto, H. Gu, M. Uchymiak, A. Bartman, M. Hedrick, D. Lara, J. Cooper, J. Faria, P.D. Christofides, Y. Cohen, Rapid field assessment of RO desalination of brackish agricultural drainage water, *Water Research* 47 (8) (2013) 2649–2660. DOI: 10.1016/j.watres.2013.02.013.
- [161] A. Rahardianto, B.C. McCool, Y. Cohen, Reverse Osmosis Desalting of Inland Brackish Water of High Gypsum Scaling Propensity: Kinetics and Mitigation of Membrane Mineral Scaling, *Environmental Science and Technology* 42 (12) (2008) 4292–4297. DOI: 10.1021/es702463a.
- [162] C. Tzotzi, T. Pahiadaki, S. Yiantsios, A. Karabelas, N. Andritsos, A study of CaCO<sub>3</sub> scale formation and inhibition in RO and NF membrane processes, *Journal of Membrane Science* 296 (1-2) (2007) 171–184. DOI: 10.1016/j.memsci.2007.03.031.
- [163] M. Filella, Freshwaters: Which NOM matters?, *Environmental Chemistry Letters* 7 (1) (2009) 21–35. DOI: 10.1007/s10311-008-0158-x.
- [164] R.S. Summers, P.V. Roberts, Activated carbon adsorption of humic substances I. Heterodisperse mixtures and desorption, *Journal of Colloid and Interface Science* 122 (2) (1988) 367–381. DOI: 10.1016/0021-9797(88)90372-4.
- [165] A.G. Fane, W. Xi, W. Rong, Membrane Filtration Processes and Fouling, in: G. Newcombe (Ed.), *Interface science in drinking water treatment: Theory and applications*, 1st ed., Elsevier, Amsterdam u.a., 2006, pp. 109–132.

- [166] F.H. Frimmel, G. Abbt-Braun, Sum Parameters: Potential and Limitations, in: P. Wilderer (Ed.), *Treatise on Water Science: Volume 3: Aquatic Chemistry and Biology*, Elsevier, Oxford, 2011, pp. 3–29.
- [167] E.M. Thurman, *Organic geochemistry of natural waters*, Nijhoff, Dordrecht, 1985.
- [168] J.D. Ritchie, E.M. Perdue, Proton-binding study of standard and reference fulvic acids, humic acids, and natural organic matter, *Geochimica et Cosmochimica Acta* 67 (1) (2003) 85–96. DOI: 10.1016/S0016-7037(02)01044-X.
- [169] P. MacCarthy, The principles of humic substances, *Soil Science* 166 (11) (2001) 738–751. DOI: 10.1097/00010694-200111000-00003.
- [170] M.E.T. Sillanpaa, *Natural organic matter in water: Characterization and treatment methods*, Butterworth-Heinemann, Oxford, UK, 2015.
- [171] K. Ghosh, M. Schnitzer, Macromolecular structures of humic substances, *Soil Science* 129 (5) (1980) 266.
- [172] V.I. Esteves, M. Otero, A.C. Duarte, Comparative characterization of humic substances from the open ocean, estuarine water and fresh water, *Organic Geochemistry* 40 (9) (2009) 942–950. DOI: 10.1016/j.orggeochem.2009.06.006.
- [173] R. L. Malcolm, The uniqueness of humic substances in each of soil, stream and marine environments, *Analytica Chimica Acta* 232 (1990) 19–30. DOI: 10.1016/S0003-2670(00)81222-2.
- [174] D.J. Repeta, T.M. Quan, L.I. Aluwihare, A. Accardi, Chemical characterization of high molecular weight dissolved organic matter in fresh and marine waters, *Geochimica et Cosmochimica Acta* 66 (6) (2002) 955–962. DOI: 10.1016/S0016-7037(01)00830-4.
- [175] J. Buffle, K.J. Wilkinson, S. Stoll, M. Filella, J. Zhang, A Generalized Description of Aquatic Colloidal Interactions: The Three-colloidal Component Approach, *Environmental Science and Technology* 32 (19) (1998) 2887–2899. DOI: 10.1021/es980217h.
- [176] F.M.M. Morel, J.G. Hering, *Principles and applications of aquatic chemistry*, Wiley, New York NY u.a., 1993.
- [177] C.L. Tiller, C.R. O'Melia, Natural organic matter and colloidal stability: models and measurements, in: T.F. Tadros, J. Gregory (Eds.), *Colloids in the Aquatic Environment*, Elsevier Science, Burlington, 1993, pp. 89–102. DOI: 10.1016/B978-1-85861-038-2.50010-3.
- [178] H. Hyung, J.-H. Kim, Natural Organic Matter (NOM) Adsorption to Multi-Walled Carbon Nanotubes: Effect of NOM Characteristics and Water Quality Parameters, *Environmental Science and Technology* 42 (12) (2008) 4416–4421. DOI: 10.1021/es702916h.
- [179] J.A. Leenheer, G.K. Brown, P. MacCarthy, S.E. Cabaniss, Models of Metal Binding Structures in Fulvic Acid from the Suwannee River, Georgia, *Environmental Science and Technology* 32 (16) (1998) 2410–2416. DOI: 10.1021/es9708979.
- [180] D.A. Rees, Polysaccharide shapes and their interactions - some recent advances, *Pure and Applied Chemistry* 53 (1) (1981) 1–14. DOI: 10.1351/pac198153010001.
- [181] G.T. Grant, E.R. Morris, D.A. Rees, P.J.C. Smith, D. Thom, Biological interactions between polysaccharides and divalent cations: The egg-box model, *FEBS Letters* 32 (1) (1973) 195–198. DOI: 10.1016/0014-5793(73)80770-7.
- [182] S. Lee, M. Elimelech, Relating Organic Fouling of Reverse Osmosis Membranes to Intermolecular Adhesion Forces, *Environmental Science and Technology* 40 (3) (2006) 980–987. DOI: 10.1021/es051825h.
- [183] X.-M. Wang, T.D. Waite, Gel layer formation and hollow fiber membrane filterability of polysaccharide dispersions, *Journal of Membrane Science* 322 (1) (2008) 204–213. DOI: 10.1016/j.memsci.2008.05.033.
- [184] X.-M. Wang, T.D. Waite, Role of gelling soluble and colloidal microbial products in membrane fouling, *Environmental Science and Technology* 43 (24) (2009) 9341–9347. DOI: 10.1021/es9013129.

- [185] J.S. Kim, E.S.K. Chian, F.M. Saunders, E.M. Perdue, M.F. Giabbai, Characteristics of Humic Substances and Their Removal Behavior in Water Treatment, in: I.H. Suffet (Ed.), *Aquatic humic substances: Influence on fate and treatment of pollutants*; Denver, Colo., April 5 - 10, 1987, American Chem. Soc, Washington, DC, 1989, pp. 473–497. DOI: 10.1021/ba-1988-0219.ch029.
- [186] S.P. Palecek, A.L. Zydney, Intermolecular electrostatic interactions and their effect on flux and protein deposition during protein filtration, *Biotechnology Progress* 10 (2) (1994) 207–213. DOI: 10.1021/bp00026a010.
- [187] W. Ang, M. Elimelech, Protein (BSA) fouling of reverse osmosis membranes: Implications for wastewater reclamation, *Journal of Membrane Science* 296 (1-2) (2007) 83–92. DOI: 10.1016/j.memsci.2007.03.018.
- [188] T. Harnislawat, R. Pongsawatmanit, D. McClements, Characterization of  $\beta$ -lactoglobulin–sodium alginate interactions in aqueous solutions: A calorimetry, light scattering, electrophoretic mobility and solubility study, *Food Hydrocolloids* 20 (5) (2006) 577–585. DOI: 10.1016/j.foodhyd.2005.05.005.
- [189] T. K ppler, C. Posten, Fractionation of proteins with two-sided electro-ultrafiltration, *Journal of biotechnology* 128 (4) (2007) 895–907. DOI: 10.1016/j.jbiotec.2007.01.002.
- [190] M.J. Barcelona, D.K. Atwood, Gypsum-organic interactions in natural seawater: Effect of organics on precipitation kinetics and crystal morphology, *Marine Chemistry* 6 (2) (1978) 99–115. DOI: 10.1016/0304-4203(78)90021-X.
- [191] X. Jin, X. Huang, E.M.V. Hoek, Role of Specific Ion Interactions in Seawater RO Membrane Fouling by Alginic Acid, *Environmental Science and Technology* 43 (10) (2009) 3580–3587. DOI: 10.1021/es8036498.
- [192] A.S. Al-Amoudi, Factors affecting natural organic matter (NOM) and scaling fouling in NF membranes: A review, *Desalination* 259 (1-3) (2010) 1–10. DOI: 10.1016/j.desal.2010.04.003.
- [193] V. Lahoussine-Turcaud, M.R. Wiesner, J.-Y. Bottero, Fouling in tangential-flow ultrafiltration: The effect of colloid size and coagulation pretreatment, *Journal of Membrane Science* 52 (2) (1990) 173–190. DOI: 10.1016/S0376-7388(00)80484-6.
- [194] S.-H. Yoon, C.-H. Lee, K.-J. Kim, A.G. Fane, Effect of calcium ion on the fouling of nanofilter by humic acid in drinking water production, *Water Research* 32 (7) (1998) 2180–2186. DOI: 10.1016/S0043-1354(97)00416-8.
- [195] A.I. Sch fer, A.G. Fane, T.D. Waite, Nanofiltration of natural organic matter: Removal, fouling and the influence of multivalent ions, *Desalination* 118 (1-3) (1998) 109–122. DOI: 10.1016/S0011-9164(98)00104-0.
- [196] W. Yuan, Humic acid fouling during microfiltration, *Journal of Membrane Science* 157 (1) (1999) 1–12. DOI: 10.1016/S0376-7388(98)00329-9.
- [197] A. Braghetta, F.A. DiGiano, W.P. Ball, NOM Accumulation at NF Membrane Surface: Impact of Chemistry and Shear, *Journal of Environmental Engineering* 124 (11) (1998) 1087–1098. DOI: 10.1061/(ASCE)0733-9372(1998)124:11(1087).
- [198] J. Nilson, F.A. DiGiano, Influence of NOM composition on nanofiltration: American Water Works Association 88 (5) (1996) 53–66.
- [199] C. Jucker, M.M. Clark, Adsorption of aquatic humic substances on hydrophobic ultrafiltration membranes, *Journal of Membrane Science* 97 (1994) 37–52. DOI: 10.1016/0376-7388(94)00146-P.
- [200] S. Lee, W.S. Ang, M. Elimelech, Fouling of reverse osmosis membranes by hydrophilic organic matter: implications for water reuse, *Integrated Concepts in Water Recycling* 187 (1–3) (2006) 313–321. DOI: 10.1016/j.desal.2005.04.090.
- [201] W.S. Ang, S. Lee, M. Elimelech, Chemical and physical aspects of cleaning of organic-fouled reverse osmosis membranes, *Journal of Membrane Science* 272 (1-2) (2006) 198–210. DOI: 10.1016/j.memsci.2005.07.035.

- [202] Q. Li, J. Song, H. Yu, Z. Li, X. Pan, B. Yang, Investigating the microstructures and surface features of seawater RO membranes and the dependencies of fouling resistance performances, *Desalination* 352 (2014) 109–117. DOI: 10.1016/j.desal.2014.08.015.
- [203] C.Y. Tang, Y.-N. Kwon, J.O. Leckie, The role of foulant–foulant electrostatic interaction on limiting flux for RO and NF membranes during humic acid fouling – Theoretical basis, experimental evidence, and AFM interaction force measurement, *Journal of Membrane Science* 326 (2) (2009) 526–532. DOI: 10.1016/j.memsci.2008.10.043.
- [204] C.Y. Tang, J.O. Leckie, Membrane Independent Limiting Flux for RO and NF Membranes Fouled by Humic Acid, *Environmental Science and Technology* 41 (13) (2007) 4767–4773. DOI: 10.1021/es063105w.
- [205] W. Lee, C.H. Ahn, S. Hong, S. Kim, S. Lee, Y. Baek, J. Yoon, Evaluation of surface properties of reverse osmosis membranes on the initial biofouling stages under no filtration condition, *Journal of Membrane Science* 351 (1-2) (2010) 112–122. DOI: 10.1016/j.memsci.2010.01.035.
- [206] T. Luxbacher, *The Zeta potential for solid surface analysis: A practical guide to streaming potential measurement*, 1st ed., Anton Paar GmbH, Austria, 2014.
- [207] E.M.V. Hoek, M. Elimelech, Cake-Enhanced Concentration Polarization: A New Fouling Mechanism for Salt-Rejecting Membranes, *Environmental Science and Technology* 37 (24) (2003) 5581–5588. DOI: 10.1021/es0262636.
- [208] T.H. Chong, F.S. Wong, A.G. Fane, Enhanced concentration polarization by unstirred fouling layers in reverse osmosis: Detection by sodium chloride tracer response technique, *Journal of Membrane Science* 287 (2) (2007) 198–210. DOI: 10.1016/j.memsci.2006.10.035.
- [209] T.H. Chong, A.G. Fane, Implications of critical flux and cake enhanced osmotic pressure (CEOP) on colloidal fouling in reverse osmosis: Modeling approach, *Desalination and Water Treatment* 8 (1-3) (2012) 68–90. DOI: 10.5004/dwt.2009.792.
- [210] F. Wang, V. Tarbara, Coupled effects of colloidal deposition and salt concentration polarization on reverse osmosis membrane performance, *Journal of Membrane Science* 293 (1-2) (2007) 111–123. DOI: 10.1016/j.memsci.2007.02.003.
- [211] M. Herzberg, M. Elimelech, Biofouling of reverse osmosis membranes: Role of biofilm-enhanced osmotic pressure, *Journal of Membrane Science* 295 (1-2) (2007) 11–20. DOI: 10.1016/j.memsci.2007.02.024.
- [212] S. Lee, J. Cho, M. Elimelech, Influence of colloidal fouling and feed water recovery on salt rejection of RO and NF membranes, *Desalination* 160 (1) (2004) 1–12. DOI: 10.1016/S0011-9164(04)90013-6.
- [213] D. Vogel, A. Simon, A.A. Alturki, B. Bilitewski, W.E. Price, L.D. Nghiem, Effects of fouling and scaling on the retention of trace organic contaminants by a nanofiltration membrane: The role of cake-enhanced concentration polarisation, *Separation and Purification Technology* 73 (2) (2010) 256–263. DOI: 10.1016/j.seppur.2010.04.010.
- [214] Q. Li, M. Elimelech, Synergistic effects in combined fouling of a loose nanofiltration membrane by colloidal materials and natural organic matter, *Journal of Membrane Science* 278 (1-2) (2006) 72–82. DOI: 10.1016/j.memsci.2005.10.045.
- [215] F. Miller, *Elektrochemische Speziation und Charakterisierung von Gewässerinhaltsstoffen*. Dissertation. Universität Hamburg, Hamburg, 2005.
- [216] C.Y. Tang, Y.-N. Kwon, J.O. Leckie, Effect of membrane chemistry and coating layer on physiochemical properties of thin film composite polyamide RO and NF membranes II. Membrane physiochemical properties and their dependence on polyamide and coating layers, *Desalination* 242 (2009) 168–182.
- [217] I. Sutzkover, D. Hasson, R. Semiat, Simple technique for measuring the concentration polarization level in a reverse osmosis system, *Desalination* 131 (1–3) (2000) 117–127. DOI: 10.1016/S0011-9164(00)90012-2.

- [218] S.A. Huber, A. Balz, M. Abert, W. Pronk, Characterisation of aquatic humic and non-humic matter with size-exclusion chromatography--organic carbon detection--organic nitrogen detection (LC-OCD-OND), *Water Research* 45 (2) (2011) 879–885. DOI: 10.1016/j.watres.2010.09.023.
- [219] C. Goletz, M. Wagner, A. Grübel, W. Schmidt, N. Korf, P. Werner, Standardization of fluorescence excitation-emission-matrices in aquatic milieu, *Talanta* 85 (1) (2011) 650–656. DOI: 10.1016/j.talanta.2011.04.045.
- [220] A.J. Lawaetz, C.A. Stedmon, Fluorescence intensity calibration using the Raman scatter peak of water, *Applied spectroscopy* 63 (8) (2009) 936–940. DOI: 10.1366/000370209788964548.
- [221] A. Malloy, B. Carr, NanoParticle Tracking Analysis - The Halo™ System, *Particle & Particle Systems Characterization* 23 (2) (2006) 197–204. DOI: 10.1002/ppsc.200601031.
- [222] R. Jantschik, F. Nyffeler, O.F.X. Donard, Marine particle size measurement with a stream-scanning laser system, *Marine Geology* 106 (3-4) (1992) 239–250. DOI: 10.1016/0025-3227(92)90132-2.
- [223] P. Janos, S. Krízenecká, L. Madronová, Acid-base titration curves of solid humic acids, *Reactive and Functional Polymers* 68 (1) (2008) 242–247. DOI: 10.1016/j.reactfunctpolym.2007.09.005.
- [224] M.R. Collins, G.L. Amy, C. Steelink, Molecular weight distribution, carboxylic acidity, and humic substances content of aquatic organic matter: Implications for removal during water treatment, *Environmental Science and Technology* 20 (10) (1986) 1028–1032. DOI: 10.1021/es00152a011.
- [225] M. Schulz, S. Bünting, M. Ernst, Impact of Powdered Activated Carbon Structural Properties on Removal of Organic Foulants in Combined Adsorption-Ultrafiltration, *Water* 9 (8) (2017) 580. DOI: 10.3390/w9080580.
- [226] X. Jin, A. Jawor, S. Kim, E.M.V. Hoek, Effects of feed water temperature on separation performance and organic fouling of brackish water RO membranes, *Desalination* 239 (1-3) (2009) 346–359. DOI: 10.1016/j.desal.2008.03.026.
- [227] L.D. Nghiem, T. Cath, A scaling mitigation approach during direct contact membrane distillation, *Separation and Purification Technology* 80 (2) (2011) 315–322. DOI: 10.1016/j.seppur.2011.05.013.
- [228] G. Kortüm, M. Kortüm-Seiler, Nephelometrie, in: F. Ender, W. Esselborn, B. Flaschenträger, E. Hellman, L. Kofler, G. Kortüm, M. Kortüm-Seiler, H. Lieb, H.M. Rauen, A. Rittmann, G. Schmid, W. Schöniger, W. Stamm, E. Wiedemann (Eds.), *Allgemeine Untersuchungsmethoden: Erster Teil*, Springer, Berlin, Heidelberg, 1953, pp. 435–440. DOI: 10.1007/978-3-642-85550-4\_9.
- [229] E. Drioli, G. Di Profio, E. Curcio, *Membrane-assisted crystallization technology*, Imperial College Press, London, 2015.
- [230] G.L. Amy, S.G. Salinas Rodriguez, M.D. Kennedy, J.C. Schippers, S. Rapenne, P.-J. Remize, C. Barbe, C.-L. de O. Manes, N.J. West, P. Lebaron, D. van der Kooij, H. Veenendaal, G. Schaule, K. Petrowski, S. Huber, L.N. Sim, V. Chen, A.G. Fane, Chapter 1: Water quality assessment tools, in: E. Drioli, A. Criscuoli, F. Macedonio (Eds.), *Membrane-based desalination: An integrated approach (MEDINA)*, IWA Publishing, London, 2011, pp. 3–32.
- [231] U. Lankes, M.B. Müller, M. Weber, F.H. Frimmel, Reconsidering the quantitative analysis of organic carbon concentrations in size exclusion chromatography, *Water Research* 43 (4) (2009) 915–924. DOI: 10.1016/j.watres.2008.11.025.
- [232] M. Mulder, *Basic Principles of Membrane Technology*, Springer Netherlands, Dordrecht, 1996. DOI: 10.1007/978-94-009-1766-8.
- [233] I. Sutzkover-Gutman, D. Hasson, R. Semiat, Humic substances fouling in ultrafiltration processes, *Desalination* 261 (3) (2010) 218–231. DOI: 10.1016/j.desal.2010.05.008.
- [234] H.P. Erickson, Size and shape of protein molecules at the nanometer level determined by sedimentation, gel filtration, and electron microscopy, *Biological Procedures Online* 11 (2009) 32–51. DOI: 10.1007/s12575-009-9008-x.

- [235] O. Prodanovic, D. Spasojevic, M. Prokopijevic, K. Radotic, N. Markovic, M. Blazic, R. Prodanovic, Tyramine modified alginates via periodate oxidation for peroxidase induced hydrogel formation and immobilization, *Reactive and Functional Polymers* 93 (2015) 77–83. DOI: 10.1016/j.reactfunctpolym.2015.06.004.
- [236] F.L. Rosario-Ortiz, J.A. Korak, Oversimplification of Dissolved Organic Matter Fluorescence Analysis: Potential Pitfalls of Current Methods, *Environmental Science and Technology* 51 (2) (2017) 759–761. DOI: 10.1021/acs.est.6b06133.
- [237] M. Wagner, W. Schmidt, Charakterisierung des aquatischen DOC: energie | wasser-praxis 5 (2012) 48–53.
- [238] J. Chen, E.J. LeBoeuf, S. Dai, B. Gu, Fluorescence spectroscopic studies of natural organic matter fractions, *Chemosphere* 50 (5) (2003) 639–647. DOI: 10.1016/S0045-6535(02)00616-1.
- [239] N.W. Green, D. McInnis, N. Hertkorn, P.A. Maurice, E.M. Perdue, Suwannee River Natural Organic Matter: Isolation of the 2R101N Reference Sample by Reverse Osmosis, *Environmental Engineering Science* 32 (1) (2015) 38–44. DOI: 10.1089/ees.2014.0284.
- [240] E.B.H. Santos, V.I. Esteves, J.P.C. Rodrigues, A.C. Duarte, Humic substances' proton-binding equilibria: Assessment of errors and limitations of potentiometric data, *Analytica Chimica Acta* 392 (2-3) (1999) 333–341. DOI: 10.1016/S0003-2670(99)00227-5.
- [241] E.M. Perdue, Acidic functional groups of humic substances, in: G.R. Aiken (Ed.), *Humic substances in soil, sediment, and water*, Wiley, New York, 1985, pp. 493–527.
- [242] S.J. Driver, E.M. Perdue, Acidic Functional Groups of Suwannee River Natural Organic Matter, *Humic Acids, and Fulvic Acids*, in: S. Ahuja, K. Hristovski (Eds.), *Novel Solutions to Water Pollution*, American Chemical Society, Washington, DC, 2013, pp. 75–86. DOI: 10.1021/bk-2014-1160.ch004.
- [243] M.L. Ferrer, R. Duchowicz, B. Carrasco, J.G. de La Torre, A.U. Acuña, The Conformation of Serum Albumin in Solution: A Combined Phosphorescence Depolarization-Hydrodynamic Modeling Study, *Biophysical Journal* 80 (5) (2001) 2422–2430. DOI: 10.1016/S0006-3495(01)76211-X.
- [244] M. Ochs, B. Čosović, W. Stumm, Coordinative and hydrophobic interaction of humic substances with hydrophilic Al<sub>2</sub>O<sub>3</sub> and hydrophobic mercury surfaces, *Geochimica et Cosmochimica Acta* 58 (2) (1994) 639–650. DOI: 10.1016/0016-7037(94)90494-4.
- [245] R.C. Reynolds, Polyphenol inhibition of calcite precipitation in Lake Powell I, *Limnology and oceanography* 23 (4) (1978) 585–597. DOI: 10.4319/lo.1978.23.4.0585.
- [246] W.P. Inskeep, P.R. Bloom, Kinetics of Calcite Precipitation in the Presence of Water-soluble Organic Ligands, *Soil Science Society of America Journal* 50 (5) (1986) 1167. DOI: 10.2136/sssaj1986.03615995005000050015x.
- [247] R.A. Berner, J.T. Westrich, R. Graber, J. Smith, C.S. Martens, Inhibition of aragonite precipitation from supersaturated seawater; a laboratory and field study, *American Journal of Science* 278 (6) (1978) 816–837. DOI: 10.2475/ajs.278.6.816.
- [248] R.A. Kuntze, Retardation of the Crystallization of Calcium Sulphate Dihydrate, *Nature* 211 (5047) (1966) 406–407. DOI: 10.1038/211406a0.
- [249] Y. Miyahara, Effects of various condensed phosphates on the crystallization and crystal habit of calcium carbonates, *Chemical Abstracts* 60 (1964) 3561.
- [250] Z. Amjad, Kinetics of crystal growth of calcium sulfate dihydrate. The influence of polymer composition, molecular weight, and solution pH, *Canadian Journal of Chemistry* 66 (6) (1988) 1529–1536. DOI: 10.1139/v88-247.
- [251] M. Klučáková, R. Kolajová, Dissociation ability of humic acids: Spectroscopic determination of pK<sub>a</sub> and comparison with multi-step mechanism, *Reactive and Functional Polymers* 78 (2014) 1–6. DOI: 10.1016/j.reactfunctpolym.2014.02.005.

- [252] P.J. Sadler, A. Tucker, pH-induced structural transitions of bovine serum albumin. Histidine pKa values and unfolding of the N-terminus during the N to F transition, *European Journal of Biochemistry* 212 (3) (1993) 811–817. DOI: 10.1111/j.1432-1033.1993.tb17722.x.
- [253] K. Clare, Algin, in: J.N. BeMiller, R.L. Whistler (Eds.), *Industrial Gums: Polysaccharides and Their Derivatives*, 3rd ed., Elsevier Science, Burlington, 1992, pp. 105–143. DOI: 10.1016/B978-0-08-092654-4.50010-3.
- [254] F. Gharagheizi, Determination of Diffusion Coefficient of Organic Compounds in Water Using a Simple Molecular-Based Method, *Industrial & Engineering Chemistry Research* 51 (6) (2012) 2797–2803. DOI: 10.1021/ie201944h.
- [255] S. Lee, C. Boo, M. Elimelech, S. Hong, Comparison of fouling behavior in forward osmosis (FO) and reverse osmosis (RO), *Journal of Membrane Science* 365 (1-2) (2010) 34–39. DOI: 10.1016/j.memsci.2010.08.036.
- [256] W. Norde, A.C.I. Anusiem, Adsorption, desorption and re-adsorption of proteins on solid surfaces, *Colloids and Surfaces* 66 (1) (1992) 73–80. DOI: 10.1016/0166-6622(92)80122-I.
- [257] M.A. Bos, Z. Shervani, A.C.I. Anusiem, M. Giesbers, W. Norde, J.M. Kleijn, Influence of the electric potential of the interface on the adsorption of proteins, *Colloids and Surfaces B: Biointerfaces* 3 (1-2) (1994) 91–100. DOI: 10.1016/0927-7765(93)01109-5.
- [258] Jens Haberkamp, *Organisches Membranfouling bei der Ultrafiltration kommunaler Kläranlagenabläufe: Ursachen, Mechanismen und Maßnahmen zur Verringerung*. Dissertation. TU Berlin, Berlin, 2008.
- [259] N. Senesi, Molecular and quantitative aspects of the chemistry of fulvic acid and its interactions with metal ions and organic chemicals, *Analytica Chimica Acta* 232 (1990) 77–106. DOI: 10.1016/S0003-2670(00)81226-X.
- [260] E.L. Sharp, P. Jarvis, S.A. Parsons, B. Jefferson, Impact of fractional character on the coagulation of NOM, *Colloids and Surfaces A: Physicochemical and Engineering Aspects* 286 (1-3) (2006) 104–111. DOI: 10.1016/j.colsurfa.2006.03.009.
- [261] J.K. Edzwald, J.E. Tobiason, Enhanced coagulation: US requirements and a broader view, *Water Science and Technology* 40 (9) (1999). DOI: 10.1016/S0273-1223(99)00641-1.
- [262] C.M. Sevrain, M. Berchel, H. Couthon, P.-A. Jaffrès, Phosphonic acid: Preparation and applications, *Beilstein Journal of Organic Chemistry* 13 (2017) 2186–2213. DOI: 10.3762/bjoc.13.219.
- [263] A. Rahardianto, J. Gao, C.J. Gabelich, M.D. Williams, Y. Cohen, High recovery membrane desalting of low-salinity brackish water: Integration of accelerated precipitation softening with membrane RO, *Journal of Membrane Science* 289 (1-2) (2007) 123–137. DOI: 10.1016/j.memsci.2006.11.043.
- [264] M.A. Sari, S. Chellam, Relative contributions of organic and inorganic fouling during nanofiltration of inland brackish surface water, *Journal of Membrane Science* 523 (2017) 68–76. DOI: 10.1016/j.memsci.2016.10.005.
- [265] K. Walha, R.B. Amar, L. Firdaous, F. Quéméneur, P. Jaouen, Brackish groundwater treatment by nanofiltration, reverse osmosis and electrodialysis in Tunisia: Performance and cost comparison, *Conference Membranes in Drinking and Industrial Water Production* 207 (1-3) (2007) 95–106. DOI: 10.1016/j.desal.2006.03.583.
- [266] Y. Cohen, P. Christofides, *Reverse Osmosis Field Study, Final Report, DWR-WRCD Agreement 46000534-03, Task Order No. 22*, California Department of Water Resources, 2010.
- [267] B.C. McCool, A. Rahardianto, J. Faria, K. Kovac, D. Lara, Y. Cohen, Feasibility of reverse osmosis desalination of brackish agricultural drainage water in the San Joaquin Valley, *Desalination* 261 (3) (2010) 240–250. DOI: 10.1016/j.desal.2010.05.031.

## List of Figures

Figure 2-1: Schematic illustration of a membrane separation process.....	4
Figure 2-2: Selectivity of pressure-driven membrane processes according to [49]. .....	4
Figure 2-3: Concentration polarization over a membrane surface according to [21] and [51]. $D$ : Solute diffusion coefficient, $\delta$ : boundary layer thickness. ....	6
Figure 2-4: Schematic representation of a fully aromatic polyamide (PA) thin-film composite (TFC) reverse osmosis membrane showing the porous polysulfone support layer and the dense polyamide film with ridge-and-valley morphology according to [6,51]. Scanning electron microscopy (SEM) image was taken from a virgin FILMTEC™ BW30 (Dow Chemical, MI, USA) membrane at 50,000x magnification. ....	8
Figure 2-5: Illustration of (a) different types of membrane fouling and (b) membrane scaling during reverse osmosis desalination. ....	9
Figure 2-6: Schematic solubility-supersolubility dia-gram according to [65]. During desalination, supersaturation can be achieved by pure water separation from an initially unsaturated solution (line A-B-C).....	11
Figure 2-7: Nucleation processes and nomenclature according to [65,67]. ....	11
Figure 2-8: Ideal crystal growth without dislocations according to [65]. Crystallizing units will migrate and link into positions where attractive forces are greatest and will, by step-wise build-up, complete a crystal plane. Before a crystal face can continue to grow, a new surface nucleus must be created.....	12
Figure 2-9: Combination of two crystal forms (cube, octahedron). Resulting crystals consist of the same set of crystal forms, i.e. share the same cubo-octahedral morphology (identical “ <i>Tracht</i> ”), but have different habits. According to [65,78]. ....	14
Figure 2-10: Modification of crystal habit by impurities. (a) Disruptive effect by impurity incorporation and disruption of face growth according to [80] in [67]. (b) Blocking effect by selective adsorption of impurity on crystal face 1 according to [81]. $R_{G,i}$ : growth rate of face $i$ , $S_i$ : Surface $i$ . ....	14
Figure 2-11: Typical water recoveries $\Phi$ and resulting concentration factors ( $CF$ , with $CF = c_o/c_f$ ) of rejected feed water solutes for different RO desalination applications (SWRO: seawater RO, BWRO: brackish water RO, HR-BWRO: high recovery RO). Water recoveries according to [9].....	15
Figure 2-12: Schematic illustration of scaling mechanisms. (a) Bulk crystallization due to crystal nucleation in the fluid bulk (homogeneously or heterogeneously) followed by deposition, growth and back transport. (b) Surface crystallization due to heterogeneous crystal nucleation on the membrane surface followed by lateral growth. According to [38,84,86]. ....	16
Figure 2-13: Chemical structures of common antiscalants: (a) example of a phosphonate: 2-phosphono-butane-1,2,4-tricarboxylic acid (PBTCA), (b) polyacrylic acid (PAA) and (c) polymaleic acid (PMA). ....	19
Figure 2-14: Calculated saturation indices ( $SI$ ) as a function of $pH$ at 20 °C for a model brackish water containing 0.25 mg·l <sup>-1</sup> barium, 200 mg·l <sup>-1</sup> bicarbonate, 30 mg·l <sup>-1</sup> silica, 3,000 mg·l <sup>-1</sup> sulfate, 400 mg·l <sup>-1</sup> calcium, 1,500 mg·l <sup>-1</sup> chloride, 2,000 mg·l <sup>-1</sup> sodium. Concentrations are based on ion concentrations commonly found in natural brackish waters (see Table D-1). Calculations were performed using ‘ <i>PHREEQC</i> ’ software, version 3.0.6 and phreeqc.dat database supplied by the US Geological Survey. Solubility products of displayed salts are listed in Table 3-7. ....	21
Figure 2-15: Different morphologies of gypsum bulk crystals crystallized from supersaturated solutions. (a) needles [139], (b) platelets [139] and (c) rhombohedral prisms [36]. ....	23
Figure 2-16: Scanning electron micrographs of membrane surfaces after gypsum scaling by (a) bulk crystallization (no scale or magnification given) [85] and (b) surface crystallization [19]. ....	24

- Figure 2-17: Effect of a polyacrylic acid-based antiscalant on gypsum surface crystal morphology on a reverse osmosis membrane [19]..... 25
- Figure 2-18: Schematic chemical structures of commonly used organic macromolecules in NOM-related membrane research: (a) humic acid, (b) alginate and (c) BSA..... 29
- Figure 2-19: Cake-enhanced concentration polarization (CECP) due to colloidal NOM cake layer formation according to [207,213]..... 34
- Figure 4-1: Development of relative real permeability and concentrate turbidity during gypsum scaling experiments in the absence and presence of  $3 \text{ mg}\cdot\text{l}^{-1}$  antiscalant during (a) ‘*high CP*’ and (b) ‘*low CP operation*’. Real permeabilities are corrected for the continuous increase of osmotic pressure according to Equation 3-3. Experimental conditions:  $SI_{g,b,0} = -0.02$ ,  $\Delta p = 25 \text{ bar}$ ,  $T = 25.0 \pm 0.1 \text{ }^\circ\text{C}$  ( $\pm \text{SD}$ ),  $pH = 6.4 \pm 0.3$  ( $\pm \text{SD}$ ). ..... 50
- Figure 4-2: Scanning electron micrographs of the membrane surface showing (a) rosette-like gypsum surface crystals after ‘*high CP operation*’, (b) evenly deposited needle-like gypsum bulk crystals after ‘*low CP operation*’, (c) distorted gypsum crystals after ‘*high CP operation*’ in the presence of  $3 \text{ mg}\cdot\text{l}^{-1}$  antiscalant (AS) and (d) the absence of deposited gypsum bulk crystals after ‘*low CP operation*’ in the presence of  $3 \text{ mg}\cdot\text{l}^{-1}$  antiscalant (crystal deposition was prevented by the ‘*crystal dispersion effect*’ of the antiscalant). ..... 51
- Figure 4-3: Comparison of normalized real permeability and concentrate turbidity development during ‘*low CP operation*’ starting at a  $VCF_0 = 1.0$  and  $VCF_0 = 1.5$  (previously shown in Figure 4-1b). ..... 52
- Figure 4-4: Development of concentrate turbidity during recirculation of a supersaturated gypsum solution ( $SI_{g,b} = 0.39$ ) employing low CP operation without permeation ( $\Delta p = 0 \text{ bar}$ )..... 52
- Figure 4-5: Linear correlation of gypsum supersaturation ( $S_{g,b}$ ) and observed induction time ( $\tau$ ) of the stirred beaker experiments ( $T = 24.9 \pm 0.3 \text{ }^\circ\text{C}$  ( $\pm \text{SD}$ ),  $pH = 7.0 \pm 0.2$  ( $\pm \text{SD}$ )), the RO recirculation experiment of Figure 4-4 and reported literature values. Hasson et al. (2001, 2003): RO permeation,  $T = 28 \pm 3 \text{ }^\circ\text{C}$ , periodic flux and turbidity measurement [89,90]; Li et al. (2017): RO permeation at different Reynolds numbers,  $T$  not specified, periodic flux and turbidity measurement [149]; Lancia et al. (1999): stirred beaker,  $T = 25 \text{ }^\circ\text{C}$ , laser transmittance and scattering [127]; He et al. (1994): stirred beaker,  $T = 25 \text{ }^\circ\text{C}$ ; turbidity and calcium measurements [130]; Reznik et al. (2012): shaker experiments,  $T = 25 \text{ }^\circ\text{C}$ , sulfate measurements [129]. ..... 54
- Figure 4-6: (a) Turbidity increase after exceeding the induction time ( $t - \tau$ ) during gypsum bulk crystallization experiments ( $T = 24.9 \pm 0.3 \text{ }^\circ\text{C}$  ( $\pm \text{SD}$ ),  $pH = 7.0 \pm 0.2$  ( $\pm \text{SD}$ )). Data points represent mean values  $\pm \text{SD}$  ( $n = 2 - 16$ , Table C-1) and lines represent exponential fits according to Equation 4-1. (b) Linear correlation of  $\ln^{-2}(S_{g,b})$  and  $\ln(\lambda_i)$ . ..... 55
- Figure 4-7: Development of (a) gypsum crystal concentration and (b) crystal mean diameter during gypsum bulk crystallization experiments ( $T = 25.1 \pm 0.1 \text{ }^\circ\text{C}$  ( $\pm \text{SD}$ ),  $pH = 6.9 \pm 0.1$  ( $\pm \text{SD}$ )) determined by laser obscuration time (LOT) measurement of consecutive samples taken at 5, 20, 50, 100 and 200 FNU. Experiments were repeated once and each sample was measured twice. Lines represent exponential fits according to Equation 4-1. ..... 56
- Figure 4-8: Impact of supersaturation on gypsum crystal morphology. Samples taken from stirred beaker experiments at a turbidity of 5 FNU ( $T = 24.9 \pm 0.3 \text{ }^\circ\text{C}$  ( $\pm \text{SD}$ ),  $pH = 7.0 \pm 0.2$  ( $\pm \text{SD}$ )). ..... 56
- Figure 4-9: Effects of  $pH$  on observed induction time of gypsum bulk crystallization at  $SI_g = 0.56$  ( $T = 25.1 \pm 0.1 \text{ }^\circ\text{C}$  ( $\pm \text{SD}$ )). (a) Individual data points; an additional experiment (red square) was spiked with an amount of NaCl equivalent to the amount of NaOH ( $0.1 \text{ mmol}\cdot\text{l}^{-1}$ ) that is required to achieve a  $pH$  of 10.0 in clean water. (b) Mean values for  $pH = 4.0 - 8.4$  and  $pH \approx 10.0$  with error bars indicating the 95 % confidence interval..... 57

- Figure 4-10: Scanning electron micrograph (200x magnification) showing three-dimensional rosette like gypsum crystals on the RO membrane surface after termination of the experiments at  $t = 270$  min. Red circles indicate individual rosettes detectable by the real-time imaging method ( $d_p > 49.3 \mu\text{m}$ ), whereas red arrows indicate crystals or crystal fragments that are smaller than the detection limit. .... 59
- Figure 4-11: Temporal development of (a) gypsum surface crystal number density ( $CND$ ) ( $d_p > 49.3 \mu\text{m}$ ), (b) fractional membrane surface coverage ( $FSC$ ) and (c) mean crystal diameter ( $d_p > 49.3 \mu\text{m}$ ) on 11 virgin RO membrane samples detected by real-time membrane surface imaging. Error bars of mean values represent determined minimal and maximal values of individual experiments. .... 60
- Figure 4-12: Real-time images ( $t = 180$  min) and determined crystal number density ( $CND$ ), fractional surface coverage ( $FSC$ ) and mean crystal diameter ( $d_p$ ) of three identically performed experiments. In (b), areas with comparably small crystals (dashed line) and areas free of detectable crystals (solid line) are highlighted. .... 61
- Figure 4-13: Axial gypsum crystal mass distribution on the membrane surface (determined from  $40 \text{ cm}^{-2}$  membrane subsections).  $L$ : length of the feed flow channel ( $L = 100 \text{ cm}$ ). Mean values ( $n = 7$ ) with corresponding determined minimal and maximal values of individual experiments as error bars. .... 62
- Figure 4-14: Correlations between increase of applied transmembrane pressure ( $\Delta p$ ) and (a) total gypsum crystal mass ( $\Delta m_{total}$ ) and (b) fractional surface coverage ( $FSC$ ). .... 63
- Figure 4-15: Temporal development of (a) gypsum surface crystal number density ( $CND$ ) ( $d_p > 49.3 \mu\text{m}$ ), (b) fractional membrane surface coverage ( $FSC$ ) and (c) mean crystal diameter ( $d_p > 49.3 \mu\text{m}$ ) during RO desalination at (i) increased feed ion concentration ( $c_g = 17.7 \text{ mmol}\cdot\text{l}^{-1}$  compared to  $c_g = 17.0 \text{ mmol}\cdot\text{l}^{-1}$  during reference experiments) and at (ii) increased feed solution turbidity ( $\kappa_f = 0.22 \text{ NTU}$  compared to  $\kappa_f = 0.05 \text{ NTU}$  during reference experiments) caused by stainless steel colloids and particles. Reference experiments are displayed as mean values ( $n = 9$ ) with minimal and maximal values represented as error bars. .... 64
- Figure 4-16: Real-time micrographs showing gypsum crystals at  $t = 240$  min for three consecutive gypsum scaling experiments reusing the same membrane sample after in-situ membrane cleaning according to the cleaning procedure described in Chapter 3.2.3. .... 65
- Figure 4-17: Temporal development of (a) gypsum surface crystal number density ( $CND$ ) ( $d_p > 49.3 \mu\text{m}$ ), (b) fractional membrane surface coverage ( $FSC$ ) and (c) mean crystal diameter ( $d_p > 49.3 \mu\text{m}$ ) during repeated pure gypsum scaling experiments using an in-situ cleaned membrane sample. Reference experiments are displayed as mean values ( $n = 9$ ) with minimal and maximal values represented as error bars. .... 66
- Figure 4-18: Relationship between transmembrane pressure increase ( $\Delta p$ ) and crystal number density. .... 67
- Figure 4-19: Scanning electron micrographs showing (a) a virgin RO membrane sample rinsed with ultrapure water, (b) an RO membrane sample after dissolution of a heterogeneous gypsum crystal leaving behind the characteristic rosette pattern and (c) the physically altered membrane surface after gypsum crystal dissolution. .... 67
- Figure 5-1: LC-OCD-UVD chromatograms of the selected NOM samples. All samples were diluted with ultrapure water to a DOC concentration of  $3.0 \text{ mg}\cdot\text{l}^{-1}$  as quantified by combustion catalytic oxidation after  $0.45 \mu\text{m}$  filtration and adjusted to  $pH = 7.0$ . OC signal intensities were normalized by the sample maximum signal. UV signal intensities were multiplied by the corresponding normalization factor to display the relative differences in UV absorbance of the individual NOM samples. .... 70
- Figure 5-2: Size distribution of organic bulk parameters ( $DOC$ ,  $SAC_{254}$  and  $SAC_{436}$ ) of the selected humic substances determined by fractionation using ultrafiltration and nanofiltration membranes with different molecular weight cutoffs ( $0.4 \text{ kDa} - 150 \text{ kDa}$ ). .... 71

- Figure 5-3: Nanoparticle tracking analysis (NTA) of NOM samples dissolved in ultrapure water and  $17 \text{ mmol}\cdot\text{l}^{-1}$   $\text{CaCl}_2$  solution after  $0.45 \mu\text{m}$  pre-filtration at  $\text{pH} = 7.0$  ( $n = 4 - 5$ ,  $\pm 95$  % confidence interval). (a) DOC-specific colloid concentration and (b) mean colloid diameter ( $d_c$ ). ..... 72
- Figure 6-1: Relative induction times ( $\tau$ ) of gypsum bulk crystallization obtained from stirred beaker experiments at (a)  $SI_{g,b} = 0.71$  and (b)  $SI_{g,b} = 0.56$  in the presence of NOM at varying concentrations. ‘HSNOM after PAC’ was previously treated by powdered activated carbon to remove NOM by adsorption (Chapter 3.1.1). Experimental conditions:  $T = 25.0 \pm 0.1 \text{ }^\circ\text{C}$  ( $\pm$  SD),  $\text{pH} = 6.8 \pm 0.2$  ( $\pm$  SD). ..... 78
- Figure 6-2: Relative crystallization times ( $\Delta t$ ) of gypsum bulk crystallization obtained from stirred beaker experiments at (a)  $SI_{g,b} = 0.71$  and (b)  $SI_{g,b} = 0.56$  in the presence of NOM at varying concentrations. ‘HSNOM after PAC’ was previously treated by powdered activated carbon to remove NOM by adsorption (Chapter 3.1.1). Experimental conditions:  $T = 25.0 \pm 0.1 \text{ }^\circ\text{C}$  ( $\pm$  SD),  $\text{pH} = 6.8 \pm 0.2$  ( $\pm$  SD). ..... 79
- Figure 6-3: (a) Mean crystal diameter ( $d_p$ ) and crystal concentration ( $c$ ) determined by LOT measurement of crystal suspensions taken from stirred beaker experiments at a solution turbidity of  $\kappa = 200 \text{ FNU}$  in the absence (‘Reference’) and presence of NOM (open symbols:  $3 \text{ mg C}\cdot\text{l}^{-1}$ , solid grey symbols:  $5 \text{ mg C}\cdot\text{l}^{-1}$ ). (b) Corresponding crystal size distribution (number distribution) in the presence of  $5 \text{ mg C}\cdot\text{l}^{-1}$  NOM. The area below the reference curve is shaded grey. Experimental conditions:  $SI_{g,b} = 0.56$ ,  $T = 25.0 \pm 0.1 \text{ }^\circ\text{C}$  ( $\pm$  SD),  $\text{pH} = 6.8 \pm 0.2$  ( $\pm$  SD). ..... 81
- Figure 6-4: Scanning electron micrographs of gypsum crystals developed in the (a) absence of NOM (‘Reference’) and (b) presence of  $3 \text{ mg C}\cdot\text{l}^{-1}$  SA. Samples were taken from the stirred beaker at the end of the experiment. Experimental conditions:  $SI_{g,b} = 0.56$ ,  $T = 25.0 \text{ }^\circ\text{C}$ ,  $\text{pH} = 7.0$ . ..... 82
- Figure 6-5: Effects of  $\text{pH}$  on (a) relative induction times ( $\tau_{rel}$ ) and (b) relative crystallization times ( $\Delta t_{rel}$ ) of gypsum bulk crystallization obtained from stirred beaker experiments at  $SI_{g,b} = 0.56$ ,  $T = 25.0 \pm 0.1 \text{ }^\circ\text{C}$  ( $\pm$  SD) and  $3 \text{ mg C}\cdot\text{l}^{-1}$  NOM. Prior to calculation of relative values ( $\tau_{rel}$  and  $\Delta t_{rel}$ ), absolute values of  $\tau$  and  $\Delta t$  obtained at  $\text{pH} \approx 10$  were corrected for the previously observed higher values during reference experiments at  $\text{pH} \approx 10$  (Chapter 4.2 and Figure 4-9). ..... 85
- Figure 6-6: Development of relative real permeability (symbols, left axis) and concentrate turbidity (lines, right axis) during gypsum scaling experiments in the absence (‘Reference’) and presence of (a) BSA, (b) RHA and (c) SA at  $3 \text{ mg C}\cdot\text{l}^{-1}$  (‘+ NOM’) and during pure NOM fouling experiments (‘Fouling’, substitution of  $\text{Na}_2\text{SO}_4$  by  $\text{NaCl}$ ). Experiments were performed using RO system configuration I (permeate withdrawal mode) at ‘low CP operation’. Real permeability was normalized to the initial real permeability at  $t = 0 \text{ min}$  and averaged for 5 min intervals. Experimental conditions:  $T = 25.0 \pm 0.1 \text{ }^\circ\text{C}$  ( $\pm$  SD),  $\Delta p = 25.0 \pm 0.1 \text{ bar}$  ( $\pm$  SD),  $\text{pH} = 6.9 \pm 0.4$  ( $\pm$  SD),  $k_{w,real} = 2.71 \pm 0.09 \text{ l}\cdot\text{m}^{-2}\cdot\text{h}^{-1}\cdot\text{bar}^{-1}$  ( $\pm$  SD),  $SI_{g,b,0} = -0.02$ . ..... 88
- Figure 6-7: Scanning electron micrographs (1,000x magnification) of membrane surfaces after RO scaling experiments displayed in Figure 6-6. Arrows highlight gypsum surface crystals underneath deposited bulk crystals. .... 91
- Figure 7-1: Temporal development of (a) gypsum surface crystal number density (CND) ( $d_p > 49.3 \mu\text{m}$ ), (b) fractional membrane surface coverage (FSC) and (c) mean crystal diameter ( $d_p > 49.3 \mu\text{m}$ ) on virgin and NOM-pre-fouled RO membrane samples. For repeated experiments ( $n > 1$ ), mean values are presented with error bars representing determined minimal and maximal values. .... 94
- Figure 7-2: Real-time membrane surface images (5x magnification, top row) and scanning electron micrographs (200x magnification, bottom row) showing gypsum surface crystals on (a, b) virgin and (c – j) NOM pre-fouled membranes after 240 – 270 min of operation. Arrow in (h) indicates a crystal that grew within SA fouling layer. .... 95

- Figure 7-3: Relationships between (i) mean crystal diameter ( $d_p$ ) and crystal number density ( $CND$ ) and (ii) fractional surface coverage ( $FSC$ ) and crystal number density ( $CND$ ) observed in pure gypsum experiments, i.e. all experiments where growth of regular rosette-like gypsum surface crystals was not distorted by dissolved NOM in solution. Based on final values at  $t = 240$  min. .... 96
- Figure 7-4: Schematic illustration of proposed mechanisms of interaction ( $I - IV$ ) between NOM fouling and gypsum surface scaling on RO membrane surfaces including proposed effects on scaling behavior ( $CND$ : crystal number density,  $d_p$ : mean crystal diameter,  $\uparrow$ : indicates increase,  $\downarrow$ : indicates decrease). It is important to note that the four mechanisms are simplified and will likely occur simultaneously. Fundamentals of ‘cake-enhanced concentration polarization ( $CECP$ )’ by NOM fouling ( $II$ ) are described in Chapter 2.4.5. .... 99
- Figure 7-5: Real-time (5x, top row) and scanning electron (middle row: 200x magnification, bottom row: 5,000x – 50,000x magnification) micrographs of membrane surfaces showing gypsum surface crystals and fouling layers after different intensities of HSNOM pre-fouling. ‘low’: 3 mg C·l<sup>-1</sup> HSNOM diluted in ultrapure water, ‘medium’: 3 mg C·l<sup>-1</sup> HSNOM diluted in 17 mmol·l<sup>-1</sup> CaCl<sub>2</sub> solution, ‘intensive’: 10 mg C·l<sup>-1</sup> HSNOM diluted in 17 mmol·l<sup>-1</sup> CaCl<sub>2</sub> solution. .... 101
- Figure 7-6: Temporal development of (a) gypsum surface crystal number density ( $CND$ ) ( $d_p > 49.3 \mu\text{m}$ ), (b) fractional membrane surface coverage ( $FSC$ ) and (c) mean crystal diameter ( $d_p > 49.3 \mu\text{m}$ ) on virgin membrane samples (‘no fouling’) and membrane samples after different intensities of HSNOM pre-fouling. For repeated experiments ( $n > 1$ ), mean values are presented with error bars representing determined minimal and maximal values. ‘low’: 3 mg C·l<sup>-1</sup> HSNOM diluted in ultrapure water; ‘medium’: 3 mg C·l<sup>-1</sup> HSNOM diluted in 17 mmol·l<sup>-1</sup> CaCl<sub>2</sub> solution; ‘intensive’: 10 mg C·l<sup>-1</sup> HSNOM diluted in 17 mmol·l<sup>-1</sup> CaCl<sub>2</sub> solution. .... 102
- Figure 7-7: Temporal development of (a) gypsum surface crystal number density ( $CND$ ) ( $d_p > 49.3 \mu\text{m}$ ), (b) fractional membrane surface coverage ( $FSC$ ) and (c) mean crystal diameter ( $d_p > 49.3 \mu\text{m}$ ) during RO desalination in the absence (‘Reference’) and presence of different NOM sources at 3 mg C·l<sup>-1</sup>. For repeated experiments ( $n > 1$ ), mean values are presented with error bars representing determined minimal and maximal values. .... 104
- Figure 7-8: Scanning electron micrographs (150x – 3,500x magnification) of membrane surfaces showing gypsum surface crystals after scaling experiments in the presence of different NOMs. .... 105
- Figure 7-9: Scanning electron micrographs (200x – 5,000x magnification) of membrane surfaces showing gypsum surface crystals after scaling experiments in the presence of different HSNOM concentrations. .... 107
- Figure 7-10: Temporal development of (a) gypsum surface crystal number density ( $CND$ ) ( $d_p > 49.3 \mu\text{m}$ ), (b) fractional membrane surface coverage ( $FSC$ ) and (c) mean crystal diameter ( $d_p > 49.3 \mu\text{m}$ ) during RO desalination in the absence (‘Reference’) and presence of different HSNOM concentrations (0.5 – 5 mg C·l<sup>-1</sup>). For repeated experiments ( $n > 1$ ), mean values are presented with error bars representing determined minimal and maximal values. .... 108
- Figure 7-11: Temporal development of (a) gypsum surface crystal number density ( $CND$ ) ( $d_p > 49.3 \mu\text{m}$ ), (b) fractional membrane surface coverage ( $FSC$ ) and (c) mean crystal diameter ( $d_p > 49.3 \mu\text{m}$ ) during RO desalination in the absence (‘Reference’) and presence of SAHA and  $\leq 150$  kDa SAHA fraction. For repeated experiments ( $n > 1$ ), mean values are presented with error bars representing determined minimal and maximal values. .... 109
- Figure 7-12: Scanning electron micrographs (200x – 5,000x magnification) of membrane surfaces showing gypsum surface crystals after (a) reference scaling experiments and experiments in the presence of (b) 3 mg C·l<sup>-1</sup> SAHA and (c) 0.5 mg C·l<sup>-1</sup>  $\leq 150$  kDa SAHA fraction and (d) 3.0 mg C·l<sup>-1</sup>  $\leq 150$  kDa SAHA fraction. .... 110

- Figure 7-13: Temporal development of (a) gypsum surface crystal number density (*CND*) ( $d_p > 49.3 \mu\text{m}$ ), (b) fractional membrane surface coverage (*FSC*) and (c) mean crystal diameter ( $d_p > 49.3 \mu\text{m}$ ) during RO desalination in the absence (*Reference*) and presence of HSNOM and HSNOM fractions after 5 kDa UF filtration and PAC adsorption. For repeated experiments ( $n > 1$ ), mean values are presented with error bars representing determined minimal and maximal values. .... 111
- Figure 7-14: Scanning electron micrographs (150x – 250x magnification) of membrane surfaces showing gypsum surface crystals after scaling experiments (a) without NOM (reference) and in the presence of (b)  $3.0 \text{ mg C}\cdot\text{l}^{-1}$  HSNOM (HS), (c) *HSNOM after PAC* fraction ( $0.1 \text{ mg C}\cdot\text{l}^{-1}$ ), (d)  $0.8 \text{ mg C}\cdot\text{l}^{-1} \leq 5 \text{ kDa}$  HSNOM fraction and (e)  $3.0 \text{ mg C}\cdot\text{l}^{-1} \leq 5 \text{ kDa}$  HSNOM fraction. .... 112
- Figure 7-15: Temporal development of (a) gypsum surface crystal number density (*CND*) ( $d_p > 49.3 \mu\text{m}$ ), (b) fractional membrane surface coverage (*FSC*) and (c) mean crystal diameter ( $d_p > 49.3 \mu\text{m}$ ) during RO desalination in the absence (*Reference*) and presence of  $3 \text{ mg}\cdot\text{l}^{-1}$  antiscalant (AS) and  $3 \text{ mg C}\cdot\text{l}^{-1}$  HSNOM. For repeated experiments ( $n > 1$ ), mean values are presented with error bars representing determined minimal and maximal values. Note that reference experiments were always terminated after 240 min due to severe increases of transmembrane pressure. .... 114
- Figure 7-16: (a – d) Scanning electron micrographs (200x – 500x magnification) of membrane surfaces showing gypsum surface crystals after scaling experiments (a) without additive (*Reference*), (b) in the presence of  $3 \text{ mg C}\cdot\text{l}^{-1}$  HSNOM (HS) and (c, d) in the presence of  $3 \text{ mg}\cdot\text{l}^{-1}$  antiscalant (AS). (e) Detached crystal agglomerate captured from the recycled concentrate stream during operation in the presence of  $3 \text{ mg}\cdot\text{l}^{-1}$  antiscalant (AS). .... 115
- Figure 7-17: Transmembrane pressure ( $\Delta p$ ) increase during gypsum surface scaling experiments in the presence of  $3 \text{ mg}\cdot\text{l}^{-1}$  antiscalant and  $3 \text{ mg C}\cdot\text{l}^{-1}$  HSNOM. Grey areas identifies standard deviation of reference ( $n = 11$ ) and antiscalant-spiked ( $n = 2$ ) experiments. .... 116

### **List of Figures in Appendix II**

- Figure B-1: Laboratory scale reverse osmosis system used for the gypsum scaling and NOM fouling experiments. (a) configuration I was operated at  $\Delta p = 25 \text{ bar}$ ,  $T = 25 \text{ }^\circ\text{C}$  and two different operating modes as exhibited in Table 3-5. (b) configuration II was operated at  $J_w = 30 \text{ l}\cdot\text{m}^{-2}\cdot\text{h}^{-1}$ ,  $T = 20 \text{ }^\circ\text{C}$  and  $v_{cf} = 0.19 \text{ m}\cdot\text{s}^{-1}$ . See Table B-1 for specifications of system components. .... 154
- Figure B-2: Photography of the laboratory scale RO system. .... 155
- Figure B-3: Illustration of different experimental procedures employed during operation of the RO system in configuration II. .... 156

### **List of Figures in Appendix IV**

- Figure D-1: Micrographs of gypsum bulk crystals in concentrate samples taken from experiments displayed in Figure 4-1. Sample turbidity: (a) 10 NTU, (b) 7 NTU and (c) 13 NTU. .... 161
- Figure D-2: XRD diagram of (a) rosette-like surface crystals and (b) needle-like bulk crystals on RO membrane surface. Analysis identified  $\text{CaSO}_4\cdot 2\text{H}_2\text{O}$  (gypsum) according to ICDD® (International Centre for Diffraction Data®) code 00-006-0046 to be the only detected crystalline matter. .... 161
- Figure D-3: XRD diagram of bulk crystals recovered from gypsum bulk crystallization experiments at  $SI_{g,b} = 0.56$ ,  $T = 25.0 \text{ }^\circ\text{C}$  and (a)  $pH = 4.0$ , (b)  $pH = 7.0$  and (c)  $pH = 10.0$ . Analysis identified  $\text{CaSO}_4\cdot 2\text{H}_2\text{O}$  (gypsum) according to ICDD® (International Centre for Diffraction Data®) code 00-006-0046 to be the only detected crystalline matter in all three cases. .... 162
- Figure D-4: Detectable colloid concentration by nanoparticle tracking analysis (NTA) of control and concentrate

- solutions during pure gypsum scaling experiment II\_11 (mean values  $\pm$  95 % confidence interval,  $n = 5 - 7$ ). Control solution is clean water which was temporarily stored in a PE canister. Detection range is limited to  $100 \text{ nm} < d_c < 2,000 \text{ nm}$ . ..... 162
- Figure D-5: Linear correlations between feed solution electrical conductivity ( $EC_f$ ) and (a) total crystal mass and (b) final fractional surface coverage during pure gypsum surface scaling experiments. .... 163
- Figure D-6: (a) Micrograph showing heterogeneous rosette-like gypsum crystals on a DOW FILMTEC™ BW30 reverse osmosis membrane ( $A_{active} = 14.6 \text{ cm}^2$ ) after permeation of 10 ml using a non-agitated dead-end RO permeation cell at constant flux of  $30 \text{ l}\cdot\text{m}^{-2}\cdot\text{h}^{-1}$ , constant temperature of  $25 \text{ }^\circ\text{C}$  and a feed water composition of  $17 \text{ mmol}\cdot\text{l}^{-1} \text{ CaCl}_2\cdot 2\text{H}_2\text{O}$  and  $17 \text{ mmol}\cdot\text{l}^{-1} \text{ Na}_2\text{SO}_4$  in ultrapure water. (b) Micrograph showing significantly higher number of heterogeneous gypsum rosette-like crystals after repetition of the same experiment using the same membrane after cleaning. Cleaning was facilitated in a glass bottle filled with 500 ml ultrapure water, placed on a shaker at 120 rpm for 15 min. Microscopic investigation (63x) after cleaning showed no visible remaining crystals, however, marked physical perforations of the membrane surface in locations where crystals had existed (micrograph not shown due to low contrast). .... 163
- Figure D-7: SEM-EDX analysis performed on membrane surface after gypsum scale had been cleaned off. Cleaning was achieved by shaking at 120 rpm for 48 h in ultrapure water. The SEM taken at 2,000x magnification (a) shows the contours of a previously existing gypsum rosette-like crystal. Higher magnifications (b and c) show physical alterations of the membrane surface. The corresponding EDX spectra are dominated by elements of the membrane material (fully aromatic polyamide (C, O) active layer and polysulfone (C, O, S) support structure) and deposited gold (Au) from sputtering but do not exhibit calcium (Ca) signals. .... 164
- Figure D-8: LC-OCD-UVD chromatograms of selected humic acids and aquatic NOM fractions determined after fractionation by ultrafiltration membranes with different molecular weight cutoffs (0.4 kDa – 150 kDa). Fractionations were performed at a DOC concentration of  $\approx 5 \text{ mg}\cdot\text{l}^{-1}$  as quantified by combustion catalytic oxidation after  $0.45 \text{ }\mu\text{m}$  filtration. RHA, SAHA, and SRNOM samples were fractionated in the presence of  $1 \text{ mmol}\cdot\text{l}^{-1} \text{ NaHCO}_3$  and  $1 \text{ mmol}\cdot\text{l}^{-1} \text{ CaCl}_2$ . OC signal was normalized to maximum sample OC-signal and UV-signal intensity was multiplied by corresponding normalization factor. RHA: malfunctioning of analytical device led to erroneous signals at elution times larger than 50 min. .... 166
- Figure D-9: DOC-specific colloidal size distribution determined by nanoparticle tracking analysis (NTA) of NOM samples dissolved in (a) ultrapure water and (b)  $17 \text{ mmol}\cdot\text{l}^{-1} \text{ CaCl}_2$  solution. Samples were filtrated by  $0.45 \text{ }\mu\text{m}$  and analyzed at  $pH = 7.0$ . Measurements were repeated at least 4 times. .... 167
- Figure D-10: Visual appearance of humic substance samples diluted in ultrapure water to a DOC concentration of  $19.15 \text{ mg}\cdot\text{l}^{-1}$  and at  $pH = 7.0$ . From left to right: SAHA, RHA, SRNOM and HSNOM. .... 167
- Figure D-11: FEEMs obtained from fluorescence spectroscopy of selected NOM samples diluted in ultrapure water to a DOC concentration of  $3.0 \text{ mg}\cdot\text{l}^{-1}$  and adjusted to  $pH = 7.0$ . .... 168
- Figure D-12: (a) NaOH consumption and (b) DOC-specific net NaOH consumption as a function of solution  $pH$  determined by direct base titration of NOM samples. Titrations were performed in duplicate with  $0.1 \text{ mol}\cdot\text{l}^{-1} \text{ NaOH}$  from  $pH = 3.0$  to  $pH = 10.0$  in the background of  $0.1 \text{ mol}\cdot\text{l}^{-1} \text{ NaCl}$  at a DOC concentration of  $19.15 \text{ mg}\cdot\text{l}^{-1}$  and ambient temperature of  $T = 22.2 \pm 0.6 \text{ }^\circ\text{C}$  ( $\pm$  SD). Equilibration time in between titrant addition was 3 min. Blank titrations were performed with NOM-free  $0.1 \text{ mol}\cdot\text{l}^{-1} \text{ NaCl}$  solutions and used to determine the net NaOH consumption. .... 169

- Figure D-13: XRD diagram of bulk crystals recovered from gypsum bulk crystallization experiments at  $SI_{g,b} = 0.56$ ,  $T = 25.0 \pm 0.1$  °C ( $\pm$  SD),  $pH = 7.0 \pm 0.2$  ( $\pm$  SD) in the presence of different NOMs at  $3 \text{ mg C}\cdot\text{l}^{-1}$ . Analysis identified  $\text{CaSO}_4\cdot 2\text{H}_2\text{O}$  (gypsum) according to ICDD® (International Centre for Diffraction Data®) code 00-006-0046 to be the only detected crystalline matter in all five cases. .... 170
- Figure D-14: Micrographs (200x) exhibiting gypsum bulk crystals developed in (a) the absence and (b–d) presence of  $12 \text{ mg C}\cdot\text{l}^{-1}$  NOM and (e)  $1.5 \text{ mg}\cdot\text{l}^{-1}$  antiscalant. Samples were taken from stirred beaker experiments conducted at  $SI_{g,b} = 0.71$ ,  $T = 25.0 \pm 0.1$  °C ( $\pm$  SD),  $pH = 6.8 \pm 0.2$  ( $\pm$  SD) and a turbidity of 5 FNU. .... 170
- Figure D-15: Micrographs (200x – 1,000x magnification) exhibiting gypsum bulk crystals in (a) the absence and (b–d) presence of NOM and (e) antiscalant. Samples were taken from the RO system concentrate stream after the onset of bulk crystallization as observed by turbidity increase. .... 171
- Figure D-16: Scanning electron micrographs (50,000x magnification) of membrane surfaces after NOM pre-fouling. .... 173
- Figure D-17: (a) Flux decline during NOM pre-fouling and (b) increase of relative transmembrane pressure ( $\Delta p$ ) during subsequent gypsum surface scaling. Grey area in (b) identifies standard deviation of reference experiments ( $n = 11$ ). .... 173
- Figure D-18: (a) Flux decline during different HSNOM pre-fouling intensities and (b) increase of relative transmembrane pressure ( $\Delta p$ ) during subsequent gypsum surface scaling experiments. Grey area in (b) identifies standard deviation of reference experiments ( $n = 11$ ). .... 175
- Figure D-19: (a) Increase of relative transmembrane pressure ( $\Delta p$ ) during gypsum surface scaling experiments in the presence of different NOM sources at a concentration of  $3 \text{ mg C}\cdot\text{l}^{-1}$  NOM. Grey area identifies standard deviation of reference experiments. (b) Corresponding final total crystal masses with error bars representing standard deviation. .... 176
- Figure D-20: Fouling layer by SAHA (a) before and (b) after gentle rinsing with ultrapure water. .... 176
- Figure D-21: Increase of relative transmembrane pressure ( $\Delta p$ ) during gypsum surface scaling in the absence ('Reference') and presence of different HSNOM concentrations. Grey area ('Reference') and error bars (HSNOM at  $3 \text{ mg C}\cdot\text{l}^{-1}$ ) indicate standard deviation of repeated experiments. .... 177
- Figure D-22: LC-OCD chromatograms of (a) SAHA and SAHA  $\leq 150$  kDa fraction and (b) HSNOM,  $\leq 5$  kDa HSNOM fraction and non-adsorbable HSNOM fraction ('HSNOM after PAC'). All samples except for 'HSNOM after PAC' were diluted to a DOC concentration of  $3.0 \text{ mg}\cdot\text{l}^{-1}$  as quantified by combustion catalytic oxidation. 'HSNOM after PAC' was analyzed without further dilution at a DOC concentration of  $0.3 \text{ mg}\cdot\text{l}^{-1}$  as quantified by combustion catalytic oxidation. .... 178
- Figure D-23: FEEMs obtained from fluorescence spectroscopy of (a) SAHA, (b) SAHA  $\leq 150$  kDa fraction, (d) HSNOM and (e) HSNOM  $\leq 5$  kDa fraction diluted in ultrapure water to a DOC concentration of  $3.0 \text{ mg}\cdot\text{l}^{-1}$  and a  $pH$  of 7.0. FEEMs in (c) and (f) show the fluorescent fractions removed by UF fractionation. .... 179
- Figure D-24: FEEM obtained from fluorescence spectroscopy of 'HSNOM after PAC'. Sample DOC concentration was  $0.3 \text{ mg}\cdot\text{l}^{-1}$  and  $pH$  was 7.0. .... 180
- Figure D-25: Increase of relative transmembrane pressure ( $\Delta p$ ) during gypsum surface scaling in the presence of (a) SAHA and  $\leq 150$  kDa SAHA fraction and (b) HSNOM,  $\leq 5$  kDa HSNOM fraction and HSNOM after PAC. Grey areas identify standard deviation of reference experiments ( $n = 11$ ). .... 180

## List of Tables

Table 2-1: Examples and properties of commonly used organic macromolecules in NOM-related membrane research: (a) humic acid, (b) alginate and (c) BSA. Sources: <sup>(a)</sup> [170], <sup>(b)</sup> [175], <sup>(c)</sup> manufacturer's data (Sigma Aldrich Co., MO, USA), <sup>(d)</sup> [182], <sup>(e)</sup> [185], <sup>(f)</sup> [25], <sup>(g)</sup> [168], <sup>(h)</sup> [186], <sup>(i)</sup> [187], <sup>(j)</sup> [188], <sup>(k)</sup> [189].	29
Table 3-1: Summary of natural organic matter sources used in this study. (a) Commercially available products obtained in powder or crystalline form. Suppliers: <sup>1</sup> Sigma-Aldrich Co. (MO, USA), <sup>2</sup> Carl Roth GmbH + Co KG (Germany), <sup>3</sup> International Humic Substances Society. (b) Aquatic NOM sampled from lake 'Hohlohsee'.	35
Table 3-2: Preparation protocol, final DOC concentrations ( $\pm$ SD) and maximum duration of usage (storage life at 4 °C) of NOM stock solutions listed in Table 3-1a. All substances were dissolved in ultrapure water.	35
Table 3-3: Composition of the 'Hohlohsee' water (HSNOM) after pre-filtration by 0.45 $\mu$ m (sample ID: HO29). Concentrations of inorganic constituents were determined by ICP-OES or IC and supplied by the Engler-Bunte-Institut Karlsruhe, Germany.	36
Table 3-4: Select properties of the employed reverse osmosis membrane.	37
Table 3-5: Specifications of 'high' and 'low CP operation' during RO desalination experiments using configuration I. Mass transfer coefficients were experimentally determined according to [217].	39
Table 3-6: Overview of membranes used for fractionation of NOM samples.	45
Table 3-7: Solubility products ( $K_{sp}$ ) at 25 °C for major scale-forming salts used by the phreeqc.dat database.	47
Table 4-1: (a) Critical volumetric concentration factors ( $VCF_{crit}$ ) and operating times ( $t_{crit}$ ) with corresponding water fluxes ( $J_w$ ), concentration polarization moduli ( $f_{CP}$ ), gypsum saturation indices in the bulk solution ( $SI_{g,b}$ ) and at the membrane surface ( $SI_{g,m}$ ) and dominant gypsum scaling mechanism during 'high' and 'low CP operation'. (b) Corresponding data for experiments displayed in Figure 4-3 and Figure 4-4. Initial clean water permeability coefficients ( $k_w$ ): 2.70 – 2.95 l·m <sup>-2</sup> ·h <sup>-1</sup> ·bar <sup>-1</sup> (Table C-2).	51
Table 5-1: DOC-specific spectral absorbance at $\lambda = 254$ nm ( $SUVA_{254}$ ) and $\lambda = 436$ nm ( $SA_{254}$ ) of the selected NOM sources diluted in ultrapure water to a DOC concentration of 3.0 mg·l <sup>-1</sup> and a pH of 7.0.	73
Table 5-2: Position and intensity of fluorescence peaks in the selected NOM sample's excitation emission matrices. Samples were diluted in ultrapure water to a DOC of 3.0 mg·l <sup>-1</sup> and adjusted to pH = 7.0.	74
Table 5-3: Summary of carboxylic, phenolic and total acidities of the selected NOM sources. (a) Values quantified by direct base titration performed with 0.1 mol·l <sup>-1</sup> NaOH from pH = 3.0 to pH = 10.0 in the background of 0.1 mol·l <sup>-1</sup> NaCl at a DOC concentration of 19.15 mg·l <sup>-1</sup> and at $T = 22.2 \pm 0.6$ °C ( $\pm$ SD). (b) Values collected from different literature sources.	75
Table 6-1: DOC removal as absolute values during select stirred beaker experiments in the presence of varying NOM concentrations. Samples were taken at the beginning ( $\kappa = 0$ FNU) and end of an experiment ( $\kappa \approx 1,000$ FNU) and immediately filtered by 0.45 $\mu$ m. Experimental conditions: $SI_{g,b} = 0.71$ , $T = 25.0$ °C, $pH = 7.0$ .	81
Table 6-2: Rate constants of crystal growth ( $\lambda_G$ ) of gypsum bulk crystallization in the presence of selected NOM sources. Values for $\lambda_G$ were obtained from the temporal evolution of the mean crystal diameter (LOT measurements analogue to the procedure described in Chapter 4.2) during stirred beaker experiments at $SI_{g,b} = 0.51$ . A complete list including supplemental experimental conditions and Pearson correlation coefficients can be found in Table D-3.	83

- Table 6-3: Relative induction ( $\tau_{rel}$ ) and crystallization ( $\Delta t_{rel}$ ) times of gypsum bulk crystallization from supersaturated solution ( $SI_{g,b} = 0.71$ ,  $T = 25.0 \pm 0.2$  °C ( $\pm$  SD),  $pH = 6.8 \pm 0.3$  ( $\pm$  SD) in the presence of antiscalant at varying dosage ( $c_{AS} = 1.5 - 12$  mg·l<sup>-1</sup>). ..... 87
- Table 6-4: Critical volumetric concentration factors ( $VCF_{crit}$ ), critical operating time ( $t_{crit}$ ) and gypsum bulk supersaturation ( $SI_{g,b}$ ) determined at the onset of gypsum scaling during RO desalination ('low CP operation') in the presence of NOM (Figure 6-6) by (a) bulk crystallization based on turbidity increase and (b) bulk and surface crystallization based on real permeability decline. Data in the presence of antiscalant (AS) was extracted from Figure 4-1. From complementary NOM fouling experiments, concentrate DOC concentrations ( $c_{DOC,c}$ ) for the critical  $VCFs$  were quantified and corresponding total masses of DOC that were adsorbed or deposited on the membrane surface ( $\Delta m_{DOC}$ ) were calculated. Experimental conditions:  $T = 25.0 \pm 0.1$  °C ( $\pm$  SD),  $\Delta p = 25.0 \pm 0.1$  bar ( $\pm$  SD),  $pH = 6.9 \pm 0.4$  ( $\pm$  SD),  $k_{w,real} = 2.71 \pm 0.09$  l·m<sup>-2</sup>·h<sup>-1</sup>·bar<sup>-1</sup> ( $\pm$  SD),  $SI_{g,b,0} = -0.02$ ,  $c_{NOM,0} = 3$  mg C·l<sup>-1</sup>. ..... 89

### **List of Tables in Appendix II**

- Table B-1: List and specifications of major laboratory scale RO system components. .... 155

### **List of Tables in Appendix III**

- Table C-1: List of conducted stirred beaker gypsum bulk crystallization experiments including relevant parameters (mean  $\pm$  SD). ..... 157
- Table C-2: List of conducted RO desalination experiments including relevant parameters using RO setup – configuration I. Concentrations are initial feed solution concentrations at the beginning of an experiment ( $t = 0$  min). Transmembrane pressure ( $\Delta p$ ),  $pH$  and temperature ( $T$ ) are average values of the respective experiment. Observed NaCl rejection coefficients ( $R(NaCl)$ ) are based on rejection of electrical conductivity during NaCl conditioning. .... 158
- Table C-3: List of conducted RO desalination experiments including relevant parameters using RO setup – configuration II. Clean water permeabilities ( $k_{w,0}$ ) were determined during ultrapure water conditioning. Observed CaCl<sub>2</sub> rejection coefficients ( $R(CaCl_2)$ ) were determined during CaCl<sub>2</sub> conditioning; for experiments in (b), CaCl<sub>2</sub> conditioning was performed after NOM pre-fouling and  $R(CaCl_2)$  represents CaCl<sub>2</sub> rejection after pre-fouling. Concentrate electrical conductivity ( $EC_{c,0}$ ) are initial values at  $t = 0$  min. Concentrate turbidity ( $\kappa$ ),  $pH$  and temperature ( $T$ ) are average values of the respective experiment. .... 159

### **List of Tables in Appendix IV**

- Table D-1: Solution compositions of different brackish waters and calculated saturation indices for gypsum ( $SI_g$ ), calcite ( $SI_c$ ) and barite ( $SI_b$ ) at  $T = 20$  °C and  $pH = 7$  for raw waters and concentrates at 75 % recovery. .... 160
- Table D-2: Quantification results of LC-OCD-UVD chromatograms according to Huber et al. (2011) [218] using ChromCALC Software (DOC Labor Dr. Huber, Germany) for peak integration. Prior to analysis, each sample was diluted with ultrapure water to a DOC concentration of 3.0 mg·l<sup>-1</sup> as quantified by combustion catalytic oxidation after 0.45  $\mu$ m filtration and adjusted to  $pH = 7.0$ . cOC (chromatographable organic carbon): OC quantified from the hull curve of the LC-OCD chromatogram, HOC (hydrophobic organic carbon): OC retained in the LC column,  $\Phi_{UV}$  (oxidation yield): ratio between the DOC quantified in the LC column bypass and the DOC quantified by combustion catalytic oxidation,  $\Phi_{HOC}$  (fraction of HOC): % fraction of the OC retained in the LC column, i.e. ration between the concentrations of HOC and bypass DOC, LMW: low molecular weight. .... 165

Table D-3: Rate constants of crystal growth ( $\lambda_G$ ) of gypsum bulk crystallization in the presence of selected NOM sources. Obtained from the temporal evolution of the mean crystal diameter (LOT measurements, analogue to the procedure described in Chapter 4.2) during stirred beaker experiments at $SI_{g,b} = 0.51$ . .....	171
Table D-4: Zeta potential ( $\zeta$ ) and contact angle ( $\theta_c$ ) measurements of virgin BW30 ('Reference') and organically fouled BW30 membrane samples. Different sample preparations were performed: (a) static fouling experiments: membrane samples were soaked in ultrapure water or NOM solutions at a DOC concentration of $\approx 25 \text{ mg}\cdot\text{l}^{-1}$ and a $pH$ of $\approx 7.0$ for at least 72 h at 150 rpm, (b) dead-end membrane filtration: samples were permeated with ultrapure water or 100 ml of an NOM solution (DOC concentration $\approx 25 \text{ mg}\cdot\text{l}^{-1}$ ) at $\Delta p = 18 \text{ bar}$ , (c) cross-flow membrane filtration: membrane samples were prepared according to the protocol for NOM fouling experiments described in Chapter 3.2.3. ....	172
Table D-5: Axial distribution of crystal mass after scaling experiments: (a) pre-fouling experiments, (b) HSNOM pre-fouling experiments at different intensities and (c) experiments in the presence of $3.0 \text{ mg C}\cdot\text{l}^{-1}$ dissolved NOM. For repeated experiments values are presented as mean $\pm$ SD. ....	174
Table D-6: DOC concentrations during scaling experiments on virgin ('Reference') and NOM pre-fouled membranes. For 'Reference', values are presented as mean values $\pm$ SD (n = 10).....	175
Table D-7: DOC depletion during gypsum surface scaling experiments in the presence of $3 \text{ mg C}\cdot\text{l}^{-1}$ NOM (Figure 7-7). ....	176
Table D-8: Colloid concentration (NTA measurement), DOC removal, DOC-specific UV-vis absorbance at $\lambda = 254 \text{ nm}$ ( $SUVA_{254}$ ) and $\lambda = 436 \text{ nm}$ ( $SA_{436}$ ) and oxidation yields ( $\Phi_{UV}$ ) before and after UF fractionation of SAHA and HSNOM stock solutions. * Oxidation yields were obtained from LC-OCD analysis performed at a DOC concentration of $3 \text{ mg}\cdot\text{l}^{-1}$ . n.d.: none detected.....	177

## Abbreviations and Quantities

### Abbreviations

<b>ACS</b>	American Chemical Society	<b>NTU</b>	nephelometric turbidity unit
<b>AS</b>	antiscalant	<b>OC</b>	organic carbon
<b>BDL</b>	below detection limit	<b>OH</b>	hydroxyl group
<b>BSA</b>	bovine serum albumin	<b>PA</b>	polyamide
<b>BWRO</b>	brackish water reverse osmosis	<b>PAA</b>	polyacrylic acid
<b>C=O</b>	carbonyl group	<b>PAC</b>	powdered activated carbon
<b>CECP</b>	cake-enhanced concentration polarization	<b>PBTCA</b>	2-Phosphono-butane-1,2,4-tricarboxylic acid
<b>CI</b>	confidence interval	<b>PMA</b>	polymaleic acid
<b>cOC</b>	OC (chromatographable organic ca	<b>PTFE</b>	polytetrafluoroethylene
<b>COOH</b>	carboxyl group	<b>PVA</b>	polyvinyl alcohol
<b>CP</b>	concentration polarization	<b>QCM</b>	quartz crystal microbalance
<b>DOC</b>	dissolved organic carbon	<b>r.u.</b>	Raman units
<b>EC</b>	electrical conductivity	<b>RHA</b>	humic acid supplied by Carl Roth GmbH + Co KG (Germany)
<b>EDTA</b>	ethylenediaminetetraacetic acid	<b>rms</b>	root mean square
<b>EDX</b>	energy dispersive X-ray spectroscopy	<b>RO</b>	reverse osmosis
<b>FEEM</b>	fluorescence excitation-emission matrix	<b>S<sub>i</sub></b>	Crystal surface i
<b>FNU</b>	formazin nephelometric unit	<b>SA</b>	sodium alginate
<b>FO</b>	forward osmosis	<b>SAHA</b>	humic acid supplied by Sigma-Aldrich Co. (MO, USA)
<b>HOC</b>	hydrophobic organic carbon	<b>SD</b>	standard deviation
<b>HR-BWRO</b>	high recovery brackish water reverse osmosis	<b>SEM</b>	scanning electron microscopy
<b>HSNOM</b>	'Hohlohsee' NOM	<b>SI</b>	saturation index
<b>IC</b>	ion chromatography	<b>SRNOM</b>	Suwannee River NOM supplied by the IHSS
<b>ICDD</b>	International Centre for Diffraction Data	<b>SWRO</b>	seawater reverse osmosis
<b>ICP-OES</b>	inductively coupled plasma optical emission spectrometry	<b>TDS</b>	total dissolved solids
<b>IHSS</b>	International Humic Substances Society	<b>TFC</b>	thin-film composite
<b>ISO</b>	International Organization for Standardization	<b>TOC</b>	total organic carbon
<b>LC-OCD-UVD</b>	liquid chromatography coupled with detection of organic carbon and spectral UV absorbance	<b>UF</b>	ultrafiltration
<b>LED</b>	light-emitting diode	<b>UV</b>	ultraviolet
<b>LOT</b>	laser obscuration time	<b>XRD</b>	X-ray powder diffraction
<b>MD</b>	membrane distillation		
<b>MF</b>	microfiltration		
<b>NDIR</b>	nondispersive infrared sensor		
<b>NF</b>	nanofiltration		
<b>NH<sub>2</sub></b>	amino group		
<b>NOM</b>	natural organic matter		

**Quantities – Latin Symbols**

$A_{active}$	$m^2$	active membrane area	$f_{CP}$	–	concentration polarization modulus
$A_i$	$m^2$	active membrane area of subsection i	$FSC$	–	fractional surface coverage
$c$	$mg \cdot l^{-1} / mol \cdot l^{-1}$	concentration	$\Delta G^*$	$J \cdot mol^{-1}$	Gibbs free energy
$c_{AS}$	$mg \cdot l^{-1}$	antiscalant concentration	$HRT$	s	hydraulic residence time
$c_{AS,0}$	$mg \cdot l^{-1}$	antiscalant concentration at $t = 0$ s	$i$	–	van't Hoff factor
$c_b$	$mg \cdot l^{-1} / mol \cdot l^{-1}$	concentration in the bulk solution	$IAP$	$mol^2 \cdot l^{-2}$	ion activity product
$c_c$	$mg \cdot l^{-1} / mol \cdot l^{-1}$	concentration in the concentrate stream	$J_N$	$s^{-1}$	nucleation rate
$c_{DOC}$	$mg \cdot l^{-1}$	DOC concentration	$J_w$	$l \cdot m^{-2} \cdot h^{-1}$	water flux
$c_{DOC,c}$	$mg \cdot l^{-1}$	DOC concentration in the concentrate stream	$k$	$m \cdot s^{-1}$	mass transfer coefficient
$c_f$	$mg \cdot l^{-1} / mol \cdot l^{-1}$	concentration in the feed stream	$k_s$	$m \cdot s^{-1}$	solute permeability coefficient
$c_g$	$mol \cdot l^{-1}$	gypsum concentration	$K_{sp}$	$mol^2 \cdot l^{-2}$	solubility product
$c_m$	$mg \cdot l^{-1} / mol \cdot l^{-1}$	concentration at the membrane surface	$k_w$	$l \cdot m^{-2} \cdot h^{-1} \cdot bar^{-1}$	clean water permeability coefficient
$\Delta c_m$	$mol \cdot l^{-1}$	concentration difference across membrane	$k_{w,real}$	$l \cdot m^{-2} \cdot h^{-1} \cdot bar^{-1}$	real water permeability
$c_{NOM}$	$mg \cdot C \cdot l^{-1}$	NOM concentration	$L$	m	length
$c_{NOM,0}$	$mg \cdot C \cdot l^{-1}$	NOM concentration at $t = 0$ s	$M_w$	Da / $g \cdot mol^{-1}$	molecular weight
$c_p$	$mg \cdot l^{-1} / mol \cdot l^{-1}$	concentration in the permeate stream	$MWCO$	Da / $g \cdot mol^{-1}$	molecular weight cut-off
$c_s$	$mol \cdot l^{-1}$	salt concentration	$\Delta m$	mg	crystal mass
$c_{TDS}$	$mg \cdot l^{-1}$	total dissolved solids concentration	$\Delta m_{DOC}$	mg	total adsorbed or deposited mass of DOC
$CF$	–	concentration factor	$\Delta m_{total}$	mg	total crystal mass
$CND$	$cm^{-2}$	crystal number density	$n$	–	number of experiments
$D$	$m^2 \cdot s^{-1}$	solute diffusion coefficient	$p$	–	significance level
$d_c$	nm	colloid diameter	$pH$	–	negative logarithm to the base 10 of $H^+$ activity
$d_{c,max}$	$\mu m$	maximal colloid diameter	$pH_{IEP}$	–	isoelectric point
$d_{c,min}$	$\mu m$	minimal colloid diameter	$pK_a$	–	negative logarithm to the base 10 of acidity constant
$d_{min}$	nm	minimum diameter	$\Delta p$	bar	transmembrane pressure
$d_p$	$\mu m$	particle or crystal diameter	$R$	$J \cdot mol^{-1} \cdot K^{-1}$	ideal gas constant
$d_{p,min}$	$\mu m$	minimum particle or crystal diameter	$R$	–	Pearson correlation coefficient
$d_{p,max}$	$\mu m$	maximum particle or crystal diameter	$R^2$	–	Square of the Pearson correlation coefficient
$EC$	$\mu S \cdot cm^{-1}$	electrical conductivity	$R_{int}$	%	intrinsic salt rejection coefficient
$EC_{c,0}$	$\mu S \cdot cm^{-1}$	electrical conductivity of the concentrate stream at $t = 0$ s	$R_{obs}$	%	observed salt rejection coefficient
$EC_f$	$\mu S \cdot cm^{-1}$	electrical conductivity of the feed stream	$R(CaCl_2)$	%	observed $CaCl_2$ rejection coefficient
			$R(NaCl)$	%	observed $NaCl$ rejection coefficient
			$R_G$	$m \cdot s^{-1}$	growth rate

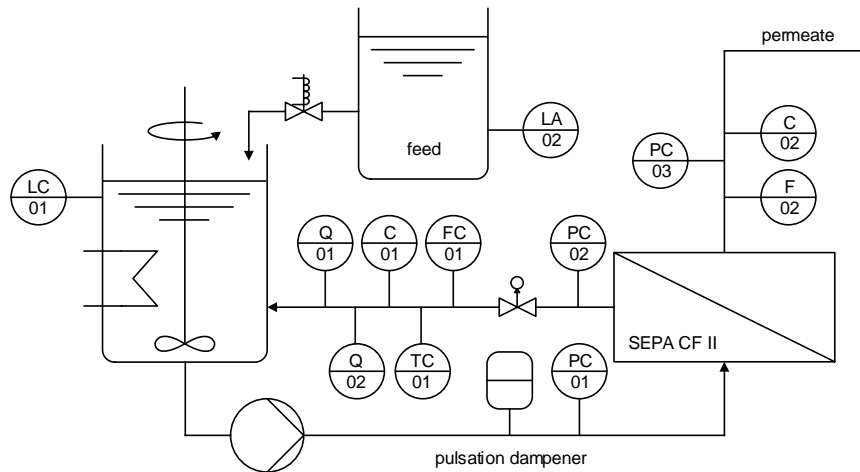
$R_{G,i}$	$\text{m}\cdot\text{s}^{-1}$	growth rate of crystal face i	$SI_{g,c}$	–	supersaturation index of gypsum in the concentrate stream
$r_{min}$	nm	minimum radius	$SI_{g,f}$	–	supersaturation index of gypsum in the feed stream
$S_{g,m}$	–	supersaturation ratio of gypsum at the membrane surface	$SI_{g,m}$	–	supersaturation index of gypsum at the membrane surface
$SA_{436}$	$\text{l}\cdot\text{mg}^{-1}\cdot\text{m}^{-1}$	specific absorbance at $\lambda = 436$ nm	$SUVA_{254}$	$\text{l}\cdot\text{mg}^{-1}\cdot\text{m}^{-1}$	specific UV absorbance at $\lambda = 254$ nm
$SAC$	$\text{m}^{-1}$	spectral absorption coefficient	$t$	s	time
$SAC_{254}$	$\text{m}^{-1}$	spectral absorption coefficient at $\lambda = 254$ nm	$t_{crit}$	s	critical operating time
$SAC_{436}$	$\text{m}^{-1}$	spectral absorption coefficient at $\lambda = 436$ nm	$\Delta t$	s	crystallization time
$SI$	–	supersaturation index	$\Delta t_{rel}$	–	relative crystallization time
$SI_{b,c}$	–	supersaturation index of barite in the concentrate stream	$T$	K or $^{\circ}\text{C}$	temperature
$SI_{b,f}$	–	supersaturation index of barite in the feed stream	$v_{CF}$	$\text{m}\cdot\text{s}^{-1}$	cross-flow velocity
$SI_{c,c}$	–	supersaturation index of calcite in the concentrate stream	$VCF$	–	volumetric concentration factor
$SI_{c,f}$	–	supersaturation index of calcite in the feed stream	$VCF_0$	–	volumetric concentration factor at $t = 0$ s
$SI_{g,b}$	–	supersaturation index of gypsum in the bulk solution	$VCF_{crit}$	–	critical volumetric concentration factor
$SI_{g,b,0}$	–	supersaturation index of gypsum in the bulk solution at $t = 0$ s	$V_p$	l	permeate volume
			$V_{reservoir}$	l	reservoir volume
			$x$	m	axial position

### Quantities – Greek Symbols

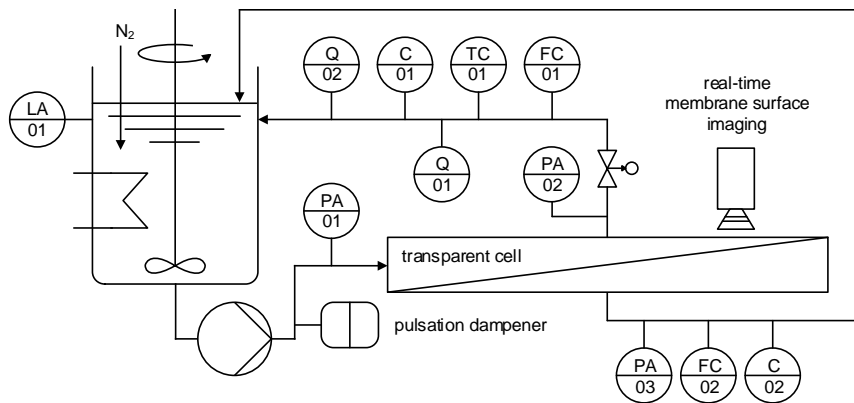
$\alpha$	–	degree of dissociation	$\pi_f$	bar	osmotic pressure of the feed stream
$\delta$	m	boundary layer thickness	$\pi_m$	bar	osmotic pressure at the membrane surface
$\zeta$	mV	zeta potential	$\pi_p$	bar	osmotic pressure of the permeate stream
$\theta_c$	$^{\circ}$	contact angle	$\Delta\pi_b$	bar	osmotic pressure difference between bulk and permeate
$\kappa$	FNU / NTU	turbidity	$\Delta\pi_f$	bar	osmotic pressure difference between feed and permeate
$\kappa_0$	FNU / NTU	turbidity at $t = 0$ s	$\Delta\pi_m$	bar	osmotic pressure difference across membrane
$\kappa_f$	FNU / NTU	turbidity of the feed stream	$\sigma$	$\text{J}\cdot\text{m}^{-2}$	solution-mineral interfacial energy
$\lambda$	nm	wavelength	$\tau$	s	induction time
$\lambda_{Em}$	nm	emission wavelength	$\tau_{rel}$	–	relative induction time
$\lambda_{Ex}$	nm	excitation wavelength	$\Phi$	%	water recovery
$\lambda_G$	$\text{s}^{-1}$	rate constant of crystal growth	$\omega$	$\text{min}^{-1}$	stirring speed
$\lambda_t$	$\text{s}^{-1}$	rate constant of turbidity increase	$\Phi_{HOC}$	%	fraction of hydrophobic organic carbon
$\nu$	–	number of dissociated ions of a respective molecule or salt	$\Phi_{UV}$	%	oxidation yield
$\pi$	bar	osmotic pressure			
$\pi_b$	bar	osmotic pressure of the bulk solution			

## B. Appendix II – Supplemental Material and Methods

- (a) Configuration I: permeate withdrawal, stainless steel membrane cell (model: SEPA CF II, Sterlitech Corp., USA)



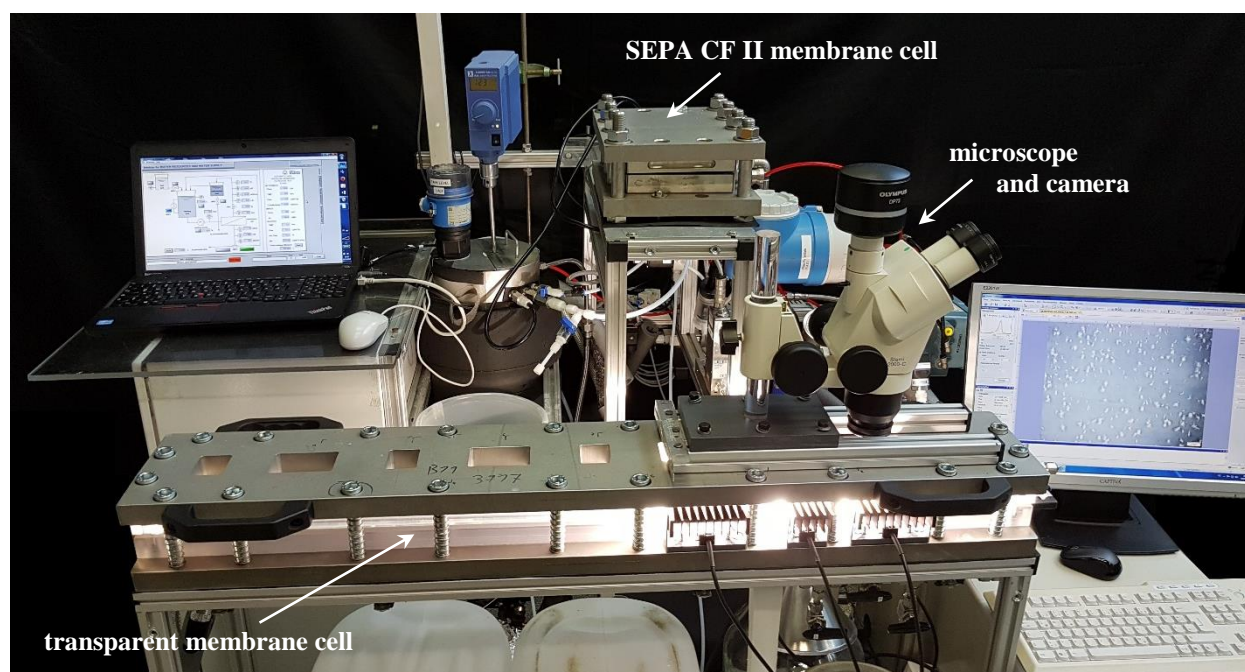
- (b) Configuration II: full recirculation, transparent membrane cell (Convergence Industry B.V., Netherlands) and real-time membrane surface imaging



**Figure B-1:** Laboratory scale reverse osmosis system used for the gypsum scaling and NOM fouling experiments. (a) configuration I was operated at  $\Delta p = 25$  bar,  $T = 25$  °C and two different operating modes as exhibited in Table 3-5. (b) configuration II was operated at  $J_w = 30$  l·m<sup>-2</sup>·h<sup>-1</sup>,  $T = 20$  °C and  $v_{cf} = 0.19$  m·s<sup>-1</sup>. See Table B-1 for specifications of system components.

**Table B-1: List and specifications of major laboratory scale RO system components.**

<b>component</b>	<b>specifications</b>	<b>model and supplier</b>
<i>feed pump</i>	3 piston positive displacement diaphragm pump	G03B; Verder Deutschland GmbH & Co. KG, Germany
<i>level sensors:</i>		
LC/LA 01	capacitive level sensor	Liquicap T; E + H Messtechnik GmbH+Co. KG, Germany
<i>flow meters:</i>		
FC 01	magnetic inductive flow meter 15 – 420 l·h <sup>-1</sup>	Promag 50H04; E + H Messtechnik GmbH+Co. KG, Germany
F 02/FC 02	Coriolis mass flow meter 0 – 3,500 g·h <sup>-1</sup>	M14-AGD-33-0-S; Bronkhorst High-Tech B.V., Netherlands
<i>pressure transmitters:</i>		
PC/A 01/02	0 – 100 bar	A-10; WIKA Alexander Wiegand SE & Co. KG, Germany
PC/A 03	0 – 1,000 mbar	A-10; WIKA Alexander Wiegand SE & Co. KG, Germany
<i>measurement of electrical conductivity:</i>		
C 01/02	1 μS·cm <sup>-1</sup> – 2 S·cm <sup>-1</sup>	TetraCon® 325/LRD 325; Xylem Analytics Germany Sales GmbH & Co. KG, WTW, Germany
<i>pH measurement:</i>		
Q 01	gel electrolyte, pH = 0 – 14	PL82120pHT-VP; SI Analytics GmbH, Germany
<i>temperature measurement:</i>		
TC 01	-5 – 100 °C	PL82120pHT-VP; SI Analytics GmbH, Germany
<i>turbidity measurement:</i>		
Q 02	0 – 10,000 NTU	Turb® 555; Xylem Analytics Germany Sales GmbH & Co. KG, WTW, Germany

**Figure B-2: Photography of the laboratory scale RO system.**

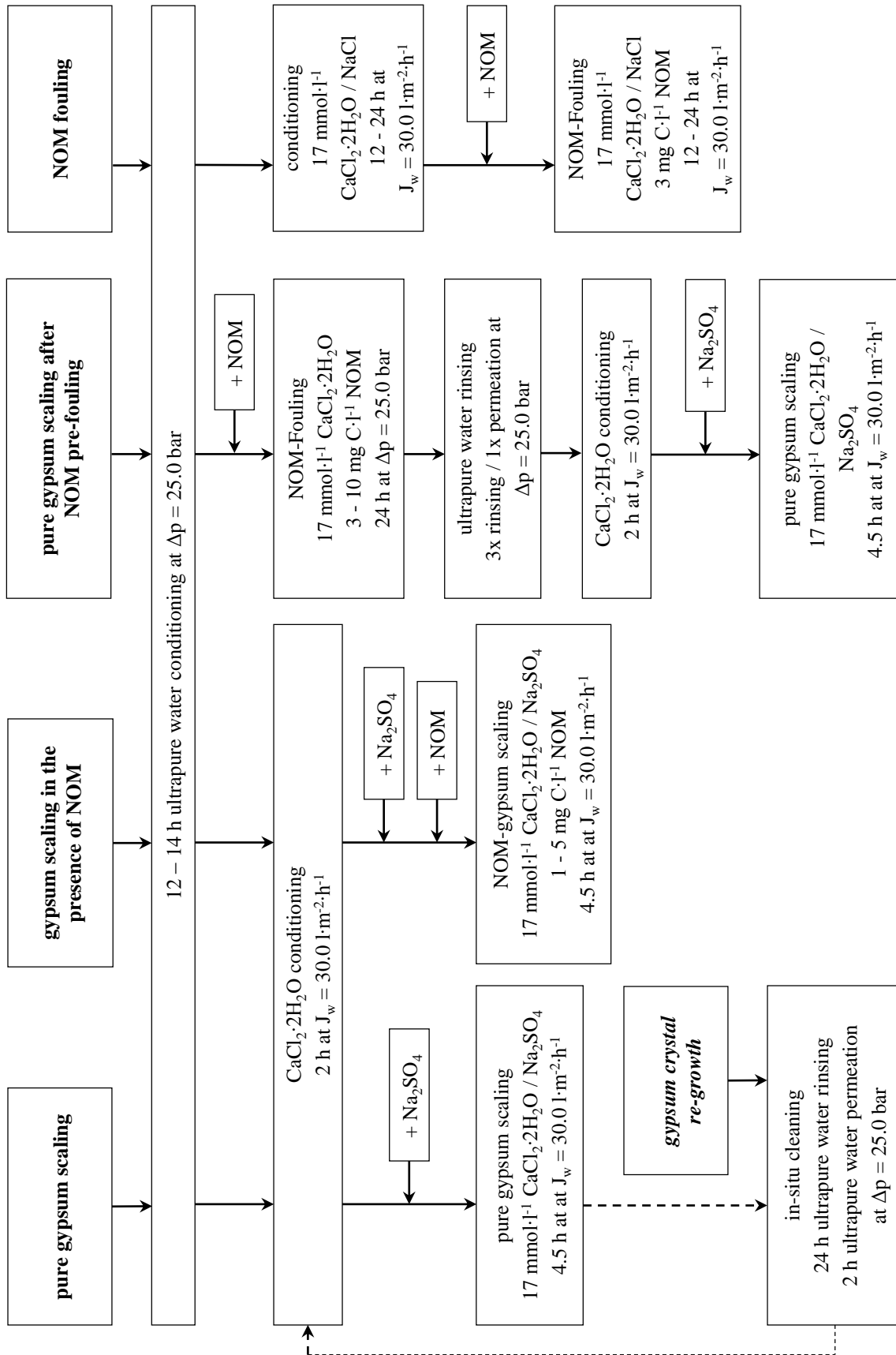


Figure B-3: Illustration of different experimental procedures employed during operation of the RO system in configuration II.

## C. Appendix III – Lists of Conducted Experiments

### I. Stirred Beaker Experiments

**Table C-1: List of conducted stirred beaker gypsum bulk crystallization experiments including relevant parameters (mean  $\pm$  SD).**

#	CaCl <sub>2</sub> mmol·l <sup>-1</sup>	Na <sub>2</sub> SO <sub>4</sub> mmol·l <sup>-1</sup>	AS mg·l <sup>-1</sup>	DOC mg C·l <sup>-1</sup>	NOM –	T °C	pH –	SI <sub>g,b</sub> –	n –	$\tau \pm SD$ s	$At \pm SD$ s	$\lambda_t \pm SD$ ·10 <sup>-4</sup> s <sup>-1</sup>	R ( $\lambda_t$ ) –
Ref_34_7	31	31	–	–	–	25.1	7.0	0.35	2	22,356 $\pm$ 1,986	15,246 $\pm$ 3,029	2.5 $\pm$ 0.4	0.997
Ref_51_7	51	51	–	–	–	25.1	7.1	0.56	10	627 $\pm$ 180	834 $\pm$ 289	54.4 $\pm$ 22.2	0.998
Ref_68_7	68	68	–	–	–	24.8	6.9	0.71	16	174 $\pm$ 64	260 $\pm$ 120	194.6 $\pm$ 81.8	0.997
Ref_85_7	85	85	–	–	–	25.0	7.0	0.83	2	87 $\pm$ 0	164 $\pm$ 15	202.2 $\pm$ 15.6	0.994
Ref_51_4.0	51	51	–	–	–	25.1	4.3	0.56	5	747 $\pm$ 149	806 $\pm$ 168	57.5 $\pm$ 8.9	0.999
Ref_51_5.5	51	51	–	–	–	25.1	5.5	0.56	3	613 $\pm$ 31	641 $\pm$ 44	68.5 $\pm$ 2.4	0.999
Ref_51_8.5	51	51	–	–	–	25.0	8.2	0.56	4	674 $\pm$ 218	672 $\pm$ 186	69.2 $\pm$ 18.8	0.999
Ref_51_10.0	51	51	–	–	–	25.1	10.0	0.56	5	1,424 $\pm$ 369	1,098 $\pm$ 314	47.9 $\pm$ 8.0	0.999
RHA_68_7_3	68	68	–	3	RHA	25.1	6.7	0.71	2	762 $\pm$ 153	443 $\pm$ 14	98.0 $\pm$ 9.4	0.998
RHA_68_7_6	68	68	–	6	RHA	25.0	7.2	0.71	2	1,171 $\pm$ 173	866 $\pm$ 24	78.7 $\pm$ 2.4	0.997
RHA_68_7_12	68	68	–	12	RHA	25.0	7.0	0.71	2	1,766 $\pm$ 345	3,051 $\pm$ 718	12.6 $\pm$ 3.1	0.999
RHA_68_4_6	68	68	–	6	RHA	25.0	4.1	0.71	1	331	297	120.1	0.996
RHA_68_10_6	68	68	–	6	RHA	25.0	9.8	0.71	1	2,415	1,878	54.3	0.996
SAHA_68_7_1	68	68	–	1	SAHA	25.1	6.8	0.71	2	588 $\pm$ 15	1,008 $\pm$ 21	88.6 $\pm$ 1.8	0.999
SAHA_68_7_3	68	68	–	3	SAHA	25.2	6.7	0.71	2	721 $\pm$ 40	1,169 $\pm$ 163	77.5 $\pm$ 0.8	1.000
SAHA_68_7_5	68	68	–	5	SAHA	25.1	6.8	0.71	2	1,292 $\pm$ 109	3,541 $\pm$ 255	38.0 $\pm$ 0.8	0.998
SAHA_68_4_3	68	68	–	3	SAHA	25.0	4.5	0.71	3	552 $\pm$ 57	888 $\pm$ 93	120.6 $\pm$ 13.6	0.999
SAHA_68_10_3	68	68	–	3	SAHA	25.1	9.9	0.71	2	867 $\pm$ 100	2,285 $\pm$ 170	57.5 $\pm$ 4.2	0.999
SAHA_51_7_1	51	51	–	1	SAHA	25.1	6.8	0.56	1	970	1,265	61.1	0.999
SAHA_51_7_3	51	51	–	3	SAHA	25.1	6.6	0.56	2	2,568 $\pm$ 470	2,635 $\pm$ 211	60.1 $\pm$ 1.0	0.995
SAHA_51_7_5	51	51	–	5	SAHA	25.0	6.6	0.56	1	3,710	3,555	20.1	0.981
SAHA_51_4_3	51	51	–	3	SAHA	25.0	4.0	0.56	2	426 $\pm$ 33	1,692 $\pm$ 112	47.5 $\pm$ 5.4	1.000
SAHA_51_10_3	51	51	–	3	SAHA	25.0	9.5	0.56	2	4,808 $\pm$ 117	5,838 $\pm$ 1,057	20.7 $\pm$ 3.5	0.961
HSNOM_51_7_1	51	51	–	1	HSNOM	25.1	6.9	0.56	2	1,739 $\pm$ 66	1,121 $\pm$ 278	54.2 $\pm$ 4.1	1.000
HSNOM_51_7_3	51	51	–	3	HSNOM	25.1	6.8	0.56	2	4,049 $\pm$ 176	4,496 $\pm$ 6	14.4 $\pm$ 3.1	0.985
HSNOM_51_7_5	51	51	–	5	HSNOM	25.1	7.1	0.56	2	4,282 $\pm$ 130	9,828 $\pm$ 795	6.9 $\pm$ 5.9	1.000
HSNOM_51_4_3	51	51	–	3	HSNOM	25.1	4.0	0.56	2	1,146 $\pm$ 117	869 $\pm$ 39	51.8 $\pm$ 1.5	0.999
HSNOM_51_10_3	51	51	–	3	HSNOM	25.0	9.5	0.56	2	9,437 $\pm$ 384	13,223 $\pm$ 963	3.6 $\pm$ 0.1	0.998
HSNOM_51_7_3_PAC	51	51	–	3	HSNOM	25.0	7.1	0.56	2	835 $\pm$ 74	734 $\pm$ 177	45.4 $\pm$ 20.3	0.990
SRNOM_51_7_3	51	51	–	3	SRNOM	25.0	7.0	0.56	1	2,449	3,962	45.2	0.991
SA_68_7_3	68	68	–	3	SA	25.0	6.8	0.71	3	1,028 $\pm$ 606	750 $\pm$ 343	97.4 $\pm$ 51.9	0.998
SA_68_7_6	68	68	–	6	SA	25.0	6.8	0.71	2	1,894 $\pm$ 590	2,089 $\pm$ 120	23.8 $\pm$ 0.3	0.999
SA_68_7_12	68	68	–	12	SA	25.0	6.8	0.71	1	3,328	3,447	10.4	0.998
SA_51_7_1	51	51	–	1	SA	25.0	6.7	0.56	3	1,350 $\pm$ 267	3,625 $\pm$ 154	33.9 $\pm$ 1.2	0.997
SA_51_7_3	51	51	–	3	SA	25.0	6.8	0.56	3	2,527 $\pm$ 693	5,366 $\pm$ 735	10.7 $\pm$ 1.4	0.999
SA_51_7_5	51	51	–	5	SA	25.0	6.9	0.56	3	2,941 $\pm$ 814	6,457 $\pm$ 620	8.1 $\pm$ 0.5	1.000
SA_51_4_3	51	51	–	3	SA	25.0	4.3	0.56	3	2,271 $\pm$ 438	5,845 $\pm$ 1,338	11.7 $\pm$ 0.6	0.999
SA_51_10_3	51	51	–	3	SA	25.0	9.6	0.56	3	3,122 $\pm$ 708	7,679 $\pm$ 1,701	11.5 $\pm$ 5.7	0.988
BSA_68_7_3	68	68	–	3	BSA	25.0	6.9	0.71	3	219 $\pm$ 31	419 $\pm$ 106	140.2 $\pm$ 27.6	0.999
BSA_68_7_6	68	68	–	6	BSA	25.0	6.9	0.71	1	311	474	72.5	0.997
BSA_68_7_12	68	68	–	12	BSA	25.0	6.7	0.71	1	496	628	55.0	0.997
BSA_51_7_1	51	51	–	1	BSA	25.0	6.8	0.56	3	1,170 $\pm$ 156	2,297 $\pm$ 1,259	43.5 $\pm$ 11.2	1.000
BSA_51_7_3	51	51	–	3	BSA	25.1	6.8	0.56	3	1,310 $\pm$ 16	4,450 $\pm$ 313	20.1 $\pm$ 10.4	0.999
BSA_51_7_5	51	51	–	5	BSA	25.0	6.7	0.56	3	1,474 $\pm$ 286	5,716 $\pm$ 1,320	17.1 $\pm$ 5.8	0.998
BSA_51_4_3	51	51	–	3	BSA	25.0	4.3	0.56	3	1,140 $\pm$ 340	2,974 $\pm$ 185	24.8 $\pm$ 2.3	1.000
BSA_51_10_3	51	51	–	3	BSA	25.0	9.8	0.56	3	3,235 $\pm$ 712	5,972 $\pm$ 1,224	14.1 $\pm$ 2.8	0.999
AS_68_7_1.5	68	68	1.5	–	–	24.9	7.1	0.71	1	3,276	2,016	61.7	0.940
AS_68_7_3	68	68	3	–	–	25.3	6.8	0.71	1	7,884	4,932	19.1	0.908
AS_68_7_12	68	68	12	–	–	25.0	6.5	0.71	4	28,314 $\pm$ 19,171	14,850 $\pm$ 6,693	2.5 $\pm$ 0.7	0.990

## II. RO Experiments

**Table C-2: List of conducted RO desalination experiments including relevant parameters using RO setup – configuration I. Concentrations are initial feed solution concentrations at the beginning of an experiment ( $t=0$  min). Transmembrane pressure ( $\Delta p$ ),  $pH$  and temperature ( $T$ ) are average values of the respective experiment. Observed NaCl rejection coefficients ( $R(NaCl)$ ) are based on rejection of electrical conductivity during NaCl conditioning.**

#	figure	symbol	CaCl <sub>2</sub>	Na <sub>2</sub> SO <sub>4</sub>	NaCl	AS	DOC	NOM	$k_{w,0}$	$\Delta p$	$R(NaCl)$	$pH$	$T$
–	–	–	mmol·l <sup>-1</sup>	mmol·l <sup>-1</sup>	mmol·l <sup>-1</sup>	mg·l <sup>-1</sup>	mg C·l <sup>-1</sup>	–	l·m <sup>-2</sup> ·h <sup>-1</sup> ·bar <sup>-1</sup>	bar	%	–	°C
<b>pure gypsum scaling experiments</b>													
1A	4-1a	○	17	17	–	–	–	–	2.95	25	96.4	6.7	24.9
1B	4-1a	○	17	17	–	–	–	–	2.87	25	97.0	6.8	24.9
1AS	4-1a	□	17	17	–	–	–	–	2.70	25	97.6	6.1	24.8
2A	4-1b	○	17	17	–	–	–	–	2.87	25	98.9	6.3	25.0
2B	4-1b	○	17	17	–	–	–	–	2.74	25	98.9	6.5	25.0
2AS	4-1b	□	17	17	–	–	–	–	2.70	25	99.0	6.1	25.0
VCF 1.5	4-3	○	25.5	25.5	–	–	–	–	2.95	25	98.9	6.8	24.9
SI 0.39	4-4	---	35.7	35.7	–	–	–	–	–	0	–	7.7	25.0
<b>NOM fouling experiments</b>													
BSA	6-6a	□	17	–	23	–	3	BSA	2.62	25	98.8	6.9	25.1
RHA	6-6b	△	17	–	23	–	3	RHA	2.80	25	98.5	7.2	25.1
SA	6-6c	◇	17	–	23	–	3	SA	2.58	25	97.9	7.0	25.0
<b>NOM-gypsum scaling experiments</b>													
BSA	6-6a	□	17	17	–	–	3	BSA	2.68	25	99.0	7.0	25.0
RHA	6-6b	△	17	17	–	–	3	RHA	2.74	25	98.9	7.2	25.1
SA	6-6c	◇	17	17	–	–	3	SA	2.64	25	98.2	7.1	25.0

**Table C-3: List of conducted RO desalination experiments including relevant parameters using RO setup – configuration II. Clean water permeabilities ( $k_{w,0}$ ) were determined during ultrapure water conditioning. Observed  $\text{CaCl}_2$  rejection coefficients ( $R(\text{CaCl}_2)$ ) were determined during  $\text{CaCl}_2$  conditioning; for experiments in (b),  $\text{CaCl}_2$  conditioning was performed after NOM pre-fouling and  $R(\text{CaCl}_2)$  represents  $\text{CaCl}_2$  rejection after pre-fouling. Concentrate electrical conductivity ( $EC_{c,0}$ ) are initial values at  $t = 0$  min. Concentrate turbidity ( $\kappa$ ),  $\text{pH}$  and temperature ( $T$ ) are average values of the respective experiment.**

#	Figure	symbol	$k_{w,0}$	$R(\text{CaCl}_2)$	$EC_{c,0}$	$\kappa$	$\Delta m_{total}$	$T$	$\text{pH}$	1 <sup>st</sup> crystal
–	–	–	$\text{l}\cdot\text{m}^{-2}\cdot\text{h}^{-1}\cdot\text{bar}^{-1}$	%	$\mu\text{S}\cdot\text{cm}^{-1}$	NTU	mg	$^{\circ}\text{C}$	–	min
<b>(a) pure gypsum surface scaling on virgin membranes</b>										
II_1	4-11 / 4-14	+	3.46	94.8	5728	0.04	516	20.0	6.9	9
II_2	4-11 / 4-14	×	3.22	97.0	5717	0.08	391	20.0	6.7	10
II_3	4-11 / 4-14	*	2.86	96.5	5635	0.10	461	20.0	7.0	8
II_4	4-11 / 4-14	☆	3.04	97.8	5645	0.10	476	20.0	7.0	12
II_5	4-11 / 4-14	◇	3.50	95.9	5625	0.01	248	20.1	6.8	7
II_6	4-11 / 4-14	▽	3.39	95.4	5663	0.02	–	20.0	6.6	8
II_7	4-11 / 4-14	△	3.94	95.8	5672	0.05	–	20.0	6.6	10
II_8	4-11 / 4-14	○	3.09	97.1	5742	–	423	20.1	6.9	13
II_9	4-11 / 4-14	□	3.40	96.6	5731	0.03	588	20.0	7.0	5
II_10	4-11 / 4-14	▷	3.12	92.8	5630	0.01	322	19.8	7.0	18
II_11	4-11 / 4-14	◁	3.22	97.4	5630	0.01	283	19.7	7.2	4
II_High	4-15	◇	3.90	95.7	5825	0.01	393	20.0	6.7	10
II_Particles	4-15	○	3.12	96.8	5668	0.22	392	20.0	7.1	20
Re-Ref_II_0	4-17	▷	3.94	95.8	5672	0.05	–	20.0	6.6	10
Re-Ref_II_1	4-17	◁	3.61	91.8	5663	0.02	–	20.0	6.8	8
Re-Ref_II_2	4-17	△	3.27	92.0	5668	0.02	382	20.0	7.0	7
<b>(b) pure gypsum surface scaling on NOM pre-fouled membranes</b>										
SAHA_PRE	7-1 / D-17	△	3.44	96.7	5651	0.07	623	20.0	6.8	24
BSA_PRE	7-1 / D-17	□	3.72	97.6	5662	0.01	272	20.0	6.8	37
SA_PRE	7-1 / D-17	◇	3.75	95.6	5637	0.02	441	20.0	6.8	36
<b>HSNOM_PRE</b>										
medium_a	7-1 / -6 / D-17 / -18	▷	3.77	97.1	5671	0.03	129	20.0	6.7	19
medium_b	7-1 / -6 / D-17 / -18	▷	3.53	98.4	5557	0.06	230	19.8	7.2	46
low	7-6 / D-18	▷	3.34	98.3	5643	0.03	228	20.0	6.6	6
intensive	7-6 / D-18	▷	4.01	94.5	5659	0.01	83	20.0	6.7	40
<b>(c) gypsum surface scaling in the presence of dissolved NOM</b>										
SAHA_I	7-7 / -11 / D-19a / -25a	△	3.78	95.0	5635	1.86	591	20.1	6.9	22
SAHA_II	7-7 / -11 / D-19a / -25a	△	3.16	96.4	5557	2.39	468	19.8	7.1	21
SAHA_III	7-7 / -11 / D-19a / -25a	△	3.51	96.7	5760	–	731	20.0	7.0	24
BSA_I	7-7 / D-19a	□	3.79	97.3	5630	0.09	129	20.0	6.8	10
BSA_II	7-7 / D-19a	□	3.40	95.7	5724	0.04	309	19.9	7.0	14
SA_I	7-7 / D-19a	◇	3.70	94.7	5607	0.14	153	20.0	6.9	45
SA_II	7-7 / D-19a	◇	3.34	93.1	5754	0.22	87	19.9	7.2	29
HSNOM_I	7-7 / -10 / -13 D-19a / -21 / -25b	▷	3.28	97.3	5721	0.27	235	20.0	7.0	30
HSNOM_II	7-7 / -10 / -13 / -15 / -17 D-19a / -21 / -25b	▷	3.36	97.5	5656	0.09	416*	20.0	7.1	120
SRNOM	7-7 / D-19a	◁	3.71	96.0	5589	0.03	86	19.8	7.1	13
RHA	7-7 / D-19a	○	3.79	95.7	5546	1.81	73	19.8	6.9	60
<b>HSNOM</b>										
0.5 mg C·l <sup>-1</sup>	7-10 / D-21	▷	3.45	97.2	5568	0.01	139	19.8	7.2	9
5 mg C·l <sup>-1</sup>	7-10 / D-21	▷	3.67	96.9	5608	0.07	35	19.7	7.5	270
≤ 5 kDa	7-13 / D-25b	▷	3.33	94.5	5594	0.01	402	19.8	7.0	9
≤ 5 kDa, 3 mg C·l <sup>-1</sup>	7-13 / D-25b	▷	3.51	96.9	5507	0.02	306	19.8	7.2	10
after PAC	7-13	▷	3.56	96.5	5566	0.01	295	19.9	6.7	8
<b>SAHA</b>										
≤ 150 kDa	7-11 / D-25a	△	3.39	93.7	5555	0.08	367	19.8	7.1	3
≤ 150 kDa, 3 mg C·l <sup>-1</sup>	7-11 / D-25a	△	2.92	93.3	5508	1.88	79	19.8	7.3	–
AS_I	7-15	○	3.47	97.5	5754	0.04	–	19.9	6.7	10
AS_II	7-15	○	3.47	96.6	5756	0.04	130*	20.0	6.8	16

\* after 24 h scaling experiments

## D. Appendix IV – Supplemental Data

### I. Supplemental Data of Chapter 2: Theoretical Background

**Table D-1: Solution compositions of different brackish waters and calculated saturation indices for gypsum ( $SI_g$ ), calcite ( $SI_c$ ) and barite ( $SI_b$ ) at  $T = 20\text{ }^\circ\text{C}$  and  $pH = 7$  for raw waters and concentrates at 75 % recovery.**

Water type	brackish surface water					brackish groundwater					brackish agricultural drainage water				
Reference	(a)	(b)	(c)	(d)	(e)	(f)	(g)	(h)	(i)	(j)	(k)	(l)	(m)	(n)	(o)
	$pH / -$					$pH / -$					$pH / -$				
	9.1	8.4	-	-	7.86	7.60	7.80	-	7.6	-	7.6	7.6	7.5	7.6	8.0
	analyte / $\text{mg}\cdot\text{l}^{-1}$					analyte / $\text{mg}\cdot\text{l}^{-1}$					analyte / $\text{mg}\cdot\text{l}^{-1}$				
TOC	12	-	-	-	-	-	-	-	-	-	5.1	3.4	4.5	6.2	16.7
DOC	-	-	-	1.4	8.02	-	-	-	-	-	5.1	4.6	4.2	6.2	15.8
Barium	0.10	0.1	0.1	0.06	-	-	-	-	< 0.5	-	< 0.5	< 0.5	< 0.3	< 2.5	< 0.5
Boron	-	-	-	-	-	-	-	-	23.5	1.74	23.5	17.5	13.5	43.4	2.6
Calcium	29.0	95	175	179	281.5	365	320	176	492	164	462	625	350	422	88
Chloride	410.0	164	72	1867	90.2	674	1,900	1,370	1,190	236	1,060	3,020	324	1,910	632
Fluoride	-	-	-	-	-	1.28	1.2	0.61	-	1	< 10	< 10	< 5	< 5	< 5
Iron	0.02	-	-	-	-	0.2	0.001	-	-	-	0.05	0.15	0.17	1.4	0.28
Bicarbonate	59	212	260	146	114.5	120	167	75	274.5	370	259	156	279	448	853
Magnesium	31.0	34.5	58	132	238.1	64	106	38.4	255	49	284	198	236	962	59
Nitrate	0.01	-	-	-	-	2	12	0.11	337	72	47	155	344	52	51
Potassium	6.10	-	-	-	12.8	42	55	15.9	4.3	6.1	< 5	< 5	46.7	7.8	3.5
Silica	-	11.6	-	-	14.0	-	-	29.4	31.4	45	31	38	24	43	38
Sodium	180.0	165.5	170	905	180.5	409	1,430	745	1,810	333	2,780	2,820	1,250	9,270	1,250
Strontium	0.33	1.24	-	26.4	6.4	-	-	-	7.83	1.55	5.5	10.0	17.2	9.6	0.9
Sulfate	25.0	322	670	384	1,757	1,040	1,450	301	4,080	570	6,360	4,520	3,700	21,400	1,570
$\text{cms} / \text{g}\cdot\text{l}^{-1}$	0.90	0.94	1.32	3.66	2.91	2.63	5.29	3.17	8.50	1.63	11.02	11.27	6.37	28.78	4.12
	raw water, $pH = 7$					raw water, $pH = 7$					raw water, $pH = 7$				
$SI_{g,f} / -$	-2.63	-1.14	-0.69	-1.09	-0.31	-0.35	-0.54	-1.09	0.00	-0.81	0.06	0.08	-0.13	0.15	-0.88
$SI_{c,f} / -$	-1.43	-0.45	-1.04	-0.49	-0.48	-0.29	-0.34	-0.73	-0.05	-0.07	-0.04	0.14	-0.02	-0.07	0.00
$SI_{b,f} / -$	-0.33	0.56	0.70	0.13	-	-	-	-	1.55	-	1.60	1.53	1.26	1.38	1.47
	75 % recovery, $pH = 7$					75 % recovery, $pH = 7$					75 % recovery, $pH = 7$				
$SI_{g,c} / -$	-1.79	-0.34	0.08	-0.36	0.42	0.39	0.16	-0.34	0.73	-0.05	0.79	0.82	0.59	0.97	-0.18
$SI_{c,c} / -$	-0.41	0.51	0.76	0.47	0.45	0.65	0.63	0.23	0.90	0.88	0.91	1.10	0.90	1.03	0.90
$SI_{b,c} / -$	0.49	1.30	1.41	0.83	-	-	-	-	2.23	-	2.29	2.23	1.94	3.20	2.14

<b>References:</b>	(a)	Grampians Ranges, GWMWater, Victoria, Australia	[64]
	(b)	Colorado River Water, Yuma, AZ, USA	[263]
	(c)	Port Hueneme, USA, CA, USA	[9]
	(d)	Martin County, FL, USA	[9]
	(e)	Foss Reservoir, OK, USA	[264]
	(f)	Gabes, Tunisia	[265]
	(g)	Zarzis, Tunisia	[265]
	(h)	Airport Wells, El Paso Water Utilities, TX, USA	[44]
	(i)	Panoche Water District, San Joaquin Valley, CA, USA	[266]
	(j)	Indian Wells Valley Water District, CA, USA	[44]
	(k) – (o)	San Joaquin Valley, CA, USA	[267]

## II. Supplemental Data of Chapter 4: Characterization of Gypsum Scaling

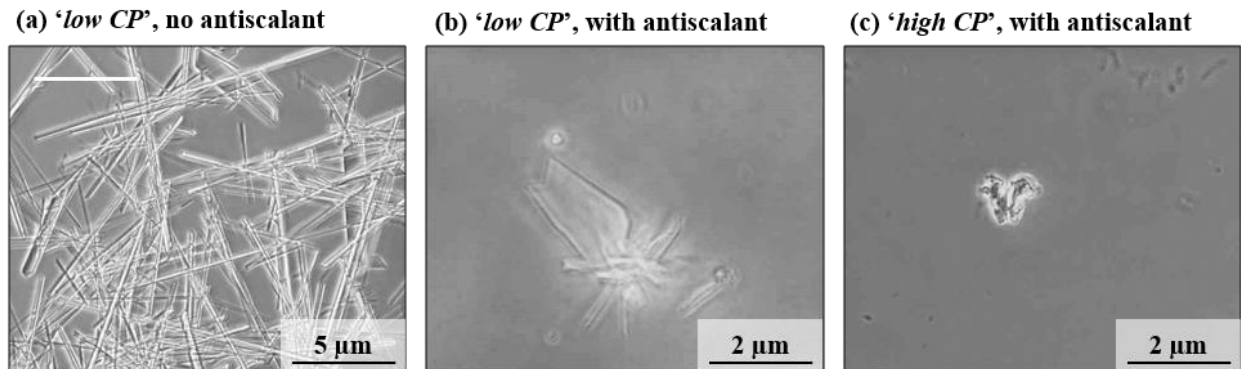


Figure D-1: Micrographs of gypsum bulk crystals in concentrate samples taken from experiments displayed in Figure 4-1. Sample turbidity: (a) 10 NTU, (b) 7 NTU and (c) 13 NTU.

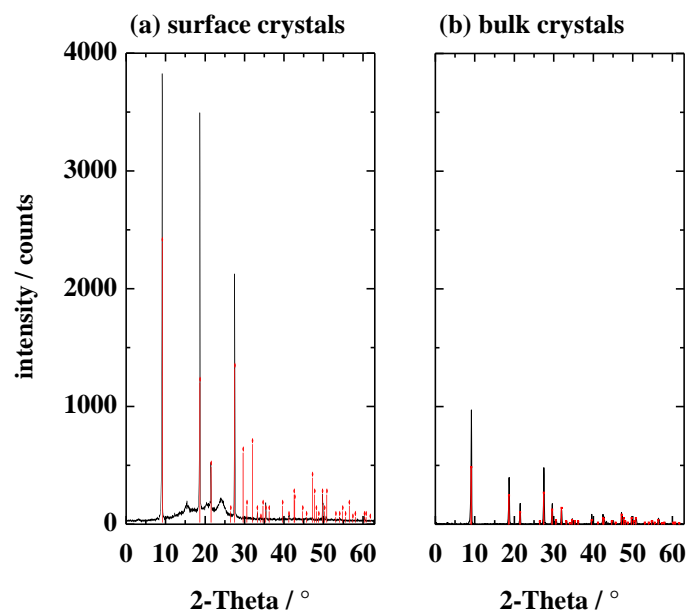


Figure D-2: XRD diagram of (a) rosette-like surface crystals and (b) needle-like bulk crystals on RO membrane surface. Analysis identified  $\text{CaSO}_4 \cdot 2\text{H}_2\text{O}$  (gypsum) according to ICDD<sup>®</sup> (International Centre for Diffraction Data<sup>®</sup>) code 00-006-0046 to be the only detected crystalline matter.

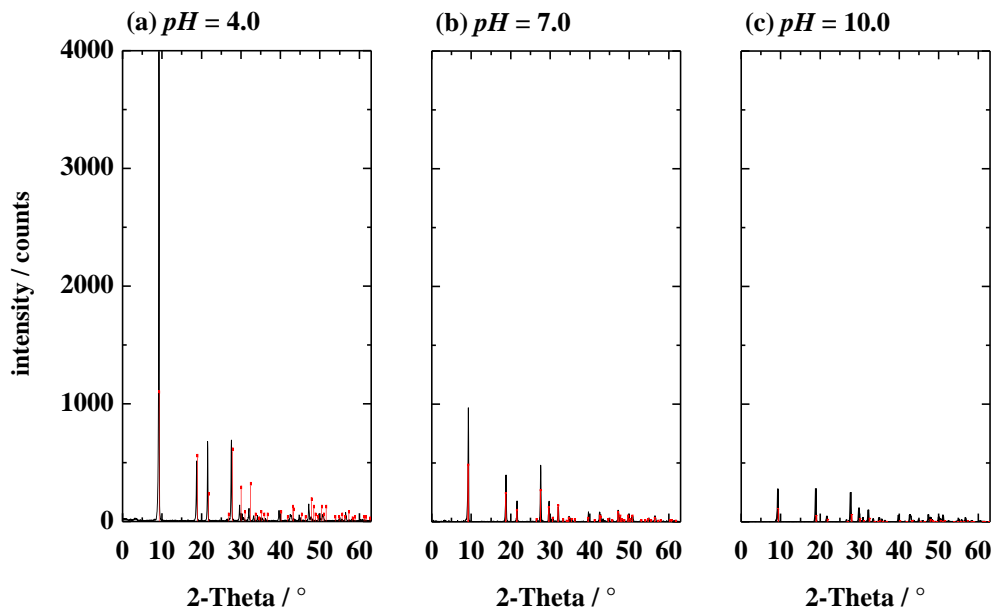


Figure D-3: XRD diagram of bulk crystals recovered from gypsum bulk crystallization experiments at  $SI_{g,b} = 0.56$ ,  $T = 25.0\text{ }^{\circ}\text{C}$  and (a)  $pH = 4.0$ , (b)  $pH = 7.0$  and (c)  $pH = 10.0$ . Analysis identified  $\text{CaSO}_4 \cdot 2\text{H}_2\text{O}$  (gypsum) according to ICDD<sup>®</sup> (International Centre for Diffraction Data<sup>®</sup>) code 00-006-0046 to be the only detected crystalline matter in all three cases.

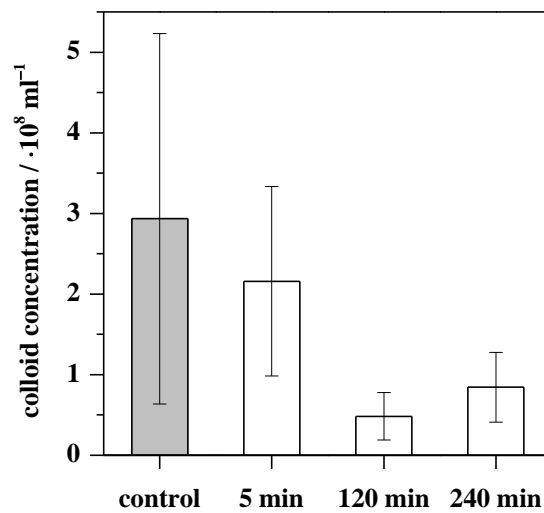


Figure D-4: Detectable colloid concentration by nanoparticle tracking analysis (NTA) of control and concentrate solutions during pure gypsum scaling experiment II\_11 (mean values  $\pm 95\%$  confidence interval,  $n = 5 - 7$ ). Control solution is clean water which was temporarily stored in a PE canister. Detection range is limited to  $100\text{ nm} < d_c < 2,000\text{ nm}$ .

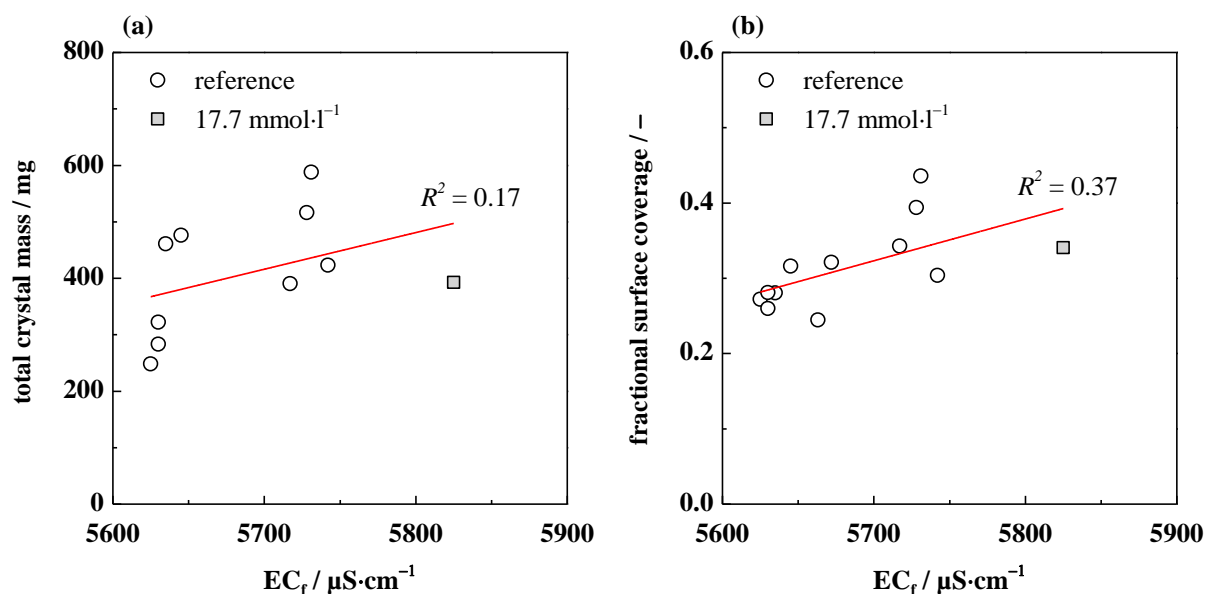


Figure D-5: Linear correlations between feed solution electrical conductivity ( $EC_f$ ) and (a) total crystal mass and (b) final fractional surface coverage during pure gypsum surface scaling experiments.

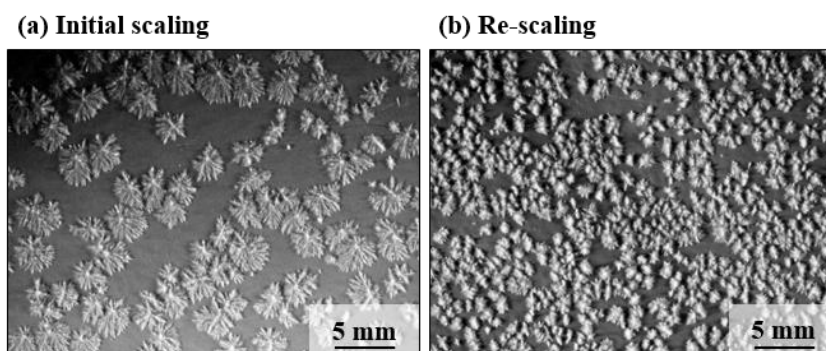


Figure D-6: (a) Micrograph showing heterogeneous rosette-like gypsum crystals on a DOW FILMTEC™ BW30 reverse osmosis membrane ( $A_{active} = 14.6 \text{ cm}^2$ ) after permeation of 10 ml using a non-agitated dead-end RO permeation cell at constant flux of  $30 \text{ l}\cdot\text{m}^{-2}\cdot\text{h}^{-1}$ , constant temperature of  $25 \text{ }^\circ\text{C}$  and a feed water composition of  $17 \text{ mmol}\cdot\text{l}^{-1} \text{ CaCl}_2\cdot 2\text{H}_2\text{O}$  and  $17 \text{ mmol}\cdot\text{l}^{-1} \text{ Na}_2\text{SO}_4$  in ultrapure water. (b) Micrograph showing significantly higher number of heterogeneous gypsum rosette-like crystals after repetition of the same experiment using the same membrane after cleaning. Cleaning was facilitated in a glass bottle filled with 500 ml ultrapure water, placed on a shaker at 120 rpm for 15 min. Microscopic investigation (63x) after cleaning showed no visible remaining crystals, however, marked physical perforations of the membrane surface in locations where crystals had existed (micrograph not shown due to low contrast).

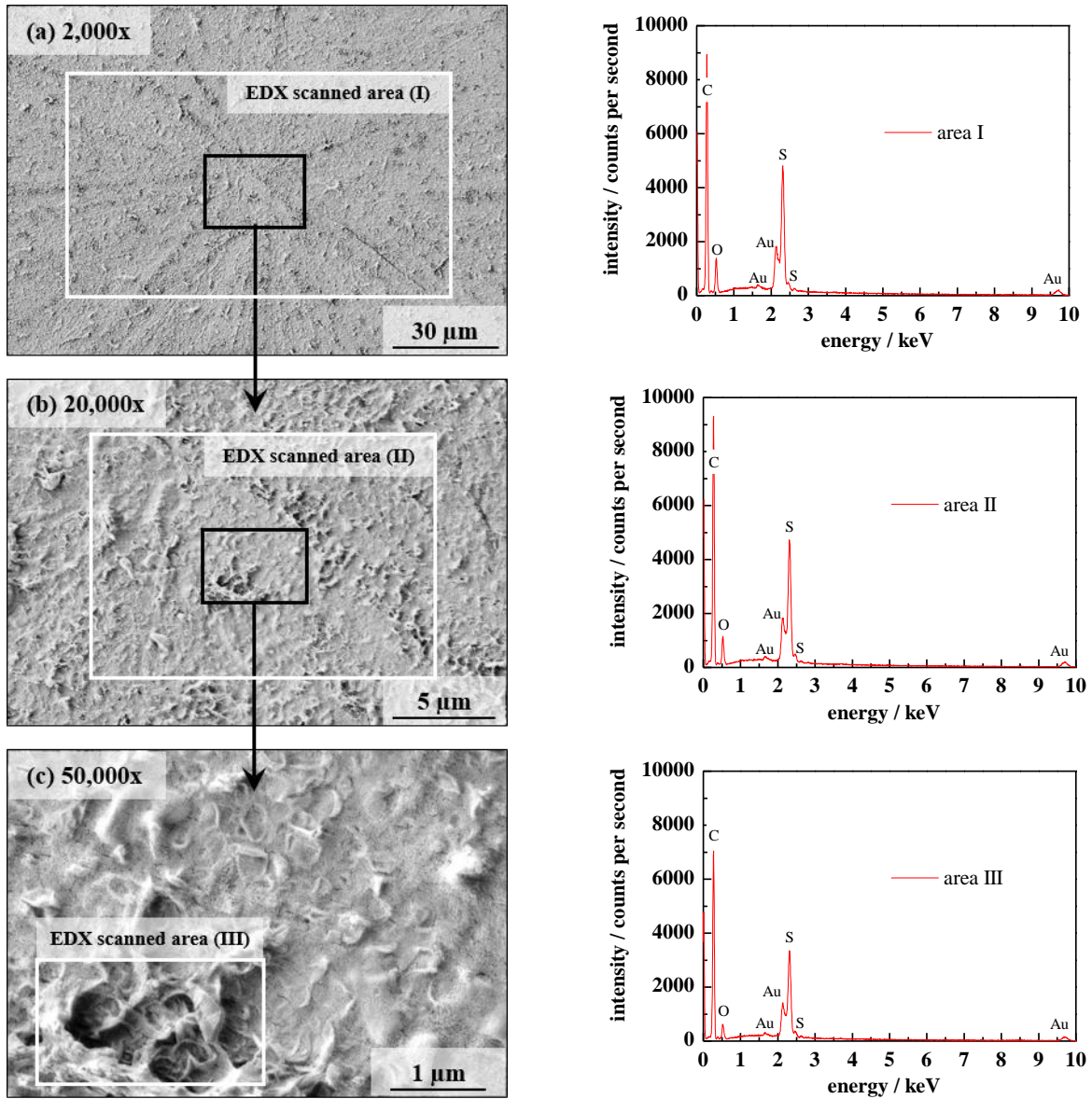


Figure D-7: SEM-EDX analysis performed on membrane surface after gypsum scale had been cleaned off. Cleaning was achieved by shaking at 120 rpm for 48 h in ultrapure water. The SEM taken at 2,000x magnification (a) shows the contours of a previously existing gypsum rosette-like crystal. Higher magnifications (b and c) show physical alterations of the membrane surface. The corresponding EDX spectra are dominated by elements of the membrane material (fully aromatic polyamide (C, O) active layer and polysulfone (C, O, S) support structure) and deposited gold (Au) from sputtering but do not exhibit calcium (Ca) signals.

### III. Supplemental Data of Chapter 5: Characterization of the Selected Natural Organic Matter (NOM) Sources

Table D-2: Quantification results of LC-OCD-UVD chromatograms according to Huber et al. (2011) [218] using ChromCALC Software (DOC Labor Dr. Huber, Germany) for peak integration. Prior to analysis, each sample was diluted with ultrapure water to a DOC concentration of  $3.0 \text{ mg}\cdot\text{l}^{-1}$  as quantified by combustion catalytic oxidation after  $0.45 \mu\text{m}$  filtration and adjusted to  $pH=7.0$ . cOC (chromatographable organic carbon): OC quantified from the hull curve of the LC-OCD chromatogram, HOC (hydrophobic organic carbon): OC retained in the LC column,  $\Phi_{UV}$  (oxidation yield): ratio between the DOC quantified in the LC column bypass and the DOC quantified by combustion catalytic oxidation,  $\Phi_{HOC}$  (fraction of HOC): % fraction of the OC retained in the LC column, i.e. ration between the concentrations of HOC and bypass DOC, LMW: low molecular weight.

	SA	BSA	RHA	SAHA	HSNOM	SRNOM
DOC (catalytic combustion) / $\text{mg}\cdot\text{l}^{-1}$	3.0	3.0	3.0	3.0	3.0	3.0
DOC (LC column bypass) / $\mu\text{g}\cdot\text{l}^{-1}$	3036	1315	2018	1656	2546	2589
cOC / $\mu\text{g}\cdot\text{l}^{-1}$	3036	633	2018	1395	2546	2589
HOC / $\mu\text{g}\cdot\text{l}^{-1}$	–	683	–	261	–	–
oxidation yield ( $\Phi_{UV}$ ) / %	101.2	43.8	67.3	55.2	86.3	84.9
fraction of HOC ( $\Phi_{HOC}$ ) / %	0	51.9	0	15.8	0	0
biopolymers / $\mu\text{g}\cdot\text{l}^{-1}$	2668	461	2	27	12	2
humic substances/ $\mu\text{g}\cdot\text{l}^{-1}$	–	–	1631	922	2163	2163
building blocks/ $\mu\text{g}\cdot\text{l}^{-1}$	299	60	212	298	251	179
LMW acids/ $\mu\text{g}\cdot\text{l}^{-1}$	55	101	172	149	163	186
LMW neutrals/ $\mu\text{g}\cdot\text{l}^{-1}$	14	10	–	–	–	16
SUVA of humic substances / $\text{l}\cdot\text{mg}^{-1}\cdot\text{m}^{-1}$	–	–	15.8	19.4	7.4	6.2

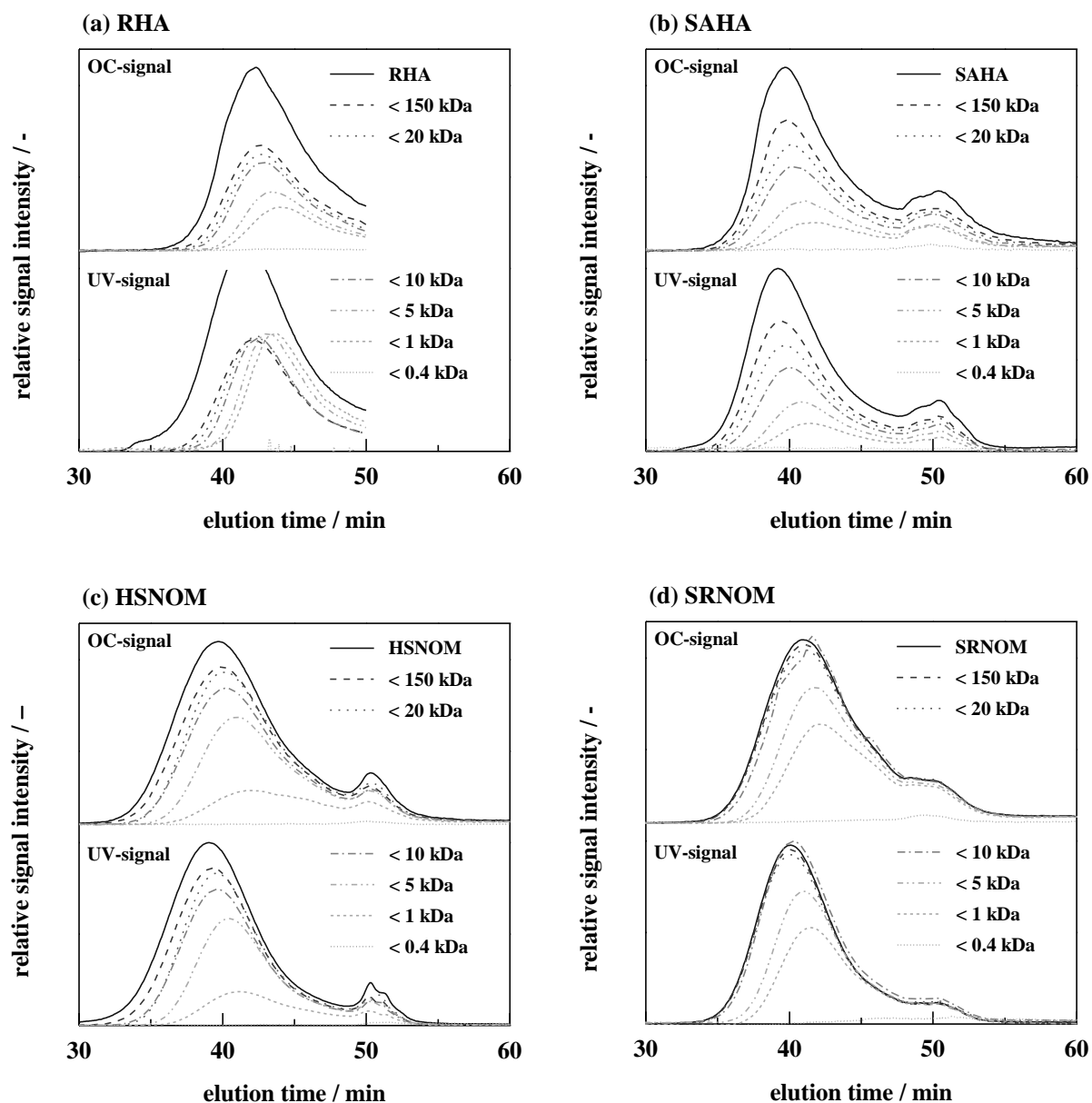


Figure D-8: LC-OCD-UVD chromatograms of selected humic acids and aquatic NOM fractions determined after fractionation by ultrafiltration membranes with different molecular weight cutoffs (0.4 kDa – 150 kDa). Fractionations were performed at a DOC concentration of  $\approx 5 \text{ mg}\cdot\text{l}^{-1}$  as quantified by combustion catalytic oxidation after  $0.45 \mu\text{m}$  filtration. RHA, SAHA, and SRNOM samples were fractionated in the presence of  $1 \text{ mmol}\cdot\text{l}^{-1} \text{ NaHCO}_3$  and  $1 \text{ mmol}\cdot\text{l}^{-1} \text{ CaCl}_2$ . OC signal was normalized to maximum sample OC-signal and UV-signal intensity was multiplied by corresponding normalization factor. RHA: malfunctioning of analytical device led to erroneous signals at elution times larger than 50 min.

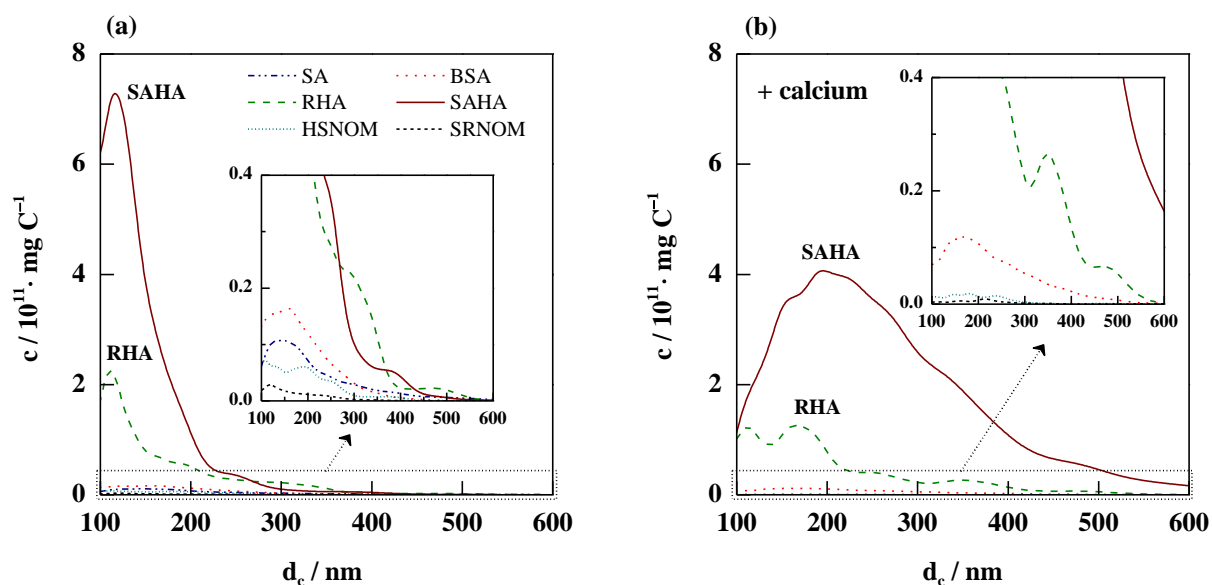


Figure D-9: DOC-specific colloidal size distribution determined by nanoparticle tracking analysis (NTA) of NOM samples dissolved in (a) ultrapure water and (b) 17 mmol·l<sup>-1</sup> CaCl<sub>2</sub> solution. Samples were filtrated by 0.45 μm and analyzed at  $pH = 7.0$ . Measurements were repeated at least 4 times.



Figure D-10: Visual appearance of humic substance samples diluted in ultrapure water to a DOC concentration of 19.15 mg·l<sup>-1</sup> and at  $pH = 7.0$ . From left to right: SAHA, RHA, SRNOM and HSNOM.

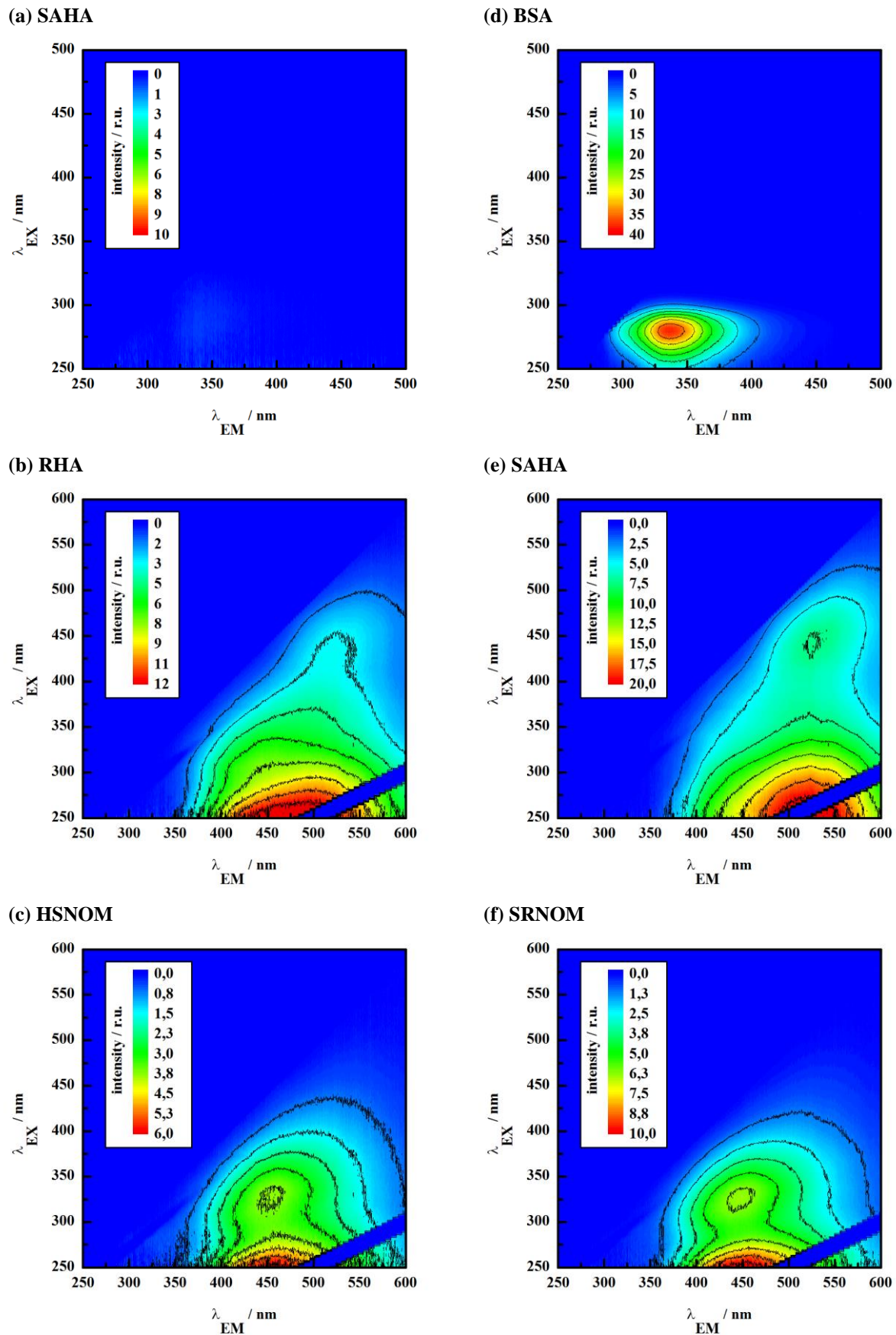
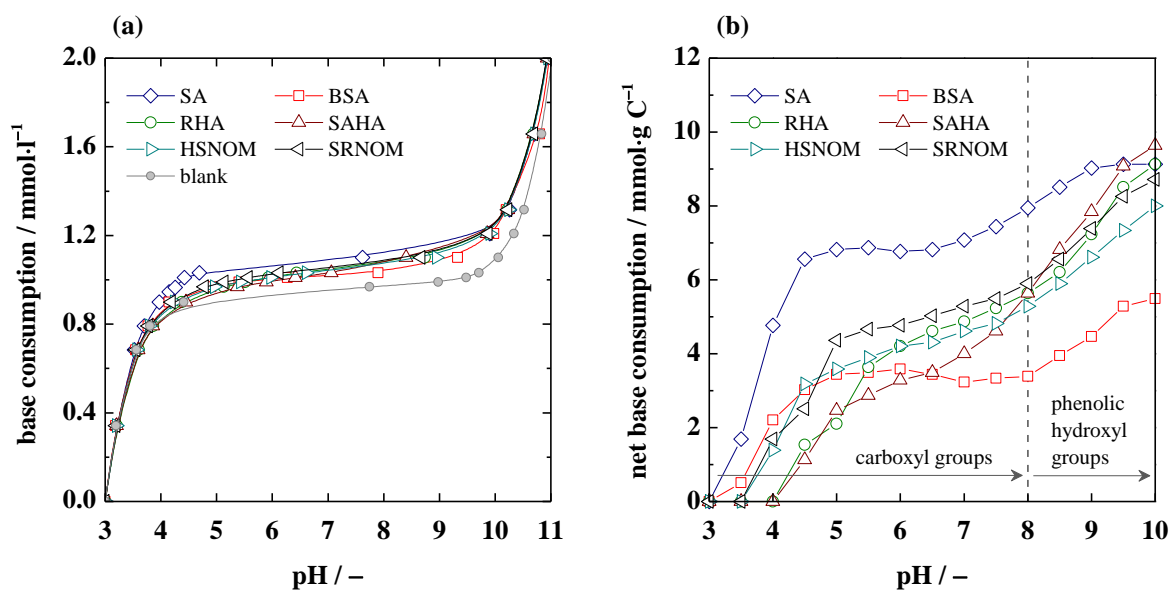


Figure D-11: FEEMs obtained from fluorescence spectroscopy of selected NOM samples diluted in ultrapure water to a DOC concentration of  $3.0 \text{ mg}\cdot\text{l}^{-1}$  and adjusted to  $pH = 7.0$ .



**Figure D-12: (a) NaOH consumption and (b) DOC-specific net NaOH consumption as a function of solution  $pH$  determined by direct base titration of NOM samples. Titrations were performed in duplicate with  $0.1 \text{ mol}\cdot\text{l}^{-1}$  NaOH from  $pH = 3.0$  to  $pH = 10.0$  in the background of  $0.1 \text{ mol}\cdot\text{l}^{-1}$  NaCl at a DOC concentration of  $19.15 \text{ mg}\cdot\text{l}^{-1}$  and ambient temperature of  $T = 22.2 \pm 0.6 \text{ }^\circ\text{C}$  ( $\pm$  SD). Equilibration time in between titrant addition was 3 min. Blank titrations were performed with NOM-free  $0.1 \text{ mmol}\cdot\text{l}^{-1}$  NaCl solutions and used to determine the net NaOH consumption.**

#### IV. Supplemental Data of Chapter 6: Effects of NOM on Gypsum Bulk Crystallization

##### Crystallization

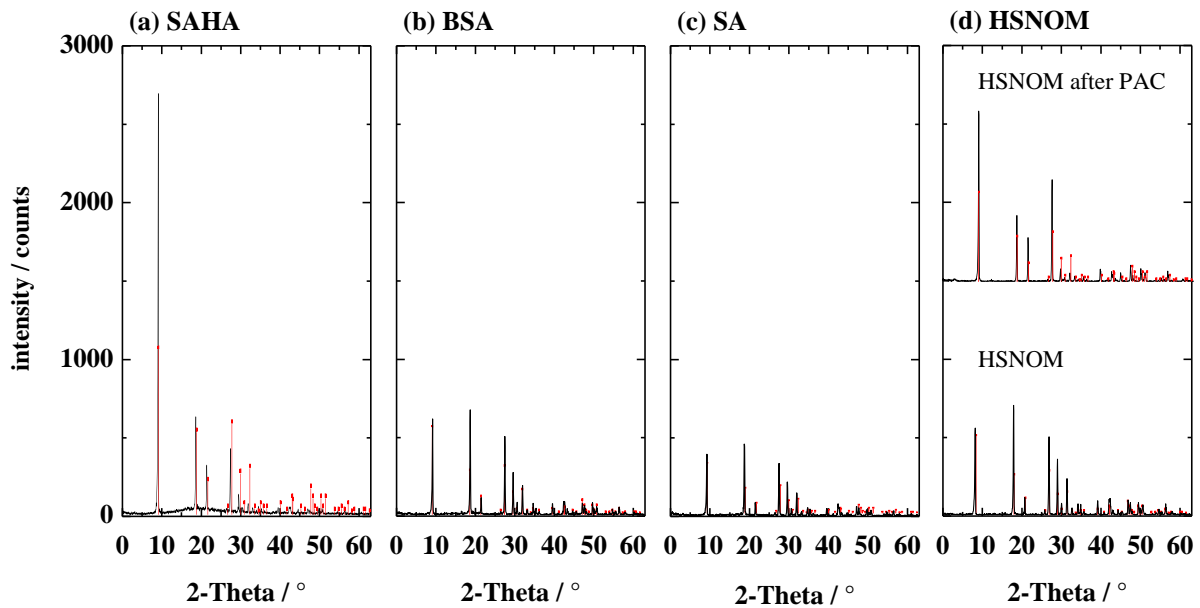


Figure D-13: XRD diagram of bulk crystals recovered from gypsum bulk crystallization experiments at  $SI_{g,b} = 0.56$ ,  $T = 25.0 \pm 0.1$  °C ( $\pm$  SD),  $pH = 7.0 \pm 0.2$  ( $\pm$  SD) in the presence of different NOMs at  $3 \text{ mg C}\cdot\text{l}^{-1}$ . Analysis identified  $\text{CaSO}_4\cdot 2\text{H}_2\text{O}$  (gypsum) according to ICDD<sup>®</sup> (International Centre for Diffraction Data<sup>®</sup>) code 00-006-0046 to be the only detected crystalline matter in all five cases.

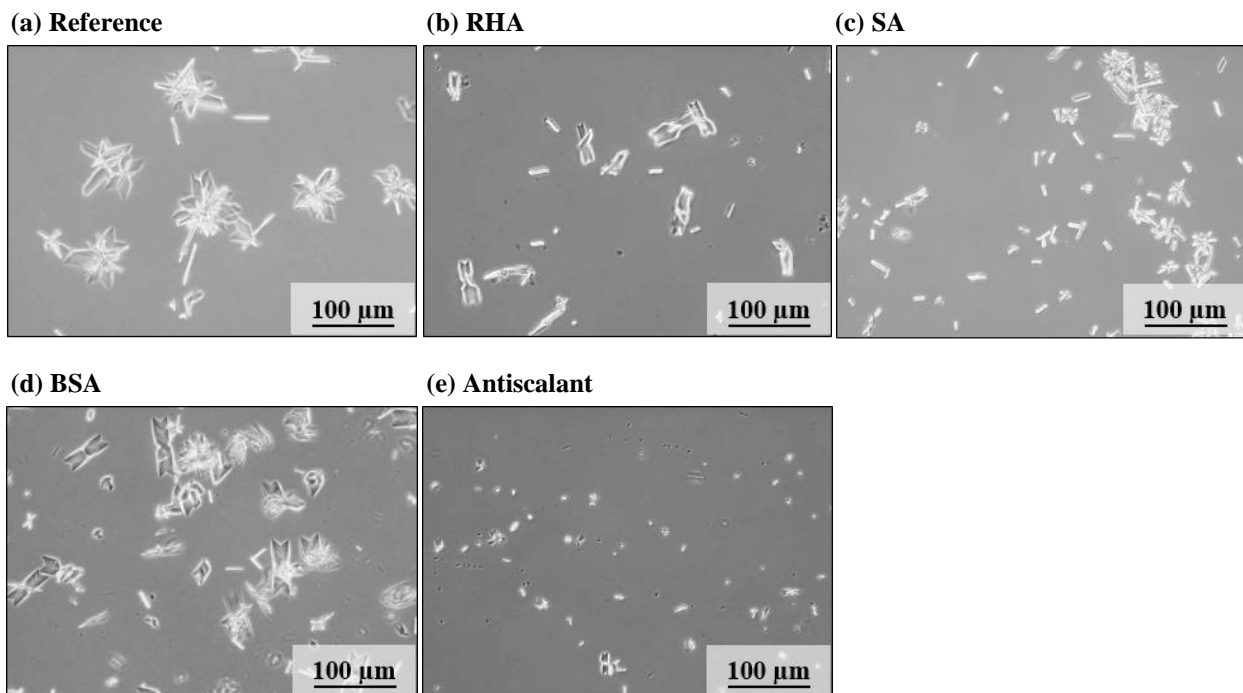
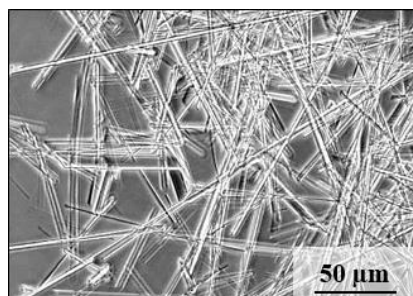


Figure D-14: Micrographs (200x) exhibiting gypsum bulk crystals developed in (a) the absence and (b – d) presence of  $12 \text{ mg C}\cdot\text{l}^{-1}$  NOM and (e)  $1.5 \text{ mg}\cdot\text{l}^{-1}$  antiscalant. Samples were taken from stirred beaker experiments conducted at  $SI_{g,b} = 0.71$ ,  $T = 25.0 \pm 0.1$  °C ( $\pm$  SD),  $pH = 6.8 \pm 0.2$  ( $\pm$  SD) and a turbidity of 5 FNU.

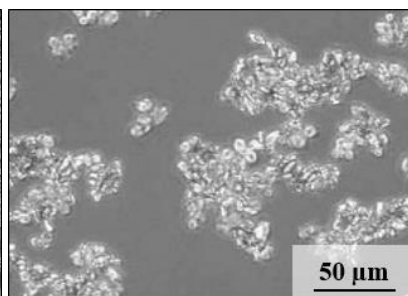
**Table D-3: Rate constants of crystal growth ( $\lambda_G$ ) of gypsum bulk crystallization in the presence of selected NOM sources. Obtained from the temporal evolution of the mean crystal diameter (LOT measurements, analogue to the procedure described in Chapter 4.2) during stirred beaker experiments at  $SI_{g,b} = 0.51$ .**

	$pH / -$	$T / ^\circ C$	$c_{NOM} / mg\ C \cdot l^{-1}$	$\lambda_G / \cdot 10^{-3}\ s^{-1}$	Pearson $R / -$
<b>Reference</b>	6.9	25.2	0	1.72	0.999
<b>SAHA</b>	6.6	25.1	3	0.56	0.909
	6.6	25.0	5	0.37	0.987
	4.0	25.0	3	0.55	0.922
	9.5	25.0	3	0.16	0.936
<b>HSNOM</b>	6.8	25.1	3	0.26	0.908
	7.1	25.1	5	0.09	0.981
	4.0	25.1	3	0.54	0.991
	9.5	25.0	3	0.08	0.977
<b>BSA</b>	6.8	25.2	3	1.14	0.993
	6.7	25.0	5	1.29	1.000
	4.3	25.0	3	0.85	0.995
	9.8	25.0	3	0.56	0.950
<b>SA</b>	6.8	24.9	3	0.71	0.982
	6.9	24.9	5	0.44	0.977
	4.3	25.0	3	0.92	0.989
	9.6	25.1	3	0.35	0.944

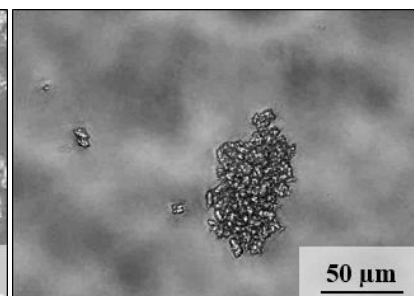
(a) Reference



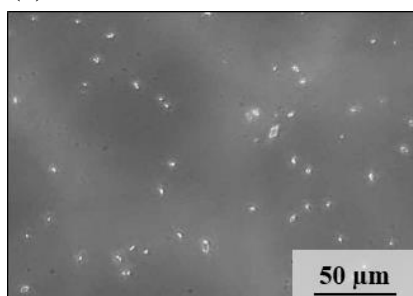
(b) RHA



(c) SA



(d) BSA



(e) Antiscalant

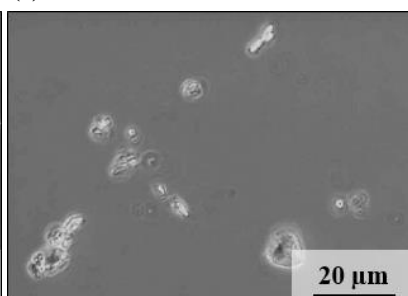


**Figure D-15: Micrographs (200x – 1,000x magnification) exhibiting gypsum bulk crystals in (a) the absence and (b – d) presence of NOM and (e) antiscalant. Samples were taken from the RO system concentrate stream after the onset of bulk crystallization as observed by turbidity increase.**

## V. Supplemental Data of Chapter 7: Effects of NOM on Gypsum Surface Crystallization on RO Membranes

Table D-4: Zeta potential ( $\zeta$ ) and contact angle ( $\theta_c$ ) measurements of virgin BW30 (*Reference*) and organically fouled BW30 membrane samples. Different sample preparations were performed: (a) static fouling experiments: membrane samples were soaked in ultrapure water or NOM solutions at a DOC concentration of  $\approx 25 \text{ mg}\cdot\text{l}^{-1}$  and a  $pH$  of  $\approx 7.0$  for at least 72 h at 150 rpm, (b) dead-end membrane filtration: samples were permeated with ultrapure water or 100 ml of an NOM solution (DOC concentration  $\approx 25 \text{ mg}\cdot\text{l}^{-1}$ ) at  $\Delta p = 18 \text{ bar}$ , (c) cross-flow membrane filtration: membrane samples were prepared according to the protocol for NOM fouling experiments described in Chapter 3.2.3.

	zeta potential ( $\zeta$ ) / mV			n	contact angle ( $\theta_c$ ) / °	
	$pH = 3$	$pH = 7$	$pH = 9$		$pH = 7$	n
<b>(a) static</b>						
<b>Reference</b>	$5.5 \pm 0.8$	$-30.3 \pm 0.7$	$-34.8 \pm 0.8$	3	$30.8 \pm 2.7$	36
<b>SAHA</b>	$0.3 \pm 1.0$	$-38.5 \pm 1.0$	$-42.4 \pm 1.5$	3	$22.5 \pm 3.4$	36
<b>HSNOM</b>	$2.0 \pm 0.3$	$-34.0 \pm 1.2$	$-36.7 \pm 1.4$	1	$26.1 \pm 1.3$	3
<b>SA</b>	$4.7 \pm 0.7$	$-28.9 \pm 0.6$	$-31.8 \pm 0.9$	2	$27.8 \pm 2.9$	27
<b>BSA</b>	$13.0 \pm 0.6$	$-29.4 \pm 0.4$	$-33.1 \pm 0.6$	3	$30.0 \pm 4.4$	27
<b>(b) dead-end</b>						
<b>Reference</b>	$0.0 \pm 2.0$	$-25.9 \pm 1.5$	$-34.3 \pm 1.3$	1	$26.7 \pm 1.7$	27
<b>SAHA</b>	–	–	–	–	–	–
<b>HSNOM</b>	$-6.6 \pm 0.5$	$-38.8 \pm 0.1$	$-41.1 \pm 0.1$	1	$27.1 \pm 1.6$	27
<b>SA</b>	$-13.6 \pm 0.8$	$-55.1 \pm 0.1$	$-56.1 \pm 0.2$	1	$26.9 \pm 1.6$	27
<b>BSA</b>	–	–	–	–	–	–
<b>(c) cross-flow</b>						
<b>Reference</b>	$-10.1 \pm 0.2$	$-35.5 \pm 0.3$	$-35.7 \pm 0.5$	1	$28.3 \pm 0.3$	3
<b>SAHA</b>	$-30.3 \pm 1.1$	$-81.0 \pm 3.1$	$-82.5 \pm 3.8$	1	–	–
<b>HSNOM</b>	$-23.0 \pm 0.3$	$-81.5 \pm 1.0$	$-86.8 \pm 1.3$	1	–	–
<b>SA</b>	–	–	–	–	–	–
<b>BSA</b>	–	–	–	–	–	–
<b>RHA</b>	$-21.4 \pm 1.0$	$-51.5 \pm 2.1$	$-52.7 \pm 2.8$	1	$24.2 \pm 0.7$	3
<b>SRNOM</b>	$-21.2 \pm 0.7$	$-63.6 \pm 0.9$	$-67.4 \pm 1.2$	1	$21.1 \pm 0.7$	3

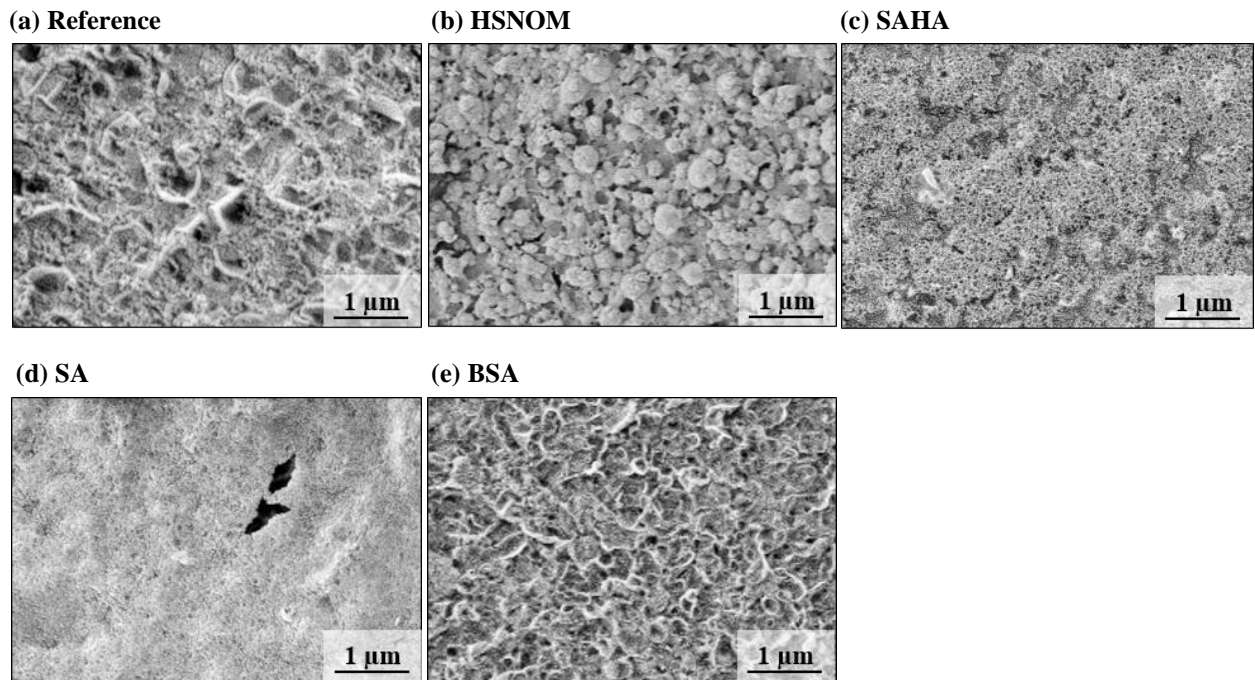


Figure D-16: Scanning electron micrographs (50,000x magnification) of membrane surfaces after NOM pre-fouling.

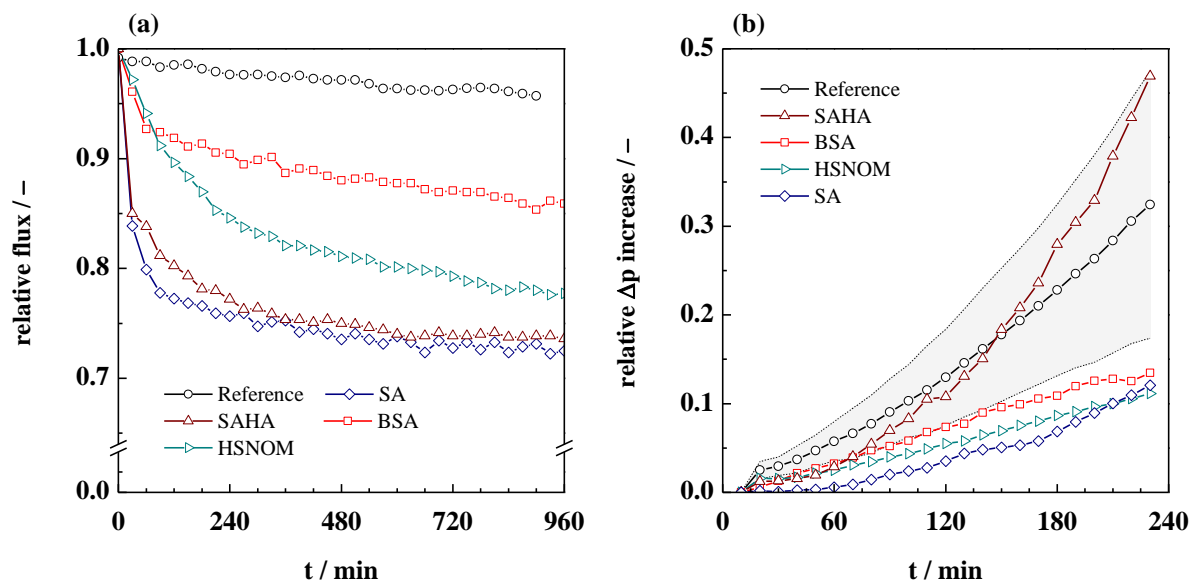


Figure D-17: (a) Flux decline during NOM pre-fouling and (b) increase of relative transmembrane pressure ( $\Delta p$ ) during subsequent gypsum surface scaling. Grey area in (b) identifies standard deviation of reference experiments ( $n = 11$ ).

**Table D-5: Axial distribution of crystal mass after scaling experiments: (a) pre-fouling experiments, (b) HSNOM pre-fouling experiments at different intensities and (c) experiments in the presence of 3.0 mg C·l<sup>-1</sup> dissolved NOM. For repeated experiments values are presented as mean ± SD.**

crystal mass / mg						
<b>(a) pre-fouling</b>	<b>section 1</b>	<b>section 2</b>	<b>section 3</b>	<b>section 4</b>	<b>section 5</b>	<b>sum</b>
Reference (n = 9)	9 ± 6	35 ± 21	76 ± 23	114 ± 26	150 ± 31	<b>412 ± 112</b>
SAHA	11	86	140	185	201	<b>623</b>
SA	6	14	59	145	217	<b>441</b>
BSA	3	12	31	89	138	<b>272</b>
HSNOM	8	11	29	54	77	<b>180</b>
<b>(b) HSNOM pre-fouling intensity</b>	<b>section 1</b>	<b>section 2</b>	<b>section 3</b>	<b>section 4</b>	<b>section 5</b>	<b>sum</b>
Reference (n = 9)	9 ± 6	35 ± 21	76 ± 23	114 ± 26	150 ± 31	<b>412 ± 112</b>
'low'	3	6	22	78	120	<b>228</b>
'medium'	8	11	29	54	77	<b>180</b>
'intensive'	3	11	13	16	37	<b>83</b>
<b>(c) dissolved NOM, 3.0 mg C·l<sup>-1</sup></b>	<b>section 1</b>	<b>section 2</b>	<b>section 3</b>	<b>section 4</b>	<b>section 5</b>	<b>sum</b>
Reference (n = 9)	9 ± 6	35 ± 21	76 ± 23	114 ± 26	150 ± 31	<b>412 ± 112</b>
SAHA (n = 3)	15 ± 10	75 ± 31	122 ± 50	173 ± 26	212 ± 28	<b>597 ± 132</b>
BSA (n = 2)	5 ± 1	15 ± 10	31 ± 30	65 ± 45	103 ± 42	<b>219 ± 127</b>
HSNOM	10	20	24	57	124	<b>235</b>
SA (n = 2)	18 ± 4	11 ± 6	15 ± 7	27 ± 17	49 ± 20	<b>120 ± 47</b>
RHA	2	6	2	11	52	<b>73</b>
SRNOM	1	4	12	22	23	<b>61</b>
SAHA ≤ 150 kDa, 0.5 mg C·l <sup>-1</sup>	11	43	67	114	132	<b>367</b>
SAHA ≤ 150 kDa, 3.0 mg C·l <sup>-1</sup>	4	3	4	12	56	<b>76</b>
HSNOM after PAC	6	24	53	90	122	<b>295</b>
HSNOM ≤ 5 kDa, 0.8 mg C·l <sup>-1</sup>	1	42	79	121	159	<b>402</b>
HSNOM ≤ 5 kDa, 3.0 mg C·l <sup>-1</sup>	4	25	74	84	120	<b>306</b>
HSNOM 0.5 mg C·l <sup>-1</sup>	3	4	14	38	80	<b>139</b>
HSNOM 5.0 mg C·l <sup>-1</sup>	0	3	8	2	22	<b>35</b>

Table D-6: DOC concentrations during scaling experiments on virgin (*Reference*) and NOM pre-fouled membranes. For *Reference*, values are presented as mean values  $\pm$  SD ( $n = 10$ ).

<i>operating time</i>	5 min	120 min	240 min
<b>Reference</b>			
	<i>c</i> <sub>DOC</sub> / mg·l <sup>-1</sup>		
virgin	0.40 $\pm$ 0.21	0.42 $\pm$ 0.16	0.50 $\pm$ 0.23
<b>pre-fouling</b>			
	<i>c</i> <sub>DOC</sub> / mg·l <sup>-1</sup>		
HSNOM	0.25	0.34	0.39
SAHA	0.36	0.32	0.43
BSA	0.26	0.29	0.31
SA	0.25	0.31	0.35
<b>HSNOM fouling intensity</b>			
	<i>c</i> <sub>DOC</sub> / mg·l <sup>-1</sup>		
'low'	0.38	0.37	0.45
'medium'	0.25	0.34	0.39
'intensive'	0.22	0.31	0.32

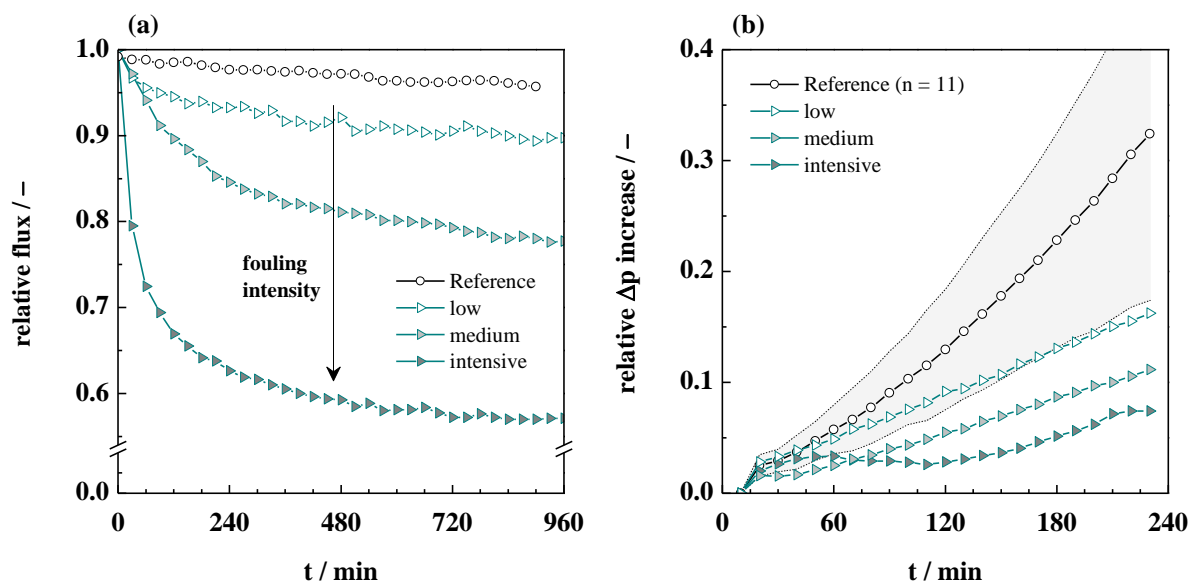


Figure D-18: (a) Flux decline during different HSNOM pre-fouling intensities and (b) increase of relative transmembrane pressure ( $\Delta p$ ) during subsequent gypsum surface scaling experiments. Grey area in (b) identifies standard deviation of reference experiments ( $n = 11$ ).

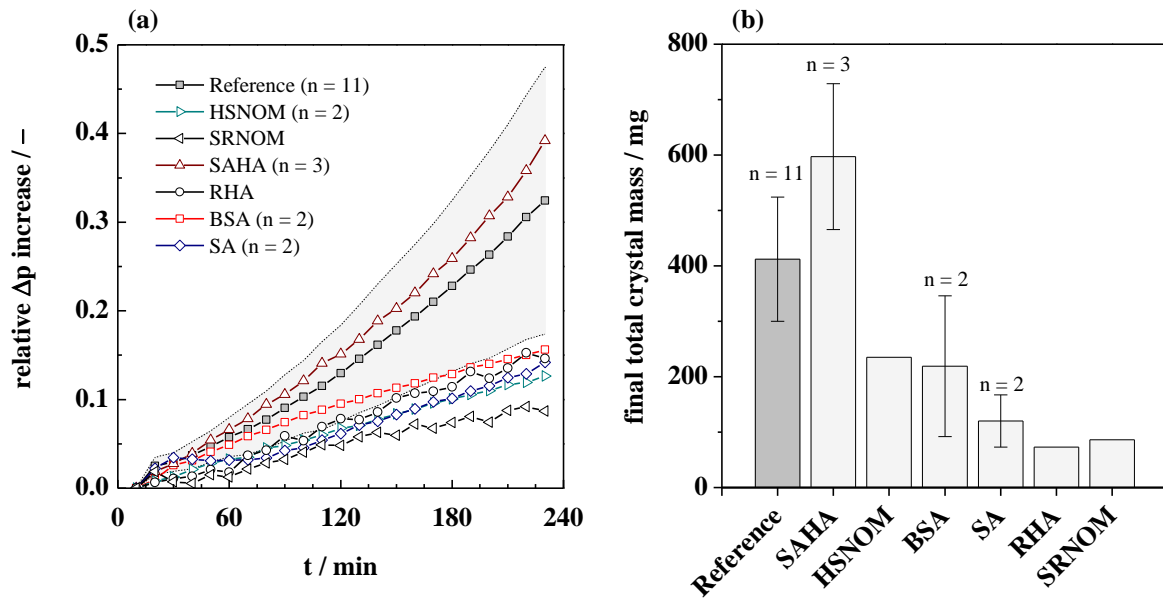


Figure D-19: (a) Increase of relative transmembrane pressure ( $\Delta p$ ) during gypsum surface scaling experiments in the presence of different NOM sources at a concentration of  $3 \text{ mg C}\cdot\text{l}^{-1}$  NOM. Grey area identifies standard deviation of reference experiments. (b) Corresponding final total crystal masses with error bars representing standard deviation.

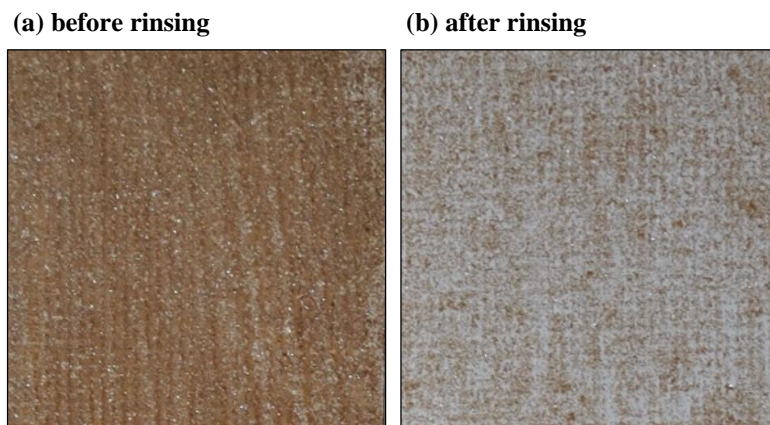
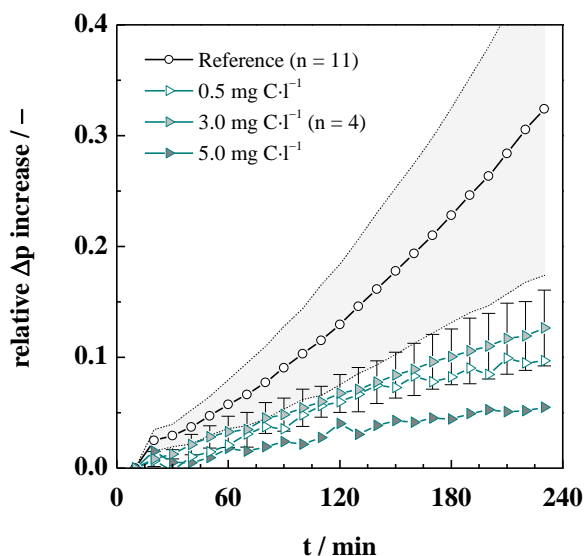


Figure D-20: Fouling layer by SAHA (a) before and (b) after gentle rinsing with ultrapure water.

Table D-7: DOC depletion during gypsum surface scaling experiments in the presence of  $3 \text{ mg C}\cdot\text{l}^{-1}$  NOM (Figure 7-7).

t / min	DOC depletion / %					
	SAHA	RHA	HSNOM	SRNOM	SA	BSA
120	32.0	25.8	2.0	8.7	57.0	4.0
240	44.4	37.9	3.6	5.3	65.3	2.1
number of experiments (n)	3	1	2	1	1	1



**Figure D-21:** Increase of relative transmembrane pressure ( $\Delta p$ ) during gypsum surface scaling in the absence (*Reference*) and presence of different HSNOM concentrations. Grey area (*Reference*) and error bars (HSNOM at 3 mg C·l<sup>-1</sup>) indicate standard deviation of repeated experiments.

**Table D-8:** Colloid concentration (NTA measurement), DOC removal, DOC-specific UV-vis absorbance at  $\lambda = 254$  nm ( $SUVA_{254}$ ) and  $\lambda = 436$  nm ( $SA_{436}$ ) and oxidation yields ( $\Phi_{UV}$ ) before and after UF fractionation of SAHA and HSNOM stock solutions. \* Oxidation yields were obtained from LC-OCD analysis performed at a DOC concentration of 3 mg·l<sup>-1</sup>. n.d.: none detected.

		SAHA	≤ 150 kDa	HSNOM	≤ 5 kDa	after PAC
<b>colloid concentration</b>	mg C <sup>-1</sup>	6.4·10 <sup>11</sup>	n.d.	0.1·10 <sup>11</sup>	n.d.	n.d.
<b>DOC removal</b>	%	–	83.5	–	74.3	98.6
<b><math>SUVA_{254}</math></b>	l·m <sup>-1</sup> ·mg <sup>-1</sup>	10.30	11.20	4.91	3.04	0.16
<b><math>SA_{436}</math></b>	l·m <sup>-1</sup> ·mg <sup>-1</sup>	1.91	1.79	0.04	0.14	0.03
<b>oxidation yield (<math>\Phi_{UV}</math>)*</b>	%	74.5	100.0	89.7	86.3	–

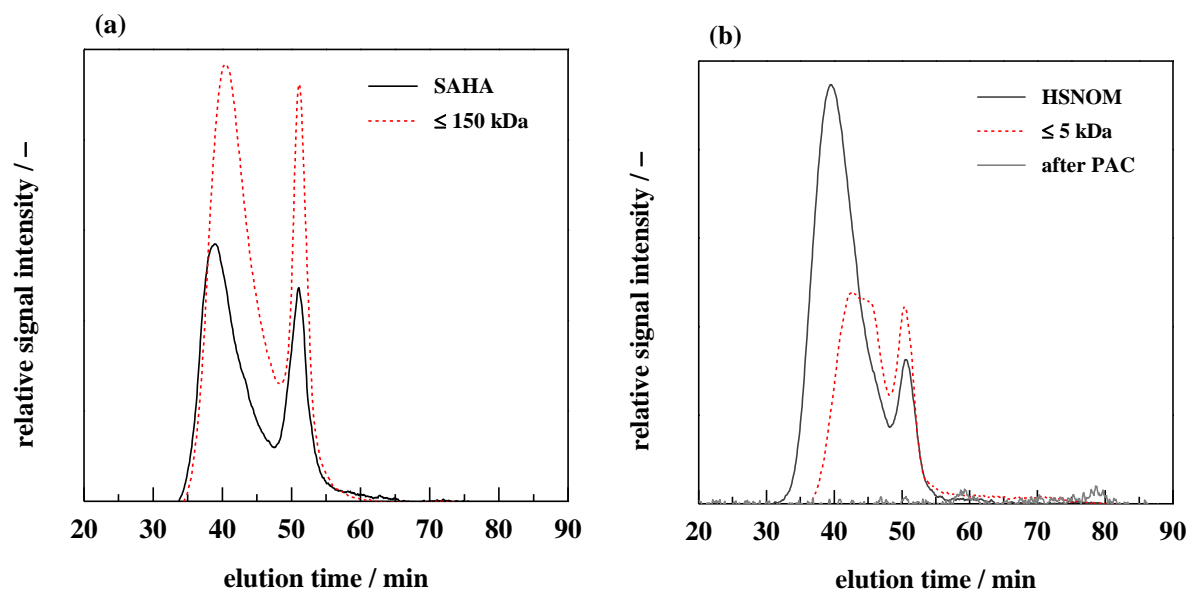


Figure D-22: LC-OCD chromatograms of (a) SAHA and SAHA  $\leq 150$  kDa fraction and (b) HSNOM,  $\leq 5$  kDa HSNOM fraction and non-adsorbable HSNOM fraction ('*HSNOM after PAC*'). All samples except for '*HSNOM after PAC*' were diluted to a DOC concentration of  $3.0 \text{ mg}\cdot\text{l}^{-1}$  as quantified by combustion catalytic oxidation. '*HSNOM after PAC*' was analyzed without further dilution at a DOC concentration of  $0.3 \text{ mg}\cdot\text{l}^{-1}$  as quantified by combustion catalytic oxidation.

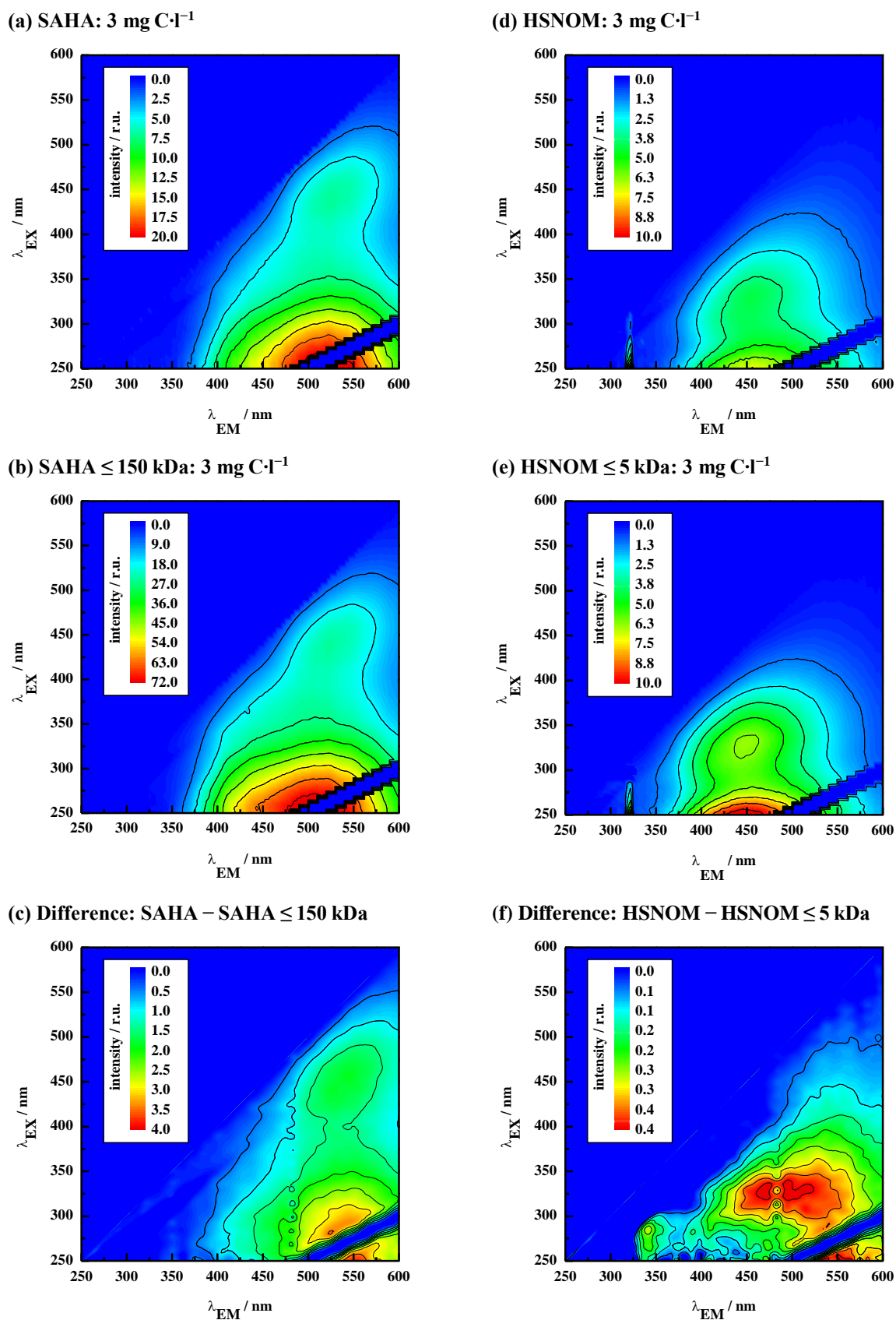


Figure D-23: FEEMs obtained from fluorescence spectroscopy of (a) SAHA, (b) SAHA ≤ 150 kDa fraction, (d) HSNOM and (e) HSNOM ≤ 5 kDa fraction diluted in ultrapure water to a DOC concentration of 3.0 mg·l<sup>-1</sup> and a pH of 7.0. FEEMs in (c) and (f) show the fluorescent fractions removed by UF fractionation.

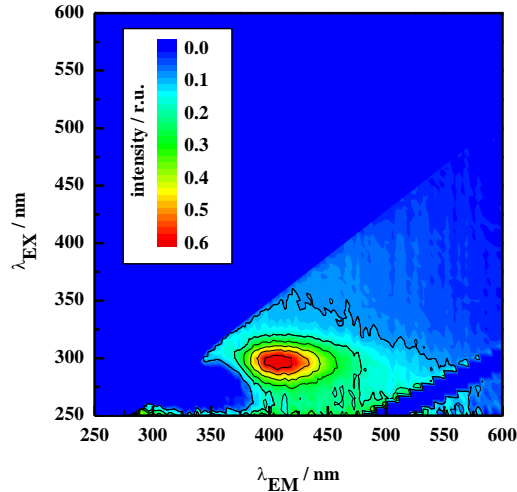


Figure D-24: FEEM obtained from fluorescence spectroscopy of ‘HSNOM after PAC’. Sample DOC concentration was  $0.3 \text{ mg}\cdot\text{l}^{-1}$  and  $pH$  was 7.0.

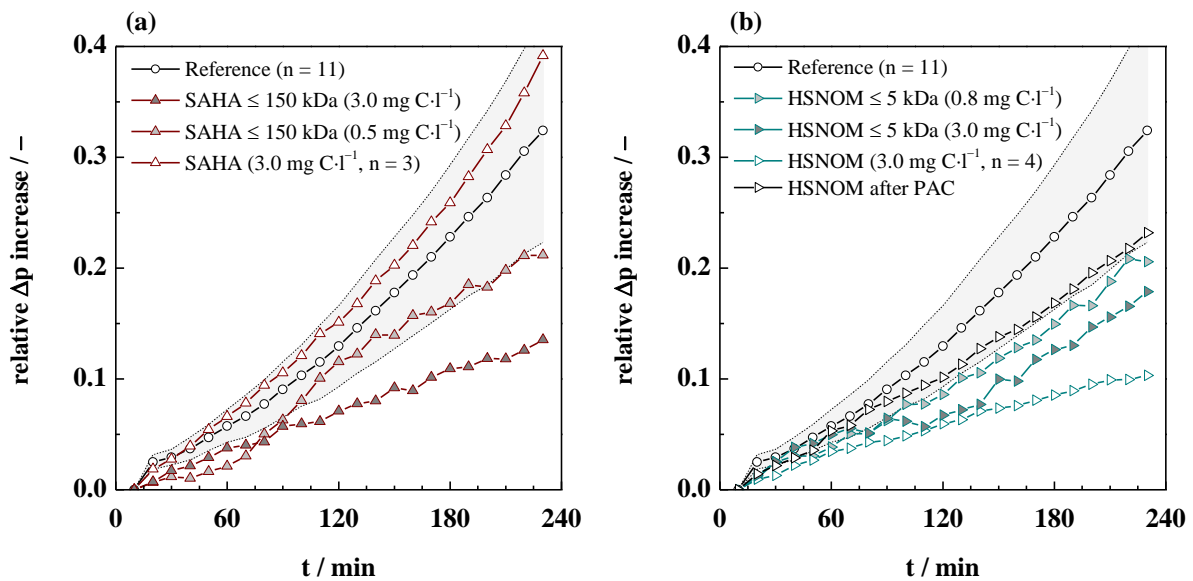


Figure D-25: Increase of relative transmembrane pressure ( $\Delta p$ ) during gypsum surface scaling in the presence of (a) SAHA and  $\leq 150 \text{ kDa}$  SAHA fraction and (b) HSNOM,  $\leq 5 \text{ kDa}$  HSNOM fraction and HSNOM after PAC. Grey areas identify standard deviation of reference experiments (n = 11).

## E. Appendix V – List of Publications

Selected contents of this thesis have been published as follows:

### Journal publications

- J. Benecke, M. Haas, F. Baur, M. Ernst, Investigating the development and reproducibility of heterogeneous gypsum scaling on reverse osmosis membranes using real-time membrane surface imaging, *Desalination* 428 (2018) 161–171. DOI: 10.1016/j.desal.2017.11.025.
- J. Benecke, J. Rozova, M. Ernst, Anti-scale effects of select organic macromolecules on gypsum bulk and surface crystallization during reverse osmosis desalination, *Separation and Purification Technology* 198 (2018) 68–78. DOI: 10.1016/j.seppur.2016.11.068.
- J. Benecke, J. Rozova, M. Ernst, Einfluss natürlicher organischer Wasserinhaltsstoffe auf das Scaling durch Gips bei der Umkehrosmose, *vom Wasser* 113 (2) (2015) 59–61.

### Oral presentations

- M. Ernst, J. Benecke, J. Rozova, F. Baur, M. Haas, Scaling-Prozesse in der Umkehrosmose: Natürliche Organik macht den Unterschied, *gat | wat* 2017, Nov 28–30, 2017, Cologne, Germany.
- J. Benecke, F. Baur, M. Haas, M. Ernst, Gypsum Scaling Behavior and Characterization during Reverse Osmosis in the Presence of Natural Organic Matter, 16<sup>th</sup> International Conference on Chemistry and the Environment 2017, Jun 18–22, 2017, Oslo, Norway.
- J. Benecke, M. Haas, F. Baur, M. Ernst, Investigation of surficial gypsum scaling during reverse osmosis desalination by real-time membrane surface imaging, IWA 9<sup>th</sup> Eastern European Young Water Professionals Conference 2017, May 24–27, 2017, Budapest, Hungary.
- J. Benecke, F. Baur, M. Haas, M. Ernst, Einfluss von Huminstoffen und deren Fouling auf das oberflächige Gipsscaling bei der Umkehrosmose, *Wasser 2017: Jahrestagung der Wasserchemischen Gesellschaft – Fachgruppe in der Gesellschaft Deutscher Chemiker e.V.*, May 22–24, 2017, Donaueschingen, Germany.
- J. Benecke, J. Rozova, M. Ernst, Anti-Scale Effects of dissolved organic carbon on gypsum scaling during reverse osmosis desalination, 12<sup>th</sup> World Filtration Congress (*WFC 12*), Apr 11–15, 2016, Taipei, Taiwan.
- J. Benecke, M. Ernst, Einfluss natürlicher organischer Makromoleküle auf das Gipsscaling bei der Umkehrosmose, 3. Workshop des FSP „Klimaschonende Energie- und Umwelttechnik“, Technische Universität Hamburg-Harburg, Jun 12, 2015, Hamburg, Germany.
- J. Benecke, J. Rozova, M. Ernst, Gypsum scaling in reverse osmosis desalination - Effects of natural organic macromolecules, 15<sup>th</sup> Network Young Membranes (*NYM 2015*), Sep 4–5, 2015, Aachen, Germany.

- J. Benecke, J. Rozova, M. Ernst, Einfluss natürlicher organischer Wasserinhaltsstoffe auf das Scaling durch Gips bei der Umkehrosmose, Wasser 2015: Jahrestagung der Wasserchemischen Gesellschaft – Fachgruppe in der Gesellschaft Deutscher Chemiker e.V., May 11–13, 2015, Schwerin, Germany.

### **Poster presentations**

- J. Benecke, F. Baur, M. Haas, M. Ernst, Gypsum scaling behavior on virgin and organically pre-fouled reverse osmosis membranes, 11<sup>th</sup> International Congress on Membranes and Membrane Processes (*ICOM 2017*), Jul 29 – Aug 4, 2017, San Francisco, USA.
- J. Benecke, M. Haas, M. Ernst, Untersuchung von Scaling während der Umkehrosmose mittels Echtzeit-Bilderfassung der Membranoberfläche, 4. Workshop des FSP „Klimaschonende Energie- und Umwelttechnik“, Technische Universität Hamburg-Harburg, Nov 30, 2016, Hamburg, Germany.
- J. Benecke, M. Haas, M. Ernst, Untersuchung von Scaling während der Umkehrosmose mittels Echtzeit-Bilderfassung der Membranoberfläche, Wasser 2016: Jahrestagung der Wasserchemischen Gesellschaft – Fachgruppe in der Gesellschaft Deutscher Chemiker e.V., May 2–4, 2016, Bamberg, Germany.
- J. Benecke, M. Ernst, Effects of organic macromolecules on gypsum scaling during reverse osmosis desalination, 1<sup>st</sup> Hamburg Membrane-Workshop: Materials, Functionalities, Applications, Technische Universität Hamburg-Harburg, Mar 30, 2015, Hamburg, Germany.
- J. Benecke, M. Ernst, Umweltverträgliche Strategien zur Prävention von Fouling- und Scalingprozessen bei der Hochdruck-Membranfiltration, 2. Workshop des FSP „Klimaschonende Energie- und Umwelttechnik“, Technische Universität Hamburg-Harburg, Dec 9, 2013, Hamburg, Germany.

## **F. Appendix VI – List of Supervised Student Theses**

The following M.Sc., B.Sc. and project theses were conducted within the scope of this thesis:

### **M.Sc. theses**

- C. Bauernschmidt, Surficial gypsum scaling on reverse osmosis membranes in the presence of humic substances, M.Sc. thesis, January 2017.
- F. Baur, Impacts of organic fouling on heterogeneous gypsum scaling during reverse osmosis desalination, M.Sc. thesis, August 2016.
- M. Haas, Kinetic observations of gypsum scale development on a reverse osmosis membrane by real-time visual surface imaging during desalination, M.Sc. thesis, January 2016.
- J. Rozova, Incipient crystallization of gypsum in aqueous solutions and reverse osmosis desalination – reproducibility and effects of antiscalants and natural organic matter, M.Sc. thesis, December 2014.

### **B.Sc. theses**

- L. Gormsen, Changes of zeta potential and contact angle of reverse osmosis membranes due to organic fouling, B.Sc. thesis, March 2016.

### **Project theses**

- T. Struve, Impact of supersaturation, pH value and natural organic macromolecules on gypsum crystallization in aqueous solution, Project work, October 2016.
- P. Shaheen, Impact of natural organic macromolecules on gypsum crystallization kinetics in aqueous solution, Project work, May 2016.

